Development of Computational Multiaxial Fatigue Modelling For Notched Components

by

Ayhan Ince

A thesis
presented to the University of Waterloo
in fulfillment of the
thesis requirement for the degree of
Doctor of Philosophy
in
Mechanical Engineering

Waterloo, Ontario, Canada, 2012

I hereby declare that I am the sole author of this thesis. This is a true copy of the thesis, including any required final revisions, as accepted by my examiners.

I understand that my thesis may be made electronically available to the public.

Abstract

Fatigue failures of driveline and suspensions components for ground vehicles under multiaxial loading conditions are common, since most those components are subjected to complex multiaxial loadings in service. In addition to the multiaxial loadings, many of those components contain notches and geometrical irregularities where the fatigue failure often occurs due to stress concentrations. Therefore, the origins of the multiaxiality can be related to various combinations of external loadings and notch geometries.

A computational fatigue analysis methodology has been proposed here for performing multiaxial fatigue life prediction for notched components using analytical and numerical methods. The proposed multiaxial fatigue analysis methodology consists of an elastic-plastic stress/strain model and a multiaxial fatigue damage parameter. The multiaxial stress-strain notch analysis method originally proposed by Buczynski and Glinka is adapted to develop the elastic-plastic stress/strain model to compute local stress-strain responses using linear elastic FE results of notched components. An original multiaxial fatigue damage parameter based on the maximum fatigue damage plane is proposed to predict the fatigue life for notched components under multiaxial loadings.

Results of the proposed multiaxial fatigue analysis methodology are compared to sets of experimental data published in the literature to verify the prediction capability of the elastic-plastic stress/strain model and the multiaxial fatigue damage parameter. Based on the comparison between calculated results and experimental data, it is found that the multiaxial elastic-plastic stress/strain model correlates well with experimental strain data for SAE 1070 steel notched shafts subjected to several non-proportional load paths. The proposed

multiaxial fatigue damage parameter, when applied to the uniaxial loading to account for the mean stress effect on fatigue life, is found to correlate very well with four sets of experimental uniaxial mean stress fatigue data. In the case of multiaxial loadings, the proposed multiaxial fatigue damage parameter provides very good correlation with experimental fatigue data of thin-walled tube specimens of 1045 steel and Inconel 718. In addition, the proposed fatigue damage parameter is found to correlate reasonably well with experimental fatigue data of SAE 1045 steel notched shafts subjected to proportional and non-proportional loadings.

The proposed multiaxial fatigue analysis methodology enables rapid durability evaluation for notched components design. The effect of changes in material, geometry and loads on the fatigue life can then be assessed in a short time frame. The proposed multiaxial fatigue analysis methodology provides more efficient and appropriate analysis methods preferable to very expensive experimental durability tests and more complex and time consuming life prediction methods using non-linear FE stress-strain analysis.

Acknowledgements

I would like to thank my supervisors, Professor Grzegorz Glinka and Professor Hamid Jahed for their guidance, technical support, and helpful discussions during the course of this project.

I would also like to thank all my fellow graduate students for their support and encouragement. In particular, I am grateful to Mohammad Noban for his help and friendship. Additionally, I would also like to thank my colleague, Terry Martin for his time spent by reading my thesis and correcting my grammars.

Finally, I would like to express my profound gratitude to my wife, Munise and my son, Beren for their support and encouragement throughout my education and professional career.

Table of Contents

List of Figures

List of Tables

Nomenclature

a_{ij}	back stress tensor
b	axial fatigue strength exponent
c	axial fatigue ductility exponent
D	fatigue damage
ΔD_i	damage increment associated with the critical plane
$D_{\max}$	maximum damage on the critical plane
dp	equivalent plastic strain rate
e	nominal section strain
E_T^p	current value of the plastic modules
ΔE_A	total strain energy due to pure tension
ΔE_T	total strain energy due to pure torsion
E	modulus of elasticity
F	yield function
G	shear modulus
K'	cyclic strength coefficient
K_t	elastic stress concentration factor
P	axial load
Q	torsional load
n_{ij}	components of the unit normal to the yield surface
n'	cyclic strain hardening exponent
N	number of cycle
N_f	number of cycle to failure
R	stress ratio
S_{ij}	deviatoric stress tensor
S	stress for nominal section
t	time
T	torque

W^t	total strain energy density
W^p	plastic strain energy density
W^{e+}	positive elastic strain energy density
$d\lambda$	scalar valued function
ε	strain
ε_a	strain amplitude
ε 'f	fatigue ductility coefficient
ε_{ij}	strain tensor
$d\varepsilon_{ij}^{\ p}$	plastic strain increment tensor
$d\varepsilon_{ij}^{\ e}$	elastic strain increment tensor
$\Delta\varepsilon$	strain range
$\Delta\varepsilon_{ij}^{\ p}$	plastic strain increments
$\Delta\varepsilon_{ij}^{\ e}$	elastic strain increments
$\Delta\varepsilon_{ij}^{\ a}$	actual elastic-plastic strain increments
$\Delta\sigma_{ij}^{\ e}$	pseudo-elastic stress components
$\Delta\sigma_{ij}^{\ a}$	actual stress components
$\Delta\varepsilon_n$	normal strain range on the plane of maximum shear strain
$\Delta\varepsilon_n^{\ e}$	elastic normal strain range on the plane of maximum shear strain
$\Delta\varepsilon_n^{\ p}$	elastic normal strain range on the plane of maximum shear strain
$\Delta\varepsilon_{eq}^{pa}$	equivalent plastic strain increment
$\varepsilon_{eq}^{\ p}$	equivalent total plastic strain
ε^e	fictitious strain
ε^a	elastic-plastic notch tip strain
$\Delta\gamma_{max}$	maximum shear strain range
$\Delta\gamma_{max}^{\ e}$	maximum elastic shear strain range
$\Delta\gamma_{max}^{\ p}$	maximum plastic shear strain range

δ_{ij}	kronecker delta δ_{ij} = 1 for i = j and δ_{ij} = 0 for i ≠ j
ϕ	scalar valued function dependent on the equivalent stress
ν	Poisson's ratio
ν_e	elastic Poisson's ratios
ν_p	plastic Poisson's ratios
σ^a	elastic-plastic notch tip stress
σ_{max}	maximum principal stress
σ_{min}	minimum principal stress
σ_x, σ_y, τ_{xy}	stress components
σ	stress
σ'_f	fatigue strength coefficient
σ^e	fictitious stress
σ_{ij}	stress tensor
$\sigma_{ij,max}$	components of maximum stress tensor
σ_{eq}	equivalent stress
$\Delta\sigma_{eq}{}^a$	actual equivalent stress increment
σ_a	stress amplitude
$\Delta\sigma$	stress range
σ_m	mean stress
$\sigma_{n,mean}$	mean normal stress on the plane of maximum shear strain
$\sigma_{n,max}$	maximum normal stress on the plane of maximum shear strain
σ_y	yield strength
$\sigma(t)$	instantaneous microscopic hydrostatic stress
$\tau(t)$	instantaneous microscopic shear stress
τ_{max}	maximum shear stress
τ'_f	shear fatigue strength coefficient

Chapter 1
Introduction and Research Objectives

Most driveline and suspensions components, such as axles and shafts for ground vehicles, are subjected to combined cyclic tension, bending and torsional loads during operations in service. These complex cyclic loadings are defined as multiaxial loadings, where principal stresses rotate and change non-proportionally their magnitudes during a loading cycle. In addition, many of machine components contain notches and geometrical irregularities because of design requirements. These geometric discontinuities cause significant stress concentrations. Multiaxial loading paths produce complex stress and strain states near notches and can cause a fatigue failure even without any evident large-scale plastic deformation. Unfortunately, the combination of multiaxial loading paths and complex geometries of mechanical components is unavoidable in practice and experiments performing durability test are often not feasible because of time and cost considerations. Therefore, analytical and numerical methods are an indispensable approach to conduct fatigue and durability analyses for notched components design process.

Due to the fact that notch regions are under the effect of multiaxial stress state, the fatigue strength and durability estimations of notched components subjected to multiaxial loading paths require detail knowledge of stresses and strains in such regions. Although Finite Element Analysis (FEA) using commercial software tools can be used to determine notch tip stresses in the elastic and elastic-plastic state induced by short loading histories (a few cycles), such methods are still impractical in the case of long load histories experienced by real machine components. Cyclic loading histories experienced

by notched components in driveline and suspension systems may contain from thousands to millions of cycles. Therefore, an incremental elastic-plastic finite element analysis for long loading histories would require impractically long computation times and excessive data storage. For these reasons, more efficient and simpler methods of elastic-plastic stress-strain analysis and fatigue life estimations are necessary for notched bodies subjected to lengthy cyclic load histories.

The main goal of the research scope of this thesis develops and validates an integrated multiaxial fatigue analysis methodology. The computational methodology developed here focuses on the multiaxial elastic-plastic stress/strain analysis and fatigue life predictions for notched bodies subjected to proportional and non-proportional loading histories. More specifically, the following research objectives were undertaken:

- To create finite element model(s) to compute linear elastic stress histories for notched specimens under multiaxial loading paths.
- To develop an algorithm and computer program for the implementation of the multiaxial stress/strain analysis in notches by integrating the Garud cyclic plasticity model with the multiaxial Neuber rule. The linear elastic stress data from the FE model is used as input to this computer program.
- To develop and validate a multiaxial fatigue damage parameter based on a critical plane approach to estimate fatigue life of notched components.
- To develop a general algorithm for the numerical implementation of the integrated multiaxial fatigue analysis for notched components.

In order to accomplish these objectives, an integrated multiaxial fatigue analysis methodology has been proposed. The proposed analysis methodology is composed of:

- An elastic-plastic stress/strain model for computing the material stress-strain response of notched components under multiaxial loadings.
- A multiaxial fatigue damage parameter to estimate fatigue life.

The elastic-plastic stress/strain model consist of two parts namely the cyclic plasticity model and the multiaxial Neuber notch correction rule to compute the actual elastic-plastic stress-strain response at notches using the FE linear elastic stress data. The computed elastic-plastic stress-strain responses are subsequently used as input to the proposed multiaxial fatigue damage parameter to estimate the fatigue life.

A general computational process, shown in Figure 1-1, is proposed to implement the multiaxial fatigue analysis methodology. The following procedure summarizes the three main computation steps necessary for carrying the methodoloy.

I. Multiaxial elastic-plastic stress-strain analysis

- Calculate elastic-plastic stress-strain histories at the critical notch location using the input linear elastic stress histories obtained from the linear elastic FE analysis (Multiaxial elastic-plastic stress-strain analysis in Figure 1-1).

II. Multiaxial fatigue analysis

- Transform the stress and strain time history to potential candidate planes (Stress-strain tensor rotation in Figure 1-1).

- Calculate fatigue damage on each potential critical plane using the proposed fatigue damage parameter (Fatigue damage parameter in Figure 1-1).
- Determine the critical plane experiencing the maximum fatigue damage and predict the fatigue life on that plane (Fatigue life prediction in Figure 1-1).

III. Fatigue damage map

- Plot the fatigue damage on the FE model to obtain the damage map (Damage contour of FE model in Figure 1-1).

A schematic representation of these computation steps mentioned above is shown in Figure 1-1. This dissertation is structured as follows: Existing literature in the area of cyclic plasticity, notch correction methods, and multiaxial fatigue damage parameters is reviewed in Chapter 2. The literature review is followed by a detailed description of the elastic-plastic stress-strain analysis method for notched bodies subjected to multiaxial cyclic load paths in Chapter 3. Chapter 4 describes the proposed multiaxial fatigue damage parameter and the implementation of the integrated multiaxial fatigue analysis procedure by incorporating the elastic-plastic stress/strain model and multiaxial fatigue damage parameter. Chapter 5 presents case studies for validation of the elastic-plastic stress/strain model and the multiaxial fatigue damage parameter. Chapter 6 contains concluding remarks and recommendations for future research activities.

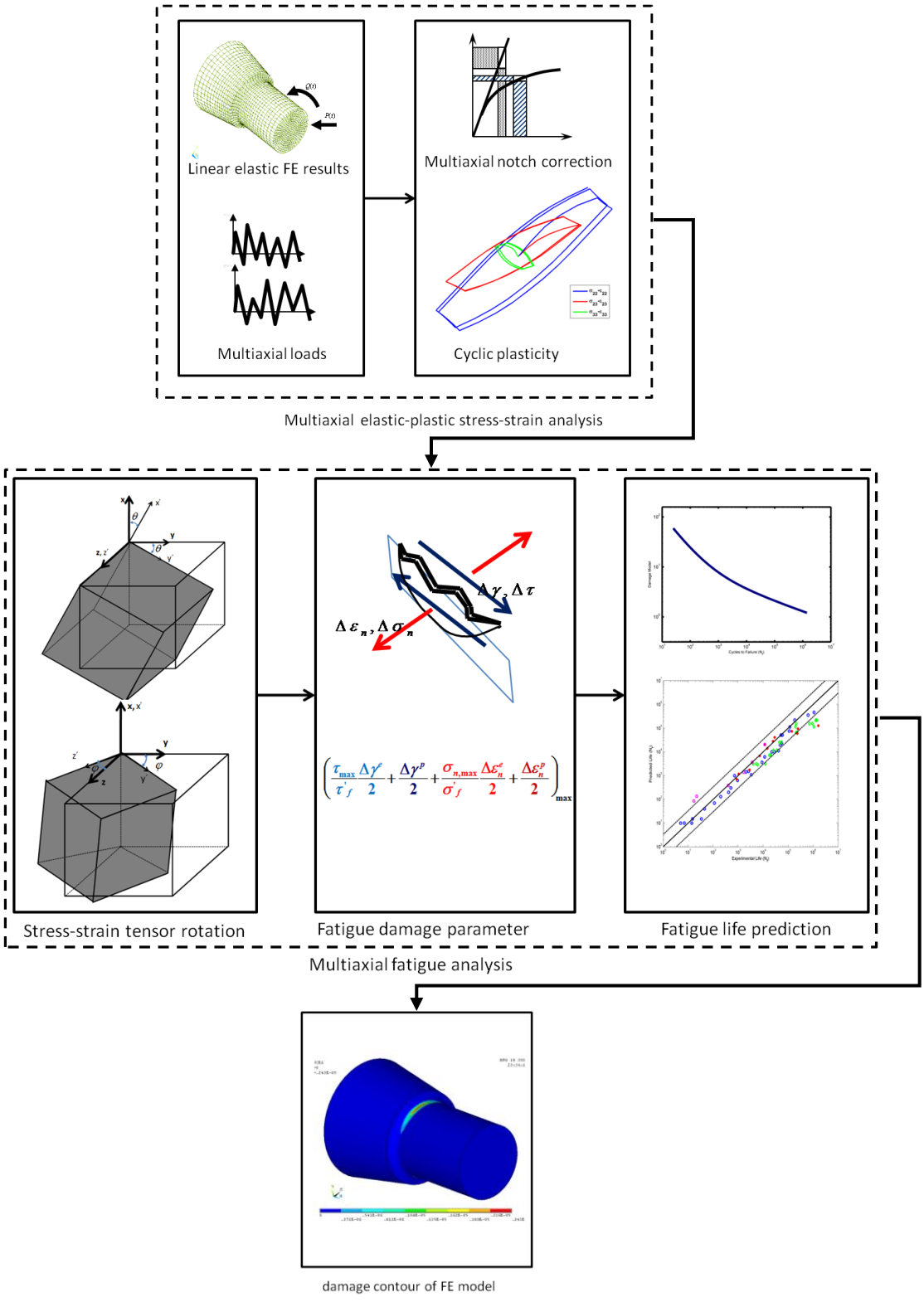

Figure 1-1: Computational flow chart of the integrated multiaxial fatigue analysis

Chapter 2
Literature Review

Fatigue failure is considered to be the most common type of failure mode experienced by most engineering components. Many mechanical components contain geometric discontinuities and stress concentrations which cannot be avoided in practice. Fatigue cracks in most cases occur at or near notch roots, therefore notches have been considered as one of the most important problems in the design of machine components. Fatigue life prediction for notched components experiencing cyclic loadings has long been subject of research in many different industries, particularly in the automotive industry. In addition, most of mechanical notched components are subjected to biaxial/multiaxial loadings such as combinations of bending and torsion or tension and torsion in services. Fatigue life prediction for notched components based on the local strain approach and equivalent stress/strain criteria has shown limited success in case of relatively simple load cases e.g. uniaxial and proportional loadings [1]. However, no successful fatigue life prediction methodology has been developed, which accurately account for the complex nature of material behavior and multiaxial stress state in notches under complex non-proportional loadings. As a result, the design of notched components, particularly for those under complex multiaxial loadings has been based on the use of conservative factors of safety, expensive prototype testing, and experience. There is growing need for a reliable and efficient multiaxial fatigue prediction methodology for notched components in order to satisfy the increasing demand in design requirements in terms of weight savings, cost reductions and life expectancies. In order to model the fatigue failure of notched components under the multiaxial cyclic loadings, it is essential

to provide a good understanding of how external loads relate to the state of stress and strain at the critical location, material constitutive behavior, multiaxial damage parameter and cumulative damage. In this section, an attempt has been made to review stress-strain analysis using material constitutive behavior, coupling of stress-strain analysis with notch correction method, multiaxial fatigue damage parameters and cumulative damage rule.

The effort to develop more reliable and efficient multiaxial fatigue life evaluation procedure for notched components must begin with a review of stress-strain analysis at notch roots and multiaxial fatigue life prediction methods.

2.1 **Stress Strain Plasticity Modelling**

Most components are designed never to exceed the yield stress. However, local plastic deformations are common in stress concentration areas under cyclic loadings. Even though the material behavior in the net section area is in the elastic range, the stress-strain response at the notch area may often show elastic-plastic behavior. Therefore, a cyclic plastic model coupled with the notch correction method is required to determine the elastic-plastic material behavior at the notch area.

The Ramberg-Osgood equation originally proposed [2] as a monotonic stress-strain relation, is commonly used to represent a uniaxial stress-strain model for cyclic loadings. The response of material subjected to cyclic loadings typically takes the form of stress-strain hysteresis loops, shown in Figure 2-1 for several different strain amplitudes. The line O-A-B-C, which passes through the tips of the loops, is the cyclic stress-strain curve.

$$\varepsilon_a = \frac{\sigma_a}{E} + \left(\frac{\sigma_a}{K'}\right)^{1/n'} \tag{2.1}$$

Massing [3] hypothesized that the stabilized hysteresis loop curves may be approximated by doubling the cyclic stress-strain curve. Therefore, the stresses and strains for the unloading part of the load history, such as C-H-F in Figure 2-1, can be determined using Eq. (2.2).

$$\frac{\Delta\varepsilon}{2} = \frac{\Delta\sigma}{2E} + \left(\frac{\Delta\sigma}{2K'}\right)^{1/n'} \tag{2.2}$$

When the multiaxial loading induces elastic deformation, relations between stresses and strains are determined based on Hooke's Law as follows

$$\varepsilon_{ij} = \frac{1}{2G}\sigma_{ij} - \frac{\nu}{E}\sigma_{kk}\delta_{ij} \tag{2.3}$$

Where ε_{ij}, σ_{ij}, G, E, ν and δ_{ij} are the strain tensor, stress tensor, shear module, Young's module, Poisson's ratio and Kronecker's delta respectively. Stresses are computed from any set of strains independent of the strain history.

However, when the cyclic multiaxial loading induces the local plastic deformation on components due to presence of notches and geometric discontinues, stresses and strains during cyclic plastic deformation are dependent on the previous loading history, and an incremental plasticity model is required for proper stress and strain analyses of plastically deformed locations. The cyclic plasticity modelling is employed to model the stress/strain response of a material subject to a known load path.

Unlike the uniaxial cycle stress-strain curve, the multiaxial stress-strain state during cyclic plastic deformation requires a cyclic plasticity model to model multiaxial

stress-strain behavior of a material. These cyclic plasticity models are employed in incremental form. An appropriate cyclic plasticity model includes three major components, yield function, flow rule and hardening rule respectively. A yield function describes a region for elastic and plastic material behavior, a flow rule defines relations between stresses and increments of plastic strain, and a hardening rule describes how the yield function changes during the course of plastic deformation.

In several past decades, many plasticity models have been developed modelling the material behavior using different levels of complexity from simple to complicated solutions. Modelling complex material behaviour such as cyclic hardening/softening, ratcheting, and non-proportional hardening requires extensive material testing to determine material constants required for the modelling of complex material behaviours. It is intended in this research to focus on a plasticity model for its simplicity and efficiency to model the material stress-strain responses with a reasonable accuracy. Such a plasticity model is considered to be suitable for multiaxial fatigue analysis in the ground vehicle industry.

2.1.1 Yield Function

An important subject in plasticity is the concept of yield surface. For the perfect plastic materials, the yield surface does not change after yielding. In contrast, for most materials, this surface changes for the values of stress beyond the initial yield point according to a hardening rule. The criterion for initiation of plastic deformation in uniaxial loading is when the axial load reaches the yield stress point, σ_y. The material yield is the stress point where a material starts to deform plastically. In a multiaxial stress state, a yield criterion describes how each stress component contributes to yielding. In other words, the

yield criterion describes how a multiaxial state of stress combines to create an equivalent stress that induce to the plastic deformation. Thus the multiaxial state of stress can be represented by the equivalent stress as a scalar value. The yield surface concept is used to describe a yield function. The yield function represented by 9 dimensional hypersurface in stress spaces and each stress component in the stress tensor corresponds to a dimension. If $f(\sigma_{ij})$is the loading function and σ_y is a yield function depending on previous stress and strain history of the material, yielding occurs as $f(\sigma_{ij})$ becomes equal to σ_y, and the yield function is defined as follows

$$F(\sigma_{ij}) = f(\sigma_{ij}) - \sigma_y = 0 \tag{2.4}$$

Three different loading conditions may occur for stress state on the yield surface. These loading conditions for the yield surface can be illustrated as follows.

- Elastic Loading: the stress state that is within the hyper surface or its direction is toward inside of the surface is elastic loading/unloading (Figure 2-2(a))
- Plastic Loading: the stress state on the boundary with its direction toward outside of the hyper surface is plastic loading (Figure 2-2 (b))
- Neutral Loading: the stress state on the boundary with its direction tangent to the hyper surface is neutral loading (Figure 2-2 (c))

There are two popular yield functions for ductile metals, Tresca and von Mises Criterion. Tresca criterion is defined as:

$$F(\sigma_{ij}) = |\sigma_{\max} - \sigma_{\min}| - \sigma_y = 0 \tag{2.5}$$

Where σ_{max} and σ_{min} maximum and minimum are principal stresses, and σ_y is the yield strength.

The von Mises criterion is the most popular for isotropic materials. The von Mises criterion states that material yielding starts when the distortion energy for the multiaxial stress state is equal to the distortion energy at yield in simple tension, and the von Mises criterion for a complex stress state is defined as:

$$F(\sigma_{ij}) = \frac{1}{2}\left[(\sigma_1 - \sigma_2)^2 + (\sigma_2 - \sigma_3)^2 + (\sigma_3 - \sigma_1)^2\right] - \sigma_y = 0 \tag{2.6}$$

The von Mises criterion can be described in deviatoric stress space as

$$\left(\frac{3}{2} S_{ij} S_{ij}\right) - \sigma_y{}^2 = 0 \tag{2.7}$$

For a general stress state, preference is usually given to von Mises criterion because it has a continuous and smooth shape in stress space.

2.1.2 Flow Rule

Another important component of the cyclic plasticity modelling is the flow rule. The flow rule represents the relationship between stresses and plastic strains during plastic deformation. For elastic-plastic loading, total strain tensor is the sum of elastic strain determined by Hooke's law and plastic strain governed by the flow rule. Hencky [4] proposed a relationship between total plastic strains and stresses. Assuming small strains, stress- the plastic strain relation proposed by Hencky can be written as

$$\varepsilon_{ij}{}^p = \phi S_{ij} \tag{2.8}$$

where ϕ is a scalar valued function depending on the equivalent stress (e.g. Mises equivalent stress), σ_{eq}, which may be regarded as a function of an equivalent total plastic strain, ${\varepsilon_{eq}}^{p}$, defined as

$$ {\varepsilon_{eq}}^{p} = \sqrt{\frac{2}{3}{\varepsilon_{ij}}^{p}{\varepsilon_{ij}}^{p}} \tag{2.9} $$

Experiments have shown that Hencky's equations are not consistent for all stress states and the stress is path dependent for non-proportional loading. However, Hencky's equations estimate unique state of stress for a given plastic strain, i.e. path independent. Therefore, they can be used for proportional loading, but are not suitable for non-proportional loading. The flow rule defines the relationship between stresses and plastic strain increments. The form of this relation, which uses the plastic strain increment, proposed by Prandtl [5] for plane strain and by Reuss [6] for an arbitrary state of strain in the following form

$$ d{\varepsilon_{ij}}^{p} = d\phi S_{ij} \tag{2.10} $$

where $d\phi$ is a factor of proportionality, which can be found using plastic work increments.

Drucker [7] later derived a more explicit form of the rule from thermodynamic considerations. The flow rule based on the normality postulate by Drucker implies that increment of plastic strain is in normal direction to the yield surface during plastic deformation. The flow rule can be described as

$$ d{\varepsilon_{ij}}^{p} = d\lambda\frac{\partial F}{\partial \sigma_{ij}} \tag{2.11} $$

Where $d\varepsilon_{ij}^{\ p}$ is the plastic strain increment tensor, σ_{ij} is the stress tensor, F is yield function, and $d\lambda$ is a scalar valued function.

The flow rule can be written in a more general form as

$$d\varepsilon_{ij}^{\ p} = \frac{1}{E_t^p} n_{ij}\left(n_{kl} d\sigma_{kl}\right) \tag{2.12}$$

Where E_t^p is the multiaxial representation of the plastic modulus and n_{ij} are the components of the unit normal to the yield surface and are defined as

$$n_{ij} = \frac{\dfrac{\partial F}{\partial S_{ij}}}{\left(\dfrac{\partial F}{\partial S_{ij}}\dfrac{\partial F}{\partial S_{ij}}\right)^{(1/2)}} \tag{2.13}$$

Based on consistency condition, upon unloading from stress above yield point, the initial behavior of the metal is always elastic, and during the plastic loading, yield surface follows the stress in stress space. As a result, the stress always remains on the yield surface. This is illustrated in Figure 2-3. Consistency condition leads to a basis for determining the movement of yield surface center in the hardening rule.

2.1.3 Hardening Rule

This dissertation is intended to review only major hardening models since more complex hardening models for ratcheting, transient hardening and nonlinear hardening are beyond the scope of this study.

A hardening rule, another important component for the plasticity modelling, describes how yield surfaces change during the course of plastic deformation. Based on

the consistency, the yield surface follows the stress during plastic loading. There are the three possible alternatives to explain the evolution of the yield surface.

- Yield surface expands with plastic loading, isotropic hardening.
- Yield surface translates without any expansion with plastic loading, kinematic hardening.
- Yield surface expands and translates with plastic loading, combined isotropic-kinematic hardening rules.

Isotropic hardening developed by Hill [8] describes the expansion of the yield surface during plastic deformation. In other words, the yield surface grows, however the center of the yield surface remains fixed. Such behavior for the uniaxial stress-strain curve is plotted in deviatoric stress space in Figure 2-4.

The yield surface for the isotropic hardening can be represented as

$$F = \frac{3}{2} S_{ij} S_{ij} - \sigma_y{}^2(k) = 0 \tag{2.14}$$

Where S_{ij} is the deviatoric stress tensor and $\sigma_y(k)$ is the current size of the yield surface as a function of k. The flow rule associated with the yield surface for the isotropic hardening can be described

$$d\varepsilon_{ij}{}^p = d\lambda \frac{3}{2} \frac{S_{ij}}{\sigma_e} \tag{2.15}$$

Where $\sigma_e = \sqrt{\frac{3}{2} S_{ij} S_{ij}}$ is the von Mises equivalent surface.

Isotropic hardening is capable of handling proportional and non-proportional loadings. However, if unloading and reverse loading is included, then the isotropic hardening rule is not able to model reverse yielding appropriately and hence is not useful in cyclic plasticity. The isotropic hardening rule is mainly used for the application of metal forming because of its ability to describe material behavior for large strain. The isotropic hardening rule can also be used with kinematic hardening for modelling cyclic plasticity.

In kinematic hardening, the yield surface is allowed to translate in stress space with no change in size or shape. Kinematic hardening for uniaxial stress-strain curve is shown in Figure 2-5. If a specimen is uniaxialy loaded beyond the yield stress, and then is unloaded and reloaded in uniaxial compression, the new yield stress in compression will be smaller than the original one. This is known as Bauschinger effect [9], as shown in Figure 2-5. Prager [10] was the first to introduce kinematic hardening. Based on the Prager's rule to satisfy consistency condition, yield surface has to move without any expansion to follow stress point in the stress space. He postulated that the center of the yield surface moves in the direction of the plastic increment:

$$da_{ij} = c d\varepsilon_{ij}^{\ p} \tag{2.16}$$

Where da_{ij} is the movement of the center of the yield surface, which has been also referred to as back stress, and c is a scalar constant determined from consistency condition.

For Prager's model, the yield surface for the kinematic hardening can be represented as

$$F = \frac{3}{2}\left(S_{ij} - a_{ij}\right)\left(S_{ij} - a_{ij}\right) - \sigma_{yo}^{\ 2} = 0 \tag{2.17}$$

The flow rule associated with the yield surface can be described as

$$d\varepsilon_{ij}^{\ p} = d\lambda \frac{3}{2} \frac{\left(S_{ij} - a_{ij}\right)}{\sigma_{yo}} \tag{2.18}$$

and the hardening rule is as

$$da_{ij} = c d\varepsilon_{ij}^{\ p} \tag{2.19}$$

One of the disadvantages of the Prager model was its application to only bilinear stress-strain curve. Mroz [11] defined a field of plastic moduli in stress space for better approximation of the stress-strain curve and generalization of the plastic modulus in multiaxial case. Each surface is represented by its center coordinates, a_{ij}^{k} , a yield stress, σ_{yo}^{k} and a plastic modulus, $E_t^{p(k)}$. If the von Mises criterion is used to represent the surface, the yield surface is defined as

$$F^{k}\left(S_{ij}, a_{ij}\right) = \frac{3}{2}\left(S_{ij} - a_{ij}^{k}\right)\left(S_{ij} - a_{ij}^{k}\right) - \sigma_{yo}^{k\ 2} = 0 \tag{2.20}$$

Figure 2-6 shows how these fields are defined and related to the stress-strain curve. For a virgin material this distribution is isotropic. When a stress point meets a stress surface, this surface will be activated. By increasing the load, the active surface and all of the previously activated surfaces (inner surfaces) move together, until unloading occurs. The plastic modulus takes on a value equal to that of the largest surface in contact with the stress point. Figure 2-7 (b)-(d) shows the evolution of the stress surfaces for a sequence of two loading paths, Figure 2-7 (a). Garud [12] showed a possibility of intersecting yield surfaces for Mroz model under certain loading, therefore he modified Mroz model to prevent such intersection. Movement of the surfaces in Garud's model is dependent on the stress direction. Chu [13] proposed an infinite surface model that does not require a

discrete number of surfaces. Chu's model only requires position and radius for the current active surface, thus eliminating the storage requirements of the multi surface discrete model for numerical solution of the cyclic plasticity model.

Two surfaces plasticity model initially was proposed by Krieg [14], and Dafalias and Popov [15] to reduce the multi surface model to two surfaces, the yield surface and limit surface. Two surfaces plasticity models were developed to improve computational efficiency by reducing the storage requirement of the multi surface models. Two surfaces models were later modified by Philips [16], Tseng and Lee [17].

Armstrong and Frederick [18] proposed a nonlinear kinematic model by considering the strain memory effect by a recovery term. Armstrong and Frederick specified the movement of the yield surface in deviatoric stress space by the nonlinear hardening rule.

$$da_{ij} = \frac{2}{3} C_1 d\varepsilon_{ij}^{\ p} + C_2 a_{ij} dp \tag{2.21}$$

Where dp is the equivalent plastic strain rate, and C_1 and C_2 are material constant determined from uniaxial tests.

Chaboche [19,20] made significant contributions to Armstrong-Frederick model by decomposing the backstress into several parts, each of which independently obeys the Armstrong-Frederick hardening rule.

$$da_{ij}^k = \frac{2}{3} C_k d\varepsilon_{ij}^{\ p} - \gamma_k a_{ij}^k dp \quad k = 1,...N \tag{2.22}$$

Where $d\varepsilon_{ij}^{\ p}$, dp and da_{ij}^{k} are increments of the plastic strain tensor, the equivalent plastic strain and the kth term of the increment of the back stress. C_k and γ_k are material constants which can be defined using the material's cyclic stress-strain curve.

Many other researchers, like Bower [21], Ohno [22], Voyijadis [23], Jiang and Kurath [24], and Chen et al [25] have since added various features to the original Armstrong-Frederick model. Many of plasticity models mentioned above require a large number of material constants and complex subroutine for calculating strain increments, thus making them impractical for application in the ground vehicle industry.

2.1.4 Garud Cyclic Plasticity Model

Most cyclic plasticity models that have been reviewed previously are based on a concept of translating yield surface. The differences in the plasticity models generally are based on the translation rule which governs the movement of the yield surface. However, the Mroz and Garud cyclic plasticity models are relatively simpler to implement in comparison to other models. The Mroz multi surface model has a disadvantage of the possibility of intersection between stress surfaces during non-proportional loading. This intersection causes computational problems. Garud proposed [12] an improved translation rule that prevents any intersections of plasticity surfaces. Therefore, the Garud model is presented in detail for purpose of numerical implementation associated with the incremental stress-strain notch analysis in Chapter 3.

Garud suggested that the movement of the stress surface depends not only on the current state of stress but also on the direction of stress increment. Garud postulated that increases in stress induce the evolution of plastic deformation, and the surfaces are

subject to translation, keeping constant shape and size without rotation in the stress space. The assumed direction of movement provides locations of the current state of stress on the surface at the new location, and eliminates the possibility of intersection between adjacent surfaces. The principle idea of the Garud translation rule is demonstrated in the following steps.

It is assumed that an applied torsion-tension load results in the current stress state settled at the point σ and the two yield surfaces F_1 and F_2 with corresponding yield limits R_{F1} and R_{F2} have been moved in the stress space, so that their centers have been located to the points α^{F1} and α^{F2} as it has been arbitrarily assumed and illustrated in Figure 2-8.

Based on the applied load path that the current stress increment induces the plastic strain increment, and it is forwarded outside the surface F_1. According to the consistency condition the yield surface must follow the stress state evolution and the updated stress state: $\sigma + \Delta\sigma$ must satisfy the updated yield function: $F_1(\sigma + \Delta\sigma, \alpha + \Delta\alpha) - R_{F1} = 0$. Taking into account the assumption that during the plastic strain evolution the yield surface with a fixed size R_{F1} translates without rotation in the stress space, the consistency condition is satisfied by the condition as the surface centered at the point $\sigma + \Delta\sigma$ corresponding to the updated stress state:

$$F_1[(\alpha + \Delta\alpha) - (\sigma + \Delta\sigma)] - R_{F1} = 0 \tag{2.23}$$

Thus, the translation rule of the yield surface must be defined.

The details of the yield surface translation rule according to Garud's proposition are discussed in the following. The translation is associated with the applied load path which generates a plastic strain evolution.

In order to translate the yield surface according to the Garud rule, the following steps should be performed:

a) Extend the line of action of the stress increment to intersect the external non-active yield surface F_2 at the point A_1^2, as it is presented in Figure 2-9.

In the index notation the following equation describes the present step:

$$\left|\overline{\sigma_{ij} + x \cdot \Delta\sigma_{ij} - \alpha_{ij}^{F2}}\right| = R_{F2} \tag{2.24}$$

where the unknown coordinates of the point A^2_1 are expressed as:

$$\sigma_{ij}^{A_1^2} = \sigma_{ij} + x \cdot \Delta\sigma_{ij} \tag{2.25}$$

Which, developed according to index *i=2,3* and *j=2,3* can be given as follows:

$$\begin{aligned}&(\sigma_{22} - \alpha_{22}^{F2} + x \cdot \Delta\sigma_{22})^2 - (\sigma_{22} - \alpha_{22}^{F2} + x \cdot \Delta\sigma_{22}) \cdot (\sigma_{33} - \alpha_{33}^{F2} + x \cdot \Delta\sigma_{33}) + \\ &(\sigma_{33} - \alpha_{33}^{F2} + x \cdot \Delta\sigma_{33})^2 + 3 \cdot (\sigma_{23} - \alpha_{23}^{F2} + x \cdot \Delta\sigma_{23})^2 = R_{F1}^2\end{aligned} \tag{2.26}$$

It can be easily obtained that the scalar factor *x* comes out as the solution

$$x = \frac{-B + \sqrt{\Delta}}{2A} \tag{2.27}$$

of the square equation

$$Ax^2 + Bx + C = 0 \tag{2.28}$$

where

$$\Delta = B^2 - 4AC \tag{2.29}$$

$$
\begin{aligned}
&A = \Delta\sigma_{22}^2 - \Delta\sigma_{22}\cdot\Delta\sigma_{33} + \Delta\sigma_{33}^2 + 3\cdot(\Delta\sigma_{23}^2)\\
&B = 2\cdot\{(\sigma_{22}-\alpha_{22}^{F2})\Delta\sigma_{22} + (\sigma_{33}-\alpha_{33}^{F2})\Delta\sigma_{33} + 3\cdot[(\sigma_{23}-\alpha_{23}^{F2})\Delta\sigma_{23}]\}\\
&-(\sigma_{22}-\alpha_{22}^{F2})\Delta\sigma_{33} - (\sigma_{33}-\alpha_{33}^{F2})\Delta\sigma_{22}\\
&C = (\sigma_{22}-\alpha_{22}^{F2})^2 - (\sigma_{22}-\alpha_{22}^{F2})\cdot(\sigma_{33}-\alpha_{33}^{F2}) + (\sigma_{33}-\alpha_{33}^{F2})^2\\
&+3\cdot(\sigma_{23}-\alpha_{23}^{F2})^2 - R_{F1}^2
\end{aligned}
\tag{2.30}
$$

b) Connect point A_1 and the center α^{F2} of the yield surface F_2. Draw through the center α^{F1} of the surface F_1 a line parallel to the line (A_1 , α^{F2}) to find point A_G on the yield surface F_1 , as it is shown in Figure 2-10.

The two operations are described in the index notation in the following form:

$$
\begin{aligned}
&(\overline{\alpha_{ij}^{F2} A_1})_{ij} = \sigma_{ij}^{A1} - \alpha_{ij}^{F2}\\
&\sigma_{ij}^{AG} = \frac{R_{F1}}{R_{F2}}\cdot(\sigma_{ij}^{A1} - \alpha_{ij}^{F2}) + \alpha_{ij}^{F1}
\end{aligned}
\tag{2.31}
$$

c) Connect the conjugate points A_1 and A_G to find the direction of translation of the yield surface F_1, as shown in Figure 2-11:

$$
(\overline{A_G A_1})_{ij} = \sigma_{ij}^{A1} - \sigma_{ij}^{AG} \tag{2.32}
$$

d) Translate the surface F_1 from point α^{F1} to (α^{F1})' in the direction of the vector (A_1 A_G) till the stress increment $\Delta\sigma$ is found on the translated surface, as presented in Figure 2-12.

In the terms of index notation the following equation can be defined:

$$
\left|\overline{\sigma_{ij} + \Delta\sigma_{ij} - \alpha_{ij}^{F1} - \Delta\alpha_{ij}^{F1}}\right| = R_{F1} \tag{2.33}
$$

in which the components $\Delta\alpha_{ij}^{F1}$ of the translation vector are expressed:

$$
\Delta\alpha_{ij}^{F1} = y\cdot(\overline{\sigma_{ij}^{A1} - \sigma_{ij}^{AG}}) \tag{2.34}
$$

Thus, the updated coordinates of the center of the yield surface F_1 are given as

$$(\alpha_{ij}^{F1})' = \alpha_{ij}^{F1} + \Delta\alpha_{ij}^{F1} \tag{2.35}$$

or

$$(\alpha_{ij}^{F1})' = \alpha_{ij}^{F1} + \Delta\alpha_{ij}^{F1} = \alpha_{ij}^{F1} + y \cdot (\sigma_{ij}^{A1} - \sigma_{ij}^{AG}) \tag{2.36}$$

Assuming the following substitutions:

$$\sigma_{ij}^{\alpha} = \sigma_{ij} + \Delta\sigma_{ij} - \alpha_{ij}^{F1} \;\; ; \;\; \sigma_{ij}^{AA} = \sigma_{ij}^{A1} - \sigma_{ij}^{AG} \tag{2.37}$$

the initial equation

$$\left|\overline{\sigma_{ij} + \Delta\sigma_{ij} - \alpha_{ij}^{F1} - \Delta\alpha_{ij}^{F1}}\right| = R_{F1} \tag{2.38}$$

can be replaced by

$$\left|\overline{\sigma_{ij}^{\alpha} - y \cdot \sigma_{ij}^{AA}}\right| = R_{F1}$$

which developed according to index *i=2,3* and *j=2,3* is presented as

$$\begin{aligned}&(\sigma_{22}^{\alpha} - y \cdot \Delta\sigma_{22}^{AA})^2 - (\sigma_{22}^{\alpha} - y \cdot \sigma_{22}^{AA}) \cdot (\sigma_{33}^{\alpha} - y \cdot \sigma_{33}^{AA}) + \\ &(\sigma_{33}^{\alpha} - y \cdot \sigma_{33}^{AA})^2 + 3 \cdot (\sigma_{23}^{\alpha} - y \cdot \sigma_{23}^{AA})^2 = R_{F1}^2\end{aligned} \tag{2.39}$$

Due to algebraic transformations, the scalar factor *y* governing the magnitude of the translation vector is obtained as the solution:

$$y = \frac{-B - \sqrt{\Delta}}{2A} \tag{2.40}$$

of the square equation:

$$Ay^2 + By + C = 0 \tag{2.41}$$

where Δ and the coefficients *A, B,* and C are defined in accordance to:

$$\Delta = \mathrm{B}^2 - 4\mathrm{AC} \tag{2.42}$$

$$\begin{aligned} A &= (\sigma_{22}^{AA})^2 + (\sigma_{33}^{AA})^2 + 3\cdot(\sigma_{23}^{AA})^2 - (\sigma_{22}^{AA})\cdot(\sigma_{33}^{AA}) \\ B &= -2\cdot[\sigma_{22}^{\alpha}\sigma_{22}^{AA} + \sigma_{33}^{\alpha}\sigma_{33}^{AA} + 3(\sigma_{23}^{\alpha}\sigma_{23}^{AA})] + \sigma_{22}^{\alpha}\sigma_{33}^{AA} + \sigma_{33}^{\alpha}\sigma_{22}^{AA} \\ C &= (\sigma_{22}^{\alpha})^2 + (\sigma_{33}^{\alpha})^2 - \sigma_{22}^{\alpha}\sigma_{33}^{\alpha} + 3\cdot(\sigma_{23}^{\alpha})^2 - R_{F1}^2 \end{aligned} \tag{2.43}$$

2.1.5 Notch Correction

Engineering components generally have stress concentrations such as notches, holes, fillets, shoulders, etc. due to their geometrical and functional constraints. Notches and stress concentrations have been of interest for many years, as these locations act to initiate fatigue crack and cause component failure. Early researches focused primarily on determining theoretical stress concentration factors using either elasticity theory or photoelastic analysis. Peterson [26] has compiled theoretical stress concentration factors for various geometries into one book. Stowell [27], Hardrath and Ohman [28] investigated stress concentrations in the plastic range. The most well known approximation formula that relates the theoretical stress concentration factor to the product of the elasto-plastic stress and strain concentration factors was originally proposed by Neuber [29]. Neuber studied a semi-infinite prismatic notched body obeying a nonlinear stress and strain law. He proposed that the product of the stress and strain at the notch tip in any arbitrary notched geometry in a prismatic body is not dependent on material's nonlinear parameters, but can be related to material's elastic parameters and the far field boundary conditions. Neuber's rule for uniaxial loading is

$$\sigma^a \varepsilon^a = K_t^{\ 2} Se \tag{2.44}$$

Where σ^a and ε^a are the elasto-plastic notch tip stress and strain, S and e are the nominal section stress and strain, and K_t is the elastic stress concentration factor. Alternatively, Neuber's rule can be written in the form:

$$\sigma^a \varepsilon^a = \sigma^e \varepsilon^e \tag{2.45}$$

Where $\sigma^e = K_t S$ and $\varepsilon^e = K_t e$ are fictitious elastic strain and stress. Eq. (2.45) states that the total strain energy density at the notch tip is equal to the fictitious strain energy density as if a material hypothetically remained elastic. A graphical representation of Neuber's rule is shown in Figure 2-13

Topper et al. [30] extended validation of Neuber's rule to several notch geometries subjected to uniaxial cyclic loading. Their results showed that Neuber's rule for cyclic loading was in good agreement with experimental results for notched aluminum alloy sheets.

Molski and Glinka [31] proposed that the equivalent strain energy density (ESED) method as an alternative to Neuber's rule. They postulated that the strain energy density at a notch equals that if the body were to hypothetically remain elastic. The authors showed [31] that the ESED method provided good agreement with experiment for several notched specimens subjected to monotonic loading. The ESED method can be written in terms of stresses and strains as

$$\frac{1}{2}\sigma^e \varepsilon^e = \int_0^{\varepsilon^a} \sigma^a \, d\varepsilon^a \tag{2.46}$$

Glinka [32] later extended the ESED method to address notched bodies subjected to cyclic loading. A graphical representation of the ESED method is shown in Figure 2-14.

As the local strain-life approach was extended to multiaxial loading using multiaxial fatigue damage parameters, these damage parameters require multiaxial strains and stresses to be determined at notch areas. Since nonlinear finite element analysis is too costly to compute multiaxial stresses and strains for a long load history, simple uniaxial notch stress and strain approximation techniques were extended to states of multiaxial stress and strain. Hoffmann and Seeger [33,34] proposed a method for multiaxial proportional loading by applying an equivalent form of Neuber's rule as

$$\sigma_{eq}{}^{a}\,\varepsilon_{eq}{}^{a} = \sigma_{eq}{}^{e}\,\varepsilon_{eq}{}^{e} \tag{2.47}$$

Where $\sigma_{eq}{}^{a}$ and $\varepsilon_{eq}{}^{a}$ are the notch tip elastic-plastic equivalent stress and strain respectively, and $\sigma_{eq}{}^{e}$ and $\varepsilon_{eq}{}^{e}$ are those which would be obtained if the material remained elastic. They assumed that the ratio of minimum principal strain components at the notch tip remain constant during loading.

The generalization of both the ESED method and Neuber's rule for proportional multiaxial loading for notched bodies was suggested by Moftakhar [35]. Numerical and experimental studies conducted by Moftakhar and Glinka [36] showed that the generalized ESED method and Neuber's rule provide an upper and a lower bounds of the actual strains. Their study concluded that Neuber's rule tend to overestimate the notch tip elastic-plastic strains and stresses and the ESED method tends to underestimate notch tip inelastic strains and stresses

Hoffman et al. [37] presented a method to estimate notch root stresses and strains for bodies subjected to non-proportional loading. In their method, the multiaxial loads are first separated and notch root strain histories are calculated for the loads independently by

following the same solution procedure as for proportional loading. Compatibility iteration is then used to account for interaction between strain components that result from non-proportional loading. Their calculations compared well with finite element analysis.

Barkey [38] and Barkey et al. [39] later proposed a method to estimate multiaxial notch strains in notched bars subject to cyclic proportional and non-proportional loading, using the concept of a structural yield surface. The structural yield surface describes the relationship between nominal stresses and notch strains. The hardening parameter is found by using the uniaxial form of the ESED method as the basis of nominal load to notch plastic strain curve. Their results showed good agreement with experimental non-proportional tension-torsion tests for a notched steel bar. However, the method does not account for elastic coupling at the notch between any two nominal stresses.

Köttgen et al. [40] extended Barkey's approach by incorporating the notch effect into the constitutive relation. They first obtained pseudo stress history by assuming elastic material behavior. The yield criterion and the flow rule were determined using elastic stress history and the hardening parameter was determined using pseudo stress and local plastic strain curve obtained from a uniaxial simplified rule. The resulting elastic-plastic strain increments were then fed back into the flow rule to calculate notch stresses. Köttgen et al. reported correlation of their method with elasto-plastic finite element analysis for various geometries and applied loads.

Singh et al. [41] extended the ESED and Neuber's methods to estimate the notch root stresses and strains for monotonic non-proportional loading. The approach is an incremental generalization of the ESED method and Neuber's rule. In generalizing the ESED method, Singh et al. suggested that for a given increment of external load, the

corresponding increment of the strain energy density at the notch tip in a elastic-plastic body is equal to the increment of strain energy density if the body were to remain elastic. Singh et al. generalized Neuber's rule in a similar way by assuming that an increment of total strain energy density is exactly same as the increment of the fictitious total strain energy.

2.2 **Fatigue Damage Mechanism**

A better understanding of the damage mechanism associated with fatigue failure is considered to be essential step to develop an accurate fatigue damage model. Fatigue damage is characterized by the crack nucleation and growth. The mechanism for the crack nucleation and growth is briefly described below. A schematic illustration for a crack formation on the surface of a ductile metal is shown in Figure 2-15. In these examples, the applied tensile stress is vertical and the resulting shear stress is at 45^0. Cyclic plastic shear strains eventually cause the nucleation of the slip band shown as one of the fine lines in Figure 2-15.

Grains that crystallographic slip planes are favorably oriented with respect to the applied shear stress will be the first to form a slip band. Since each grain has a different preferred slip plane, they will plastically deform at different applied stresses. At low stresses, only a few grains have favorable orientation and only a few slip bands form. At high stresses, a large number of slip bands form. During repeated cyclic loads, these slip bands grow and form into a single dominant crack

Polycrystallic metals have a complex nucleation process that is influenced by grain boundaries, precipitates and impurities. The intrusion-extrusion model shown in Figure 2-15 is useful to describe the nucleation process. Slip bands are formed as a result

of dislocation movement within individual grains. Cyclic shear stresses cause the dislocation to move. Plastic deformation result in a permanent offset in adjacent atomic planes. Repeated plastic deformation eventually leads to the formation of a slip band. Some slip bands that come out of the surface of material are called extrusions and intrusion go into the surface. Fatigue crack nucleation is essentially a surface phenomenon.

Fracture mechanics crack modes are shown in Figure 2-16 to illustrate how a crack is loaded. Tension loads produce Mode I and a torsion loading of a surface crack produces both Mode II and Mode III. Mode II is an in-plane shear loading and is found on the surface. Mode III is an out-of-plane shear loading and is found on at the maximum crack depth. Mode II causes the crack to growth along the surface and Mode III loading causes the crack to grow into the surface in torsion loading.

Understanding of crack formation on the surface is the first important aspect of fatigue. Surface crack length is not as important as crack depth. A cross section of a polycrystallic material loaded in cyclic tension is shown in Figure 2-17. A crack first starts in an individual surface grain and then grows into next one. Note that the orientation of the grain in the second and third grain is slightly different than the first one because of random orientations of grains within a material. However, the overall growth path is still along the planes of maximum shear stress (Mode II). Finally, the crack will grow large enough and turn to grow perpendicular to the tensile stress axis. At this point, the crack is sufficiently large to generate its own plasticity and will grow in a planar manner through grains. This is a Mode I crack. This transition is governed by the material

microstructure and the type of loading. Torsional loading favors Stage I shear growth. Low ductility materials have predominantly Stage II growth.

Brown and Miller [51] suggested that shear cracks can grow in one of two ways, illustrated by Case A and Case B in Figure 2-20. Case A cracks grow along the free surface in a direction parallel to the length of the crack and Case B cracks grow into the surface from the crack depth.

2.3 **Multiaxial Fatigue Damage Parameters**

Fatigue failure of engineering components under multiaxial loading conditions is a common, since most engineering components are subjected to multiaxial load histories in service and the origins of multiaxiality generally result from the external loading, geometry or residual stresses. Multiaxial fatigue estimation is a very complex task in comparison to simple load cases, which are more or less satisfactorily solved by widely used uniaxial methods. Different from the uniaxial fatigue problem, the multiaxial fatigue problem involves complex stress and strain states, load histories and fatigue damage parameters relating the fatigue life. In recent decades, a large number of studies have been done to develop multiaxial fatigue damage criteria. Several reviews and comparison of existing multiaxial fatigue damage parameters can be found elsewhere [42,43,44]. Although numerous multiaxial fatigue damage parameters have been proposed during the past decades to predict the fatigue failure under multiaxial loading conditions, most of them are limited to specific materials and load cases and there is no universally accepted multiaxial fatigue damage parameter yet. In general, most of the multiaxial fatigue damage parameters can be divided into three categories as stress-based, strain-based and energy-based damage parameters. Some of these multiaxial fatigue damage parameters

are reviewed in this section to provide better understanding of the multiaxial fatigue problem and identify shortcomings and good features of those existing fatigue damage parameters.

2.3.1 Stress-Based Fatigue Damage Parameters

The stress-based damage parameter is generally used for infinite and/or high cycle fatigue where the plastic strains are small. Many investigators attempted to correlate the multiaxial fatigue data using classical static yield theories. Three most popular yield theories are the maximum principal stress theory, maximum shear stress theory and the octahedral shear stress theory. The maximum principal stress theory may be expressed as

$$\Delta\sigma_{eq} = \Delta\sigma_1 \tag{2.48}$$

The maximum shear stress theory may be expressed as

$$\Delta\tau = \frac{\Delta\sigma_{eq}}{2} = \frac{\Delta\sigma_1 - \Delta\sigma_3}{2} \tag{2.49}$$

The octahedral stress theory or von Mises theory may be expressed as

$$\Delta\sigma_{eq} = \frac{1}{\sqrt{2}}\left[(\Delta\sigma_1 - \Delta\sigma_2)^2 + (\Delta\sigma_2 - \Delta\sigma_3)^2 + (\Delta\sigma_3 - \Delta\sigma_1)^2\right] \tag{2.50}$$

The static yield theories are valid for proportional loading; however these theories do not work for the non-proportional loading.

Sinus [45, 46] reviewed much of the experimental data for combined bending and torsion loading and proposed that a linear combination of the octahedral shear stress and the mean hydrostatic stress as a fatigue damage criterion. His resulting fatigue damage criterion can be expressed as

$$\frac{\Delta\tau_{oct}}{2} + \alpha(3\sigma_h) = \beta \tag{2.51}$$

In case of combined alternating axial and shear stress, the fatigue damage parameter results in a series of concentric ellipses. Sine's formulation is defined only in case of proportional loading and has an advantage of easily being solved for complex stress states.

Findley [47] proposed that the linear form of normal stress and shear stress on a specific plane as a fatigue damage criterion.

$$\left(\frac{\Delta\tau}{2} + k\sigma_n\right)_{\max} = f \tag{2.52}$$

This specific plane is defined as a critical plane within a material subject to a maximum value of a damage criterion. Where f and k are material coefficients. Findley identifies a critical plane for fatigue crack initiation and growth that is dependent on both alternating shear stress and maximum normal stress. This criterion is effective for combination of proportional bending and torsion loadings under the same ratio of normal to shear stress amplitudes ($\sigma_a/\tau_a = \sigma_m/\tau_m$). According to Findley, the orientation of the critical plane in case of zero mean stress values depend on the direction of the maximum principal stress, σ_1 and material coefficient, k. Findley noticed that k value is small for ductile materials and the direction of the critical plane for these materials approaches to the direction of maximum shear stress. A high k value is characteristic for brittle materials and the critical plane position is then close to the position of the maximum principal stress direction. In case of mean stresses different from zero, the position of the critical plane depends not only on the direction of the maximum principal stress, σ_1 and

k value, but also on variable and static stresses. When mean stresses from bending and torsion are high in comparison with variable stresses, the critical plane approaches the plane of the maximum principal stress. The Findley criterion often is applied for the case of finite high cycle fatigue regime.

McDiarmid [48] analyzed available high cycle fatigue data and proposed a damage criterion based on the maximum shear stress amplitude, $\Delta\tau_{\max}/2$ and normal stress, $\Delta\sigma_{n,\max}$ on the critical plane. The critical plane in this criterion is the plane of the maximum shear stress range.

$$\frac{\Delta\tau_{\max}}{2t_{A,B}} + \frac{\Delta\sigma_{n,\max}}{2\sigma_{uts}} = 1 \tag{2.53}$$

This criterion distinguished case A and case B fatigue cracks. The distinction consists of applying different the shear fatigue strengths denoted as $2t_{A,B}$ for case A and case B cracking. This model is similar to Findley's model with some differences. McDiarmid's model considers both A and B type cracking modes. Case A cracking mode propagates the cracks along the free surface and case B cracking mode grow the cracks that penetrate into the material. Findley's material coefficient is replaced by the quantity, $t_{A,B}/2\sigma_{uts}$.

The critical plane is defined as the plane with the maximum shear stress amplitude and not the plane on which the damage criterion is maximized.

Dang Van [49] proposed an endurance limit criterion based on the concept of micro-stresses within a critical volume of the material. This model was developed on the basis of observation that fatigue crack nucleation is a local process and begins in grains that have undergone plastic deformation. As a result of plastic deformation, intracrystal-

line slip bands are formed in grains, which begin the crack process. Dang Van suggested that because cracks usually nucleate in intracrystal slip bands, the microscopic shear stress on the grain must be an important damage parameter. The second important parameter is the microscopic hydrostatic stress, which influences crack opening process. These two proposed fatigue parameters are involved in a linear function.

$$\tau(t) + a\sigma(t) = b \tag{2.54}$$

Where $\tau(t)$ and $\sigma(t)$ are instantaneous microscopic shear stress and hydrostatic stress, and a and b are constants. These constants are determined from material test at two different stress states. The microscopic stresses and strains within critical grains are different from the macroscopic stresses and strains commonly used for fatigue analysis. The microscopic shear stress, $\tau(t)$ is computed from the microscopic principal stresses according to Tresca maximum shear stress theory.

$$\tau(t) = \frac{1}{2}[\sigma_1(t) - \sigma_3(t)] \tag{2.55}$$

The microscopic principal stresses, $\sigma_1(t)$, $\sigma_3(t)$ are calculated from the microscopic stress tensor, $\sigma_{ij}(t)$. This tensor is calculated as the sum of macroscopic stress tensor, $\Sigma_{ij}(t)$ and deviatric parts of the stabilized residual stress tensor, $dev\rho^*$.

$$\sigma_{ij}(t) = \Sigma_{ij}(t) + dev\rho^* \tag{2.56}$$

The criterion can be expressed as combination of the microscopic shear stress, $\tau(t)$ and hydrostatic stress, $\sigma(t)$ as shown in Figure 2-18. A loading path that remains within the two bounding failure lines is expected to have infinite life, whereas any path that extends outside the damage line will have failure because the microscopic plastic strain occurs.

The Dang Van criterion is intended to be used as a method of predicting the endurance limit under complex loadings. However, it can be used in long finite life regime with different values of constants a and b for different fatigue life ranges.

The Findley, McDiarmid and Dang Van fatigue damage criteria can be described as critical plane approaches since they consider the fatigue damage as accumulating on a specific plane(s) within a material. In case of constant amplitude proportional loading, there is no significant difference among any of these shear stress-based criteria. The Dang Van and McDiarmid fatigue damage criteria have been developed more recently for situations involving complex non-proportional loading. The Dang Van fatigue damage criterion appears complex, but is easy to compute and have gained widespread acceptance for more complex loadings. Findley's criterion is reasonably accurate and simple and is gaining acceptance even for complex loading cases. However, there is no universal criterion based on stresses, and the successful application of a particular stress criterion, in a large degree, depends on experimentally established material coefficients. The most promising stress-based fatigue criteria seem to be those which can be used under the general type of loading, i.e. the multiaxial random loading. Unfortunately, only a few stress criteria were experimentally verified under such loading. The fatigue damage criteria based on stresses are not able to take into account the effects of the cyclic hardening or softening. If the fatigue tests are performed under stress controlled conditions, the effects of the cyclic hardening and softening is visible only in strain history, which is not taken into account in the stress-based fatigue damage criteria.

In Table 2-1, the stress-based fatigue damage parameters are listed and a comparison summary is given to provide better understanding their prediction capabilities.

Table 2-1: Comparison summary of stress-based fatigue damage parameters

Fatigue Damage Parameter	Mathematical Model	Prediction Capability	Mean Stress Effects
Maximum principal stress	$\Delta\sigma_{eq} = \Delta\sigma_1$	Cyclic, proportional	No
Maximum shear stress	$\Delta\tau = \frac{\Delta\sigma_{eq}}{2} = \frac{\Delta\sigma_1 - \Delta\sigma_3}{2}$	Cyclic, proportional	No
Equivalent stress	$\Delta\sigma_{eq} = f(\Delta\sigma_1, \Delta\sigma_2, \Delta\sigma_3)$	Cyclic, proportional	No
Sinus [45,46]	$\frac{\Delta\tau_{oct}}{2} + \alpha(3\sigma_h) = \beta$	Cyclic, proportional	No
Findley [47]	$\left(\frac{\Delta\tau}{2} + k\sigma_n\right)_{\max} = f$	Cyclic, proportional	No
McDiarmid [48]	$\frac{\Delta\tau_{\max}}{2t_{A,B}} + \frac{\Delta\sigma_{n,\max}}{2\sigma_{uts}} = 1$	Cyclic, proportional Cyclic, non-proportional	Yes
Dang Van [49]	$\tau(t) + a\sigma(t) = b$	Random, proportional	Yes

2.3.2 Strain-Based Fatigue Damage Parameters

Strain-based fatigue damage criteria for multiaxial fatigue are associated with low cycle fatigue where significant plasticity may occur. Like stress-based criteria, the first strain-based criteria for multiaxial fatigue were formulated on the basis of static yield criteria. The most popular strain-based yield criteria are: criterion of maximum normal strain, criterion of maximum shear strain and criterion of maximum octahedral shear strain.

According to the maximum normal strain criterion, the maximum normal strain is responsible for material fatigue failure. This criterion may be expressed as

$$\Delta\varepsilon_{eq} = \Delta\varepsilon_1 \tag{2.57}$$

In this case, the critical plane is the plane of maximum normal strain range.

The maximum shear strain criterion may be expressed as

$$\Delta\gamma_{eq} = \frac{\Delta\varepsilon_1 - \Delta\varepsilon_3}{2} \tag{2.58}$$

According to this assumption, the critical plane is the plane of maximum shear strain range.

The octahedral strain theory or von Mises theory may be expressed as

$$\Delta\varepsilon_{eq} = \frac{1}{\sqrt{2}(1+\nu)}\left[(\Delta\varepsilon_1 - \Delta\varepsilon_2)^2 + (\Delta\varepsilon_2 - \Delta\varepsilon_3)^2 + (\Delta\varepsilon_3 - \Delta\varepsilon_1)^2\right] \tag{2.59}$$

and the critical plane is the octahedral plane.

Yokobori et al. [50] in 1965 showed that the equivalent strain did not correlate the data from tension and torsion tests as shown in Figure 2-19 for 1035 steel. On the basis of plastic octahedral shear strain, torsion loading is less damaging than tension.

Equivalent strain approaches do not explain the observed nucleation and propagation of fatigue cracks on specific planes of material being tested. Equivalent strain criteria may prove successful for proportional loadings and certain materials, however is unsuitable for the case of non-proportional loadings.

Strain-based critical plane fatigue damage parameters have evolved from experimental observation of the nucleation and growth of cracks during loadings. Fatigue life usually will be governed by crack growth along either shear planes or tensile planes

depending the material, stress states and strain amplitude. A critical plane fatigue damage parameter will include dominant damage parameters governing either type of crack growth.

Brown and Miller [51] proposed a damage criterion for multiaxial fatigue, which assumes that fatigue life is generally a non-linear function of the strain state. Analogous to the shear and normal stress proposed by Findley for high cycle fatigue, Brown and Miller suggested that both the cyclic shear and normal strain on the plane of the maximum shear must be considered as the damage parameter. Brown and Miller reviewed much of the available multiaxial low cycle fatigue literature with particular emphasis on the formation and early growth of cracks and suggested the terms Case A and Case B cracks as shown in Figure 2-20.

Brown and Miller proposed separate criterion for each type of cracking.

Case A: $$\left(\frac{\Delta\gamma}{g}\right)^{j} = \left(\frac{\varepsilon_n}{h}\right)^{j}$$

Case B: $$\frac{\Delta\gamma}{2} = \text{constant} \tag{2.60}$$

Where g, h and j are constants used to fit the ellipse of the Γ plane. The value of j ranged from 1 for brittle materials to 2 for ductile materials.

Later, Kandil, Brown and Miller [52] proposed a simplified formulation for Case A cracks.

$$\frac{\hat{\Delta\gamma}}{2} = \frac{\Delta\gamma_{\max}}{2} + S\Delta\varepsilon_n \tag{2.61}$$

Where $\hat{\Delta\gamma}$ is the equivalent shear strain range and S is a material-dependent coefficient that represents the influence of the normal strain and is determined by correlating axial and torsion fatigue data. Here, $\Delta\gamma_{\max}$ is the maximum shear strain range, and $\Delta\varepsilon_n$ is the normal strain range on the plane experiencing the maximum shear strain range, $\Delta\gamma_{\max}$. The fatigue damage parameter can be formulated using uniaxial fatigue parameters as

$$\frac{\Delta\gamma_{\max}}{2} + S\Delta\varepsilon_n = \left((1+\nu_e)+(1-\nu_e)S\right)\frac{\sigma'_f}{E}\left(2N_f\right)^b + \left((1+\nu_p)+(1-\nu_p)S\right)\varepsilon'_f\left(2N_f\right)^c \tag{2.62}$$

Wang and Brown [53] added a mean stress term using Morrow's mean stress approach by subtracting the mean stress from the fatigue strength coefficient in the following form.

$$\frac{\Delta\gamma_{\max}}{2} + S\Delta\varepsilon_n = \left((1+\nu_e)+(1-\nu_e)S\right)\frac{\sigma'_f - 2\sigma_{n,mean}}{E}\left(2N_f\right)^b + \left((1+\nu_p)+(1-\nu_p)S\right)\varepsilon'_f\left(2N_f\right)^c \tag{2.63}$$

It should be noted that the mean stress on the maximum shear range plane is one-half of the axial mean stress.

Socie et al. [54] observing fatigue fractures reached a conclusion similar to those by Brown and Miller [51] that the normal strain, $\Delta\varepsilon_n$ on the plane of maximum shear strain accelerates the fatigue damage process through crack opening. The crack opening reduces the friction forces between irregularly shaped slip planes. Hence, the mean normal stress, $\sigma_{n,mean}$ on the plane of maximum shear strain was included in the following damage model.

$$\frac{\Delta\gamma_{\max}}{2} + \frac{\Delta\varepsilon_n}{2} + \frac{\sigma_{n,mean}}{E} = \frac{\tau'_f}{G}\left(2N_f\right)^b + \gamma'_f\left(2N_f\right)^c \tag{2.64}$$

On the basis of fatigue tests related to different materials, Fatemi and Socie [55] noticed that Brown and Miller fatigue damage parameter based on only strain values does not include additional material hardening occurring under non-proportional loading. In order to take into account this effect, they suggested that the normal strain term in the critical plane should be replaced with the maximum normal stress value, $\sigma_{n,\max}$. The conceptual basis is shown schematically in Figure 2-21.

The following fatigue damage parameter may be interpreted as the maximum shear strain amplitude corrected by the maximum normal stress to quantify fatigue damage. For uniaxial strain-life properties, the fatigue damage parameter is given as

$$\frac{\Delta\gamma_{\max}}{2}\left(1+n\frac{\sigma_{n,\max}}{\sigma_y}\right)=(1+\nu_e)\frac{\sigma'_f}{E}(2N_f)^b+\frac{n}{2}(1+\nu_e)\frac{\sigma'^2_f}{E\sigma_y}(2N_f)^{2b}+(1+\nu_p)\varepsilon'_f(2N_f)^c+\frac{n}{2}(1+\nu_p)\frac{\varepsilon'_f\sigma'_f}{\sigma_y}(2N_f)^{b+c} \tag{2.65}$$

The fatigue damage parameter based on the shear strain-life properties takes the form of

$$\frac{\Delta\gamma_{\max}}{2}\left(1+n\frac{\sigma_{n,\max}}{\sigma_y}\right)=\frac{\tau'_f}{G}(2N_f)^b+\gamma'_f(2N_f)^c \tag{2.66}$$

The fatigue damage parameter includes the mean stress effects through the maximum value of normal stress on the critical plane.

As many other fatigue damage parameters, the damage parameter proposed by Brown et al. is not able to take into account strain path dependent hardening. The Fatemi-Socie damage parameters accounts for the non-proportional hardening and mean stress effects through the normal stress term. The Brown-Miller and Fatemi-Socie fatigue damage parameters have been developed primary using materials for which the dominant

failure is shear crack nucleation and growth i.e. Mode II and Mode III fracture modes dominates.

A summary of the strain-based fatigue damage parameters is presented in Table 2-2.

Table 2-2: Comparison summary of strain-based fatigue damage parameters

Fatigue Damage Parameter	Mathematical Model	Prediction Capability	Mean Stress Effects
Maximum normal strain	$\Delta\varepsilon_{eq} = \varepsilon\sigma_1$	Cyclic, proportional	No
Maximum shear strain	$\Delta\gamma_{eq} = \frac{\Delta\varepsilon_1 - \Delta\varepsilon_3}{2}$	Cyclic, proportional	No
Octahedral shear strain	$\Delta\varepsilon_{eq} = f(\Delta\varepsilon_1, \Delta\varepsilon_2, \Delta\varepsilon_3)$	Cyclic, proportional	No
Brown and Miller [51]	$\left(\frac{\Delta\gamma}{g}\right)^j = \left(\frac{\varepsilon_n}{h}\right)^j$	Cyclic, proportional Cyclic, non-proportional	No
Kandil, Brown and Miller [52]	$\frac{\hat{\Delta\gamma}}{2} = \frac{\Delta\gamma_{\max}}{2} + S\Delta\varepsilon_n$	Cyclic, proportional Cyclic, non-proportional	No
Wang and Brown[53]	$\frac{\hat{\Delta\gamma}}{2} = \frac{\Delta\gamma_{\max}}{2} + S\Delta\varepsilon_n$	Cyclic, proportional Cyclic, non-proportional	Yes
Socie et al. [54]	$\frac{\Delta\gamma_{\max}}{2} + \frac{\Delta\varepsilon_n}{2} + \frac{\sigma_{n,mean}}{E}$	Cyclic, proportional Cyclic, non-proportional	Yes
Fatemi and Socie [55]	$\frac{\Delta\gamma_{\max}}{2}\left(1 + n\frac{\sigma_{n,\max}}{\sigma_y}\right)$	Cyclic, proportional Cyclic, non-proportional	Yes

2.3.3 Energy-Based Fatigue Damage Parameter

Several multiaxial fatigue damage parameters based on strain energy have been developed. These energy-based parameters came from the basis that strain energy per cycle may be considered as a measure of fatigue damage and the fatigue resistance of a

material may be characterized in terms of its capacity to absorb and dissipate the strain energy.

Smith and co-authors [56] proposed a fatigue damage parameter, SWT, described as stress and strain product, $\sigma_{\max}\varepsilon_a$ for fatigue life prediction. The SWT parameter was originally developed as a correction for mean stresses in uniaxial loading situations. The critical plane form of the SWT parameter was proposed by Socie [54] for proportional and non-proportional loadings of materials that fail primarily due to Mode I tensile cracking. The SWT parameter for multiaxial loading is based on principal strain range, $\Delta\varepsilon_1$ and maximum stress on the principal strain range plane, $\sigma_{n,\max}$.

$$\sigma_{n,\max}\Delta\varepsilon_1 = \frac{\sigma'_f}{E}\left(2N_f\right)^{2b} + \sigma'_f\varepsilon'_f\left(2N_f\right)^{b+c} \tag{2.67}$$

The non-proportional hardening and mean stress effects for multiaxial loading are incorporated through the stress term in this model.

Liu [57] proposed an energy-based fatigue damage parameter to estimate fatigue life based on virtual strain energy (VSE). The VSE parameter can be considered as a critical plane based because the work quantities are defined for specific planes within the material. The parameters of virtual strain energy are associated with two different modes of fatigue cracks: a mode for tensile failure, ΔW_I and a mode for shear failure, the ΔW_{II} with the shear failure mode being divided into two crack types, Type A and Type B. Failure is expected to occur on the plane in the material having maximum VSE quantity. The ΔW_I parameter is the sum of normal strain energy density, $\left(\Delta\sigma_n\Delta\varepsilon_n\right)_{\max}$ and the

shear strain energy, $(\Delta\tau\Delta\gamma)$ in the plane of the maximum normal strain energy density. The ΔW_I parameter is used to predict fatigue life according to Mode I fracture.

$$\Delta W_I = (\Delta\sigma_n \Delta\varepsilon_n)_{\max} + (\Delta\tau\Delta\gamma)$$

$$\Delta W_I = 4\sigma'_f \varepsilon'_f (2N_f)^{b+c} + \frac{4\sigma'^2_f}{E}(2N_f)^{2b} \tag{2.68}$$

The ΔW_{II} parameter is the sum of the maximum shear strain energy density, $(\Delta\tau\Delta\gamma)_{\max}$ and the normal strain energy density, $(\Delta\sigma_n \Delta\varepsilon_n)$ in the plane of the maximum shear strain energy density. The ΔW_{II} parameter is used to predict fatigue life according to Mode II fracture. According to Mode II cracking, the ΔW_{II} parameter is designated $\Delta W_{II,A}$ and $\Delta W_{II,B}$ for Case A and Case B cracks.

$$\Delta W_{II} = (\Delta\sigma_n \Delta\varepsilon_n) + (\Delta\tau\Delta\gamma)_{\max}$$

$$\Delta W_{II} = 4\tau'_f \gamma'_f (2N_f)^{b\gamma+c\gamma} + \frac{4\tau'^2_f}{G}(2N_f)^{2b\gamma} \tag{2.69}$$

The VSE parameters are essentially energy-based critical plane models and physically associated with two different modes of fatigue fracture.

Chu et al. [58] proposed a fatigue damage parameter to combine shear and normal strain work. They replaced the stress ranges with maximum stresses in order to include mean stress effects.

$$\Delta W^* = \left(\Delta\tau_{n,\max}\frac{\Delta\gamma}{2} + \sigma_{n,\max}\frac{\Delta\varepsilon_n}{2}\right)_{\max} \tag{2.70}$$

The fatigue damage parameter is based on the maximum value of ΔW^* rather than being defined on the plane of maximum normal and shear strain. The physical basis of this

model attempts to average the contribution of tensile and shears strain work. In tension, Mode I cracking occurs on 0^0 planes and Mode II cracking on 45^0 planes. Cracks usually begin in Mode II and turn to Mode I, giving an average crack direction of 22.5^o.

Glinka et al. [59,60] proposed an energy parameter of total strain energy density, expressed by stresses and strains on the critical plane.

$$\Delta W^* = \frac{\Delta\tau}{2}\frac{\Delta\gamma}{2} + \frac{\sigma_n}{2}\frac{\Delta\varepsilon_n}{2} \tag{2.71}$$

This came from the Brown-Miller damage parameter [51] that fatigue life, N_f is a function of normal and shear strains on the critical plane. Authors applied shear and normal strain energy density instead of shear and normal strains. In order to take into account the mean stress effects, authors have modified the above fatigue damage parameter as follows

$$\Delta W^* = \frac{\Delta\tau}{2}\frac{\Delta\gamma}{2}\left[\frac{\sigma'_f}{\sigma'_f - \sigma_{n,\max}} + \frac{\tau'_f}{\tau'_f - \tau_{n,\max}}\right] \tag{2.72}$$

In this fatigue damage parameter, normal mean stresses will assist in the opening of a crack and shear mean stresses will help to overcome sliding friction by deforming asperities on the crack surface.

Pan et al. [61] noticed that the influence of the strain energy in the shear direction, $(\Delta\tau/2)(\Delta\gamma/2)$ on the fatigue life is different than the influence of strain energy calculated on the normal direction, $(\Delta\sigma_n/2)(\Delta\varepsilon_n/2)$. For this reason, they proposed to modify the Glinka damage parameter by applying two coefficients determined by experiments.

$$\Delta W^{*} = \frac{\Delta\tau}{2}\frac{\Delta\gamma}{2} + k_1 k_2 \frac{\sigma_n}{2}\frac{\Delta\varepsilon_n}{2} \tag{2.73}$$

Where the coefficient are equal to $k_1 = \sigma'_f / \tau'_f$ and $k_2 = \varepsilon'_f / \gamma'_f$. The damage parameter in Eq. (2.73) was used to correlate the fatigue experimental fatigue life, N_f.

Chen et al.[62] proposed two fatigue damage parameters: the first one for materials dominated by Mode I crack, and the second one for materials dominated by Mode II crack. Both parameters assume the influence of normal and shear stresses and strains on the critical plane. For materials characterized by Mode I crack, the critical plane is the plane of maximum normal strain range, $\Delta\varepsilon_{n,\max}$.

$$\Delta\varepsilon_{n,\max}\Delta\sigma_n + \Delta\tau\Delta\gamma = \frac{4\sigma'_f}{E}\left(2N_f\right)^{2b} + 4\sigma'_f\varepsilon'_f\left(2N_f\right)^{b+c} \tag{2.74}$$

For materials characterized with Mode II crack, the critical plane is the plane of maximum shear strain range, $\Delta\gamma_{\max}$.

$$\Delta\gamma_{\max}\Delta\tau + \Delta\varepsilon_n\Delta\sigma_n + = \frac{4\tau'_f}{G}\left(2N_f\right)^{2bo} + 4\tau'_f\gamma'_f\left(2N_f\right)^{bo+co} \tag{2.75}$$

Varhani-Farahani [63] proposed a fatigue damage parameter as the summation of the normal, $\sigma_n\Delta\varepsilon_n$ and shear, $\Delta\tau_{\max}\Delta\left(\gamma_{\max}/2\right)$ strain energy density ranges calculated on the critical plane of maximum shear at the time instant when Mohr's circles of stresses and strains are the largest during a cycle. Energies of normal and shear strains are weighted through material fatigue coefficients. The proposed fatigue damage can be applied only for cyclic loading and plane stress state

$$\frac{\Delta\sigma_n\Delta\varepsilon_n}{\sigma'_f\varepsilon'_f} + \frac{1+\sigma_{n,m}/\sigma'_f}{\tau'_f\gamma'_f}\Delta\tau_{\max}\Delta\left(\frac{\gamma_{\max}}{2}\right) = f\left(N_f\right) \tag{2.76}$$

This fatigue damage parameter does not take into account the fact those positions of principal axes of stresses and strains do not coincide in case of elastic-plastic strain state.

Jahed and Varhani-Farahani [64] proposed an energy-based fatigue damage parameter. The proposed damage parameter is based on axial and shear stress and strain components responsible for cracking modes of failure dominantly Case A and Case B. Two fatigue values based on axial and shear energy are determined which corresponding the lower and upper fatigue limits.

$$\Delta E_A = E'_e \left(N_A\right)^B + E'_f \left(N_A\right)^C \tag{2.77}$$

$$\Delta E_T = W'_e \left(N_T\right)^{Bs} + W'_f \left(N_T\right)^{Cs} \tag{2.78}$$

Where ΔE_A and ΔE_T are the total energy (plastic and elastic) values due to pure tensile and pure torsional loading. Energy-based fatigue properties are calculated from energy-life curves.

For a component experiencing Case A cracking, where shear cracks grow along surface, crack growth is very slow, while the life of such component under Case B cracking where shear cracks growing into the surface is much smaller. The upper and lower limits of fatigue life coincide with these proposed models. Jahed and Varhani-Farahani suggested that real fatigue life must fall between these two limits, a method incorporating both bounds of axial and torsional loadings may be expressed by integrating these limits as

$$N_f = \frac{\Delta E_A}{\Delta E} N_A + \frac{\Delta E_T}{\Delta E} N_T \tag{2.79}$$

This energy parameter is based on the cracking mechanism and the amount of dissipated strain energy during fatigue loading cycles.

A comparison summary of the energy-based fatigue damage parameters is given in Table 2-3 to compare their prediction capabilities.

Table 2-3: Comparison summary of energy-based fatigue damage parameters

Fatigue Damage Parameter	Mathematical Model	Prediction Capability	Mean Stress Effects
Socie [54]	$\sigma_{n,\max}\,\Delta\varepsilon_1$	Cyclic, proportional Cyclic, non-proportional	Yes
Liu [57]	$\Delta W_I = (\Delta\sigma_n \Delta\varepsilon_n)_{\max} + (\Delta\tau\Delta\gamma)$ $\Delta W_{II} = (\Delta\sigma_n \Delta\varepsilon_n) + (\Delta\tau\Delta\gamma)_{\max}$	Cyclic, proportional Cyclic, non-proportional	No
Chu et al. [58]	$\Delta W^* = \left(\Delta\tau_{n,\max}\frac{\Delta\gamma}{2} + \sigma_{n,\max}\frac{\Delta\varepsilon_n}{2}\right)_{\max}$	Cyclic, proportional Cyclic, non-proportional	Yes
Glinka et al. [59,60]	$\Delta W^* = \frac{\Delta\tau}{2}\frac{\Delta\gamma}{2} + \frac{\sigma_n}{2}\frac{\Delta\varepsilon_n}{2}$	Cyclic, proportional Cyclic, non-proportional	Yes
Pan et al.[61]	$\Delta W^* = \frac{\Delta\tau}{2}\frac{\Delta\gamma}{2} + k_1 k_2 \frac{\sigma_n}{2}\frac{\Delta\varepsilon_n}{2}$	Cyclic, proportional Cyclic, non-proportional	No
Chen et al.[62]	$\Delta\varepsilon_{n,\max}\,\Delta\sigma_n + \Delta\tau\Delta\gamma$	Cyclic, proportional Cyclic, non-proportional	No
Varhani-Farahani [63]	$\frac{\Delta\sigma_n\Delta\varepsilon_n}{\sigma'_f\varepsilon'_f} + \frac{1+\sigma_{n,m}/\sigma'_f}{\tau'_f\gamma'_f}\Delta\tau_{\max}\Delta\left(\frac{\gamma_{\max}}{2}\right)$	Cyclic, proportional Cyclic, non-proportional	Yes
Jahed and Varhani-Farahani [64]	$\Delta E_A = E'_e (N_A)^B + E'_f (N_A)^C$ $\Delta E_T = E'_e (N_T)^{Bs} + E'_f (N_T)^{Cs}$ $N_f = \frac{\Delta E_A}{\Delta E} N_A + \frac{\Delta E_T}{\Delta E} N_T$	Cyclic, proportional Cyclic, non-proportional	Yes

2.4 **Cumulative Damage**

The linear damage rule proposed by Palmgren [65]-Miner [66] can be used to account for accumulated damage. The liner damage rule does not require any additional material constant to define it and it can be expressed as a

$$D=\sum \frac{n_i}{N_{fi}}=\frac{n_1}{N_{f1}}+\frac{n_2}{N_{f2}}+... \tag{2.80}$$

Where n_i is the number of cycles at a given stress or strain amplitude and N_{fi} is the number cycles to failure associated with the same stress and strain amplitude.

Although there have been many objections to assumptions of the linear damage rule, it still remains as the most widely used cumulative damage rule due to its simplicity. Sequence and interaction of loads may have significant effects on the fatigue life. The rate of damage accumulation may be a function of the load amplitude such that at low load levels, most of the life is involved in the crack initiation, while at high load levels most of the life is spent in crack growth. The linear damage rule does not account for load amplitude dependence of load sequence effects which are usually encountered in the variable amplitude loadings experienced by the driveline and suspension components. High amplitude cycles followed by low amplitude cycles are usually more damaging than low amplitude cycles followed by high amplitude cycles, even for materials without constitutive behavior sensitivity to load sequence. In order to overcome deficiencies associated with the linear damage rule, many nonlinear damage rules have been proposed

Since sequence and interaction of loads are not accounted for by the linear damage rule, a nonlinear damage accumulation rule is used to account for these effects. Markoy and Starkey [67] proposed an exponential form of a linear damage rule as:

$$D = \sum \left(\frac{n_i}{N_{fi}} \right)^{\eta_i} \tag{2.81}$$

Where η_i is based on the load level to take into account effects of sequence for loadings.

In multiaxial fatigue, variation of load path can also affect fatigue life. For example, torsion followed by tension has been found to be more damaging than tension followed by torsion [68,69]. This phenomenon has been explained by torsion cycles nucleating small cracks on planes where subsequent tensile cycles can lead to their growth, while tensile cycles do not nucleate cracks on planes which can grow by torsion cycles.

2.4.1 Critical Plane-Based Fatigue Damage Parameters

Many multiaxial fatigue damage parameters have been proposed, but unfortunately, no general agreement has been reached on the best method or approach to multiaxial fatigue. However, as it has been supported by recent studies [76,77,90], the critical plane concept is considered as one of the most successful approach in predicting multiaxial fatigue life due to their reasonable accuracy and predicting the potential crack plane orientation. The critical plane based fatigue damage parameters postulate that only shear and normal stresses and strains in these planes contribute the crack initiation and propagation. Various critical plane models such as stress-based (the Findley), strain-based (the Brown-Miller and the Fatemi-Socie) and energy-based (the Chu and the Glinka) damage parameters, which have been briefly reviewed before are discussed in great detail in this section to identify their capabilities and shortcomings in their applications of predicting fatigue life under multiaxial loading. In this study, these fatigue damage parameters for the discussion have been selected due to their general

representation of the stress-based, the strain-based and the energy-based damage parameters. This discussion will lead to development of a proposed multiaxial fatigue damage parameter in Chapter 4 by combining good features from those models. The proposed multiaxial damage model is presented in Chapter 4.

Based on physical observation of initial fatigue crack observation in steel and aluminum, Findley [47] proposed a linear combination of normal stress acting on shear stress plane. According to Findley, the critical plane is the plane of orientation theta maximizing the Findley damage parameter, Eq. (2.52). The Findley damage parameter is often applied for the case of high cycle fatigue regime where the plastic deformation is negligible and loading is proportional. This damage parameter does not contain any strain terms, and therefore does not consider the cyclic plastic deformation, thus is not applicable to low cycle fatigue. The Findley damage parameter also requires a material fitting coefficient, k for the influence of the normal stress on the maximum shear stress plane.

Many strain-based multiaxial fatigue damage parameters have been proposed. The Brown-Miller and Fatemi-Socie damage parameters are considered to be the two most popular fatigue damage parameters in the critical plane method. However both damage parameters have their weaknesses and limitations in the application of multiaxial life prediction. These strain-based critical plane damage parameters state that that the fatigue damage parameter requires at least two terms to provide satisfactory life prediction under the multiaxial loadings. These fatigue damage parameters consider the maximum shear strain range as a primary damage parameter and normal stresses or strains acting on the critical plane as a secondary damage parameter. Brown-Miller [51] proposed the normal

strain as the secondary parameter, Eq. (2.61) whereas Fatemi-Socie [55] suggested the normal stress as the secondary damage parameter, Eq. (2.65). In these models, S and k material fitting constants which require cyclic torsional testing are used to account for the sensitivity of the normal strain and normal stress on the maximum shear strain range on the critical plane. The requirement for the additional material testing determines that these material constants are not considered to be practical and efficient approach for the application of multiaxial fatigue life prediction. The Brown-Miller and Fatemi-Socie damage parameters are determined on the plane of the maximum shear strain, however, in case of in-phase loading, the Brown-Miller and the Fatemi-Socie damage parameters reach their maximum on not the plane of the maximum shear strain, but on the different plane as shown in Figure 2-22. If the normal strain in Brown-Miller damage parameter and the maximum normal stress in the Fatemi-Socie damage parameter has an effects on the maximum shear plane to assist in accelerating a crack, the effects of normal strain and stress should be present in all planes experiencing shear strain, rather than only on the plane of the maximum shear strain . Figure 2-22 shows that the maximum fatigue damage occurs on the plane near the plane of the maximum shear strain rather than the maximum shear plane due to higher normal strain and stress quantities for both the Brown-Miller and Fatemi-Socie damage parameters. However, in case of out-of-phase loading, the plane experiencing the maximum fatigue damage is exactly same as the maximum shear strain plane (Figure 2-22). Fatigue cracks for many materials for in-phase and 90^{o} out-of-phase loadings were found to be around maximum shear plane [70]. This conclusion supports the argument that the critical plane should be a plane experiencing the maximum fatigue damage, not necessarily the maximum shear strain-stress plane. Although the

Brown-Miller damage parameter can apply to both low and high cycle fatigue, the fatigue damage parameter cannot show constitutive behavior of the material such as effects of the non-proportional cyclic hardening due to missing the stress term in the damage parameter. The Brown-Miller damage parameter does not take into account effects of the mean stress because the model is only based on strain terms. Both the non-proportional and mean stress can have significant effects on multiaxial fatigue life. Unlike the Brown-Miller damage parameter, the Fatemi-Socie damage parameter has an ability to capture effects of the non-proportional hardening through the maximum normal stress in the damage parameter. The Fatemi-Socie damage parameter also takes into account the effects of the mean stress on the critical plane through the maximum normal stress, which is a sum of alternating and mean stress components. These strain-based critical planes models have been found to be applicable to both proportional and non-proportional loading conditions [1,71,76,77].

The energy-based fatigue damage parameters contain both strain and stress terms in the form of strain energy in the critical plane. Chu et al. [58] proposed a fatigue damage parameter Eq.(2.70) to combine shear and normal strain work. They replaced the stress ranges with maximum stresses in order to include mean stress effects.

The Chu damage parameter is based on the maximum value of the strain energy rather than being defined on the plane of maximum normal and shear strain. The physical basis of this model attempts to average the contribution of tensile and shears strain work.

Glinka et al. [59,60] proposed an energy parameter, Eq.(2.71) of total strain energy density. This energy parameter is expressed by stresses and strains on the critical plane of the maximum shear strain. Glinka et al. applied shear and normal strain energy density

instead of total strain energy. Later the Glinka damage parameter was modified by including the maximum shear stress and normal stress to take into account the mean stress effects, Eq. (2.72) In the Glinka damage parameter, normal stresses will assist in the opening of a crack and shear stresses will help to overcome sliding friction by deforming asperities on the crack surface.

Both the Chu and the Glinka damage parameters can be applicable to low and high cycle fatigue regimes as well as the proportional and non-proportional loading conditions because of both strains and stress components defining the damage parameter.

In consideration of strengths of the stress-based and strain-based and energy-based multiaxial fatigue damage parameters previously discussed, some of important features from these damage parameters can be summarized as: the multiaxial fatigue damage parameter should take into account that tensile mean stress is detrimental to fatigue life whereas the compressive mean stress is beneficial. A good multiaxial fatigue damage parameter should be applicable to wide range of loading conditions, i.e. proportional and non-proportional loading and low and high cycle fatigue regimes. Strengths and shortcomings of the stress-based, the strain-based and energy-based fatigue damage parameters discussed above lead a proposed multiaxial fatigue damage parameter, which integrates all these important features required for a successful fatigue damage parameter in Chapter 4.

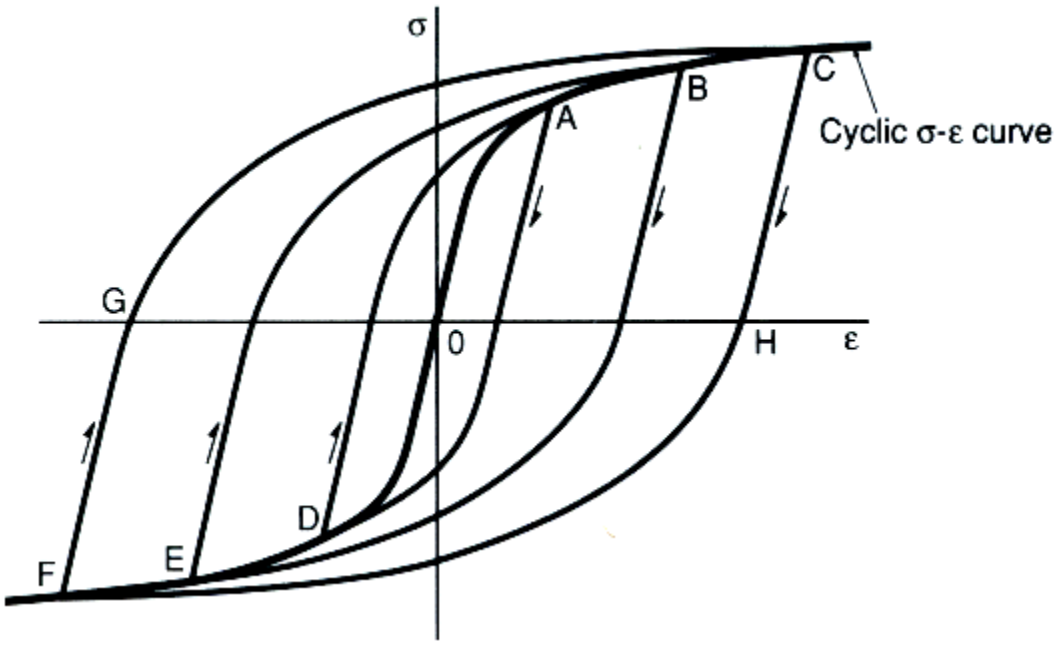

Figure 2-1: The stabilized hysteresis loops and the cyclic stress -strain curve

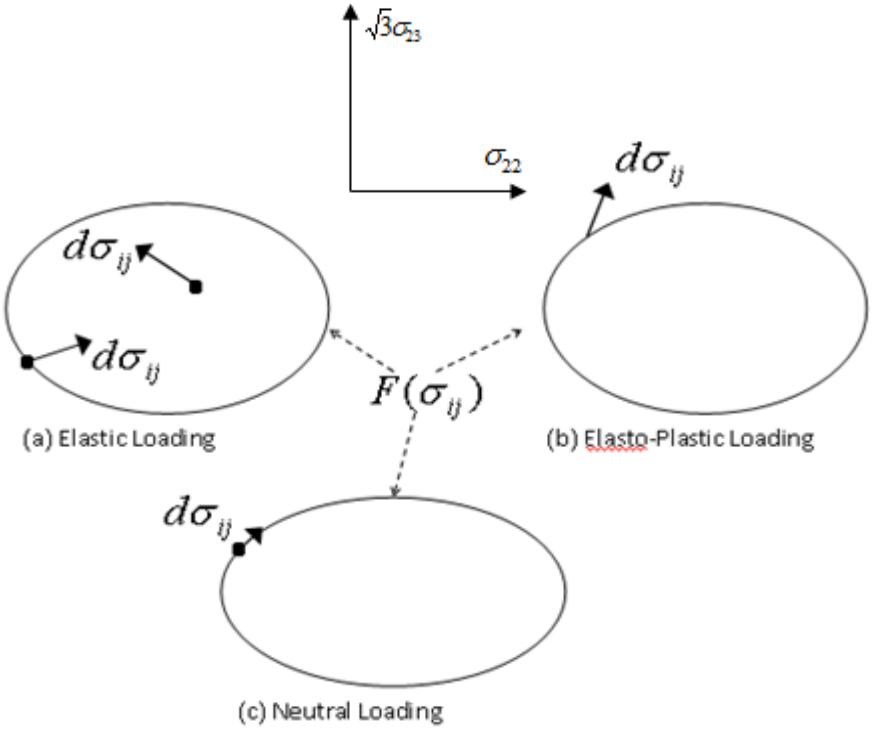

Figure 2-2: States of loading on yield surface [72]

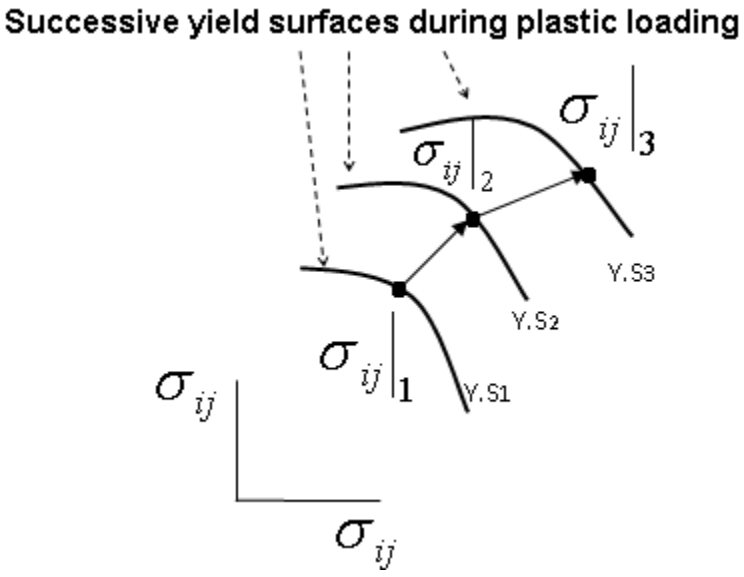

Figure 2-3: Consistency condition for the evolution of yield surfaces for a sequence of two loading paths [72]

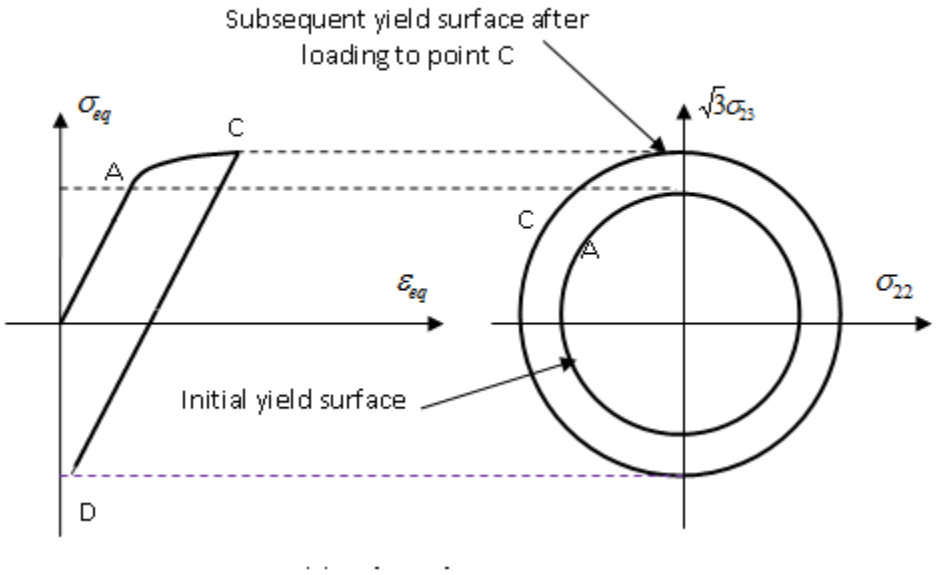

Figure 2-4: Isotropic hardening model [72]

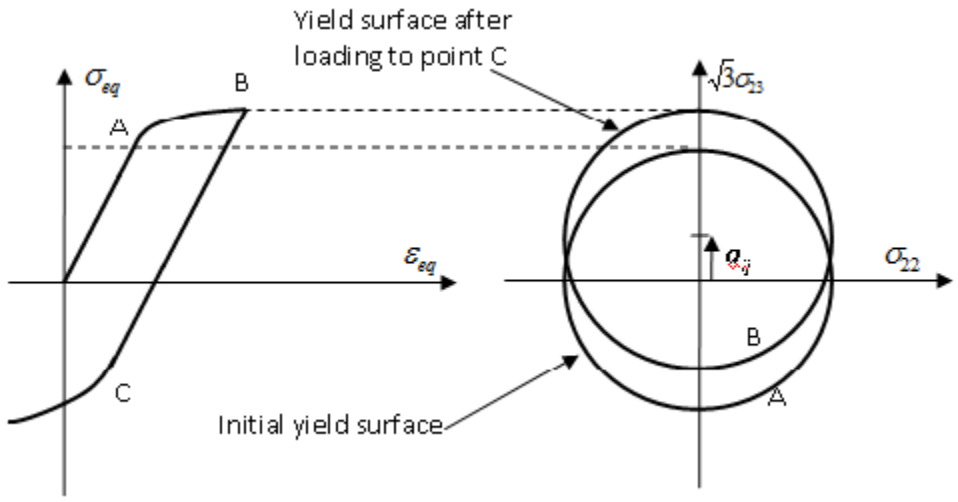

Figure 2-5: Kinematic hardening model [72]

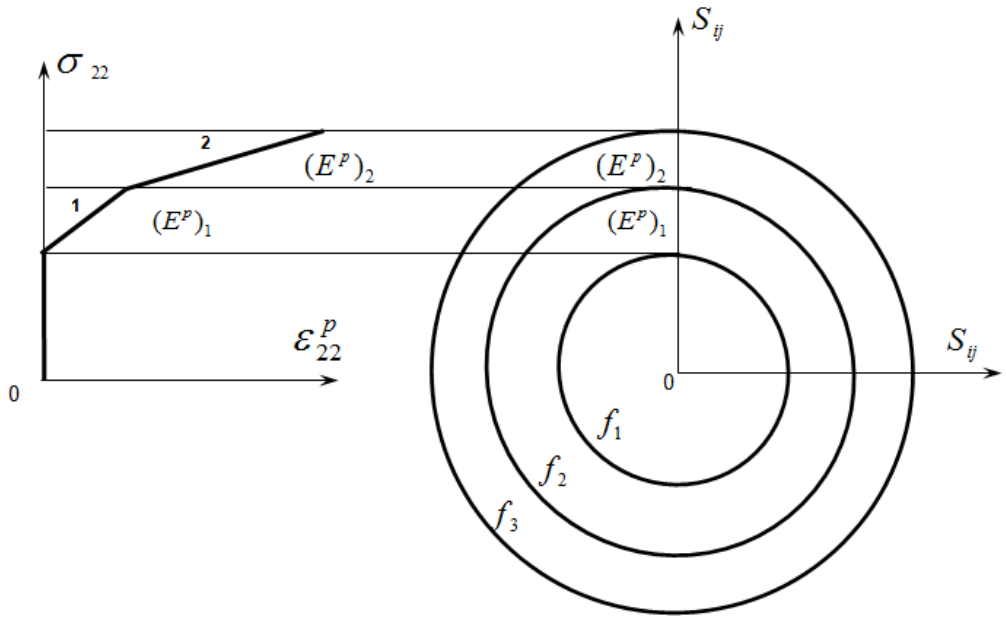

Figure 2-6: Piecewise linearization of the material $\sigma_{22} - \varepsilon_{22}^p$ curve and the corresponding field of plastic moduli

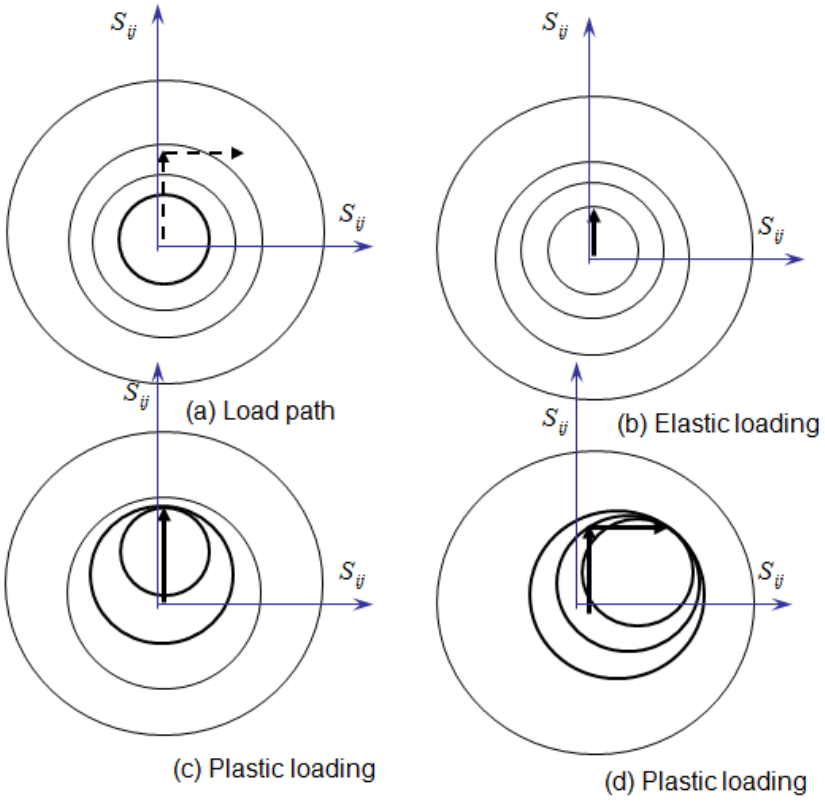

Figure 2-7: Yield surface movement in the Mroz model [72]

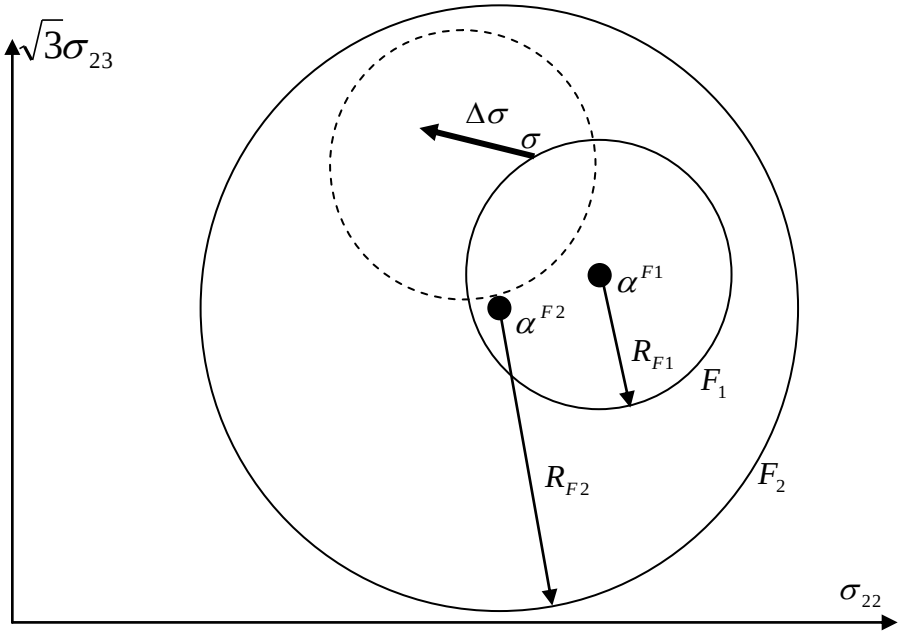

Figure 2-8: Assumed initial state of the Garud model

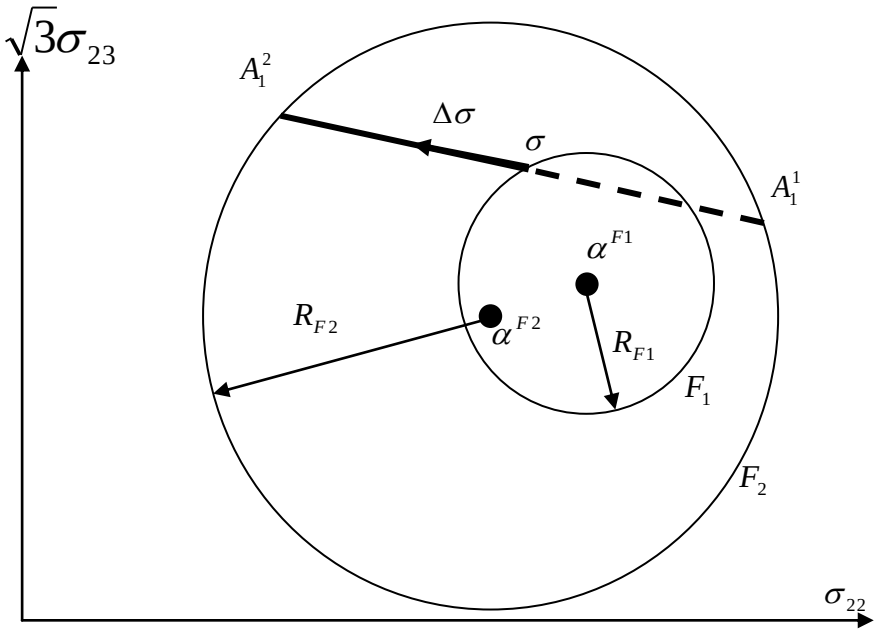

Figure 2-9: Extension of the line of the stress increment Δσ (the Garud model)

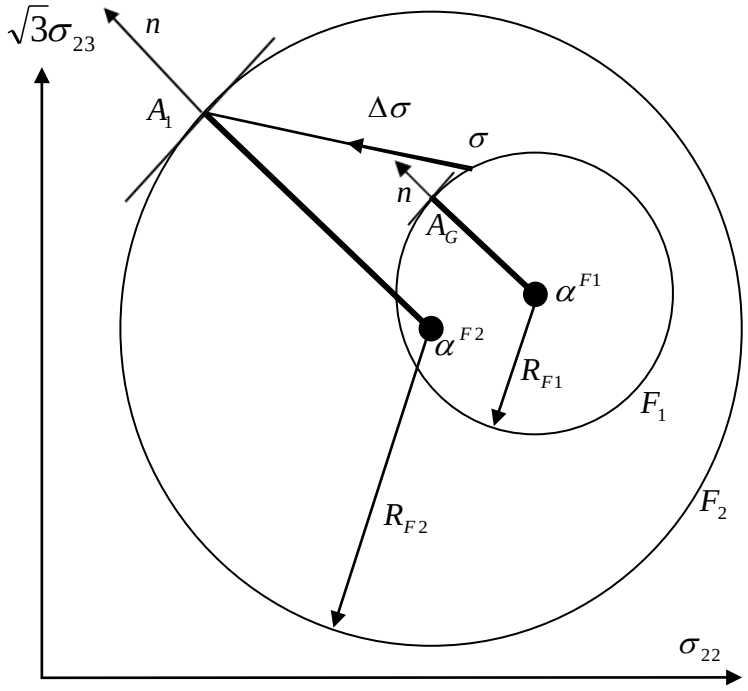

Figure 2-10: The geometrical illustration of the step (b) (the Garud model)

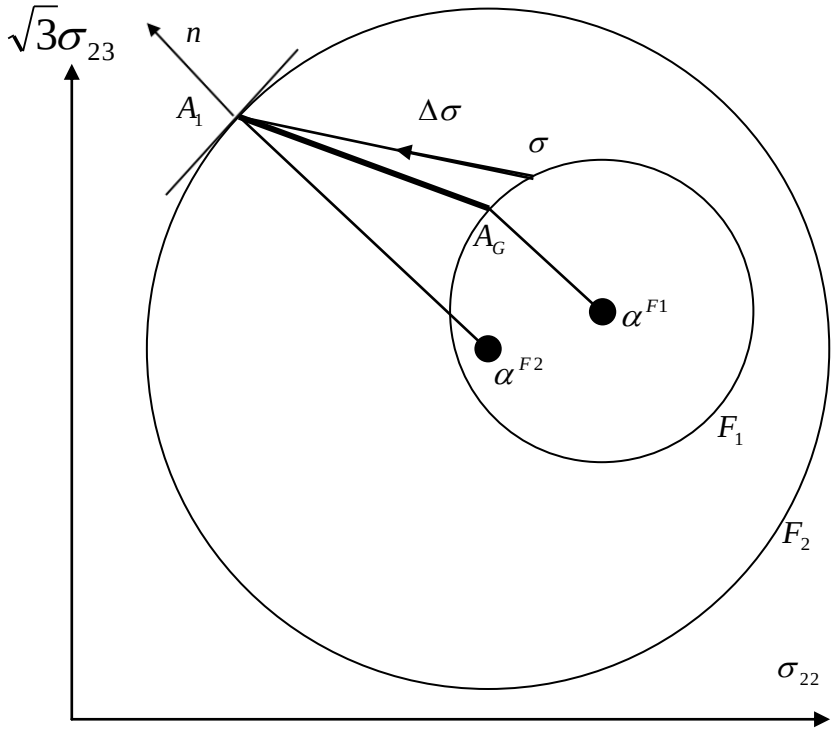

Figure 2-11: Connect the points A_1 and A_G (the Garud model)

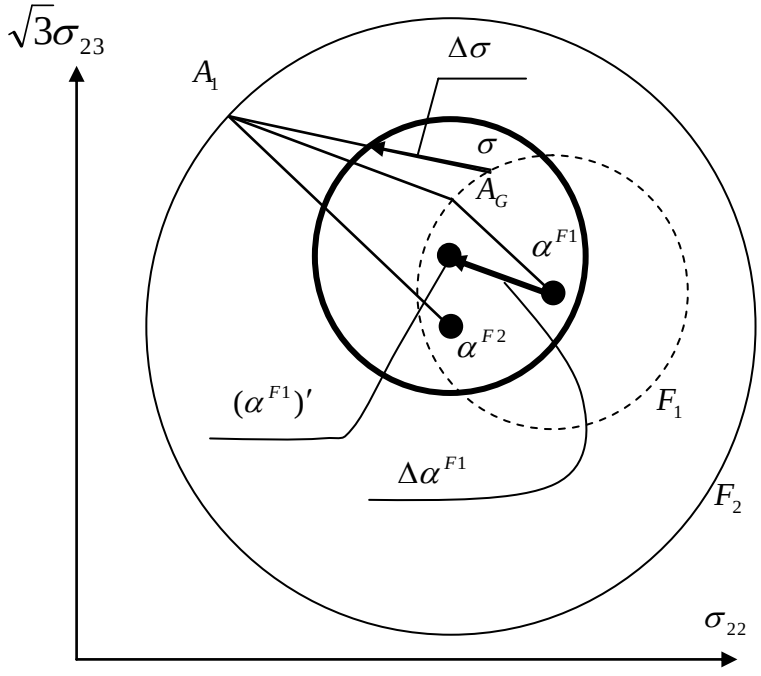

Figure 2-12: Translation of the yield surface F_1 (the Garud model)

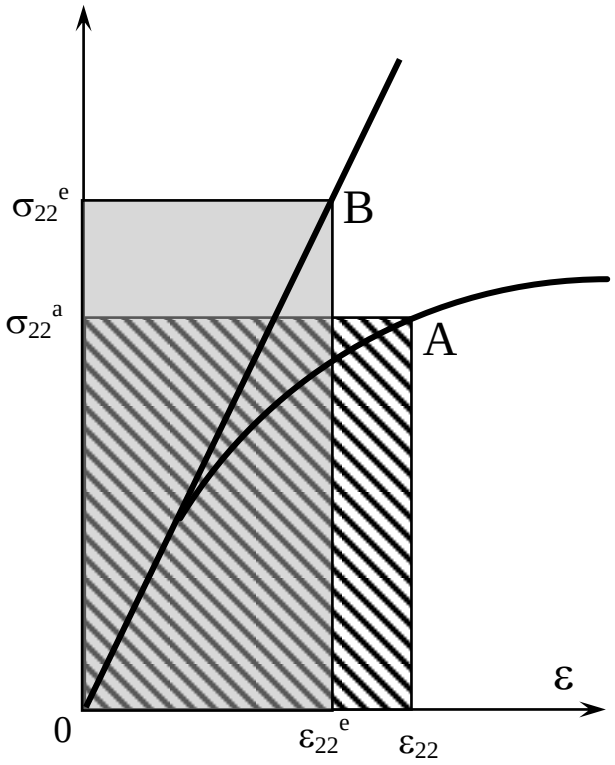

Figure 2-13: Neuber's rule principle

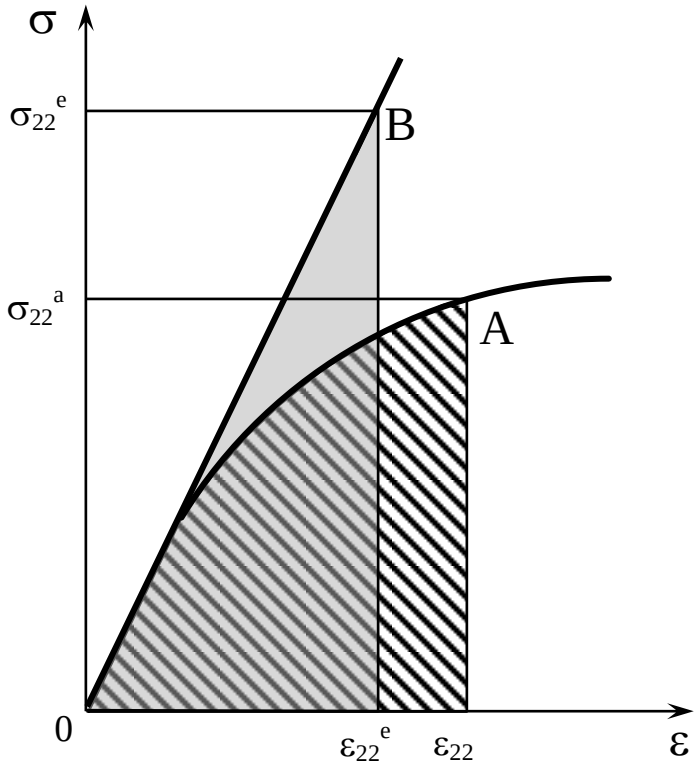

Figure 2-14: Equivalent strain energy density (ESED) method

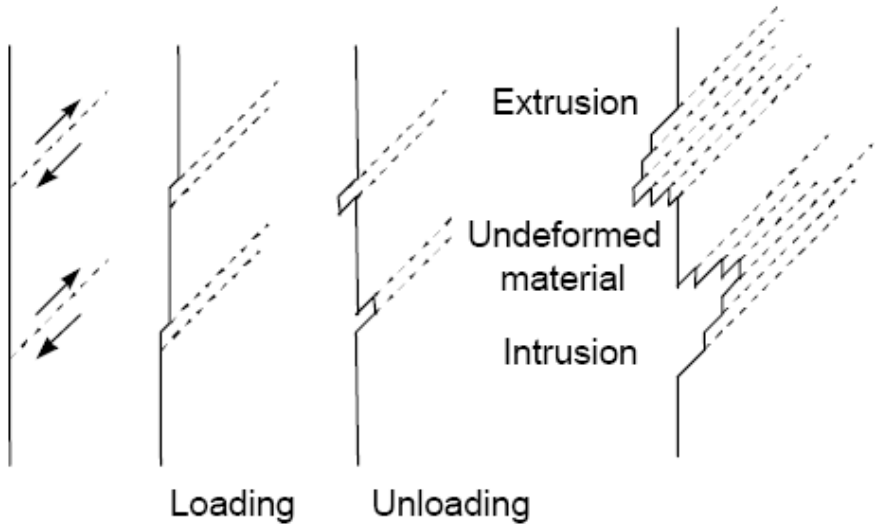

Figure 2-15: Formation of slip bands [73]

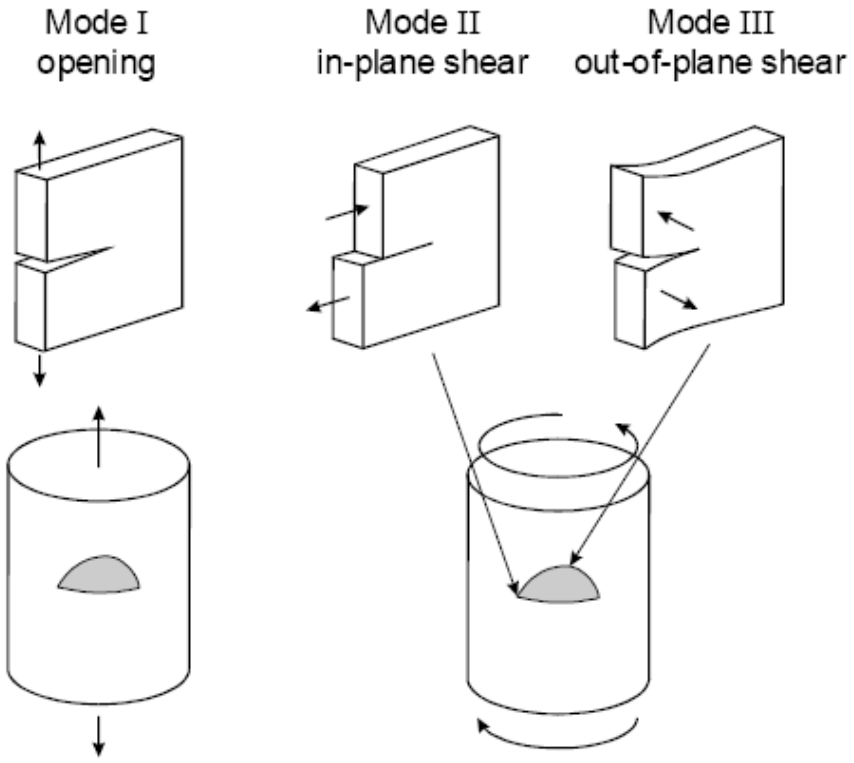

Figure 2-16: Crack propagation modes [73]

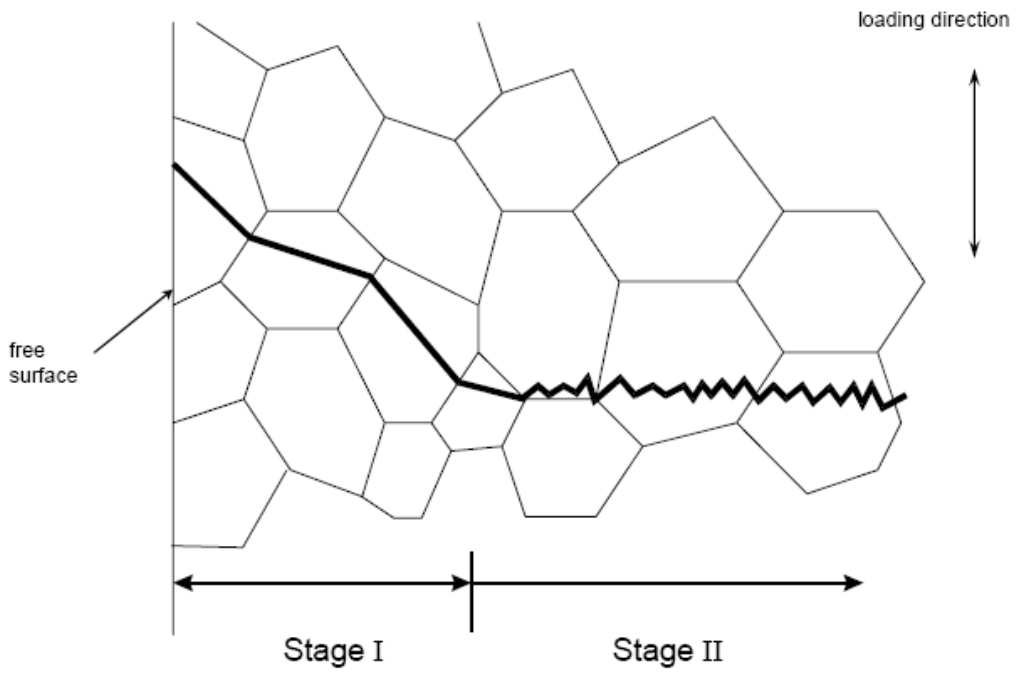

Figure 2-17: Stage I and Stage II crack growth processes [73]

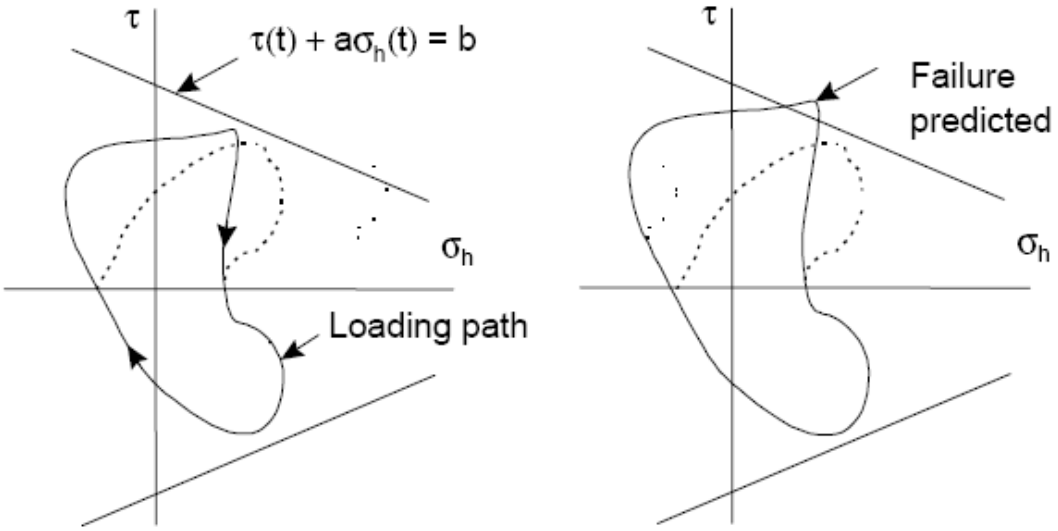

Figure 2-18: Dang Van Criterion [73]

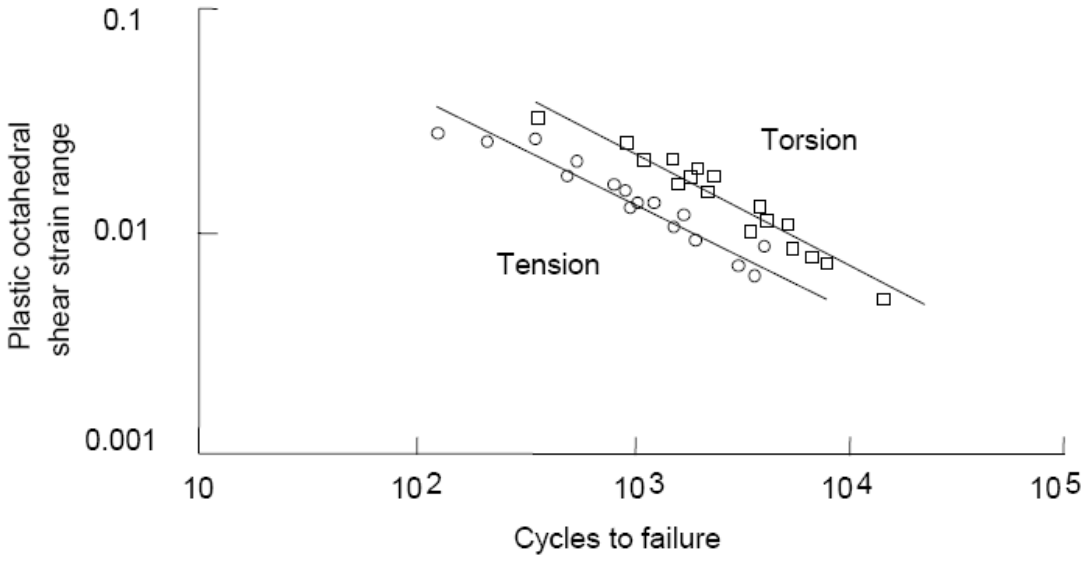

Figure 2-19: Plastic octahedral shear strain – life curve [73]

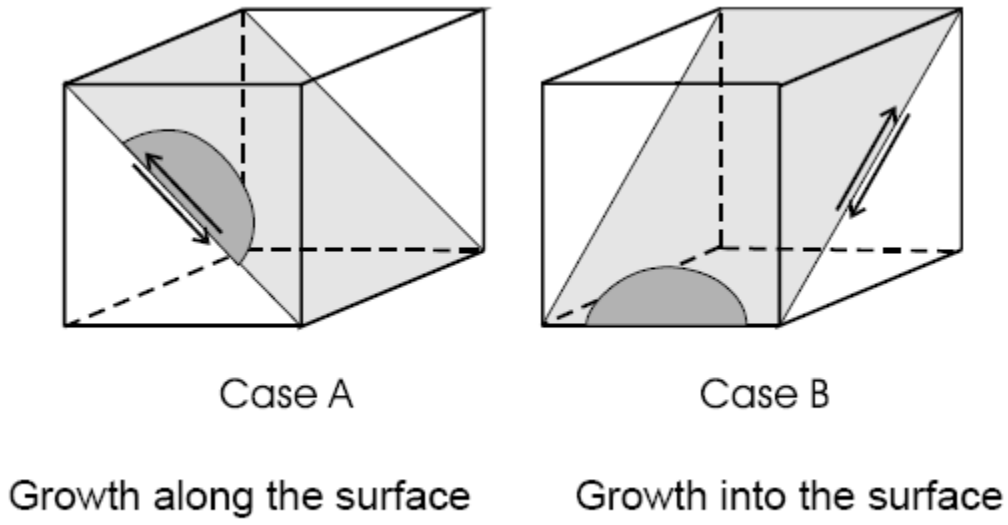

Figure 2-20: Case A and Case B crack growth [73]

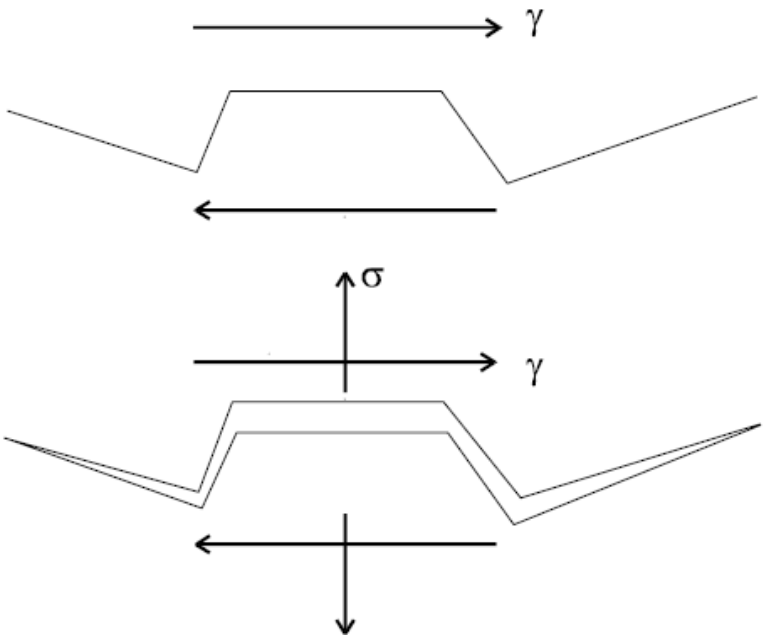

Figure 2-21: Physical basis for Fatemi and Socie model [73]

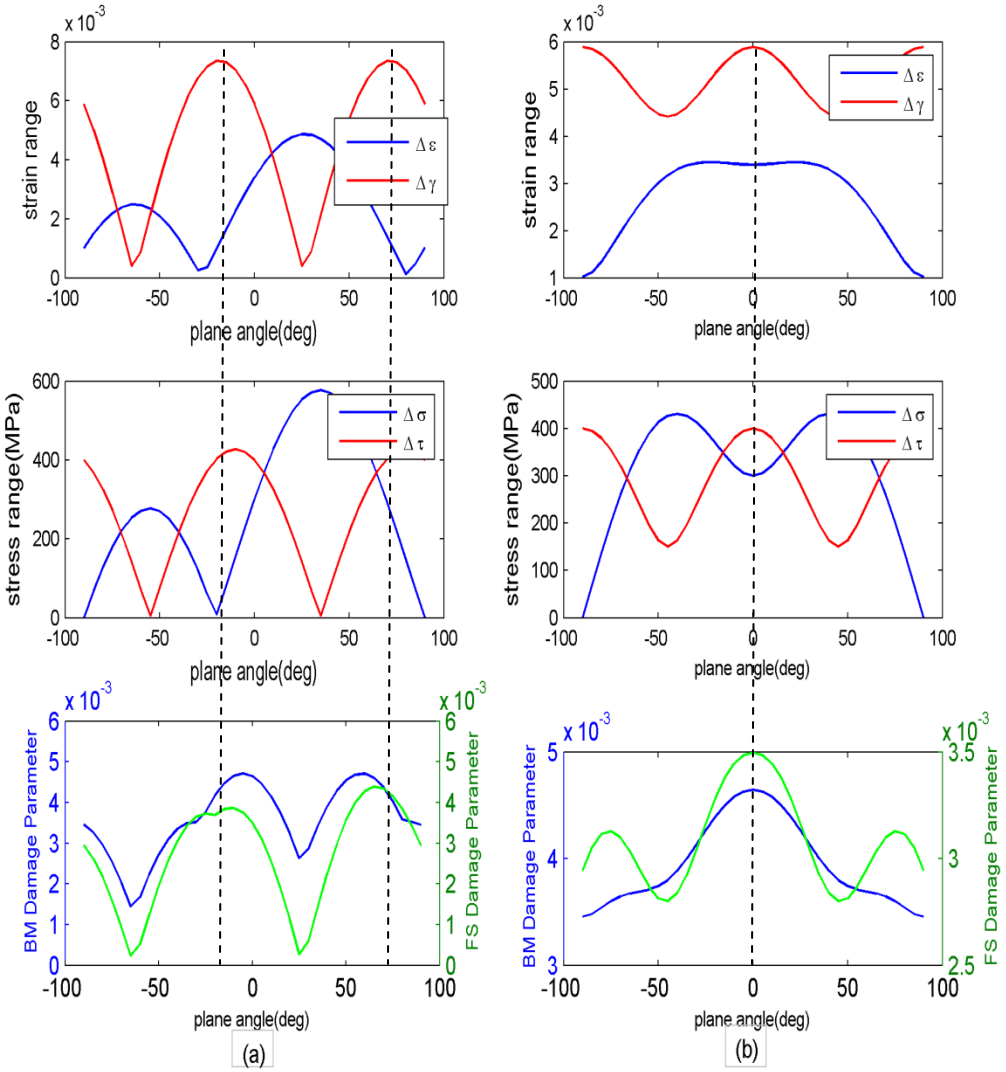

Figure 2-22: Brown-Miller (BM) and Fatemi-Socie (FS) Damage Parameters on various planes for (a) in-phase loading and (b) 90^o **out-of-phase loading**

Chapter 3

Modelling of Elasto-plastic Stress and Strain in Notches under Multiaxial Cyclic Loading

Predicting fatigue life of notched components requires detail knowledge of stresses and strains in critical notched locations. Notch root stresses and strains are dependent on the notch geometry, material properties and the loading history applied to the body. Engineers/designers need to know local stress and strain responses for the applied load history in order to appropriately design and size components to satisfy desired fatigue life. The local stress and strain at the critical location can be determined by three different methods. First method: performing tests and measuring strain data at the notch area by placing strain gauges. Measured strain data from testing can be used as an input to the cyclic plasticity model to compute local stresses and strains. However, placing strain gauges at the critical location is most often not possible due to space constraints of the notch geometry and time and cost associated with testing is too expensive. Second method: finite element modelling of the notched component and performing incremental elastic-plastic nonlinear finite element analysis to determine the local stress and strain history. However, this method is not practical in terms of computational time and a hard disk space for a long load history, which often the components are subjected to. Third method: the notch correction method can be combined with the cyclic plasticity model to compute the local stress and strain history from the pseudo elastic stress and strain at the notch area. Coupling the notch correction method and the cyclic plasticity to compute the local stresses and strains at critical locations in components provides a great advantage over tests and elastic-plastic finite

element analyses due to its simplicity, computational efficiency, low cost and reasonable accuracy. The multiaxial elasto-plastic stress-strain notch analysis method was previously proposed by Buczynski and Glinka [74] has been modified , improved and extended to such a level of sophistication that it can be used for stress-strain analysis for notched components using linear elastic FE stress results (pseudo elastic stresses). The method is based on the incremental relationships, which relate the elastic and elastic-plastic strain energy densities at the notch root and the material stress-strain behavior, simulated by the Garud cyclic plasticity model. The original algorithm used in the method has been modified to allow synchronization of elastic input and elasto-plastic output in context of material memory effects, thus ensuring closed hysteresis loops (analogy of cycle counting in case of uniaxial stress state) for non-proportional loadings. The structure of original computer algorithm was based on single point stress-strain calculation, therefore the original algorithm have been modified to allow stress-strain calculations for many nodal points which define critical notch areas of the FE model. The original computer program codes written in Fortran 77 have also been converted to Fortran 90 in order to increase computational efficiency of the program for practical engineering applications.

The stress state near the notch region is in most cases multiaxial in nature. The multiaxial Neuber notch correction rule and the Garud cyclic plasticity model can be combined to provide a complete set of governing equations to solve all unknown notch stress and strain components. In order to implement equations defined in this chapter for a notched component subjected to multiaxial loading paths, a general computation algorithm has been developed. A flow chart for the algorithm implementing the stress and strain analysis for notched components subjected to the multiaxial loading paths is shown

in Figure 3-1. The notch correction describes the relationship between nominal loads (pseudo elastic stresses and strains) and the actual elasto-plastic stresses and strains at the notch tip. The cyclic plasticity provides constitutive equations relating stresses and strains. This chapter discusses how to combine the Neuber notch correction rule and The Garud cyclic plasticity model for numerical computation of the notch stress and strain components from given pseudo elastic stress-strain histories.

3.1 **Linear Elastic Stress-Strain Histories**

FE models are used often to analyze engineering components. A linear elastic FEA can be used to calculate linear elastic stresses/strains for a notched component. Once the elastic stresses/strains are known, the elasto-plastic stress-strain analysis (combined the multiaxial notch correction and the cyclic plasticity) can be used to compute actual elastic-plastic stress and strain responses at notch areas. The linear elastic FEA assumes that there is a linear relationship between the applied external load and stress/strain results. Axle and shaft components often experience combined bending and torsion loads. Let us consider a notched shaft shown in Figure 3-2, which has two applied load histories, namely bending and torque. The FEA is performed to calculate unit-load linear elastic stress results for each applied load. The elastic stress tensor at each node from the linear elastic FEA is multiplied by the corresponding load history to compute a time history of elastically-calculated stress tensor. If the elastic stress tensor at a node is $\sigma_{ij}^{e\,p}$ for a unit load of p, the time history of elastic stress tensor, $\sigma_{ij}^{e\,P(t)}$ for the load history, $P(t)$ can be calculated as

$$\sigma_{ij}^{e\,P(t)} = P(t)\,\sigma_{ij}^{e\,p} \tag{3.1}$$

If the elastic stress tensor at the same node is $\sigma_{ij}^{e\,q}$ for a unit load of q, the time history of elastic stress tensor, $\sigma_{ij}^{e\,Q(t)}$ for the load history, $Q(t)$ can be calculated as

$$\sigma_{ij}^{e\,Q(t)} = Q(t)\,\sigma_{ij}^{e\,q} \tag{3.2}$$

Time histories of elastic stress tensor $\sigma_{ij}^{e\,P(t)}$ and $\sigma_{ij}^{e\,Q(t)}$ for the same node are then superimposed to obtain the resultant time history of elastic stress tensor for both load histories, $P(t)$ and $Q(t)$ applied simultaneously.

$$\sigma_{ij}^{e} = \sigma_{ij}^{e\,P} + \sigma_{ij}^{e\,Q} \tag{3.3}$$

Figure 3-3 shows a schematic representation of the implementation procedure for the algorithm. Since fatigue crack initiation is formed on the surface of a component, nodal stress components for surface nodes at critical notch areas are used for the fatigue life prediction. A macro routine written in ANSYS Parametric Design Language (APDL) is used to compute elastic stress results for surface nodes for the each unit load. Unit-load elastic stress results from the FEA and corresponding time histories for the each unit load are used as input to a computer program to calculate combined time histories of elastic stress tensor at critical notch areas.

If components of a stress tensor change proportionally during the loading, the loading is called proportional. When the applied load results in the change of the principal stress directions and the ratio of the principal stresses, the loading is called non-proportional. As can be seen in Figure 3-4, in case of the proportional (in-phase) loading, the size of Mohr's circle changes during cycle loading, but the direction of principal stresses remains fixed, whereas for non-proportional (out-of-phase) loading, direction of

principle stresses rotates in time (Figure 3-6). The maximum shear stress range, $\Delta\tau_{\max}$ on the maximum shear plane and the maximum normal stress range, $\Delta\sigma_{n,\max}$ on the maximum normal plane are shown for proportional and non-proportional cyclic loadings in these figures. When plastic yielding takes place at the notch tip, then the stress path at the notch tip region is usually non-proportional regardless whether the external loading is proportional or not. Non-proportional loading/stress paths are usually defined by increments of load/stress components and therefore, stress-strain calculations have to be carried out in incremental form. Time histories of elastic stresses are transformed to increments of elastic stresses. A schematic representation of elastic stress increments used as input to the stress-strain notch analysis model is shown in Figure 3-8.

For the case of general multiaxial loading applied to a notched body, the state of stress near the notch tip is tri-axial. However, the stress state at the notch tip is bi-axial because of the notch-tip stress for a free surface as shown in Figure 3-9. Since equilibrium of the infinitesimal element at the notch tip must be maintained, i.e. $\sigma^e_{23} = \sigma^e_{32}$ and $\varepsilon^e_{23} = \varepsilon^e_{32}$, there are three non-zero stress components and four non-zero strain components.

$$\sigma^e_{ij} = \begin{bmatrix} 0 & 0 & 0 \\ 0 & \sigma^e_{22} & \sigma^e_{23} \\ 0 & \sigma^e_{32} & \sigma^e_{33} \end{bmatrix} \quad \textit{and} \quad \varepsilon^e_{ij} = \begin{bmatrix} \varepsilon^e_{11} & 0 & 0 \\ 0 & \varepsilon^e_{22} & \varepsilon^e_{23} \\ 0 & \varepsilon^e_{32} & \varepsilon^e_{33} \end{bmatrix} \tag{3.4}$$

Seven fictitious linear elastic stress and strain components $(\sigma^e_{ij}, \varepsilon^e_{ij})$ are obtained from the linear elastic FE solution, however the actual elastic-plastic stress and strain components $(\sigma^a_{ij}, \varepsilon^a_{ij})$ at the notch tip are unknown. Therefore, a set of seven independent equations is

required for the calculation of actual elastic-plastic stress and strain components at the notch tip. The multiaxial Neuber notch correction rule and the Garud cyclic plasticity model are integrated to provide required seven equations to solve for all unknown stress and strain components. The cyclic plasticity provides four equations and the notch correction rule provides remaining three equations.

3.2 **Constitutive Governing Equations**

Under applied cyclic loadings, stress-strain responses at critical regions (notches) often show a transient response, but stabilize over a number of cycles. For non-proportional load histories, an incremental plasticity analysis is required to estimate the material's stress-strain response. A number of incremental plasticity models [11,12,13,18,19,20,24] have been developed to estimate constitutive material behavior and some of those models are sophisticated to include the transient hardening responses. However, these complex models require significant material testing to characterize model parameters and are not appropriate for practical engineering use. Furthermore, for the multiaxial fatigue analysis, the transient nature of deformation behavior is not as critical as the behavior of cyclically stabilized material behavior. Therefore, a relatively simple Garud hardening model is used to deal with proportional and non-proportional multiaxial loadings.

The cyclic plasticity model provides a set of governing equations to relate stress and strain components. Since the fatigue cracks most often initiate on the surface of a component, governing equations are presented for stress/strain state on the free component surface. Governing equations are presented in deviatoric space based on a

rate-independent, homogenous and isotropic material because it is easier to formulate the equations using deviatoric stress and strain quantities.

In elastic loadings, the deformation process is reversible and when the applied load is removed from the body, the deformed body returns to its original state. There is a direct relationship between stress and strain, and relations between stress and strain tensors are determined by Hooke's law, Eq. (2.3).

The generalized Hooke's law in an incremental form is represented as:

$$d\varepsilon_{ij}^{e} = \frac{1+\nu}{E} d\sigma_{ij} - \frac{\nu}{E} d\sigma_{ij}\delta_{ij} \tag{3.5}$$

When the body is deformed beyond the material's yield limit, permanent and plastic deformation occurs and the deformation process becomes irreversible. When the applied load is removed from the body, the permanent deformation remains in the body. Based on the plasticity theory, the stress and strain state is dependent on the loading path. As discussed in Chapter 2, there are three main elements required in order to model constitutive behavior of the material: a yield criterion, which defines a boundary between elastic and elastic-plastic stress state, a flow rule , which describes relationship between stress and strain increments, and a hardening rule, which describes how yield function changes during the plastic deformation. The von Mises yield criterion has been the most popular criterion for modelling of the material constitutive behavior. Since it is widely accepted that hydrostatic stresses do not influence yielding, the yield function, Eq. (2.12) for the isotropic hardening can be described as a uniformly and symmetrically expansion of the yield surface in all directions during plastic loading. The yield function, Eq. (2.15) for the kinematic hardening can be represented as a translation of the yield surface

without any expansion during plastic loading. The yield surface for the kinematic hardening maintains its shape and size.

The flow rule, Eq.(2.11) defines the relationship between stress and plastic strain increments. The flow rule, based on the normality postulate by Drucker [7] implies that the increment of plastic strain is in the normal direction to the yield surface during plastic deformation. The flow rule associated with the yield surface for the isotropic hardening can be described by Eq.(2.13) and the flow rule associated with the yield surface for the kinematic hardening can be described by Eq.(2.16).

For elastic-plastic loading, total strain tensor is the sum of elastic strain determined by Hooke's law and plastic strain determined by the flow rule.

The elastic and plastic strain can be added to obtain the total strain.

$$\varepsilon_{ij} = \varepsilon_{ij}^{\ e} + \varepsilon_{ij}^{\ p} \tag{3.6}$$

Similarly, the elastic and plastic strain increment can be added to obtain the total strain increment.

$$d\varepsilon_{ij} = d\varepsilon_{ij}^{\ e} + d\varepsilon_{ij}^{\ p} \tag{3.7}$$

Substituting Eqs. (3.5) and (2.11) into Eq. (3.7) yields a general form of the total elastic-plastic strain increment. The generalized constitutive elasto-plastic stress-strain relationships are derived from the uniaxial stress-stress curve by using principles of the theory of elasticity and plasticity.

$$d\varepsilon_{ij} = \frac{1+\nu}{E} d\sigma_{ij} - \frac{\nu}{E} d\sigma_{ij}\delta_{ij} + d\lambda \frac{\partial F}{\partial \sigma_{ij}} \tag{3.8}$$

In the case of proportional stress path, the Hencky total deformation of plasticity equations can be used for stress-strain analysis.

$$\varepsilon_{ij}^{a} = \frac{1+\nu}{E}\sigma_{ij}^{a} - \frac{\nu}{E}\sigma_{kk}^{a}\delta_{ij} + \frac{3}{2}\frac{\varepsilon_{eq}^{pa}}{\sigma_{eq}^{a}} \cdot S_{ij}^{a} \tag{3.9}$$

The normality flow rule, also called The Prandtl-Reuss relation is considered one of the most frequently used model in the incremental plasticity. The total strain increment, Eq. (3.8) can be expressed in the form of the Prandtl-Reuss strain-stress relationship:

$$\Delta\varepsilon_{ij}^{a} = \frac{1+\nu}{E}\Delta\sigma_{ij}^{a} - \frac{\nu}{E}\Delta\sigma_{kk}^{a}\delta_{ij} + \frac{3}{2}\frac{\Delta\varepsilon_{eq}^{pa}}{\sigma_{eq}^{a}} \cdot S_{ij}^{a} \tag{3.10}$$

The notch tip deviatoric stresses of the hypothetical linear-elastic body are determined as:

$$S_{ij}^{e} = \sigma_{ij}^{e} - \frac{1}{3}\sigma_{kk}^{e}\delta_{ij} \tag{3.11}$$

The elastic deviatoric strain and stress increments can be calculated from the Hooke law.

$$\Delta e_{ij}^{e} = \frac{\Delta S_{ij}^{e}}{2G} \tag{3.12}$$

The actual deviatoric stress components in the notch tip can analogously be defined as:

$$S_{ij}^{a} = \sigma_{ij}^{a} - \frac{1}{3}\sigma_{kk}^{a}\delta_{ij} \tag{3.13}$$

The incremental deviatoric stress-strain relations based on the associated the Prandtl-Reuss flow rule can be subsequently written as:

$$\Delta e_{ij}^{a} = \frac{\Delta S_{ij}^{a}}{2G} + d\lambda \cdot S_{ij}^{a} \tag{3.14}$$

where:

$$\frac{1}{2G}=\frac{1+\nu}{E},\quad d\lambda=\frac{3}{2}\frac{\Delta\varepsilon_{eq}^{p}}{\sigma_{eq}^{a}},\quad \sigma_{\mathrm{eq}}^{\mathrm{a}\ 2}=\frac{3}{2}S_{ij}^{a}S_{ij}^{a},\quad \Delta\varepsilon_{\mathrm{eq}}^{\mathrm{p}}=\frac{df(\sigma_{eq}^{a})}{d\sigma_{eq}^{a}}\Delta\sigma_{eq}^{a}$$

This relation assumes that the plastic strain increments at any instant of loading are proportional to the deviatoric stress components. The relation between the equivalent plastic strain increment and the equivalent stress increment in the uniaxial stress-strain curve can be used to determine the multiaxial incremental stress-strain relation Eq. (3.15).

$$\Delta\varepsilon_{eq}^{pa}=\frac{\Delta\sigma_{eq}^{a}}{E_{T}^{p}} \tag{3.15}$$

Where $\Delta\varepsilon_{eq}^{pa}$ is the equivalent plastic strain increment, $\Delta\sigma_{eq}^{a}$ is the equivalent stress increment and E_{T}^{p} is the current value of the generalized plastic modules.

The function, $\Delta\varepsilon_{eq}^{pa}=f\left(\Delta\sigma_{eq}^{a}\right)$, is identical to the plastic strain – stress relationship obtained experimentally from uniaxial tension test. The plastic strain – stress relationship can be expressed according to the uniaxial Ramberg-Osgood equation.

$$\sigma=K^{'}\left(\varepsilon^{p}\right)^{n'} \tag{3.16}$$

Where the constants $K^{'}$ and $n^{'}$ are determined by uniaxial tensile test.

The analytical expression of the generalized plastic modules E_{T}^{p} can be derived using the Ramberg-Osgood equation.

$$E_{T}^{p}=\frac{2}{3}\frac{d\sigma}{d\varepsilon^{p}}=\frac{2}{3}E^{p}=\frac{2}{3}K^{'}n'\left(\frac{\sigma}{K^{'}}\right)^{\frac{n'-1}{n'}} \tag{3.17}$$

Where E^p is the slope of the uniaxial stress-plastic strain curve (or the uniaxial plastic modulus).

The uniaxial stress-strain curve is divided into a desirable number of stress fields (Figure 3-10). Each stress surface defines regions with constant plastic modulus in the stress space. Figure 3-10 shows a graphic interpretation of generalizations of the $\sigma_{eq} - \varepsilon_{eq}^{p}$ curve in the stress space and stress fields of constant plastic modules.

In case of stress and strain state on the free surface of the notch, Eq.(3.14), material constitutive equations are given in terms of deviatoric stresses.

$$\begin{aligned}
\Delta e_{11}^{a} &= \frac{\Delta S_{11}^{a}}{2G} + d\lambda \cdot S_{11}^{a} \\
\Delta e_{22}^{a} &= \frac{\Delta S_{22}^{a}}{2G} + d\lambda \cdot S_{22}^{a} \\
\Delta e_{33}^{a} &= \frac{\Delta S_{33}^{a}}{2G} + d\lambda \cdot S_{33}^{a} \\
\Delta e_{23}^{a} &= \frac{\Delta S_{23}^{a}}{2G} + d\lambda \cdot S_{23}^{a}
\end{aligned} \tag{3.18}$$

Four notch strain increments ($\Delta e_{11}^{a}, \Delta e_{22}^{a}, \Delta e_{33}^{a}, \Delta e_{23}^{a}$) and three notch stress increments ($\Delta\sigma_{22}^{a}$, $\Delta\sigma_{33}^{a}$, $\Delta\sigma_{23}^{a}$) in Eq. (3.18) form seven unknowns to be solved. Four deviatoric stress increments ($\Delta S_{11}^{a}, \Delta S_{22}^{a}, \Delta S_{33}^{a}, \Delta S_{23}^{a}$) in Eq. (3.18) are functions of three notch stress increments ($\Delta\sigma_{22}^{a}$, $\Delta\sigma_{33}^{a}$, $\Delta\sigma_{23}^{a}$).

3.3 **Coupling Constitutive Equations and Neuber Notch Correction Relation**

The main goal of this section is to show how to combine a cyclic plasticity model and notch correction method to determine a set of governing equations to compute the notch stress and strain components. The cyclic plasticity model provides four governing

equations, Eq. (3.18) by establishing a relation between the stress and strain at notch root and the notch correction relation provides three additional equations by relating the pseudo-elastic and the actual elastic-plastic strains and stresses at the notch root.

The load is usually represented by the nominal stress being proportional to the remote loading for notched bodies. In the case of notched bodies in a plane stress or plane strain state, the relationship between the elastic notch tip stresses-strains and the actual elastic-plastic notch tip stresses-strains in the localized plastic zone is often approximated by the Neuber rule [29] or the Equivalent Strain Energy Density (ESED) equation [31]. It was shown [36,41] that both methods can also be extended for multiaxial proportional and non-proportional modes of loading. Similar approaches were proposed by Hoffman and Seeger [33] and Barkey et al. [39]. All methods consist of two parts namely the constitutive equations and the notch correction relating the pseudo linear elastic stress-strain state $(\sigma_{22}^{e}, \varepsilon_{22}^{e})$ at the notch tip with the actual elastic-plastic stress-strain response $(\sigma_{22}^{a}, \varepsilon_{22}^{a})$ as shown in Figure 3-11.

The Neuber rule [29] for proportional loading, where the Hencky stress-strain relationships are applicable, can be written for the uniaxial and multiaxial stress state in the form of equations (3.19) and (3.20) respectively.

$$\sigma_{22}^{e}\varepsilon_{22}^{e} = \sigma_{22}^{a}\varepsilon_{22}^{a} \tag{3.19}$$

$$\sigma_{ij}^{e}\varepsilon_{ij}^{e} = \sigma_{ij}^{a}\varepsilon_{ij}^{a} \tag{3.20}$$

The Neuber rule states that the total strain energy (sum of the strain energy and the complimentary strain energy density) at the notch tip equals to the hypothetical elastic strain energy, represented by the rectangles A and B in Figure 2-13.

The ESED method [31] represents the equality between the strain energy density at the notch tip of a linear elastic body and the notch tip strain energy density of a geometrically identical elastic-plastic body subjected to the same load. Figure 2-14 graphically shows the equality of the area under the linear-elastic curve and the area under the actual elastic-plastic $\sigma_{22}^{a} - \varepsilon_{22}^{a}$ material curve. The strain energy density equations for the uniaxial and multiaxial stress state can be written Eq. (3.21) and Eq. (3.22) respectively:

$$\int_{0}^{\varepsilon_{22}^{e}} \sigma_{22}^{e} \, d\varepsilon_{22}^{e} = \int_{0}^{\varepsilon_{22}^{a}} \sigma_{22}^{a} \, d\varepsilon_{22}^{a} \tag{3.21}$$

$$\int_{0}^{\varepsilon_{ij}^{e}} \sigma_{ij}^{e} \, d\varepsilon_{ij}^{e} = \int_{0}^{\varepsilon_{ij2}^{a}} \sigma_{ij}^{a} \, d\varepsilon_{ij}^{a} \tag{3.22}$$

The strain energy density equality Eqs. (3.20) and (3.22), relating the pseudo-elastic and the actual elastic-plastic notch strains and stresses at the notch tip, has been widely used as a good approximation method, but additional conditions are required for the complete solution of a multiaxial stress state problem. However, those conditions have been the subject of controversy. Hoffman and Seeger [33] assumed that the ratio of the actual principal strains at the notch tip is to be equal to the ratio of the fictitious elastic principal strain components while Barkey et al. [39] suggested using the ratio of principal stresses. Moftakhar [35] found that the accuracy of the stress or strain ratio based analysis depended on the degree of constraint at the notch tip. Therefore, Moftakhar el.al. proposed [36] to use the ratios of strain energy density contributed by each pair of corresponding stress and strain components. Singh et.al. [41] confirmed later that the additional energy equations provide a good accuracy when used in an incremental form. Because the ratios of strain energy density increments seem to be less dependent on the

geometry and constraint conditions at the notch tip than the ratios of stresses or strains the analyst is not forced to make any arbitrary decisions about the constraint while using these equations. It was also found that the conflict between the plasticity model (normality rule) and strain energy density equations at some specific ratios of stress components may cause singularity for set of seven equations. Such a conflict can be avoided if the principal idea of Neuber is implemented in the incremental form. It should be noted that the original Neuber rule (3.19) was derived for bodies in pure shear stress state. It means that the Neuber equation states the equivalence of only distortional strain energies. In order to formulate the set of necessary equations for a multiaxial analysis of elastic-plastic stresses and strains at the notch tip, the equality of increments of the total distortional strain energy density should be used.

Buczynski and Glinka [74] proposed, analogously to the original Neuber rule, to use the equivalence of increments of the total distortional strain energy density contributed by each pair of associated stress and strain components, i.e.,

$$\begin{aligned} \mathrm{S}_{22}^{e}\Delta e_{22}^{e} + e_{22}^{e}\Delta S_{22}^{e} &= S_{22}^{a}\Delta e_{22}^{a} + e_{22}^{a}\Delta S_{22}^{a} \\ S_{33}^{e}\Delta e_{33}^{e} + e_{33}^{e}\Delta S_{33}^{e} &= S_{33}^{a}\Delta e_{33}^{a} + e_{33}^{a}\Delta S_{33}^{a} \\ S_{23}^{e}\Delta e_{23}^{e} + e_{23}^{e}\Delta S_{23}^{e} &= S_{23}^{a}\Delta e_{23}^{a} + e_{23}^{a}\Delta S_{23}^{a} \end{aligned} \tag{3.23}$$

The equalities of strain energy increments for each set of corresponding hypothetical elastic and actual elastic-plastic strains and stress increments at the notch tip can be shown graphically in Figure 3-12. The area of dotted rectangles represents the total strain energy increment of the hypothetical elastic notch tip input stresses while the area of the hatched rectangles represents the total strain energy density of the actual elastic-plastic material response at the notch tip.

Consequently, a combination of four equations from the elastic–plastic constitutive equation (3.18) and three equations from the equivalence of increments of the total distortional strain energy density, Eq. (3.23) yields the required set of seven independent equations necessary to completely define elastic–plastic notch-tip strain and stress responses for a notched component subjected to multiaxial non-proportional cyclic loads. The final set of equations written as a set of seven simultaneous equations, Eq. (3.24) from which all unknown deviatoric strain, Δe_{ij}^{a} and stress, ΔS_{ij}^{a} increments can be calculated, based on the linear hypothetical elastic notch tip stress history, i.e., increments $\Delta\sigma_{ij}^{e}$ and Δe_{ij}^{e} are known from the linear-elastic analysis.

$$
\begin{aligned}
\Delta e_{11}^{a} &= \frac{\Delta S_{11}^{a}}{2G} + \frac{3}{2}\frac{\Delta\sigma_{eq}^{a}}{E_T^{p}\,\sigma_{eq}^{a}}\cdot S_{11}^{a} \\
\Delta e_{22}^{a} &= \frac{\Delta S_{22}^{a}}{2G} + \frac{3}{2}\frac{\Delta\sigma_{eq}^{a}}{E_T^{p}\,\sigma_{eq}^{a}}\cdot S_{22}^{a} \\
\Delta e_{33}^{a} &= \frac{\Delta S_{33}^{a}}{2G} + \frac{3}{2}\frac{\Delta\sigma_{eq}^{a}}{E_T^{p}\,\sigma_{eq}^{a}}\cdot S_{33}^{a} \\
\Delta e_{23}^{a} &= \frac{\Delta S_{23}^{a}}{2G} + \frac{3}{2}\frac{\Delta\sigma_{eq}^{a}}{E_T^{p}\,\sigma_{eq}^{a}}\cdot S_{23}^{a} \\
\mathrm{S}_{22}^{\mathrm{e}}\Delta e_{22}^{e} + e_{22}^{e}\Delta S_{22}^{e} &= S_{22}^{a}\Delta e_{22}^{a} + e_{22}^{a}\Delta S_{22}^{a} \\
S_{33}^{e}\Delta e_{33}^{e} + e_{33}^{e}\Delta S_{33}^{e} &= S_{33}^{a}\Delta e_{33}^{a} + e_{33}^{a}\Delta S_{33}^{a} \\
S_{23}^{e}\Delta e_{23}^{e} + e_{23}^{e}\Delta S_{23}^{e} &= S_{23}^{a}\Delta e_{23}^{a} + e_{23}^{a}\Delta S_{23}^{a}
\end{aligned}
\qquad (3.24)
$$

Since the equations set, Eq. (3.24) is non-linear, solution of the equations requires an iterative approach. For each increment of the external load, represented by the increments of pseudo-elastic deviatoric stresses, ΔS_{ij}^{e}, the deviatoric elastic-plastic notch tip strain and stress increments, Δe_{ij}^{a} and ΔS_{ij}^{a}, are computed from Eq. (3.24). The

calculated deviatoric stress increments, ΔS_{ij}^{a}, can subsequently be converted into the actual stress increments, $\Delta\sigma_{ij}^{a}$ using Eq. (3.25).

$$\begin{aligned}
\Delta S_{22}^{a} &= \Delta\sigma_{22}^{a} - \frac{1}{3}\left(\Delta\sigma_{22}^{a} + \Delta\sigma_{33}^{a}\right) \\
\Delta S_{33}^{a} &= \Delta\sigma_{33}^{a} - \frac{1}{3}\left(\Delta\sigma_{22}^{a} + \Delta\sigma_{33}^{a}\right) \\
\Delta S_{23}^{a} &= \Delta\sigma_{23}^{a}
\end{aligned} \tag{3.25}$$

The deviatoric and the actual stress components S_{ij}^{a} and σ_{ij}^{a} at the end of given load increment are determined from Eqs. (3.26) and (3.27).

$$S_{ij}^{an} = S_{ij}^{ao} + \sum_{k=1}^{n-1} \Delta S_{ij}^{ak} + \Delta S_{ij}^{an} \tag{3.26}$$

$$\sigma_{ij}^{an} = \sigma_{ij}^{ao} + \sum_{k=1}^{n-1} \Delta\sigma_{ij}^{ak} + \Delta\sigma_{ij}^{an} \tag{3.27}$$

where: *n* denotes the load increment number.

The actual strain increments, $\Delta\varepsilon_{ij}^{a}$, can finally be determined from Eq. (3.10).

Before the solution of plasticity equations, loading/unloading conditions must be checked. At the beginning of initial loading cycle, it is assumed that all strains/stresses are elastic and notch tip stress-strain response is equal to known elastic solution, Eq. (3.28)

$$\begin{aligned}
\sigma_{ij}^{a} &= \sigma_{ij}^{e} \\
\varepsilon_{ij}^{a} &= \varepsilon_{ij}^{e}
\end{aligned} \tag{3.28}$$

When the elastic loading reached the initial yield surface, subsequent load increment may result in elastic unloading, tangential (neutral) loading and elastic plastic (active) loading.

The mode of loading is determined based on loading criterion. When the stress increment moves inward from the yield surface, elastic unloading will take place i.e. the inner product of tensors dS , $\partial F/\partial S$ satisfies the condition Eq. (3.29):

$$\frac{\partial F}{\partial S_{ij}} dS_{ij} < 0 \tag{3.29}$$

If the stress increment is tangential to the yield surface, the neutral loading will occur i.e. the inner product of tensors dS , $\partial F/\partial S$ satisfies the condition Eq. (3.30):

$$\frac{\partial F}{\partial S_{ij}} dS_{ij} = 0 \tag{3.30}$$

Since the computer implementation of the neutral loading is virtually impossible to determine, this loading criterion is regarded as an elastic unloading. The relevant constitutive relations for the elastic unloading and tangential loading are described based on Hook's law, Eq. (3.7).

When the current state of stress increments moves out from the yield surface, the elastic-plastic loading will take place, i.e. the inner product of tensors dS , $\partial F/\partial S$ satisfies the condition Eq. (3.31):

$$\frac{\partial F}{\partial S_{ij}} dS_{ij} > 0 \tag{3.31}$$

The elastic-plastic loading condition states that the projection of the stress increment onto the normal of the yield surface must be greater than zero. The relevant constitutive relations for the elastic-plastic loading are described based on Hook's law and Prandtl-Reuss equations, Eq. (3.15).

Substituting the yield surface equation (3.6) for kinematic hardening into these loading criteria, the loading mode criterion, LC in terms of finite increments can be written for the purpose of numerical implementation as follows:

$$LC = \sum_{i=2,3}^{j=2,3} (S_{ij}^{a} - \alpha_{ij}^{n}) \Delta \sigma_{ij}^{e} \tag{3.32}$$

The loading mode criterion, LC for the incremental Neuber's method states that if elastic unloading or the elastic-plastic loading takes place as.

$$\begin{aligned} LC \leq 0 \quad & Elastic\, Unloading \\ LC > 0 \quad & Elastic - Plastic\, Loading \end{aligned} \tag{3.33}$$

The coupled constitutive governing and Neuber incremental equations discussed before are related with the Garud cyclic plasticity model to compute the actual notch tip stress-strain response of a notched component subjected to proportional and non-proportional multiaxial cyclic loading. After the notch stress increments are determined, the translation of the yield surface is updated by employing the multi-surface hardening the model proposed by Garud. The mathematics reflecting the yield surface translation process by the Garud model can be found in Section 2.1.4 in detail and will not be discussed again here.

In summary, calculation of elasto-plastic stress and strain histories in notch areas using pseudo-elastic stress history from the FE solution is based on two step calculation. The first calculation is simultaneous solution of the equation set, Eq. (3.24) defined by the incremental constitutive governing equations and the incremental Neuber notch correction equation for the increments of elasto-plastic notch strains and stresses. The

second calculation is to update yield surfaces based on the Garud cyclic plasticity model and then stress and strain tensors.

3.4 **Computer Implementation**

In order to implement equations defined in this chapter for a notched component subjected to a history of multiaxial cyclic loads, a general algorithm has been developed. The flow chart of the algorithm is shown in Figure 3-1. The algorithm starts with the linear elastic FEA results of a notch component for unit loads (a macro written in APDL is used to output linear elastic solution for each unit load). In next step, two separate computer programs written in Fortran 90 are used performing the elastic-plastic stress-strain analysis; the first computer is used to superimpose linear elastic stress histories at notch region of the FE model subjected to multiaxial loads, and the second computer program is used to implement the notch stress and strain analysis using increments of linear elastic stress histories (output from the first program).

For the implementation of first program, the linear elastic FE results for each unit load are multiplied by the corresponding load history to compute elastic stress history for that applied load history and then the elastic stress histories for all applied load histories are superimposed to obtain the combined time histories of linear elastic stresses in accordance with Eqs. (3.1) to (3.2). The resultant elastic stress history for each node at the critical notch region is divided into small increments of stresses for numerical implementation of elastic-plastic stress-strain analysis (Figure 3-8).

The second program computes the actual elastic-plastic stress and strain responses at notch areas. The computer flow chart of the second program is shown through Figure 3-13 to Figure 3-15. In the beginning of the program, loading criterion conditions must be

checked. The yield surfaces are initially centered at the origin (no loading) and all stresses are assumed to be elastic, the stress-strain solution is determined by Eq. (3.7). When the elastic loading reached the initial yield surface, unloading criterion, Eq. (3.33) is used to determine elastic unloading/tangential loading and elastic-plastic loading during state of stress increment. If the elastic-plastic loading takes place, the actual elastic-plastic strain and stress increments are calculated using Eq. (3.24). A set of seven equations (three notch correction equations from Neuber's rule and four constitutive equations are solved simultaneously to determine the actual elastic-plastic strain and stress increments. Then active surfaces are translated according to Eqs. (2.24)-(2.43). If stresses exceed the outer yield surface as governed by Eqs. (2.38)-(2.39), the stress increment is bi-sectioned, and then stresses are updated to the point where new stress state lies on the yield surface. The current state of active surface is also updated. The elastic-plastic stress-strain calculation is repeated for the remaining portion of stress increments. If the stresses after the load increment remain on the current active yield surface, the stresses are updated and the active surface and any interior surfaces are translated. The procedure is repeated until the last elastic stress increment is reached.

The crucial part of the actual stress-strain calculation is based on the cyclic plasticity model. The cyclic plasticity model enables the, $\Delta\varepsilon_{eq}^{a} - \Delta\sigma_{eq}^{a}$, relationship to be established providing the actual plastic modulus for given stress/load increment, $\Delta\sigma_i$. In other words, the plasticity model determines which piece of the stress-strain curve (Figure 2-6) has to be utilized during given stress increment. Two or more tangent yield surfaces translate together as rigid bodies and the largest moving surface indicates which linear piece of the constitutive relationship should be used for a given stress increment.

The slope of the actual element of the stress-strain curve defines the plastic modulus, $\Delta\sigma_{eq} / \Delta\varepsilon_{eq}^{p}$, necessary for the determination of parameter, $d\lambda$, in the constitutive equation (3.13). The plasticity models are described in most publications, as algorithms for calculating strain increments that result from given series of stress increments or vice versa. In the case of the notch analysis neither stresses nor strains are directly inputted into the plasticity model. The input is given in the form of the total deviatoric strain energy density increments and both the deviatoric strain and stress increments are to be found simultaneously by solving Eq. (3.24). Therefore, the plasticity model is needed only to indicate which work-hardening surface will be active during current load increment, which subsequently determines the instantaneous value of the parameter dλ. In order to find the elastic-plastic deviatoric stress and strain increment $\Delta\sigma_{ij}^{a}$ and Δe_{ij}^{a} from the equation set Eq. (3.24), the value of parameter dλ is determined first based on the current configuration of plasticity surfaces. After calculating the stress increments, $\Delta\sigma_{ij}^{a}$, the plasticity surfaces are translated as shown in Figure 2-12. The process is repeated for each subsequent increment of the "elastic" input, $\Delta\sigma_{ij}^{e}$. The cyclic plasticity model assumes a stable material response such that no transient hardening effects of the non-proportional hardening are taken into account.

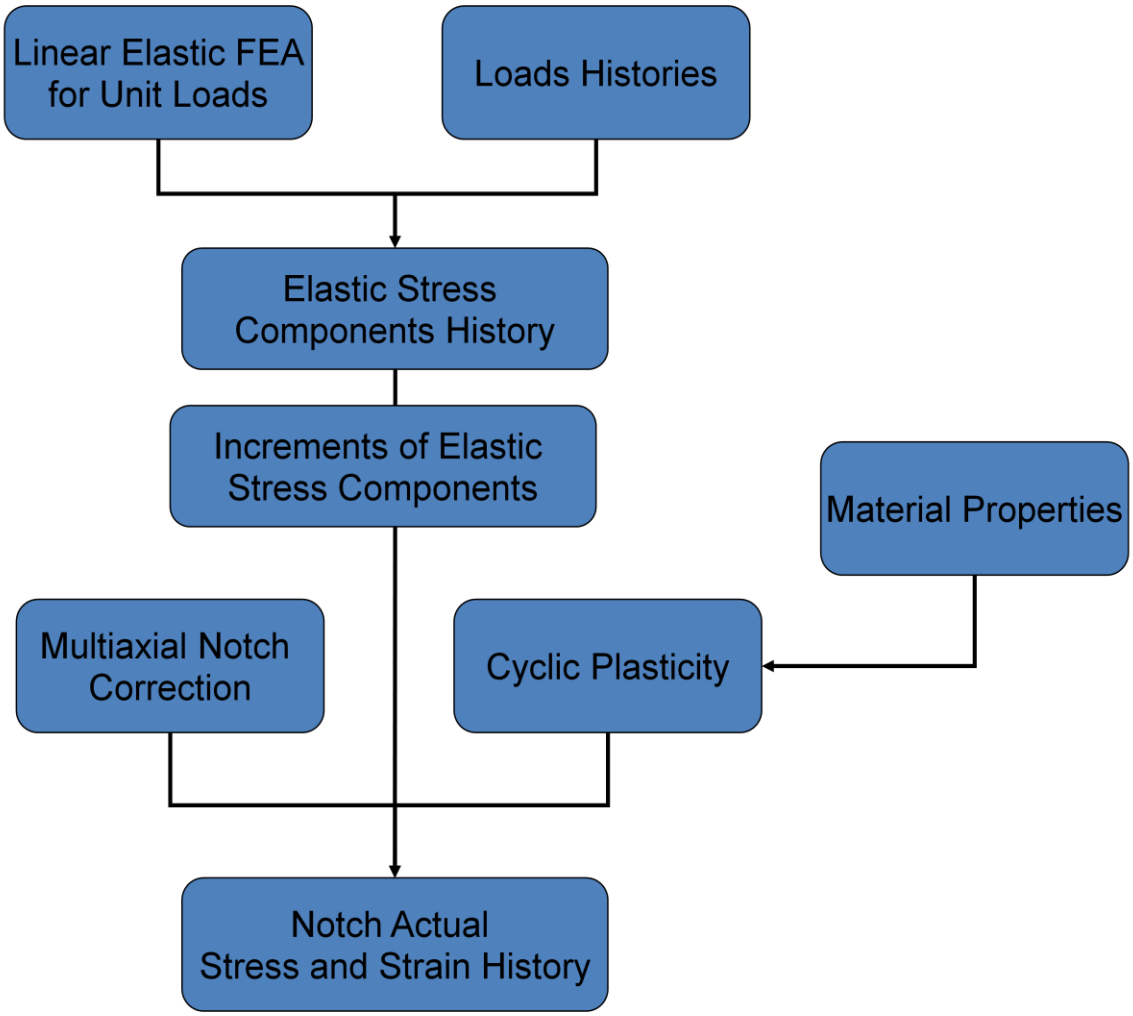

Figure 3-1: Algorithm for Notch Stress and Strain Analysis

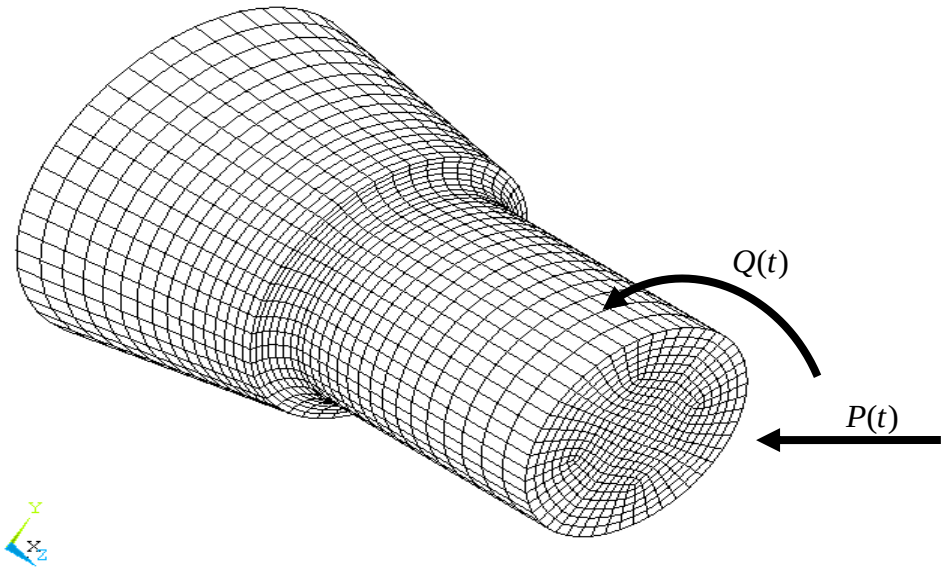

Figure 3-2: A notched shaft with applied loads histories $P(t)$ and $Q(t)$

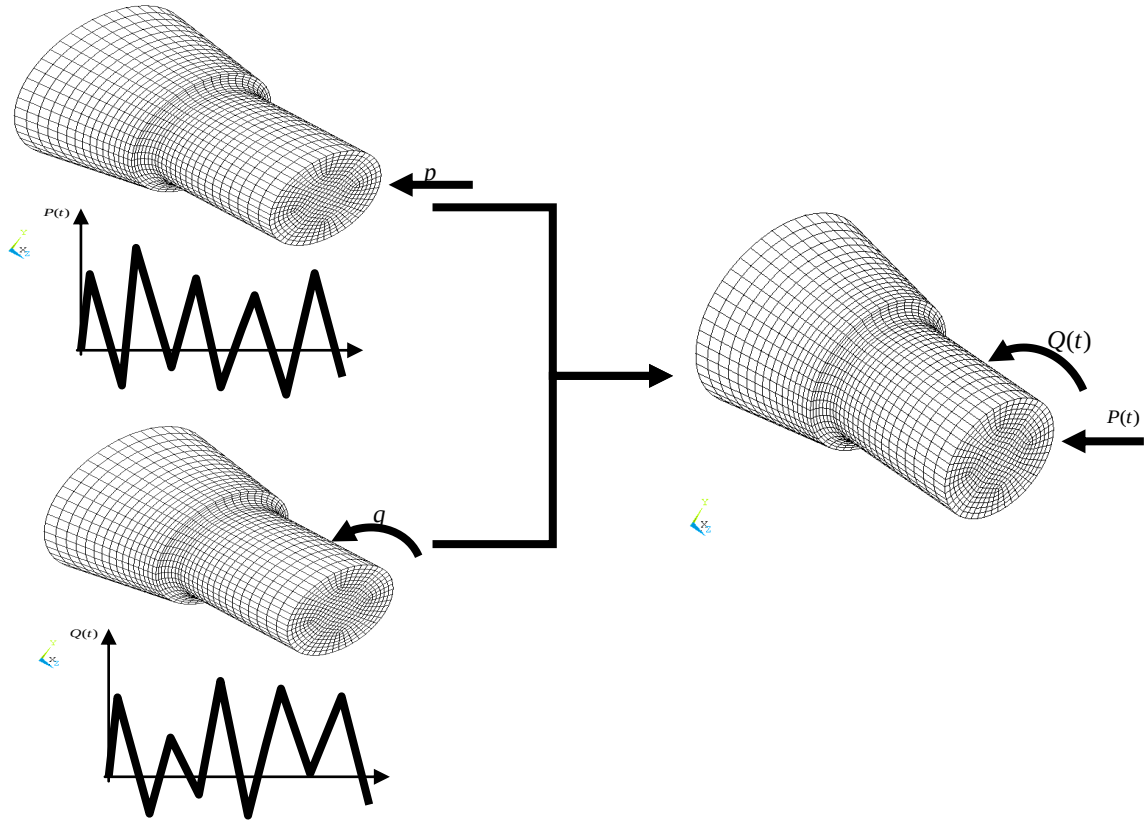

Figure 3-3: Superimposing FEA elastic stress results from two load histories

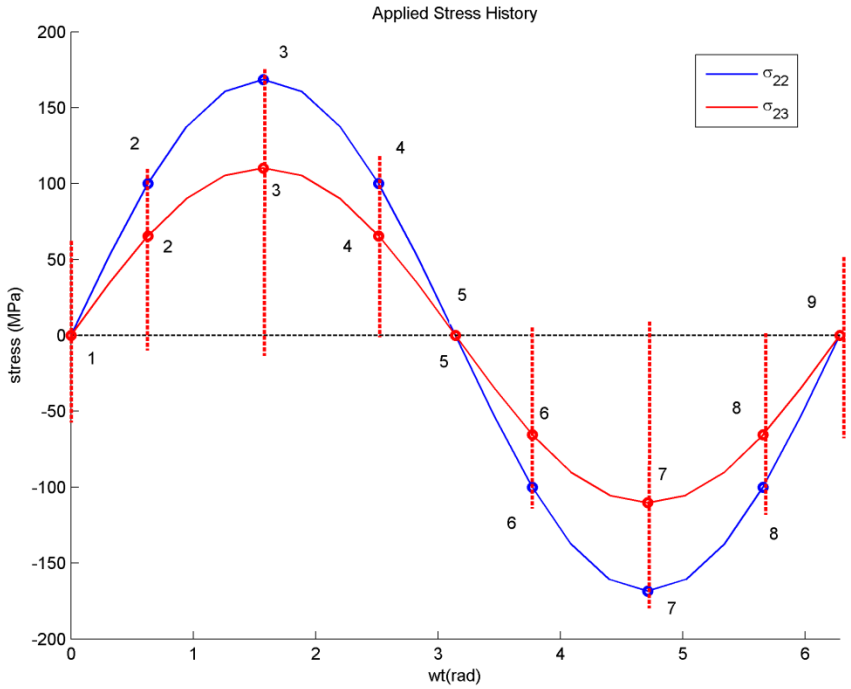

Figure 3-4: Stress history of in-phase loading

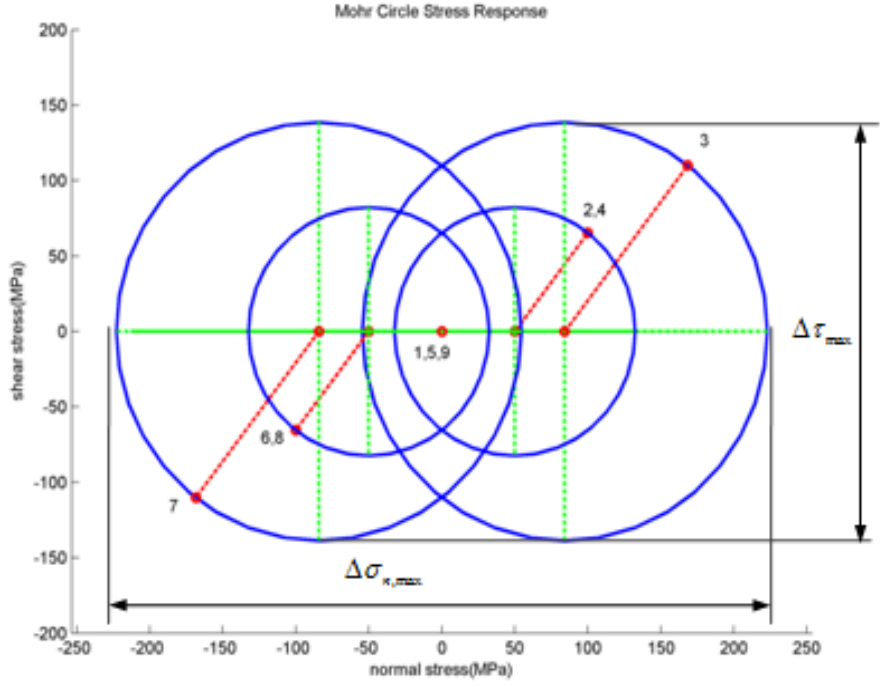

Figure 3-5: Mohr's circle stress response of in-phase loading

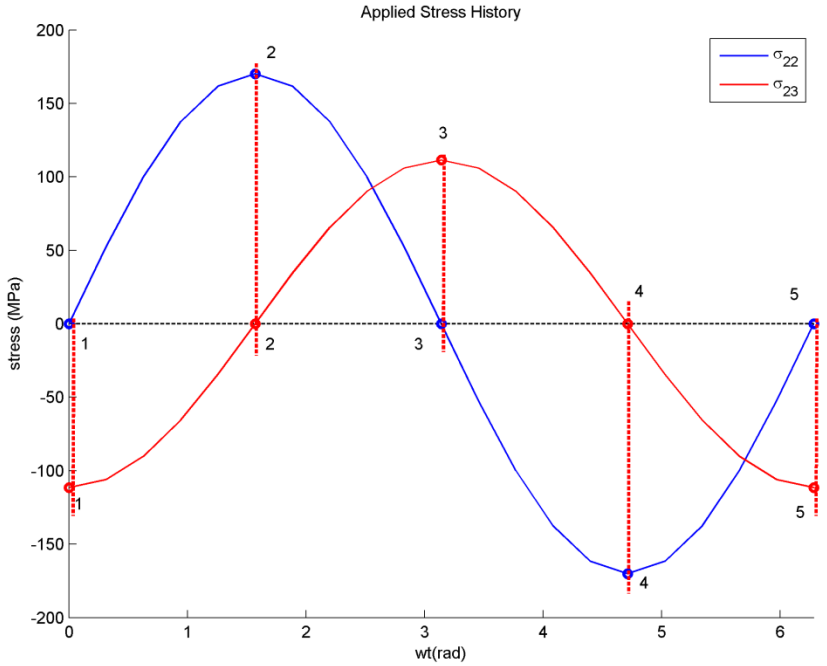

Figure 3-6: Stress history of 90^{o} out-of-phase loading

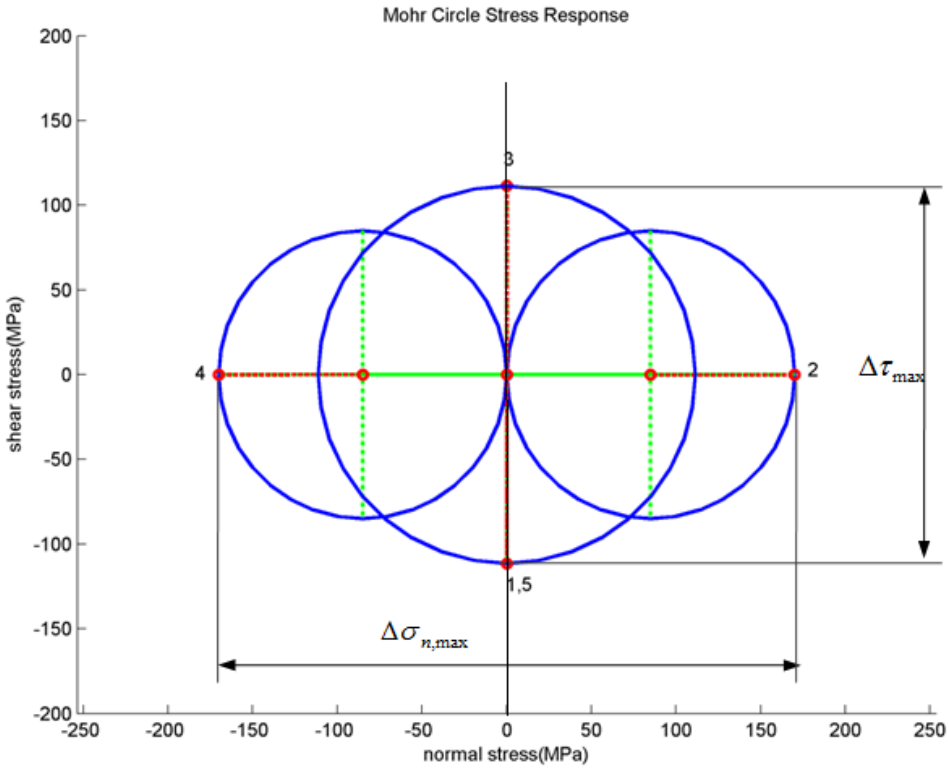

Figure 3-7: Mohr's circle stress response of 90^{o} out-of-phase loading

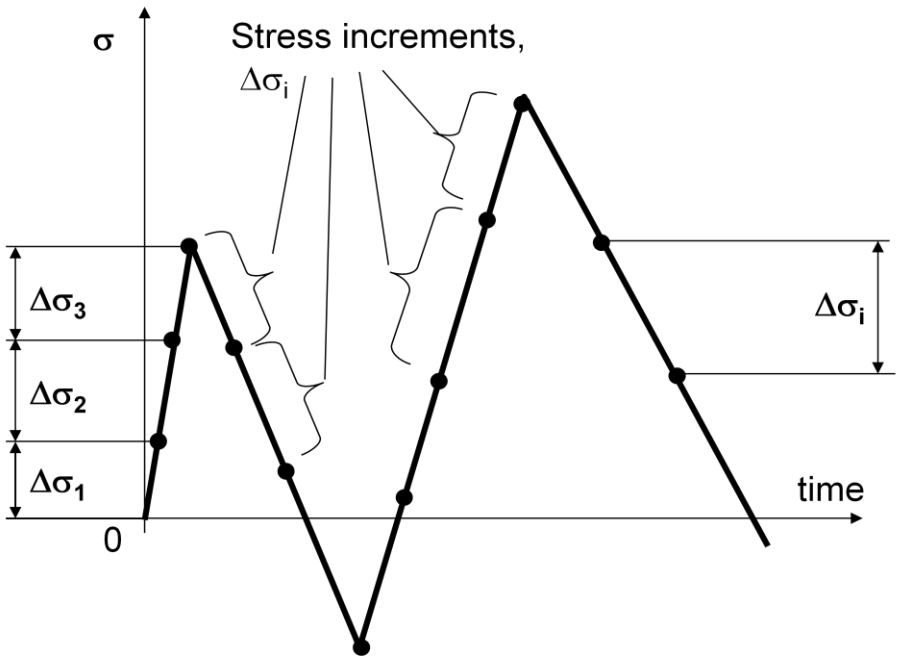

Figure 3-8: The input elastic stress increments of the stress-time history

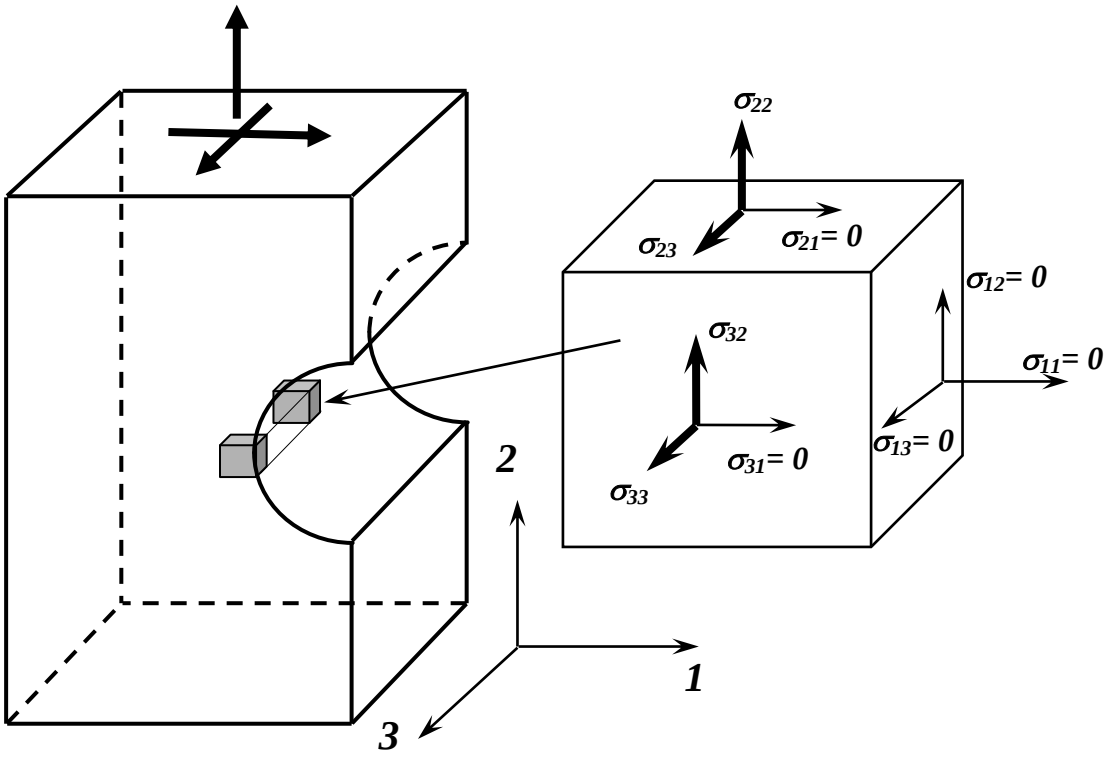

Figure 3-9: Stress state at a notch tip

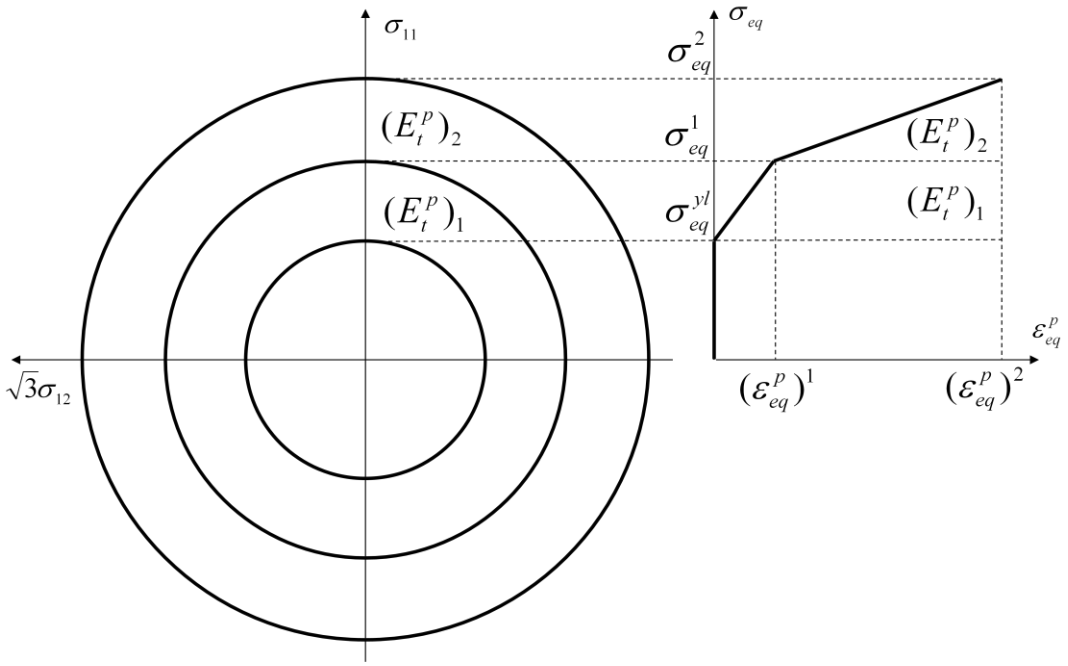

Figure 3-10: A graphical representation of fields of constant plastic modules and the multilinear material curve

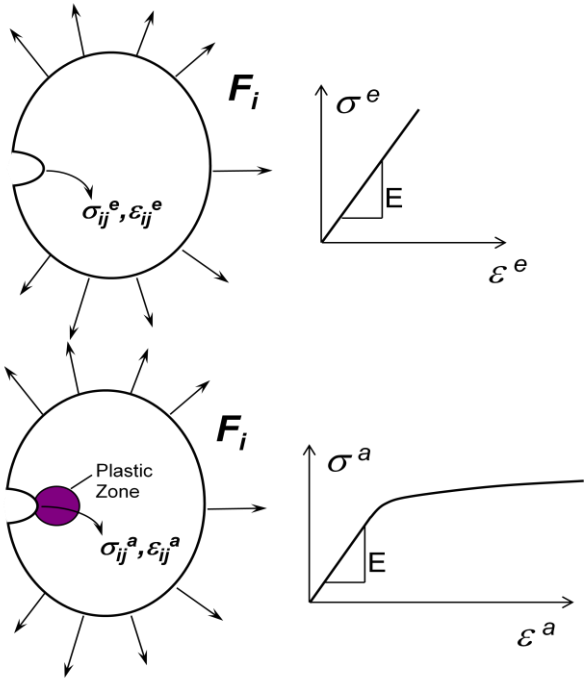

Figure 3-11: Stress states in geometrically identical elastic and elastic-plastic bodies subjected to identical boundary

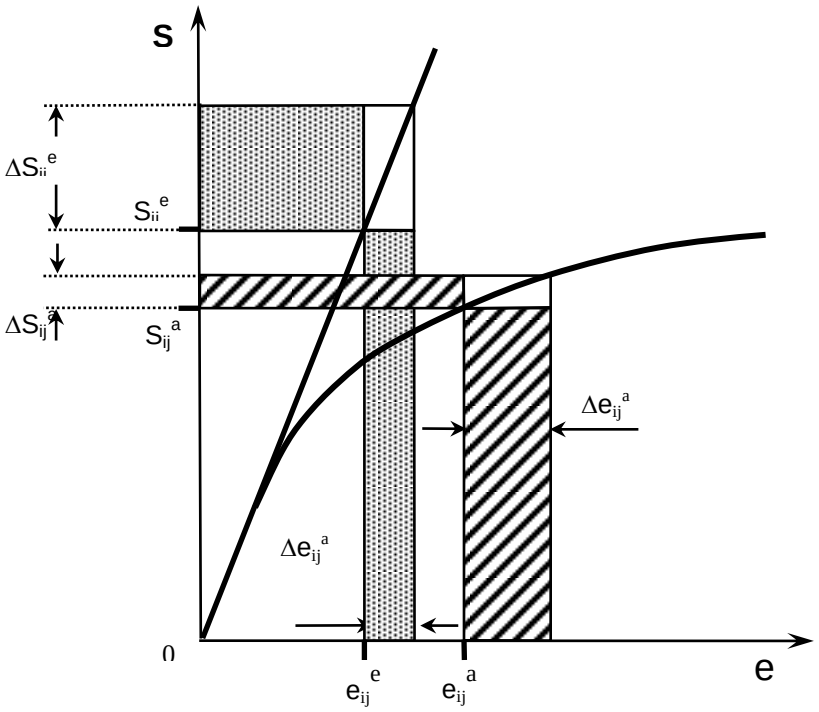

Figure 3-12: Graphical representation of the incremental Neuber rule

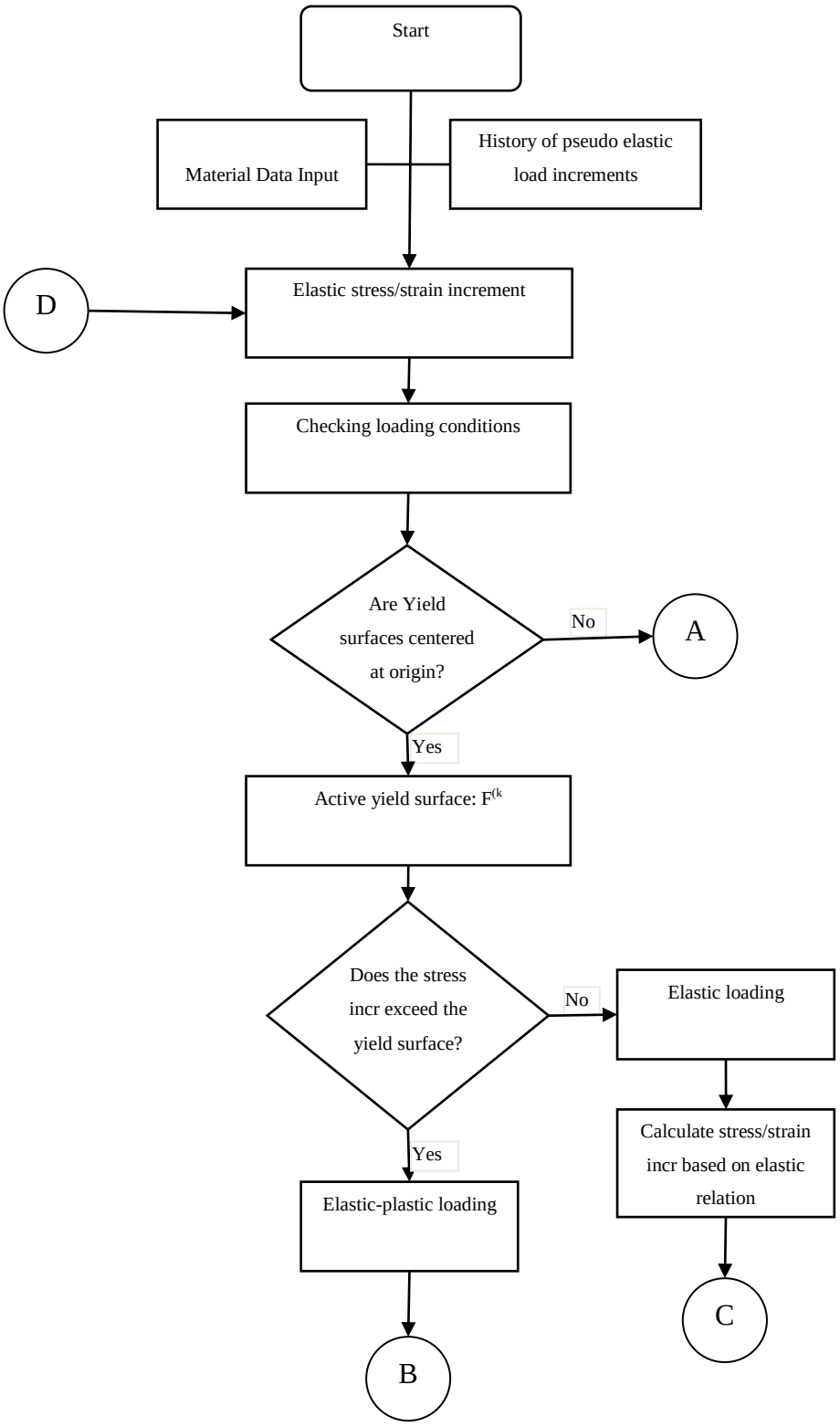

Figure 3-13: Computer flowchart of the notch elastic-plastic stress/strain analysis procedure

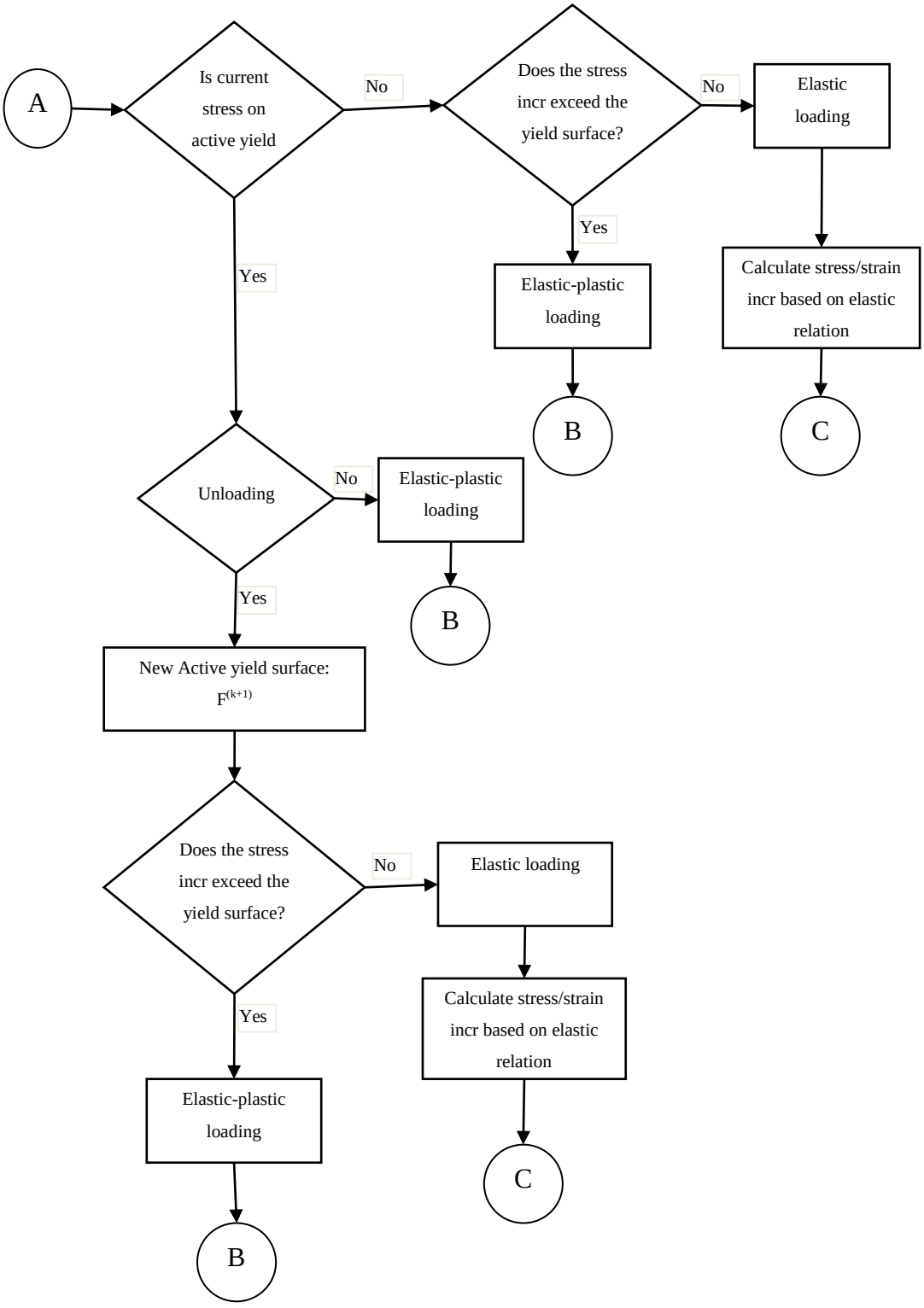

Figure 3-14: Computer flowchart of the notch elastic-plastic stress/strain analysis procedure

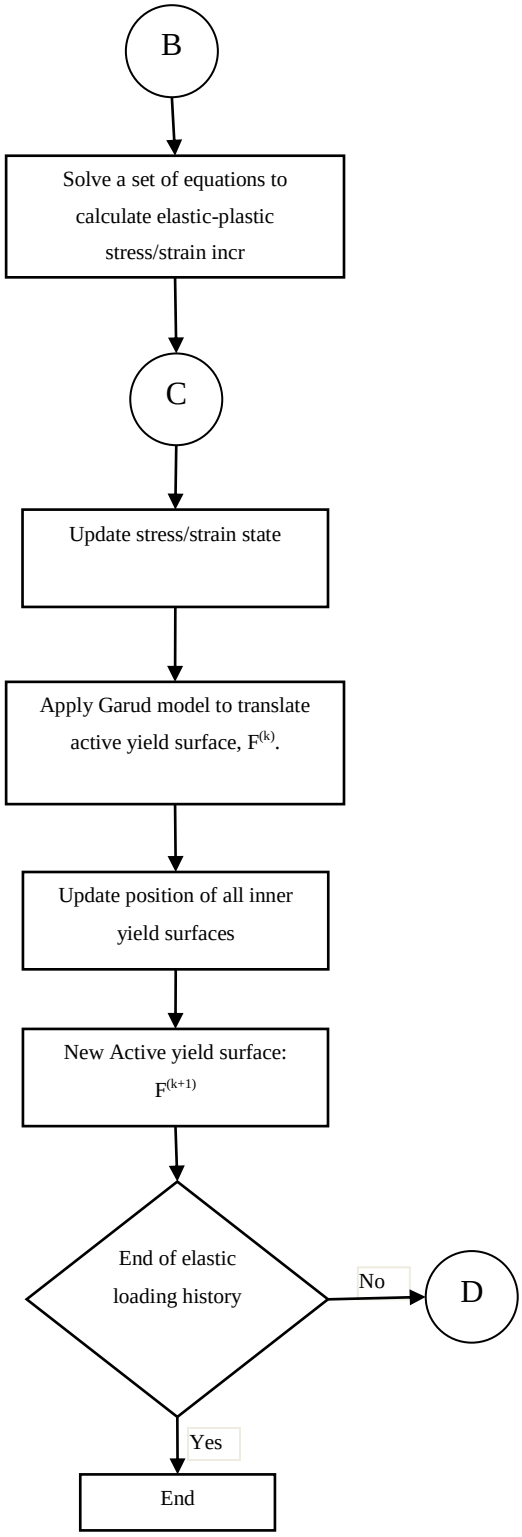

Figure 3-15: Computer flowchart of the notch elastic-plastic stress/strain analysis procedure

Chapter 4
Multiaxial Fatigue Damage Parameter

The successful design of notched components subjected to complex multiaxial loadings requires that effective methods be available, which can accurately estimate the fatigue life of those components under complex states of stresses. This chapter covers methods for computational implementation of the proposed multiaxial fatigue damage parameter from known stress-strain histories. Computing actual stress and strain responses at notches from pseudo elastic stress histories (linear-elastic FE stress histories) is discussed in the previous chapter. It is well known that the local stress-strain state controls the fatigue strength and the local strain approach has been well adapted as a practical engineering method in durability assessment of automotive components. In past few decades, a significant number of multiaxial fatigue damage parameters have been developed [43,47,51,52,58,] However, critical plane-based damage parameters have gained general popularity due to their reasonably accurate life prediction capabilities. These fatigue damage parameters postulate that cracks initiate and grow on preferred planes consistent with the physical observation. Most of the critical plane-based fatigue damage parameters are given in the form of stress and strain components or a combination of stresses and strains associated with the critical plane. However, these fatigue damage parameters have limitations taking into account mean stress effects, non-proportional hardening, and requirement for additional material constants to charaterize the fatigue damage. In order to overcome the shortcomings of the existing critical plane-based fatigue damage parameters, a multiaxial fatigue damage parameter based on the critical plane concept that considers the specific plane(s) experiencing the maximum

fatigue damage is proposed. The proposed multiaxial fatigue damage parameter is used to predict fatigue lives for notched components under a wide variety of proportional and non-proportional multiaxial loadings.

Experimental fatigue data has shown that local strain fatigue analysis using measured strains from notched components provides good correlation even though the effect of stress gradient is ignored. This suggests that the stress gradient has no significant effect on the fatigue life to crack initiation, but significant effect on the crack growth. Fatigue life prediction based on crack initiation has become a common design criterion in automotive industry and fatigue crack initiation usually starts on the surface of a component. Therefore, the proposed multiaxial fatigue analysis methodology is performed on surface nodes at critical notch locations of the FE model. The proposed multiaxial fatigue damage parameter uses the actual elasto-plastic stress-strain histories for surface nodes in notch area to predict fatigue crack initiation.

The last section of this chapter presents a numerical implementation of the proposed multiaxial fatigue analysis methodology.

4.1 **Stress and Strain State on the Critical Plane**

To evaluate fatigue damage caused by applied loads on an arbitrary plane, the local stress and strain components acting on that plane must be known. The fatigue damage parameter on a plane can be expressed in terms of stress and strain quantities as a function of the plane orientation. Critical plane approaches are generally based on either the maximum shear plane or the maximum principal plane failure mode [51,55,80]. In the proposed fatigue damage parameter, stress and strain components on potential planes are determined using the coordinate transformation matrix with respect to plane orientation.

The fatigue damage is evaluated all potential planes and fatigue failure is assumed to occur on the critical plane with the largest amount of fatigue damage.

The variation of strain and stress components on material planes for a thin-walled specimen subjected to in-phase and 90^o out-of -phase loading are presented below to provide a better understanding of characteristics of fatigue damage on various planes. Since most of the multiaxial fatigue testing is conducted using a thin-walled specimen under tension and torsion (Figure 4-1), a closed-form solution to express strain and stress components on the material plane(s) is given in Eqs.(4.7) and (4.8) for the thin-walled specimen subjected to combined tension and torsion loadings. The closed-form solution of shear and normal strain and stress components on various material planes is based on the assumption that applied axial and shear strain/stress histories are in sinusoidal form.

The strain tensor for thin-walled specimen subjected to combined tension and torsional loads under the strain-controlled loading conditions is expressed as:

$$\varepsilon_{ij} = \begin{bmatrix} \varepsilon_x & 1/2\gamma_{xy} & 0 \\ 1/2\gamma_{xy} & -\nu_{eff}\varepsilon_x & 0 \\ 0 & 0 & -\nu_{eff}\varepsilon_x \end{bmatrix} \tag{4.1}$$

Where ε_x and γ_{xy} are applied axial and shear strain histories.

The incremental plasticity model is used to compute components of the stress tensor from applied strain histories that are determined experimentally.

The state of stress tensor for the thin-walled specimen shown in Figure 4-1 is expressed as:

$$\sigma_{ij} = \begin{bmatrix} \sigma_x & \tau_{xy} & 0 \\ \tau_{xy} & 0 & 0 \\ 0 & 0 & 0 \end{bmatrix} \tag{4.2}$$

Where σ_x and τ_{xy} are resulting axial and shear stress histories.

The normal and shear strain on an arbitrary plane with angle α relative to the specimen axis is expressed as:

$$\varepsilon_\theta = \frac{\varepsilon_x + \varepsilon_y}{2} + \frac{\varepsilon_x - \varepsilon_y}{2}\cos(2\alpha) + \frac{\gamma_{xy}}{2}\sin(2\alpha) \tag{4.3}$$

$$\frac{\gamma_\theta}{2} = \frac{\varepsilon_x - \varepsilon_y}{2}\sin(2\alpha) - \frac{\gamma_{xy}}{2}\cos(2\alpha) \tag{4.4}$$

Where $\varepsilon_y = -\nu_{eff}\,\varepsilon_x$

If the applied strain time history is sinusoidal, the critical plane can be determined using an analytical method.

$$\varepsilon_x = \varepsilon_a \sin(\omega t) \tag{4.5}$$

$$\gamma_{xy} = \gamma_a \sin(\omega t - \varphi) = \lambda\varepsilon_a \sin(\omega t - \varphi) \tag{4.6}$$

Where ε_a and γ_a are applied axial and shear strain amplitudes, respectively. φ is the phase angle between the axial and shear strains, and λ is the ratio between the shear and axial strains.

Substituting Eqs .(4.6) and (4.5) into Eqs. (4.4) and (4.3), the following equations can be obtained for the normal and shear strain for any plane.

$$\varepsilon_\theta = \frac{\varepsilon_a}{2}\left\{\sqrt{\left[(1-\nu_{eff}) + (1+\nu_{eff})\cos(2\alpha) + \lambda\cos(\varphi)\sin(2\alpha)\right]^2 + \left[\lambda\sin(\varphi)\sin(2\alpha)\right]^2}\right\}\sin(\omega t - \xi)$$

(4.7)

$$\gamma_\theta = \varepsilon_a \left\{ \sqrt{\left[-\left(1+\nu_{eff}\right)\sin\left(2\alpha\right) + \lambda\cos\left(\varphi\right)\cos\left(2\alpha\right)\right]^2 + \left[\lambda\sin\left(\varphi\right)\cos\left(2\alpha\right)\right]^2} \right\} \sin\left(\omega t - \eta\right)$$

(4.8)

Where

$$\xi = \tan^{-1}\left\{ \frac{\lambda\sin\left(\varphi\right)\sin\left(2\alpha\right)}{\left(1-\nu_{eff}\right) + \left(1+\nu_{eff}\right)\cos\left(2\alpha\right) + \lambda\cos\left(\varphi\right)\sin\left(2\alpha\right)} \right\} \tag{4.9}$$

$$\eta = \tan^{-1}\left\{ \frac{\lambda\sin\left(\varphi\right)\cos\left(2\alpha\right)}{-\left(1+\nu_{eff}\right)\sin\left(2\alpha\right) + \lambda\cos\left(\varphi\right)\cos\left(2\alpha\right)} \right\} \tag{4.10}$$

Once normal and shear stress responses are computed from the applied strain histories using the incremental plasticity model, normal and shear stresses on the critical plane are determined using a similar approach.

Normal and shear stresses on an arbitrary plane with angle α relative to the specimen axis are expressed as:

$$\sigma_\alpha = \frac{\sigma_x + \sigma_y}{2} + \frac{\sigma_x - \sigma_y}{2}\cos\left(2\alpha\right) + \tau_{xy}\sin\left(2\alpha\right) \tag{4.11}$$

$$\tau_\alpha = \frac{\sigma_x - \sigma_y}{2}\sin\left(2\alpha\right) - \tau_{xy}\cos\left(2\alpha\right) \tag{4.12}$$

Where $\sigma_y = -0$

$$\sigma_x = \sigma_a \sin\left(\omega t\right) \tag{4.13}$$

$$\tau_{xy} = \tau_a \sin\left(\omega t - \varphi\right) \tag{4.14}$$

Where σ_a and τ_a are axial and shear stress amplitudes, respectively. Phi (φ) is the phase angle between the axial and shear stress.

Substituting normal and shear stress terms from Eqs. (4.13) and (4.14) into Eqs. (4.11) and (4.12), normal and shear stresses can be obtained on a plane of interest as follows:

$$\sigma_\alpha = \sqrt{\left[\frac{\sigma_a}{2} + \frac{\sigma_a}{2}\cos(2\alpha) + \tau_a \cos(\varphi)\sin(2\alpha)\right]^2 + \left[\tau_a \sin(\varphi)\sin(2\alpha)\right]^2}\,\sin(\omega t - \xi) \quad (4.15)$$

$$\tau_\alpha = \sqrt{\left[\frac{\sigma_a}{2}\sin(2\alpha) - \tau_a \cos(\varphi)\cos(2\alpha)\right]^2 + \left[\tau_a \sin(\varphi)\cos(2\alpha)\right]^2}\,\sin(\omega t - \eta) \quad (4.16)$$

Where:

$$\xi = \tan^{-1}\left\{\frac{\tau_a \sin(\varphi)\sin(2\alpha)}{\frac{\sigma_a}{2} + \frac{\sigma_a}{2}\cos(2\alpha) + \tau_a \cos(\varphi)\sin(2\alpha)}\right\} \quad (4.17)$$

$$\eta = \tan^{-1}\left\{\frac{\tau_a \sin(\varphi)\cos(2\alpha)}{\frac{\sigma_a}{2}\sin(2\alpha) - \tau_a \cos(\varphi)\cos(2\alpha)}\right\} \quad (4.18)$$

In case of proportional loading (i.e. in-phase loading, Figure 4-2a), the variation of shear and normal stress and strain ranges on various planes with respect to plane angle are shown in Figure 4-2a. As seen from this figure that while the maximum normal strain and stress ranges are maximum, shear strain and stress ranges are zero on the same plane. This explains why shear components do not contribute to the fatigue damage on the maximum principal stress/strain plane for the tensile-type failure. However, when shear strain and stress ranges reach maximum, there are non-zero normal stress and strain components on the plane.

In case of non-proportional loading (i.e. 90^{o} out-of-phase loading, Figure 4-2b), the variation of shear and normal stress and strain ranges on various planes with respect to plane angle are shown in Figure 4-2b. This figure shows that shear strains and stresses have high values on the plane of the maximum shear strain, but normal strains and stresses have reasonable high values. Therefore, the contribution of both strain and stress terms should be taken into account when formulating a fatigue damage parameter on the critical plane.

However, when stress and strain states are more complex i.e., not continuous mathematical forms, shear and normal stress/strain histories are computed in various potential planes with predefined interval plane angle. The critical plane is determined as a plane experiencing the maximum amount of fatigue damage, e.g. when the shear strain range is maximized. In order to compute the fatigue damage parameter on a particular plane, stress and strain components need to be expressed on the local coordinate system of that plane. Stress and strain components are a function of time and plane angle. The magnitude of strain and stress components and the shape of hysteresis loops are changed as a function of plane angle as shown in Figure 4-3 and Figure 4-4. Therefore, the critical plane is unknown and must be searched by analyzing all potential candidate planes. The general variation of strain and stress components on various planes as a function of phase angle, i.e. delay angle between the applied tension and torsion loadings are shown in Figure 4-5.

Since the fatigue life prediction is calculated on the free surface of the notched body and stresses and strains usually get their extreme values on the free surface, the critical plane should be searched on potential planes of the free surface. Therefore, the

transformation of stress and strain tensors is computed on planes of the free surface. The coordinate system, x-y-z on the surface of notched body is shown in Figure 4-6. Figure 4-7 shows two rotations required to transform the stress and strain tensors from the global coordinate system, x-y-z to the local coordinate system, x'-y'-z'. The local coordinate system, x'-y'-z' is fixed to the plane of interest. The plane of interest is reached by first rotating x-y plane clockwise about z axis by an angle of θ and then second clockwise the rotation about x axis by an angle of φ. Therefore, the free surface can be identified by $\theta = 0\,\text{deg}$ and the plane is perpendicular to the free surface has $\theta = 90\,\text{deg}$.

The rotation matrix for the rotation of θ and the rotation of φ are given respectively as:

$$a_\theta = \begin{bmatrix} \cos\theta & \sin\theta & 0 \\ -\sin\theta & \cos\theta & 0 \\ 0 & 0 & 1 \end{bmatrix} \tag{4.19}$$

$$a_\phi = \begin{bmatrix} 1 & 0 & 0 \\ 0 & \cos\varphi & \sin\varphi \\ 0 & -\sin\varphi & \cos\varphi \end{bmatrix} \tag{4.20}$$

A general transformation matrix to define $\theta\varphi$ rotations is defined as:

$$a_{\theta\phi} = a_\theta a_\phi = \begin{bmatrix} \cos\theta & \sin\theta & 0 \\ -\sin\theta\cos\varphi & \cos\theta\cos\varphi & \sin\varphi \\ \sin\theta\sin\varphi & -\cos\theta\sin\varphi & \cos\varphi \end{bmatrix} \tag{4.21}$$

The transformation matrix, $a_{\theta\phi}$ defines the rotation about x axis first and the z axis later. The stress and strain tensor on a specific plane can be determined as

$$\sigma_{ij}^{'} = a_{\theta\phi}\sigma_{ij}a_{\theta\phi}^{T} \tag{4.22}$$

$$\varepsilon_{ij}^{'} = a_{\theta\phi}\varepsilon_{ij}a_{\theta\phi}^{T} \tag{4.23}$$

Where σ_{ij} and ε_{ij} are given stress and strain tensors time histories and $\sigma_{ij}^{'}$ and $\varepsilon_{ij}^{'}$ are corresponding stress and strain tensor time histories transformed to any potential plane, and $a_{\theta\phi}^{T}$ is the transpose of the transformation matrix, $a_{\theta\phi}$. The stress, σ_{ij} and strain, ε_{ij} state on the surface of the notched body are given as

$$\sigma_{ij} = \begin{bmatrix} 0 & 0 & 0 \\ 0 & \sigma_{22} & \sigma_{23} \\ 0 & \sigma_{32} & \sigma_{33} \end{bmatrix} \tag{4.24}$$

$$\varepsilon_{ij} = \begin{bmatrix} \varepsilon_{11} & 0 & 0 \\ 0 & \varepsilon_{22} & \varepsilon_{23} \\ 0 & \varepsilon_{32} & \varepsilon_{33} \end{bmatrix} \tag{4.25}$$

The stress state on the free surface is the plane stress as shown in Figure 4-8**.** A graphical representation of searched planes for the rotation of φ about x axis on the plane $(\theta = 90^{0})$ perpendicular to the free surface is shown in Figure 4-9. The stress and strain tensors can be computed on any candidate planes represented by the x'-y'-z' coordinate system using Eqs. (4.22) and (4.23). The number of planes on which the fatigue damage is calculated is reduced by taking advantage of plane stress state on the component surface. For the free surface, there are only four possible damage plane systems [75,76]. For tensile loading, the plane experiencing the maximum damage must be located on the plane $(\theta = 90^{0})$. For shear loading, the plane experiencing the maximum damage must be located on the plane $(\theta = 45^{0})$. For combined loadings, the damage is calculated with $\theta = 45^{0}$ and $\varphi = 0^{0}$ *to* 180^{0} in increments of 5^{0} and $\theta = 90^{0}$ and $\varphi = 0^{0}$ *to* 180^{0} in increments of 5^{0}.

However, Chu [77] indicated that the most critical plane for multiaxial loadings is always perpendicular to the free surface $(\theta = 90^0)$. Therefore, only planes with $\theta = 90^0$ and φ varying from 0^0 to 180^0 should be searched. Only when the hoop stress component, σ_{33} becomes significantly large or when the shear stress becomes small, the critical plane deviates from such a perpendicular plane. Then the search for the critical plane should consider all combination of potential planes with angles of θ and φ. The value of 5^0 is chosen as increment angle value due to fact that the fatigue damage calculated on potential planes with smaller increment value(s) provides very close results.

Once normal and shear strains and stress components are calculated on all possible failure planes, then, the proposed fatigue damage parameter can be evaluated on each plane to determine the critical plane experiencing the maximum fatigue damage i.e. when the fatigue damage parameter is maximized.

4.2 **Proposed Fatigue Damage Parameter**

A multiaxial fatigue damage parameter, which quantifies the fatigue damage as a function of certain stress and strain variables such as normal strain, maximum stress and etc., relates a certain amount of the fatigue damage to fatigue life.

In general, a successful multiaxial fatigue damage parameter should include following important features.

- Simple, efficient and applicable to a variety of fatigue loading conditions e.g., uniaxial loadings and multiaxial loadings including proportional and non-proportional loading.
- Applicable to low and high cycle fatigue regimes.

- Includes mean stress effects in the fatigue damage parameter.
- Reflects the constitutive behavior of material and the non-proportional hardening.
- Physically correct from the continuum mechanics viewpoint.
- Defined without using any additional material coefficient.
- Load path dependent.
- Predicts the failure plane(s) and damage mechanism including tensile and shear failure modes.

In consideration of these important features desired for a successful fatigue damage parameter and shortcomings of the stress-based, the strain-based and energy-based damage parameters discussed in Chapter 2, an original multiaxial fatigue damage parameter incorporating most of these important features has been proposed for predicting multiaxial fatigue life. The critical plane of this proposed fatigue damage parameter considers a plane experiencing the maximum fatigue damage as a critical plane rather than the maximum shear or normal strains plane.

The proposed fatigue damage parameter in the form of generalized strain energy, which includes the shear and normal strain energy terms on a critical plane, can be expressed in Eq.(4.26).

$$W_{gen}^{*} = \left(\tau_{\max} \frac{\Delta\gamma^{e}}{2} + \frac{\Delta\tau}{2}\frac{\Delta\gamma^{p}}{2} + \sigma_{n,\max} \frac{\Delta\varepsilon_{n}^{e}}{2} + \frac{\Delta\sigma_{n}}{2}\frac{\Delta\varepsilon_{n}^{p}}{2} \right)_{\max} = f(N_{f}) \qquad (4.26)$$

The fatigue damage parameter in the form of the generalized strain energy includes the sum of elastic shear strain energy $\left(\tau_{\max}\ \Delta\gamma^{e}/2\right)$, plastic shear strain energy $\left(\Delta\tau/2\ \Delta\gamma^{p}/2\right)$, elastic normal strain energy $\left(\sigma_{n,\max}\ \Delta\varepsilon_{n}^{e}/2\right)$ and plastic normal strain energy $\left(\Delta\sigma_{n}/2\ \Delta\varepsilon_{n}^{e}/2\right)$ terms. This generalized strain energy based damage parameter accounts for effects of the mean stress and the non-proportional hardening through the elastic strain energy terms $\left(\tau_{\max}\Delta\gamma^{e}/2\right)$ and $\left(\sigma_{n,\max}\Delta\varepsilon_{n}^{e}/2\right)$ by including the maximum shear stress, $\tau_{\max}$ and maximum normal stress, $\sigma_{n,\max}$ components. Contrary to the strain based fatigue damage parameters, the proposed strain energy parameter, W_{gen}^{*} is acceptable from the continuum mechanics viewpoint that energy components are mathematically consistent and can be added algebraically. The fatigue damage parameter in the form of the generalized strain energy can be related to the mechanical energy input to the material. The shear strain energy terms reflect the initiation and growth of cracks, and the normal strain energy terms accelerate the crack growth. Similar to the Chu parameter, the proposed generalized strain energy parameter is based on a plane with the maximum value of the damage parameter i.e. the average contribution from tensile and shear energy terms rather than the plane of maximum normal or shear strains. It other words, it takes an average direction of Mode II which initiates a crack and Mode I which grows micro-crack as the crack orientation.

The shear strain energy terms in Eq. (4.26) can be normalized with the shear stress amplitude, $\Delta\tau/2$ and the normal strain energy terms in Eq. (4.26) can also be normalized with the normal stress amplitude, $\Delta\sigma_{n}/2$ to transform the generalized strain energy parameter, Eq. (4.26) to the form of generalized strain amplitude, Eq.(4.27)

The proposed multiaxial fatigue damage parameter in the form of generalized strain amplitude can be written as:

$$\frac{\Delta\varepsilon^{*}_{gen}}{2}=\left(\frac{\tau_{\max}}{\Delta\tau/2}\frac{\Delta\gamma^{e}}{2}+\frac{\Delta\gamma^{p}}{2}+\frac{\sigma_{n,\max}}{\Delta\sigma_{n}/2}\frac{\Delta\varepsilon^{e}_{n}}{2}+\frac{\Delta\varepsilon^{p}_{n}}{2}\right)_{\max}=f\left(N_{f}\right) \tag{4.27}$$

Based on Basquin's equation [78] the shear stress amplitude, $\Delta\tau/2$ and the normal stress amplitude, $\Delta\sigma_{n}/2$ for uniaxial stress state, can be expressed as:

$$\begin{aligned}\frac{\Delta\tau}{2}&=\tau'_{f}\left(2N_{f}\right)^{b_{\gamma}}\\ \frac{\Delta\sigma_{n}}{2}&=\sigma_{a}=\sigma'_{f}\left(2N_{f}\right)^{b}\end{aligned} \tag{4.28}$$

In the case of $2N_{f}=1$, the shear and normal stress amplitude, Eq.(4.28) can be given:

$$\begin{aligned}\frac{\Delta\tau}{2}&=\tau'_{f}\\ \frac{\Delta\sigma_{n}}{2}&=\sigma'_{f}\end{aligned} \tag{4.29}$$

Substituting the shear and normal stresses from Eq.(4.29) into Eq.(4.27), the multiaxial fatigue damage parameter based on the generalized strain amplitude can be expressed as:

$$\frac{\Delta\varepsilon^{*}_{gen}}{2}=\left(\frac{\tau_{\max}}{\tau'_{f}}\frac{\Delta\gamma^{e}}{2}+\frac{\Delta\gamma^{p}}{2}+\frac{\sigma_{n,\max}}{\sigma'_{f}}\frac{\Delta\varepsilon^{e}_{n}}{2}+\frac{\Delta\varepsilon^{p}_{n}}{2}\right)_{\max}=f\left(N_{f}\right) \tag{4.30}$$

This proposed multiaxial fatigue damage parameter is based on the assumption that all stress and strain components on the critical plane which experience the maximum damage should contribute the fatigue damage. Only the elastic shear and normal strain amplitudes are to be corrected by the corresponding maximum shear and normal stresses. The interpretation of the proposed fatigue damage parameter, Eq. (4.30) can be explained as the plastic normal strain, $\Delta\varepsilon^{p}_{n}/2$ opening the crack, reducing the friction between

crack surfaces while the plastic shear strain, $\Delta\gamma^p/2$ induces the dislocation movement along slip planes, causing nucleation of cracks. On the other hand the corrected elastic normal strain, $\frac{\sigma_{n,\max}}{\sigma'_f}\frac{\Delta\varepsilon_n^e}{2}$ on the critical plane assists in opening the crack and thus accelerates the growth and the corrected elastic shear strain, $\frac{\tau_{\max}}{\tau'_f}\frac{\Delta\gamma^e}{2}$ overcomes any sliding friction between crack surfaces. The proposed fatigue damage parameter is capable of predicting the effect of the mean stress, the path dependency of the stress response and the non-proportional hardening through incorporation of the maximum normal stress, $\sigma_{n,\max}$ and maximum shear stress, $\tau_{\max}$ components. The maximum normal stress is introduced as the normal stress correction factor, $\frac{\sigma_{n,\max}}{\sigma'_f}$ and the maximum shear stress is introduced as the shear stress correction factor, $\frac{\tau_{\max}}{\tau'_f}$ in the proposed fatigue damage parameter, Eq.(4.27). These normal and shear stress correction factors, $\left(\frac{\sigma_{n,\max}}{\sigma'_f}\right)$ and $\left(\frac{\tau_{\max}}{\tau'_f}\right)$ can reflect the fatigue damage reduction, which is caused by the tensile mean stress and the additional cyclic hardening. It should be also noticed that these stress correction factors are not constant, but varying as a function of the maximum normal and shear stresses. Unlike the Findley, the Brown-Miller, Fatemi-Socie and the Glinka damage parameters, the proposed multiaxial fatigue damage parameter do not include any material fitting constants, which requires additional material testing. The usage of material constants in the fatigue damage parameter is inconvenient for evaluating fatigue life for general engineering applications. The proposed fatigue

damage parameter shows in Figure 4-10 that a wider range of planes around the critical plane subjected to a high percentage of fatigue damage cause the activation of more slip systems. Higher values of damage distribution over a wider range of planes around the critical plane result in higher probability of crack initiation and growth, and shorter lives as compared to the Brown-Miller [51] and Fatemi-Socie [55] parameters.

The shear strain and normal strain amplitudes using the uniaxial material fatigue properties can be expressed as:

$$\begin{aligned}\frac{\Delta\gamma}{2} &= \left[(1+\nu_e)\frac{\sigma'_f}{E}(2N_f)^b + (1+\nu_p)\varepsilon'_f(2N_f)^c\right] \\ \frac{\Delta\varepsilon_n}{2} &= \left[\frac{(1-\nu_e)}{2}\frac{\sigma'_f}{E}(2N_f)^b + \frac{(1-\nu_p)}{2}\varepsilon'_f(2N_f)^c\right]\end{aligned} \tag{4.31}$$

In case of full reverse loading (R=-1), the maximum shear and normal strains using uniaxial material properties can be estimated as:

$$\begin{aligned}\tau_{\max} &= \tau_a = \tau'_f(2N_f)^{b\gamma} = \frac{\sigma'_f}{\sqrt{3}}(2N_f)^b \\ \tau'_f &= \frac{\sigma'_f}{\sqrt{3}}, b\gamma = b \\ \sigma_{n,\max} &= \sigma_a = \sigma'_f(2N_f)^b\end{aligned} \tag{4.32}$$

Substituting the shear and normal strains from Eq. (4.31) and the maximum shear and normal stresses from Eq.(4.32) into equation (4.30), the multiaxial fatigue damage parameter can be written in terms of the uniaxial fatigue properties as:

$$\left(\frac{\tau_{\max}}{\tau'_f}\frac{\Delta\gamma^e}{2}+\frac{\Delta\gamma^p}{2}+\frac{\sigma_{n,\max}}{\sigma'_f}\frac{\Delta\varepsilon_n^e}{2}+\frac{\Delta\varepsilon_n^p}{2}\right)_{\max}=\left[(1+\nu_e)\frac{\sigma'_f}{E}(2N_f)^b\frac{\sqrt{3}\sigma'_f}{\sqrt{3}\sigma'_f}(2N_f)^b+(1+\nu_p)\varepsilon'_f(2N_f)^c\right]$$
$$+\left[\frac{(1-\nu_e)}{2}\frac{\sigma'_f}{E}(2N_f)^b\frac{\sigma'_f}{\sigma'_f}(2N_f)^b+\frac{(1-\nu_p)}{2}\varepsilon'_f(2N_f)^c\right] \quad (4.33)$$

The proposed multiaxial fatigue damage parameter, Eq.(4.33), can be simplified as:

$$\left(\frac{\tau_{\max}}{\sigma'_f/\sqrt{3}}\frac{\Delta\gamma^e}{2}+\frac{\Delta\gamma^p}{2}+\frac{\sigma_{n,\max}}{\sigma'_f}\frac{\Delta\varepsilon_n^e}{2}+\frac{\Delta\varepsilon_n^p}{2}\right)_{\max}=\left[(1+\nu_e)\frac{\sigma'_f}{E}(2N_f)^{2b}+(1+\nu_p)\varepsilon'_f(2N_f)^c\right]$$
$$+\left[\frac{(1-\nu_e)}{2}\frac{\sigma'_f}{E}(2N_f)^{2b}+\frac{(1-\nu_p)}{2}\varepsilon'_f(2N_f)^c\right] \quad (4.34)$$

The proposed fatigue damage parameter, Eq.(4.34) can be criticized for the lack of physical correctness from the continuum mechanics viewpoint. This is because of difficulties concerning the physical meaning of the fatigue damage parameter, being the algebraic sum of the shear and normal strain terms acting on the plane.

The proposed fatigue damage parameter(s) can be differentiated from the existing damage parameters discussed in Chapter 2 that it includes all stress and strain components on the critical plane. In addition, it can be expressed as both the generalized strain amplitude and the generalized strain energy thus combining all good features from the stress-based, strain-based and the energy-based critical plane parameters. The proposed fatigue damage parameter in the form of the generalized strain amplitude is adapted for numerical implementation of the multiaxial fatigue analysis.

In case of the uniaxial fatigue, it is well known that the mean stress has significant effects on the high cycle fatigue regime where the elastic strain dominates. In contrast, there are little or no mean stress effects in the low cycle fatigue region. However, the

Morrow mean stress correction parameter [79] indirectly suggests that the mean stress changes the relation between the plastic and elastic strain amplitude while the SWT parameter [80] tends to underestimate the fatigue life in the low cycle fatigue resulting in author' opinion from the correction of the both elastic and plastic strain terms and the SWT parameter is also non-conservative in the presence of compressive mean stresses. Therefore, Ince and Glinka [81] suggested that the multiaxial fatigue damage parameter in the original form of generalized strain amplitude, Eq.(4.27) can be applied to a uniaxial loading as a mean stress correction parameter in order to avoid inconsistencies mentioned above. The multiaxial fatigue damage parameter, Eq.(4.27) can take the following form in case of the uniaxial loading:

$$\frac{\Delta\varepsilon^{*}_{gen}}{2} = \frac{\sigma_{\max}}{\sigma'_{f}}\frac{\Delta\varepsilon^{e}}{2} + \frac{\Delta\varepsilon^{p}}{2} = \frac{\sigma'_{f}}{E}\left(2N_{f}\right)^{2b} + \varepsilon'_{f}\left(2N_{f}\right)^{c} \tag{4.35}$$

Where $\frac{\sigma_{\max}}{\sigma'_{f}}\frac{\Delta\varepsilon^{e}}{2}$ is the corrected elastic strain amplitude accounting mean stress effect and $\frac{\Delta\varepsilon^{p}}{2}$ is the plastic strain amplitude.

The physical interpretation of this proposed mean stress correction parameter in Eq. Eq.(4.35) reflects that the mean stresses will have relatively less effect in the presence of large plastic strain. Ince and Glinka [81] reported that the proposed uniaxial mean stress correction parameter, Eq.(4.35) provides noticeable improvements to both the Morrow and the SWT parameters in predicting fatigue lives for the published mean stress fatigue data.

The key characteristic of the proposed parameter(s) is that the multiaxial fatigue damage parameter can be applied to both the multiaxial and uniaxial fatigue loading

conditions as the generalized strain amplitude in Eq. (4.30) and Eq.(4.35) respectively, thus providing a consistent approach for its application to multiaxial and uniaxial fatigue problems.

4.3 **Numerical Implementation of the Multiaxial Fatigue Damage Parameter**

A general computational methodology for multiaxial fatigue life analysis is shown in Figure 1-1 and a more detailed outline for algorithms of the computational procedure is presented in Figure 4-11. Once actual strain and stress responses at notch areas are determined, the proposed multiaxial fatigue damage parameter can be used to estimate the fatigue life. Since the critical plane is defined as the plane experiencing the maximum fatigue damage, the fatigue damage parameter is computed for all potential planes using the actual strain and stress histories rotated on those planes. Since the critical plane is not known before the analysis, the fatigue damage parameter on all potential planes is computed in order to determine the critical plane experiencing the maximum fatigue damage. The fatigue damage associated with each candidate plane is calculated using the following steps.

a) Rotation matrix, $a_{\theta\phi}$, which defines a candidate plane, is determined using Eq. (4.24).

b) History of stress and strain tensors is transformed on the candidate plane represented by θ_i, φ_i angles using Eq.(4.25) and Eq.(4.26).

c) Once strain and stress variables $\left(\Delta\gamma, \tau_{\max}, \Delta\varepsilon_n, \sigma_{n,\max}\right)$of the fatigue damage parameter are determined, the fatigue damage parameter is calculated using Eq.(4.30).

d) Fatigue life corresponding to the magnitude of this damage parameter is estimated using the Newton-Raphson iterative approach.

e) Fatigue damage associated with the candidate planes are computed for all stress and strain cycles.

f) Total fatigue damage for all candidate planes is calculated by summing up fatigue damage increments using a linear accumulation rule. The plane experiencing the maximum fatigue damage is identified by $\theta_{cr}, \varphi_{cr}$ angles.

g) Determine the fatigue life of the notched component on the maximum fatigue damage plane.

h) Plot the damage map of the FE model to visualize the fatigue damage contour.

An iterative approach is used to solve the fatigue damage parameter-life equation. The algorithm starts by guessing the life, and then an iterative solution using the Newton-Raphson method is implemented by computing a new guess for the life. The iteration is repeated until convergence criterion (calculated solution error is reached to acceptable level). The iteration loop is repeated until the fatigue life is computed for all surface nodes at notch areas of the FE model. The procedure steps for the iterative algorithm using the Newton-Raphson are shown in Figure 4-12.

The procedure steps given here are implemented in a computer program written in MATLAB for the multiaxial fatigue analysis for notched components subjected to the multiaxial loadings. Implementation of the proposed multiaxial fatigue analysis methodology, which incorporates the proposed fatigue damage parameter based on the generalized strain amplitude and the elastic-plastic stress-train model is suitable for the design evaluation of notched components used in general engineering applications, especially ground vehicles. This proposed methodology provides more efficient and

appropriate analysis approach preferable to more complex and time consuming life prediction methods using non-linear stress-strain analysis.

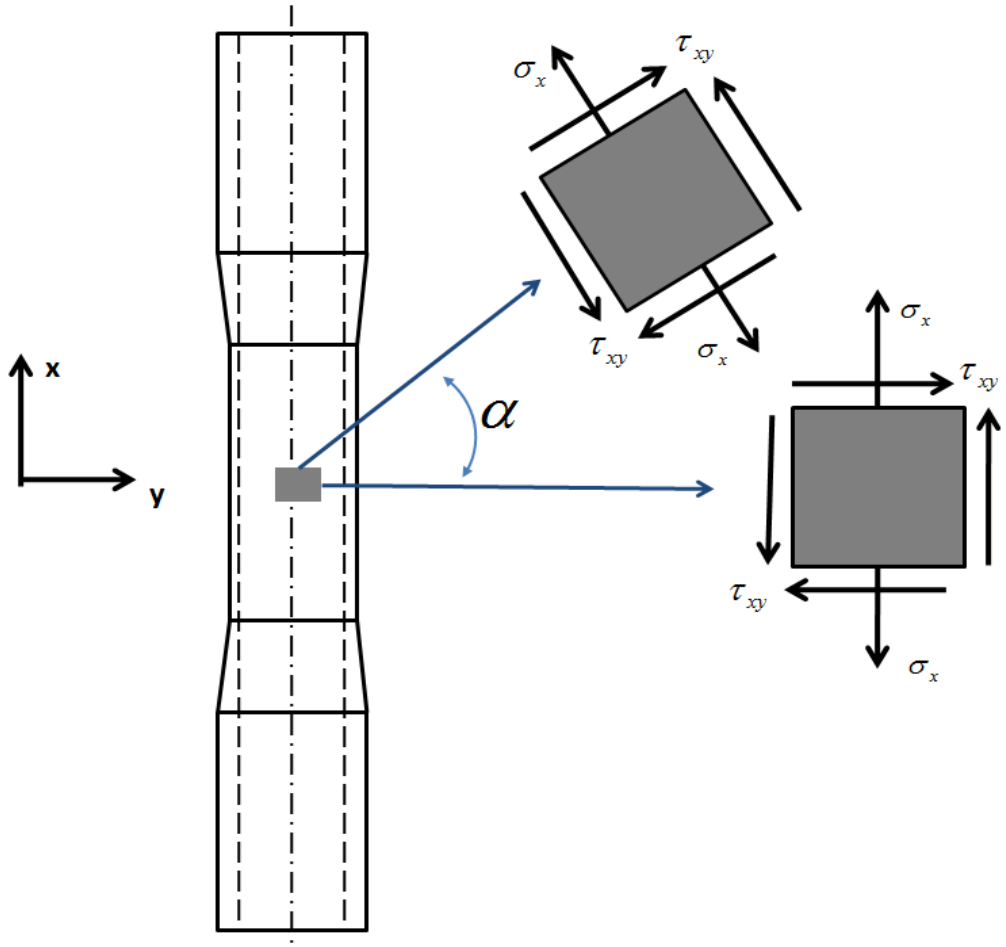

Figure 4-1: Tubular test specimen stress state and plane orientation

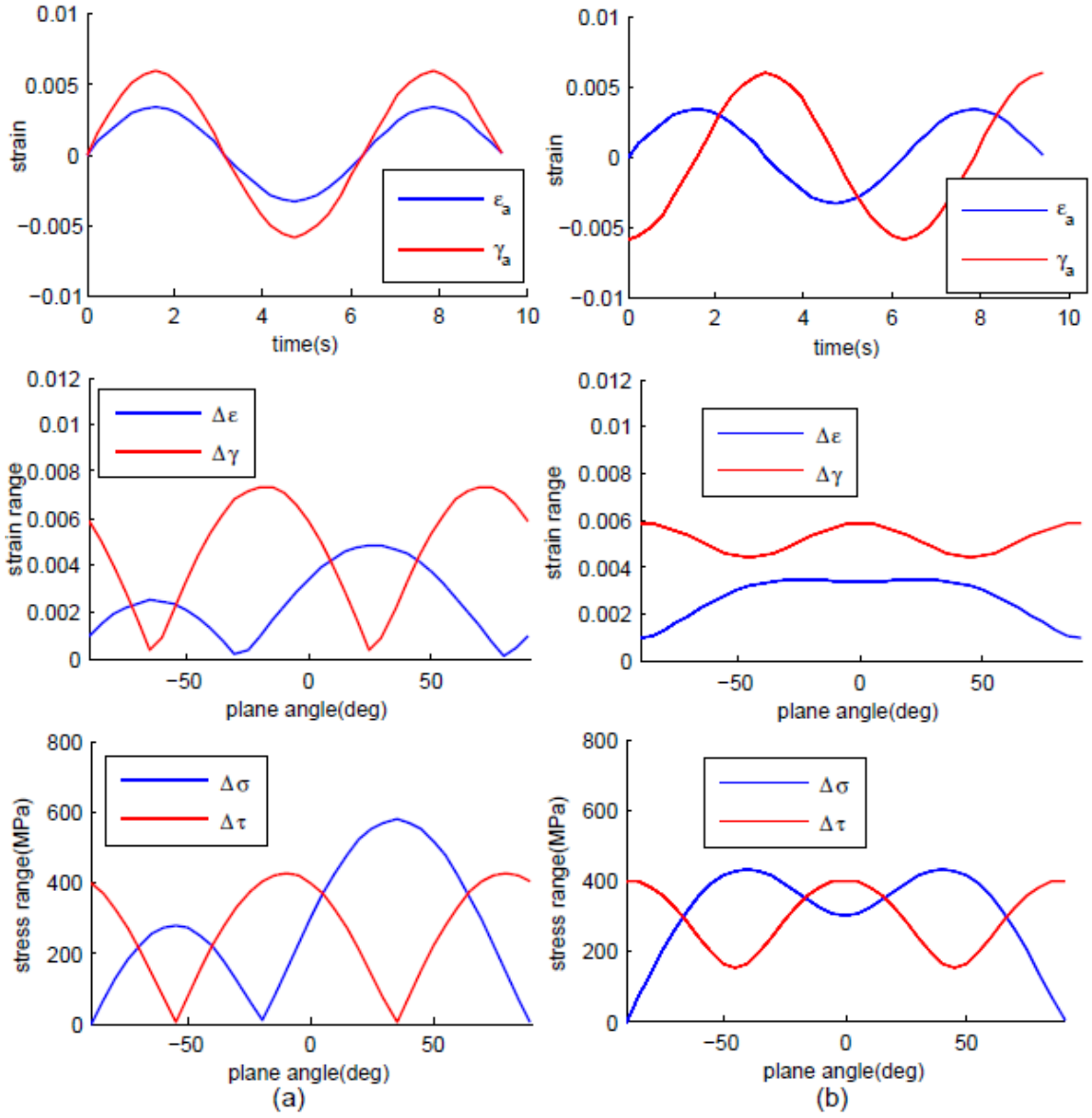

Figure 4-2: Normal and shear strain and stress ranges on various planes for (a) in-phase loading and (b) 90^o **out-of-phase loading**

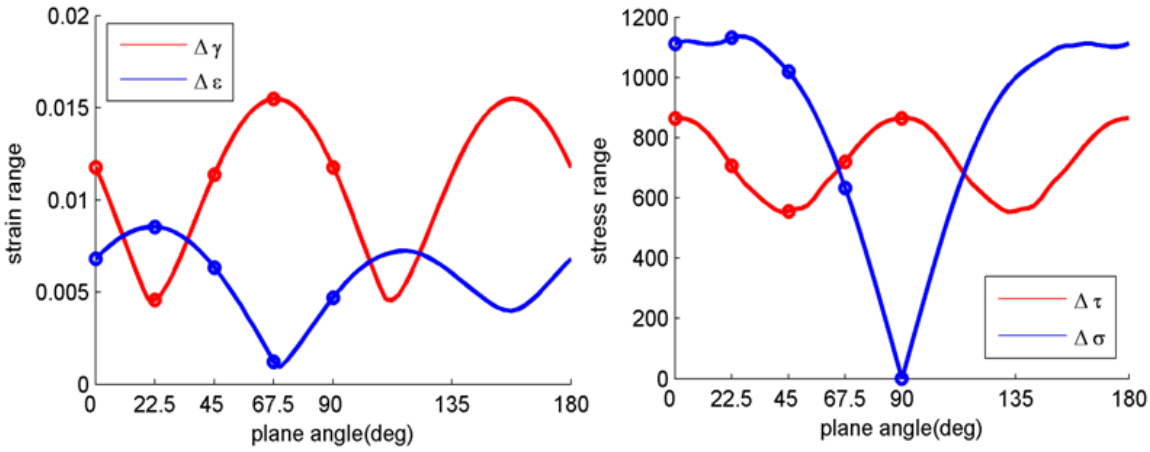

Figure 4-3: Normal and shear strain-stress ranges on various planes for 45^o out-of-phase loading

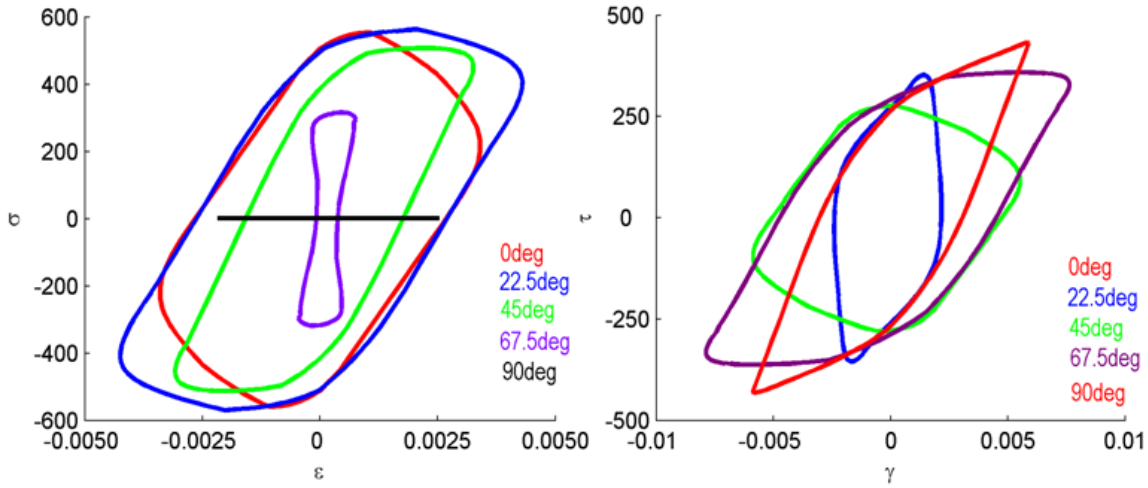

Figure 4-4: Normal and shear strain-stress hysteresis loops on various planes for 45^o out-of-phase loading

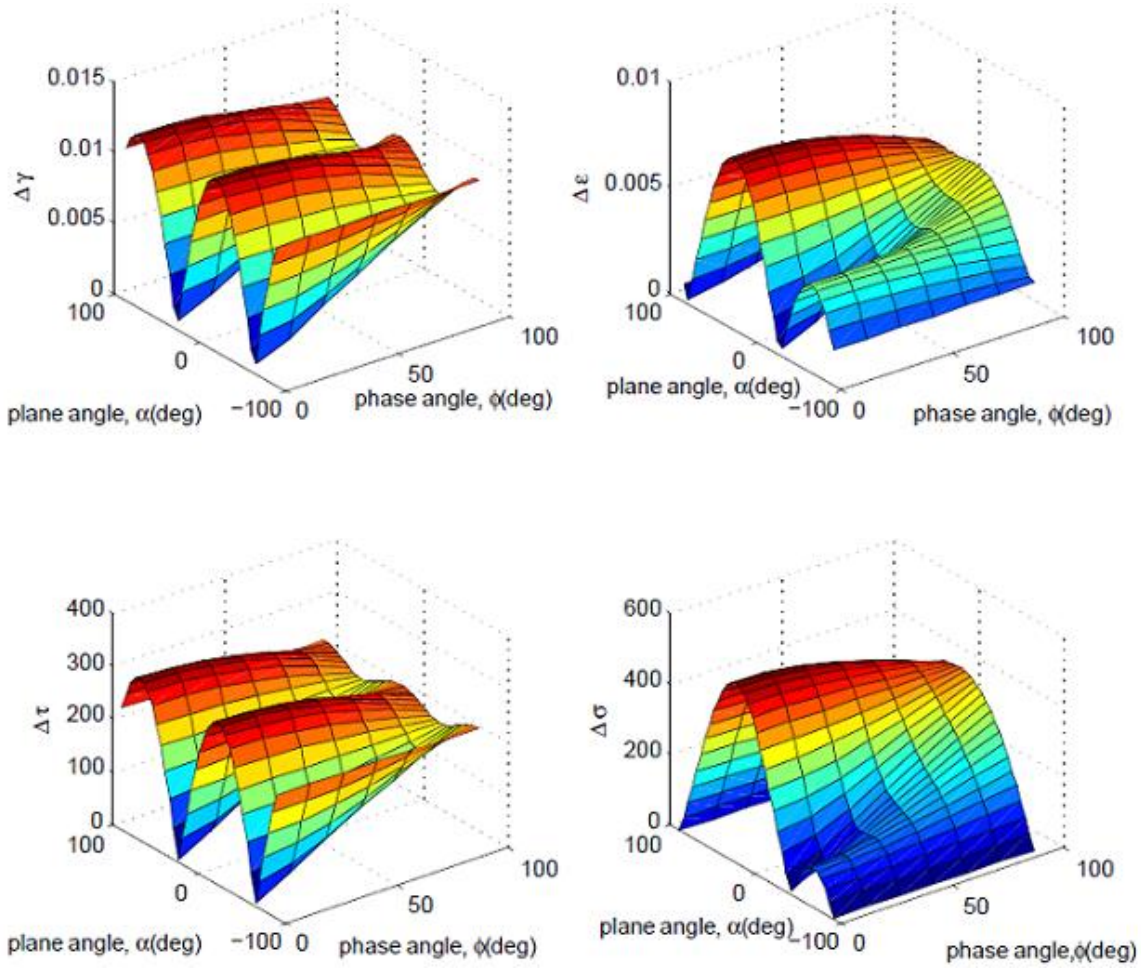

Figure 4-5: Variations of normal and shear stress/strain ranges on various planes as a function of phase angle

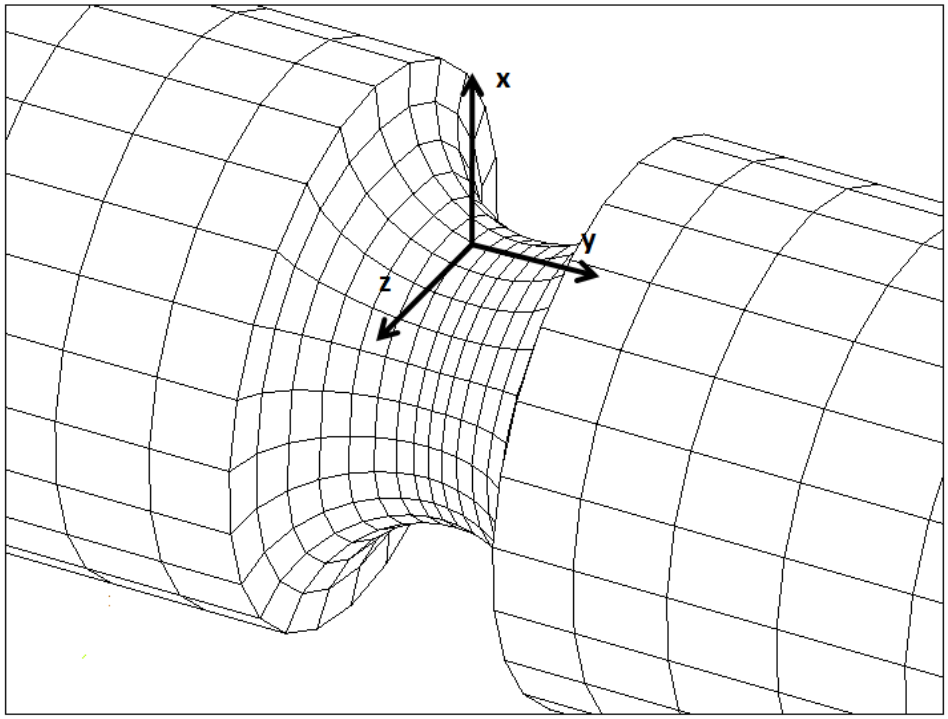

Figure 4-6: FE notched body local coordinate system

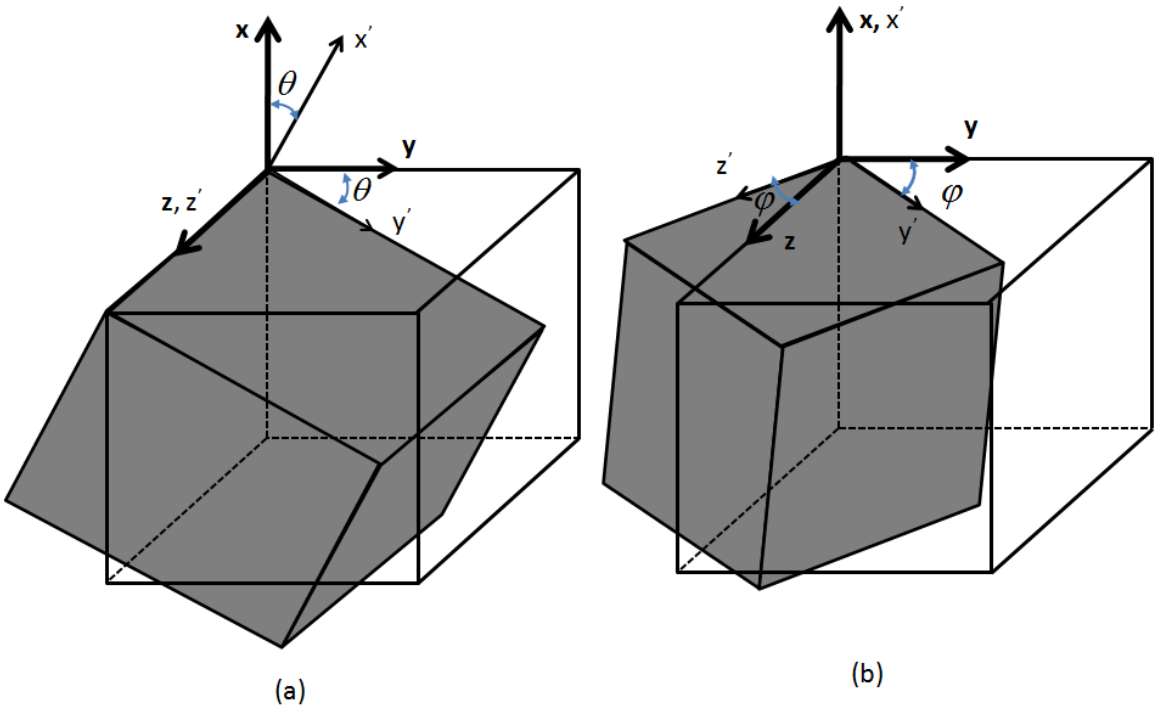

Figure 4-7: Plane rotations (a) θ rotation about z axis (a) φ rotation about x axis

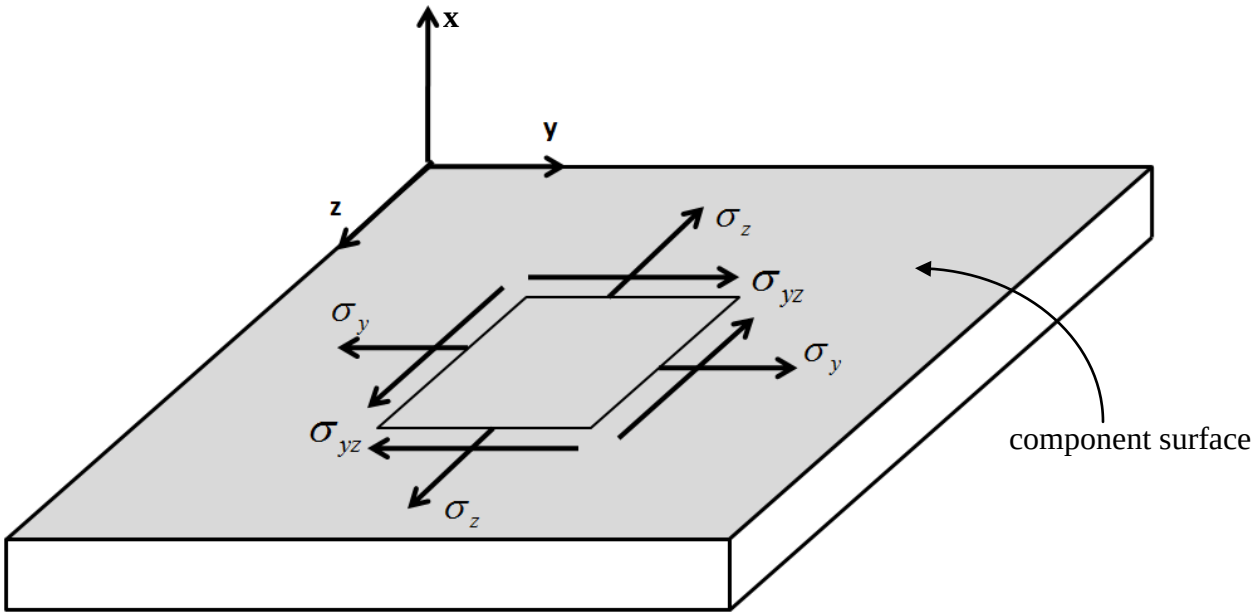

Figure 4-8: Stress state on the free surface

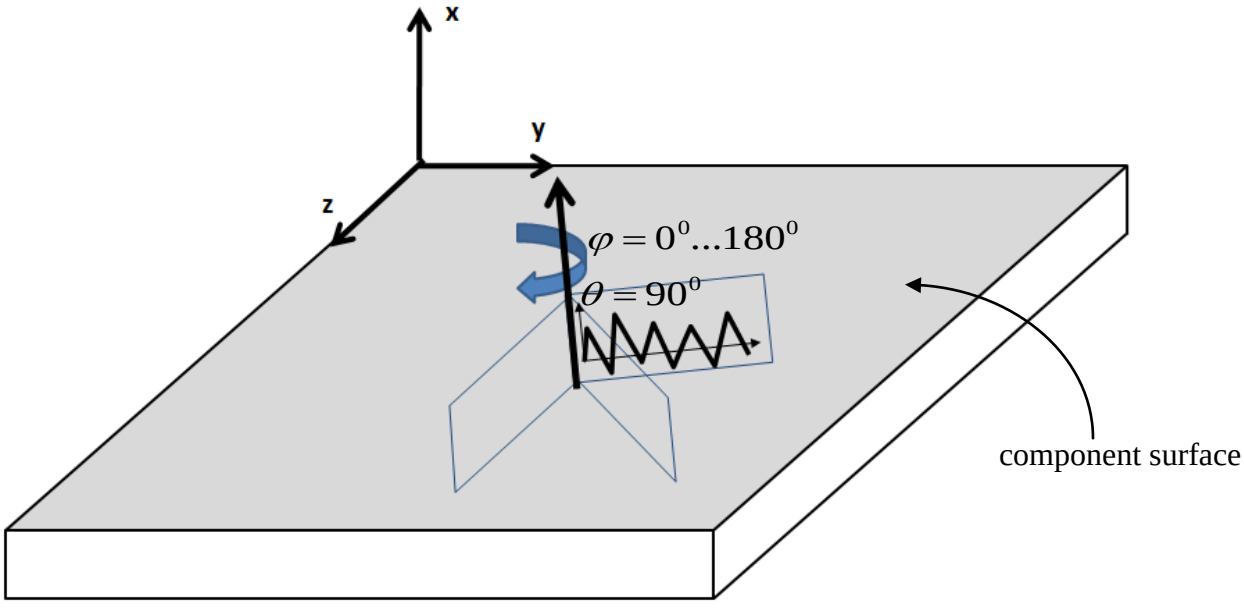

Figure 4-9: A graphical representation of stress tensor rotation on the free component surface

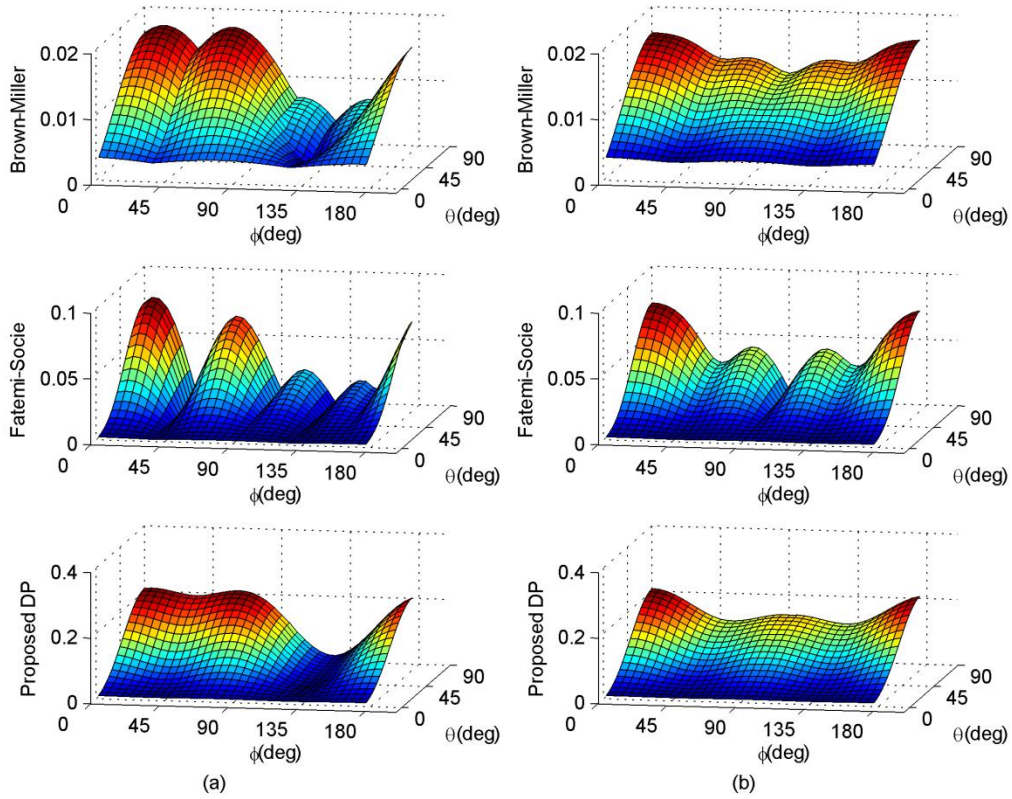

Figure 4-10: Proposed damage parameter in comparison of Fatemi-Socie and Brown-Miller for (a) in-phase loading and (b) 90^o out-of-phase loading

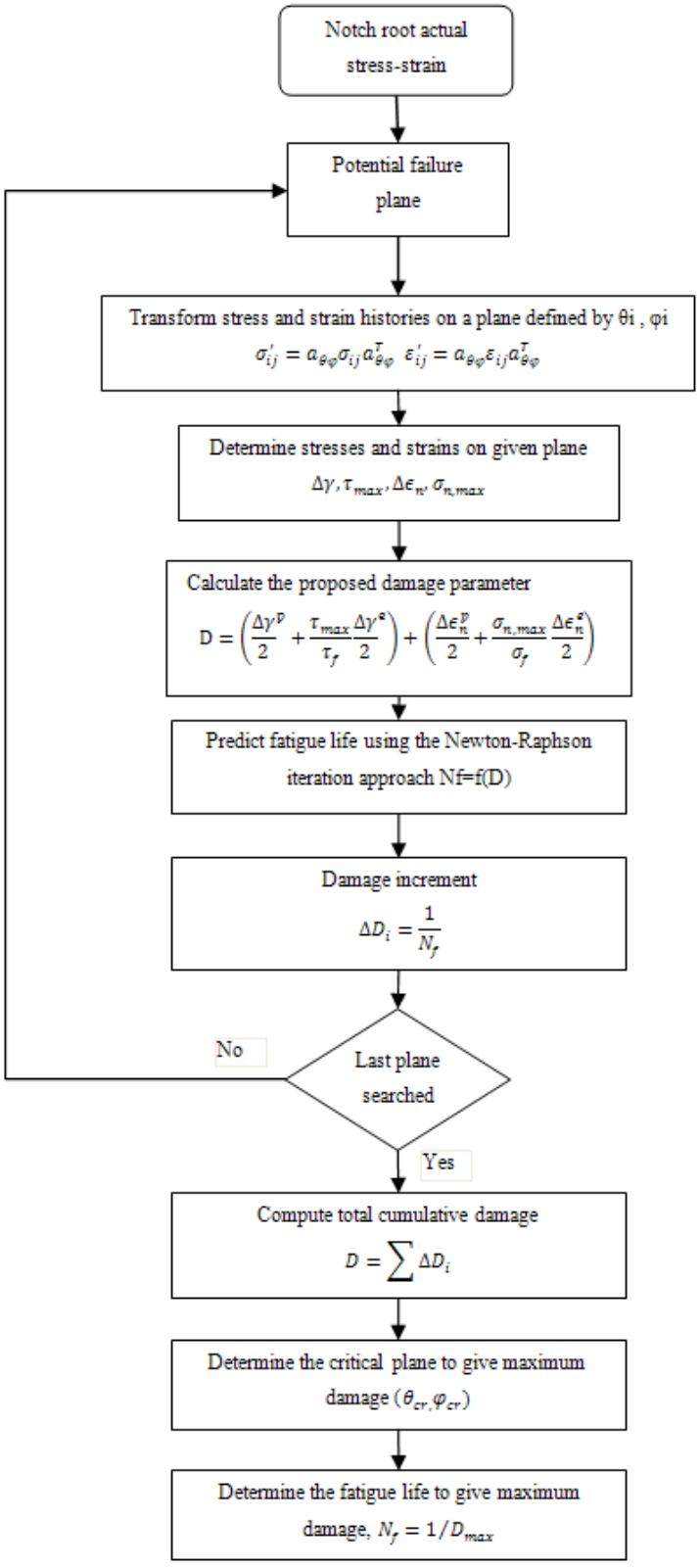

Figure 4-11: Algorithm for computing fatigue life under multiaxial loading

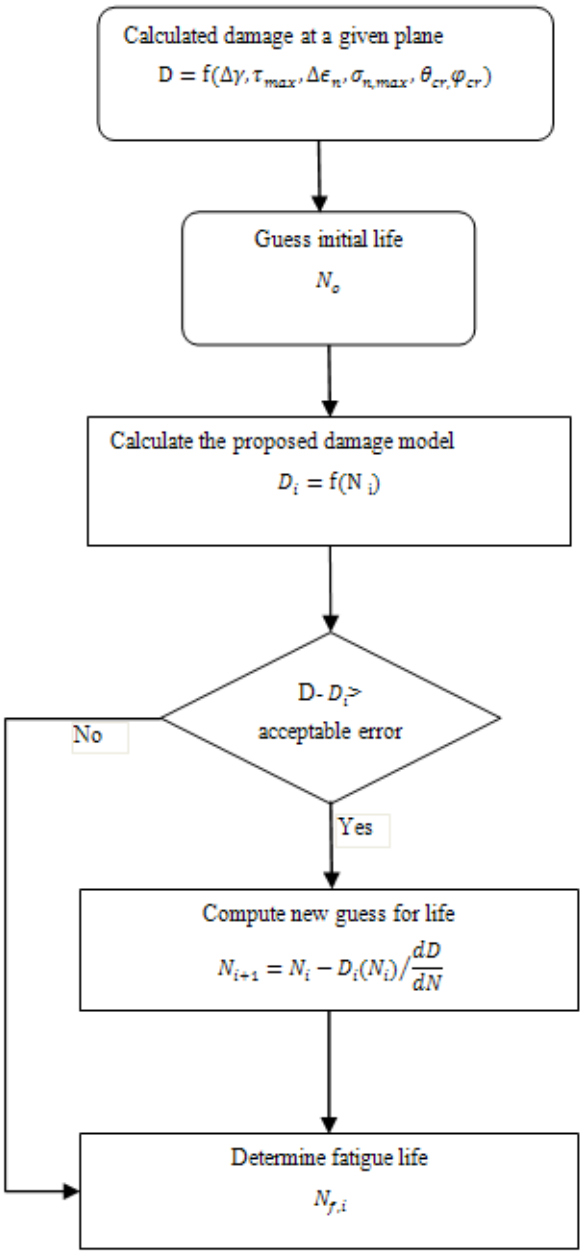

Figure 4-12: Algorithm for Newton-Raphson iterative solution of proposed damage parameter

Chapter 5
Case Studies

The proposed multiaxial fatigue analysis methodology has been implemented in computer programs making it suitable for use in the design evaluation of engineering components. The proposed multiaxial fatigue analysis methodology has been presented in previous chapters and is now applied to case studies in this chapter to correlate to various sets of experimental data. The multiaxial fatigue analysis methodology consists of the analytical elastic-plastic stress/strain model to perform the elastic-plastic stresses/strains analysis of notched bodies using FE linear elastic stress results and the proposed multiaxial fatigue damage parameter to predict the life of those notched bodies under the multiaxial loadings. The elastic-plastic stress/strain model and the multiaxial fatigue damage parameter have been previously presented in Chapter 3 and Chapter 4 respectively. In this chapter, numerical results obtained from the elastic-plastic stress/strain model and the multiaxial fatigue damage parameter are compared with various sets of the published experimental data to assess their prediction capabilities. The experimental strain data of SAE 1070 steel notched shaft [38] under various non-proportional load paths are compared to results of the elastic-plastic stress/strain model for calculations of actual elastic-plastic strains at the notch root. The proposed multiaxial fatigue damage parameter is successfully applied to the uniaxial loading as the mean stress correction parameter. The proposed stress correction parameter shows accurate predictions with experimental mean stress fatigue data for ASTM A723 steel [82], Incoloy 901 superalloy [83], 7075-T561 aluminum alloy [84] and 1045 HRC 55 steel [85]. In order to assess the prediction accuracy of the proposed multiaxial fatigue damage

parameter, predicted fatigue lives by the multiaxial fatigue damage parameter are correlated with the experimental data of the thin-walled tubular specimens machined from 1045 HR steel [86] and Inconel 718 [87] alloy subjected to the proportional (in-phase) and non-proportional (out-of-phase) loadings. Since the SAE notched shaft represents a realistic engineering component with its typical notch geometry and has a complex stress-strain state, experimental data of the SAE 1045 notched shaft [88] is used to verify predicting accuracies of the elastic-plastic stress/strain model and the multiaxial fatigue damage parameter and the robustness of the multiaxial fatigue analysis methodology for notched components. The measured strain data for the SAE 1045 notched shaft is compared to stress-strain responses obtained from the elastic-plastic stress/strain model. The experimental fatigue data is compared to predicted fatigue lives by the multiaxial fatigue damage parameter.

5.1 **Comparison of the Elastic-Plastic Stress and Strain Model with Experimental Data of SAE 1070 Steel Notched-Bar**

In this section, calculated elastic-plastic notch strains and stresses obtained from the elastic-plastic stress-strain model are compared to the experimental strain and stress data of SAE 1070 Steel Notched-Bar for six different non-proportional load paths [38]. Pseudo elastic stress histories for each load path were calculated using linear elastic FE stress results. Calculated elastic stress histories are then used as input to the analytical elastic-plastic stress/strain model to compute actual elastic-plastic strains and stresses at the critical notch area.

Barkey [38] performed experiments on circumferential notched-shafts subjected to various non-proportional load paths. The notched shafts were subjected to cyclic

tension and torsional load histories under conditions of load controls by using Instron and MTS tension-torsion biaxial test frames. Strain gauges were mounted on the notch root for strain measurements. The experimented notch shafts were a cylindrical bar with a circumferential notch similar to that one shown in Figure 5-1. Each cylindrical specimen was machined from SAE 1070 steel stack to the proper geometry, then heat treated to give uniform material properties. The actual radius of the cylindrical specimen was R=25.4 mm and notch dimensions of the cylindrical specimen were $\rho/t = 1$ and $R/t = 2$. The FEA and experimental stress concentration factors are listed in Table 5-1. These stress concentration factors are relatively mild and would exist on typical notched components such as those found in many ground vehicle applications. The ratio of the measured notch tip hoop stress to the axial stress under tensile axial loading was $\sigma_{33}^{e}/\sigma_{22}^{e} = 0.184$. The FE model and strain state for the analyzed notch-bar is shown in Figure 5-2.

The material for the notched bar was SAE 1070 steel with a cyclic stress-strain curve approximated by the Ramberg- Osgood relation (Eq. (2.1)). The material properties were given as: E = 210 GPa, $\nu = 0.3$, $S_Y = 242$ MPa, n'=0.199, and K' = 1736 MPa. The cyclic stress-strain curve was discretized into several linear segments shown in Figure 5-3 for the implementation of the Garud cyclic plasticity model.

Pseudo-elastic notch stresses, σ_{22}^{e} - σ_{23}^{e}, for clockwise and counter-clockwise box-shaped cyclic stress paths are shown in Figure 5-4 and Figure 5-6 respectively. The clockwise/counter-clockwise box-shaped load paths were repeated more than hundred cycles while recording the strains at the notch tip. The box path indicates a high degree of non-proportionality loading. This load path was designed to show regions that axial and

shear responses are uncoupled (elastic response) and where they are coupled (elastic-plastic response). Therefore, the box-shaped load path provides a critical test for the proposed stress-strain model for notch tip strain and stress calculations. The maximum nominal tensile and torsion stresses were σ_n = 296 MPa and τ_n = 193 MPa respectively. The corresponding pseudo-elastic notch stresses were σ_{22}^e = 417.3 MPa and σ_{23}^e = 221.9 MPa respectively. Comparison of the measured and calculated notch strain responses for the clockwise and counter clockwise box-shaped load paths are shown in Figure 5-5 and Figure 5-7 respectively. It can be noted that the agreement between the calculated and measured strain responses are qualitatively and quantitatively good. It can be also seen from Figure 5-5 and Figure 5-7 that the proposed elastic-plastic stress/strain model predicts the elastic unloading at each corner of the box (the axial and shear strain are uncoupled) and followed by the elastic-plastic response to the next corner (the axial and shear strain are coupled).

Several non-proportional cyclic loading paths during, which ratios of the frequency of applied loads were unequal, were applied to the notched-bar specimen. The maximum nominal stresses were σ_n = 296 MPa and τ_n = 193 MPa. Non-proportional load paths from unequal frequencies of applied loads are a common type of loadings experienced by many machine components. Four of those load paths at unequal frequencies of tensile to torsional load paths in the ratio of 3:1, 5:1, 1:3, and 1:5 are analyzed here. Three cycles of tensile load were applied in same time period as one cycle of torsional load (Figure 5-8). Five cycles of tensile load were applied in same time period as one cycle of torsional load (Figure 5-10). Three cycles of torsional load were applied in same time period as one cycle of tensile load (Figure 5-12). Five cycles of

torsional load were applied in same time period as one cycle of tensile load (Figure 5-14). Axial and shear strain histories obtained from the model and experiments are plotted in Figure 5-9 , Figure 5-11, Figure 5-13 and Figure 5-15 for the tensile to torsional frequency ratios of 3:1, 5:1,1:3 and 1:5 respectively. As seen from these figures that strain responses computed by the elastic-plastic stress/strain model agree well with experiment strain data in terms of the general trend and numerical strain values.

5.2 **Comparison of Proposed Uniaxial Mean Stress Correction Parameter with Experimental Data of Incoloy 901 super alloy, ASTM A723 steel, 7075-T561 aluminum alloy and 1045 HRC 55 steel**

Four sets of experimental fatigue data from the literature [82,83,84,85] have been chosen for the purpose of prediction assessment of the proposed fatigue damage parameter for its application to uniaxial loading. Fatigue data sets are given at various means stresses for Incoloy 901 super alloy, ASTM A723 steel, 7075-T561 aluminum alloy and 1045 HRC 55 steel. Monotonic and fatigue properties of these materials at zero mean stress are also given Table 5-2. The tensile mean stress effect is predominantly studied in this study, because this is the most important range of practical applications. Strain ranges as well as the mean stress and the maximum stress were obtained from experimental half-life stress-strain hysteresis loops.

The capability and accuracy of the proposed mean stress correction parameter is compared to the Morrow and the SWT parameter using these experimental mean stress fatigue data sets, since the Morrow and the SWT parameters are most popular mean stress correction methods in engineering applications.

Figure 5-16(a) shows the Morrow parameter gives reasonable fatigue life predictions for the fatigue data at $R = -1$ and $R = 0.01$ strain ratios for Incoloy 901 super alloy. A relatively poor correlation of the Morrow parameter at $R = 0.33$ strain ratio can be seen in Figure 5-16(a) and the Morrow parameter overestimates fatigue lives for $R = 0.33$ strain ratio particularly in the fatigue life region of 10^4-10^6 cycles. The SWT parameter provides good correlation for all given strain ratios ($R = -1$, $R = 0.01$ and $R = 0.33$) in Figure 5-16(b) even though the fatigue life predicted by the SWT parameter is slightly conservative. The proposed fatigue damage parameter shows an excellent correlation with the fatigue data at all three strain ratios in Figure 5-16 (c) as the experimental data collapse very close the fatigue damage parameter vs. fatigue life line.

The results shown in Figure 5-17(a) present reasonable correlations resulted from the Morrow parameter for fatigue data at $R = -1$ and $R = 0.0$ strain ratios for 7075-T561 aluminum alloy. However, the non-conservative life predictions by the Morrow parameter are clearly seen for $\sigma_{max} = 500$ MPa and $\sigma_{max} = 600$ MPa mean stress fatigue data in Figure 5-17(a). The experimental fatigue data of 7075-T561 aluminum alloy was generated under stress control load conditions at $\sigma_{max} = 500$ MPa and $\sigma_{max} = 600$ MPa mean stress. It has been widely accepted that the SWT parameter is particularly good for aluminum alloys. This study also indicates that a fairly good correlation between the SWT model and the mean stress fatigue data for 7075-T561 aluminum can be obtained as seen in Figure 5-17(b). Similarly to the SWT parameter, the proposed fatigue damage parameter provides good correlations for all mean stress fatigue data in Figure 5-17(c). However, it is not clear whether the proposed fatigue damage parameter is more accurate in the case of 7075-T651 aluminum alloy than the SWT model.

The results shown in Figure 5-18(a) indicate that Morrow parameter seems to overestimate the fatigue lives greater than 10^4 cycles for fatigue data at $R = 0.0$, $R = 0.50$ and $R = 0.75$ strain ratios. As seen from Figure 5-18(b), The SWT parameter indicates slightly conservative predictions by underestimating fatigue lives in the range of 10^3 and 10^5 cycles. The excellent fatigue life predictions by the proposed fatigue damage parameter for all three strain ratios ($R = 0.0$, $R = 0.50$ and $R = 0.75$ strain ratios) can be clearly seen in Figure 5-18 (c).

As reported by Wehner and Fatemi [85], predictions made by the Morrow parameter are non-conservative for tensile mean stress data at $R = 0.0$, $R = 0.50$ and $R = 0.75$ strain ratios for 1045 HRC 55 steel as shown in Figure 5-19(a). Similarly to the conclusion reached by Wehner and Fatemi [85], the SWT parameter correlated well with the mean stress fatigue data as shown in Figure 5-19(b). The proposed parameter shows similarly good predictions as the SWT parameter for 1045 HRC 55 steel in Figure 5-19(c). Similarity of the prediction trends makes it difficult to distinguish the prediction capabilities between the SWT parameter and the proposed fatigue damage parameter for 1045 HRC 55 steel.

5.3 **Comparison of Proposed Multiaxial Fatigue Damage Parameter with Experimental Data of 1045 HR Steel and Incoloy 718 Tubular Specimens Data**

The experimental multiaxial fatigue data for 1045 [86] steel and Inconel 718 [87] under in-phase and out-of-phase loading provides baseline fatigue data to verify predicting accuracy of the proposed multiaxial fatigue damage parameter. The fatigue data for 1045 steel and Inconel 718 were obtained using thin-walled tube specimens subjected to proportional (in-phase) and non-proportional (out-of-phase) tensions-torsion

loadings. The thin-walled specimen has a relatively simple stress-strain state in comparison to a notched specimen, therefore the proposed fatigue damage parameter (Eq. (4.29)) can independently be assessed in terms of its relation to life cycles, and prediction errors induced by estimating the complex stress-strain state at the critical notch area can be excluded from the proposed fatigue damage parameter. Cyclic and fatigue properties of these materials are listed in Table 5-3.

Fatemi [86] investigated fatigue behavior of thin-walled tubular specimens subject to biaxial in-phase and out-of-phase tension-torsion constant amplitude loading under strain control conditions. The out-of-phase tension-torsion tests were performed with axial and shear strain paths with a 90 deg phase difference. Thin-walled tubular specimens were prepared from 1045 HR steel in the normalized conditions. Test specimens with 25.4 mm inside diameter and 2.54 mm wall thickness and 210 mm long with the gauge length of 33 mm shown in Figure 5-20 were used for all biaxial fatigue tests.

Cyclic and fatigue properties of this steel are listed in Table 5-3. The specimens were tested under various loading conditions defined by the ratio of applied shear strain range, $\Delta\gamma_{23}$ to the applied normal strain range, $\Delta\varepsilon_{22}$. These components were measured in the plane normal to the axis of the specimen (Figure 5-21). The strain ratios used in the experiments were: $\Delta\gamma_{23}/\Delta\varepsilon_{22}$ =0 (pure tension), 0.5, 1.0, 2.0 and ∞ (pure shear). Simultaneously, the applied torque, T and the axial force, P were also measured to determine determining the corresponding shear stress range, $\Delta\sigma_{23}$ and normal stress range, $\Delta\sigma_{22}$ as below.

$$\Delta\sigma_{22} = \frac{\Delta P}{2\pi R_{av} t} \tag{5.1}$$

$$\Delta\sigma_{23} = \frac{\Delta T}{2\pi R_{av} t} \tag{5.2}$$

Where R_{av} is average radius of thin-walled tubular specimen and t is the wall thickness of the specimen.

Because of the relatively thin wall, the stress gradient through the thickness in neglected and it was also assumed that there were only two non-zero stress components acting in the specimen's cross section, i.e.

$$\Delta\sigma_{ij} = \begin{bmatrix} 0 & 0 & 0 \\ 0 & \Delta\sigma_{22} & \Delta\sigma_{23} \\ 0 & \Delta\sigma_{32} & 0 \end{bmatrix} \tag{5.3}$$

Although many more critical plane-based multiaxial fatigue damage parameters have been developed, the Brown-Miller and the Fatemi-Socie parameters are considered to be the most popular multiaxial fatigue damage parameters for general engineering applications. Therefore, predicted fatigue lives by the proposed fatigue damage parameter are compared to fatigue lives estimated by the Brown-Miller and the Fatemi-Socie parameters. Predicted fatigue lives from all three fatigue damage parameters versus experimental lives for 1045 HR thin-walled tubular specimens are shown in Figure 5-22. As seen from Figure 5-22, all three fatigue damage parameters provide a reasonable correlation within a factor of 3 for in-phase and out-of-phase loading. However, the results shown in same figure indicate that Brown-Miller and the Fatemi-Socie parameters seem to slightly overestimate the fatigue lives greater than 10^5 cycles for out-of-phase loading. The proposed fatigue damage parameter tends to show slightly conservative

predictions for in-phase loading. Figure 5-23 shows that the fatigue life predictions by the proposed fatigue damage parameter are in good agreement with both in-phase and out-of-phase experimental data of 1045 HR.

The second set of experimental data considered for the validation of the multiaxial fatigue damage parameter is that of Koch [87] studied thin-walled tubular specimens made of Inconel 718, a nickel based super alloy. The tubular specimens, which were similar to that shown in Figure 5-24 were machined from a section of forged ring with 2.05mm wall thickness, 25 mm internal diameter, 210mm in length and 33 mm gauge length. The cyclic and fatigue properties of tested Inconel 718 specimens are given in Table 5-3. MTS tension-torsion test frame was utilized to conduct strain-controlled biaxial tests.

The specimens were tested under tension, torsion and simultaneous tension and torsion with various proportional and non-proportional strain paths. Each test was conducted by maintaining a constant ratio of applied shear to normal strain range. The ratio of strain range was controlled from zero (pure tension strain path) to infinite (pure shear strain path). The fatigue life, N_f was defined as the number of cycles to initiate and grow 1 mm long surface crack.

As it can be seen from Figure 5-25, under both in-phase and out-of-phase loadings, the predicted lives by the Brown-Miller and the Fatemi-Socie parameters are satisfactory within a fatigue life factor of three, however both the Brown-Miller and the Fatemi-Socie parameters tend to give somewhat non-conservative life predictions. As clearly seen in Figure 5-26, the proposed fatigue damage parameter correlates very well with experimental fatigue data for both proportional and non-proportional loadings.

The proposed fatigue damage parameter is found to show moderate improvements to the Brown-Miller and the Fatemi-Socie parameters for the experimental fatigue data of 1045 steel and Inconel 718 thin-walled tube specimens tested under in-phase and out-of-phase loading conditions.

5.4 Comparison of Proposed Multiaxial Fatigue Damage Parameter with Experimental Data of SAE 1045 Notched-Shaft Data

The accurate fatigue life prediction of a notched component depends on the detail stress/strain analysis and the good fatigue damage parameter. In this section, prediction capability of the proposed multiaxial fatigue analysis methodology which includes the simplified elastic-plastic stress/strain model for performing elastic-plastic stresses-strain analysis at notch areas and the proposed multiaxial fatigue damage parameter for estimating fatigue life of notched bodies is assessed using test data of SAE 1045 notched-shaft [88].

In the 1980's, members of the Society of Automotive Engineers (SAE) Design and Evaluation Committee created a cooperative testing program to provide experimental data for assessment of existing multiaxial fatigue design procedures and to stimulate research and development of improved multiaxial analysis methods. Kurath et al. [88] summarized the data collected as the part of committee's test program.

The committee chose simple notched shafts as test samples made from 1045 steel in hot-rolled in normalized condition to simulate an engineering component. Each shaft, future referred to as the SAE shaft, was tested in several labs. However, several different conflicting results and material properties were published [88]. The discrepancies in detection, definition of crack initiations and testing techniques among the several labs

should account for differences in test results. A complete list of test data generated by various labs is given in Table 5-4 and Table 5-5. The SAE shaft specimen, 410 mm long and 40 mm diameter with the gauge length of 100 mm is shown in Figure 5-27. Each specimen contained shoulder radii of 5 mm. The shaft specimen was designed to initiate crack on the shoulder radius and fatigue life is defined as number of cycles, Nf required to grow a length of 1 mm crack on the surface. All specimens were tested in load control, under fully reversed constant amplitude bending, torsion and combination of bending and torsion loadings (in-phase and 90^o out-of-phase). The ratio of the torsion to bending load was kept constant during each test. Over the experimental program the ratio of the torsion to bending moment Mt/ Mb ranged from zero to infinity. Strains at the notch root were measured by strain gauges and applied bending moment and torque values and cycles to crack initiation were recorded. The strain-life, cyclic stress-strain properties approximated by the Ramberg- Osgood relation and the monotonic material properties are listed in Table 5-3.

The geometry of the SAE notched shaft was modeled in ANSYS finite element code and then meshed using 3-D hexagonal (brick) solid elements and the area near the notch root was carefully refined as shown in Figure 5-28 to increase the accuracy of the elastic stress-strain results. The FE model contains 34275 nodes and 31968 elements. Boundary and loading conditions are shown in Figure 5-29. Two separate load cases: one with 1000 Nm bending load and no torsion load and other one with 1000 Nm torsion load and no bending load were applied at 150 mm distance from the notch root to the FEA model. The strain, ε_{ij} and stress σ_{ij} tensors for the FE model is based on the cylindrical coordinate system which is defined as: y axis is the primary bending axis, z axis is the

tangent to the notch surface and x axis is perpendicular to the notch. The coordinate system, x-y-z defined for the finite element model is interchangeably used as 1-2-3 coordinate system for the stress and strain tensors.

The stress concentrations for the SAE shaft are well known. Klann's boundary element analysis results, published by Leese and Socie [88], have been corroborated by 3D FEA. An elastic FEA with two load cases determines the largest elastic stress components, thus the stress concentrations for bending and torsion loads were defined as K_P = 1.55 and K_T = 1.29 respectively. Based on strain measurements on the test specimen, the stress concentrations in bending and torsion are K_P = 1.57 and K_T = 1.25 respectively.

Both sets of linear elastic results (elastic stresses) for selected elements (nodal stresses on the critical surface area) were read and converted (using a computer program) to a format readable by the elastic-plastic stress/strain model. Linear elastic stress results from two load cases (bending and torsion) were combined with actual bending and torsion loading histories using the principle of superposition to obtain increments of pseudo elastic stress histories. The torque M_t induced the 'linear elastic' shear stress σ_{23}^e at the notch tip and the bending load M_b induced the normal stress σ_{22}^e and hoop stress σ_{33}^e. The increments of hypothetical 'elastic" stress components σ_{23}^e, σ_{22}^e and σ_{33}^e were used as input for the analytical elastic-plastic stress/strain model.

The accurate stress and strain response in the critical region of the notched shaft is a key factor in the fatigue life prediction. The elastic-plastic stress/strain model using linear elastic FE stress results as an input has been employed to calculate the notch root stress and strain histories at the critical area of the SAE notched shaft subjected to

bending-torsion proportional and non-proportional loadings. A comparison of calculated strains from the analytical stress-strain model and measured strains from the experiment for bending and torsion load cases are shown in Figure 5-30 and Figure 5-31. The elastic-plastic FE computed notch strains, which were reported by Fash [89] are also included in these Figures for a general comparison. Computed strains from both the elastic-plastic stress/strain model and the non-linear FE analysis show good correlation with measured notch strain data except two shear strain points generated by the larger torsional loading (Figure 5-31). The deviation for these points is considered to be caused by test data scatter. The computed strains by the elastic-plastic stress/strain model provide better correlation with the measured strains than the FE computed strains. However, inaccuracies in the finite element modelling due to difficulties of achieving fine mesh (coarse element mesh because of computation limitation) in a couple of decades ago may result in inaccurate FE computed strains.

Experimental fatigue lives, N_E given in Table 5-4 for in-phase and Table 5-5 for out-of phase loading are compared to predicted fatigue lives, N_P, using the Brown-Miller, Fatemi–Socie and proposed fatigue damage parameters. Fatigue lives estimated by the Brown-Miller, the Fatemi–Socie and the proposed fatigue damage parameters are shown in Figure 5-34. As seen from this figure, the Brown-Miller parameter tends to give non-conservative life predictions for cycles smaller than 10^4 cycles. On the other hand, both the proposed and the Fatemi-Socie parameters tend to show conservative predictions in high cycle regime for in-phase loading. The overestimation of fatigue life by the Brown-Miller parameter can be attributed to the less fatigue damage on the maximum shear plane as shown Figure 5-33. As seen from this figure, the Brown-Miller parameter for in-

phase loading (the bending load, M_b=1300 Nm and the torsion load, M_t=1400 Nm) reaches its maximum value not on the maximum shear strain planes of $\Phi=25^o$ and $\Phi=115^o$ (Figure 5-32), but on the different plane. The Fatemi-Socie parameter predicts higher fatigue damage on the maximum shear strain plane for the same in-phase loading. Fatigue lives estimated by the proposed fatigue damage parameter fall between the Brown-Miller and the Fatemi-Socie parameters (Figure 5-34). Thus, the proposed multiaxial fatigue damage parameter based on the maximum damage plane provides more accurate fatigue predictions in comparison of the Brown-Miller and the Fatemi-Socie parameters.

The life predictions for out-of-phase loading are shown in Figure 5-35. Fatigue damage variations for out-of-phase loading (the bending load, M_b=1295 Nm and the torsion load, M_t=1710 Nm) on various planes are shown in Figure 5-36. As seen from Figure 5-35, the maximum shear plane for this loading is identified as a plane of $\Phi=95^o$, and both the Brown-Miller and Fatemi-Socie parameters predict less fatigue damage on the maximum shear plane (Figure 5-36). Therefore, these fatigue damage parameters yield non-conservative life predictions for out-of-phase loadings in comparison with the proposed damage parameter as shown in Figure 5-37. On the other hand, the proposed fatigue damage parameter estimates greater fatigue damage on the maximum damage plane for the same out-of-phase loading condition and as a result, it shows the better correlation with experimental lives.

As can be seen from Figure 5-38, in case of both in-phase and out-of-phase loadings, correlations of the proposed fatigue damage parameter with experimental fatigue data are within a factor of 3 except a couple points in low and high cycle fatigue

regimes. The proposed fatigue damage parameter clearly provides the best correlations as compared to the Brown-Miller and the Fatemi-Socie parameters. Dan et. al. [90] analyzed the SAE shaft and suggested similar conclusion that the critical plane-based fatigue damage parameters in which critical plane is defined as plane experiencing the maximum damage provide better life estimates than the same critical plane-based fatigue damage parameters in which the critical plane is defined as the maximum shear strain plane.

The multiaxial fatigue analysis incorporating the elastic-plastic stress/strain model and the proposed multiaxial fatigue damage parameter yields satisfactory fatigue life predictions for the SAE notched shaft subjected to bending-torsion proportional and non-proportional loadings. While simple and inexpensive elastic stress histories (linear elastic results of the FE analysis) are used to compute notch root elastic-plastic stress and strain histories, the proposed fatigue damage parameter provides reasonably accurate fatigue life predictions. The proposed multiaxial fatigue analysis methodology demonstrates satisfactory accuracy and reasonable reliability in the multiaxial fatigue assessment of notched components. In addition, the proposed fatigue damage parameter has been applied to the uniaxial loading as the mean stress correction parameter and shows very good correlation with the mean stress fatigue data. Furthermore, the multiaxial fatigue analysis methodology includes the APDL macro for plotting fatigue damage contour for the critical notch area to visualize the fatigue damage map. The damage contour around notch areas for the SAE shaft under in-phase loadings (the bending load, M_b=1400 Nm and the torsion load, M_t=0 Nm, and the bending load, M_b=1150 Nm and the torsion load, M_t=2700 Nm) are shown in Figure 5-39 and Figure 5-40 respectively.

Table 5-1: FEA and Experimental Stress Concentration Factors of SAE 1070 Notched-Bar

	σ_{22}^{e}/σ_n	σ_{33}^{e}/σ_n	σ_{23}^{e}/τ_n
FEA	1.42	0.30	1.15
Experiment	1.41	0.26	1.15

Table 5-2: Monotonic, Cyclic and Fatigue properties of solid specimens for uniaxial mean stress test

Monotonic properties	**Incoloy 901** [83]	**7075-T651** [84]	**ASTM A723** [82]	**SAE 1045HRC** [85]
Yield strength, σ_y	958 MPa	501 MPa	1170 MPa	1713 MPa
Ultimate strength, σ_u	1200 MPa	561 MPa	1262 MPa	2165 MPa
Modulus of elasticity, E	202 GPa	71.7 GPa	200 GPa	205 GPa
Strength coefficient, K	1615 MPa	-	1483 MPa	3088 MPa
Strain hardening exponent, n	0.101	-	0.037	0.092
Reduction in area, RA	15 %	29.1 %	50 %	38 %
Cyclic and fatigue properties				
Fatigue strength coefficient, σ'_f	1977 MPa	1576 MPa	2123 MPa	3372 MPa
Fatigue strength exponent, b	-0.1228	-0.1609	-0.110	-0.103
Fatigue ductility coefficient, ε'_f	0.125	0.1575	0.49	0.038
Fatigue ductility exponent, c	-0.6478	-0.6842	-0.783	-0.47
Cyclic strength coefficient, K'	1566 MPa	747 MPa	1581 MPa	3082 MPa
Cyclic strain hardening exponent, n'	0.09	0.0597	0.071	0.075

Table 5-3: Monotonic, Cyclic and Fatigue properties of tubular specimens

Material		**1045**[86]	**Inconel 718**[87]
Monotonic material properties	E (MPa)	205000	208500
	ν	0.29	0.3
	σ_{ys} (MPa)	380	1160
Cyclic stress-strain curve	K'(MPa)	1258	1530
	n'	0.208	0.073
Strain-life curve	σ'_f (MPa)	980	1640
	b	-0.11	-0.060
	ε'_f	0.20	2.67
	c	-0.43	-0.82

Table 5-4: SAE 1045 notched shaft, in-phase test

Bending moment, M_b (Nm)	Torsion moment, M_t (Nm)	M_t/M_b	Life cycle, N_f					
			IL	IL	JD	BC	RN	AOS
1400	0	0.00	4,494,000					
1460	0	0.00						430,000
1475	0	0.00			464,000			230,000
1708	0	0.00						163,800
1730	0	0.00	60,000	49,200			30,000	130,000
1875	0	0.00			41,360	55,000		
2586	0	0.00						14,000
2600	0	0.00	3,000		8,111			7,930
2800	0	0.00			2,571			
1680	900	0.54			84,950			
1680	960	0.57				30,000		
2325	1350	0.58	2,810	3,000				
1250	800	0.64					325,000	
1550	1090	0.70	80,000	97,500				
1250	880	0.70	600,000					
1720	1350	0.78	17,070	212,450				
1150	1090	0.95	2,294,000	2,381,000				
920	880	0.96	3,473,000					
2000	2100	1.05			5,998			
1300	1400	1.08			84,680			
1850	2100	1.14	6,700				4,780	
1850	2550	1.38	2,200					
1220	1710	1.40	72,000		107,500		60,800	
990	1390	1.40	933,000				350,000	
1355	2550	1.88	5,500					
725	1390	1.92	200,000					
845	1800	2.13			259,900			
1250	2700	2.16			6,402			
1150	2700	2.35	3,000					
780	2180	2.79	70,000	70,680				
840	2700	3.21	100,000	9,000				
570	2180	3.82	76,100	99,560				
460	1760	3.83	3,027,000	2,350,000				
80	2534	31.68						
0	1500	∞			1,515,000			
0	1700	∞			2,324,000			
0	2000	∞	1,584,000				750,000	
0	2400	∞	75,700			65,000		
0	3000	∞	7,000		4,057			

IL - University of Illinois, JD - Jonn & Co., BC - Battelle Columbus Lab., RN - Rexnord Corp., AOS - A. O. Smith Corp.

Table 5-5: SAE 1045 notched shaft, out of-phase test

Bending moment, M_b (Nm)	Torsion moment, M_t (Nm)	M_t/M_b	Life cycle, N_f					
			IL	IL	JD	BC	RN	AOS
2300	1325	0.58			17,720			
1850	2100	1.14			12,660			
1800	2100	1.17			21,600			
1698	2242	1.32				6,725		
1295	1710	1.32				25,580		
1220	1710	1.40			157,500			
1220	1710	1.40			173,300			
985	1400	1.42			1000000			
1150	2700	2.35			10,600			
770	2180	2.83			151,900			

IL - University of Illinois, JD - Jonn & Co., BC - Battelle Columbus Lab., RN - Rexnord Corp., AOS - A. O. Smith Corp.

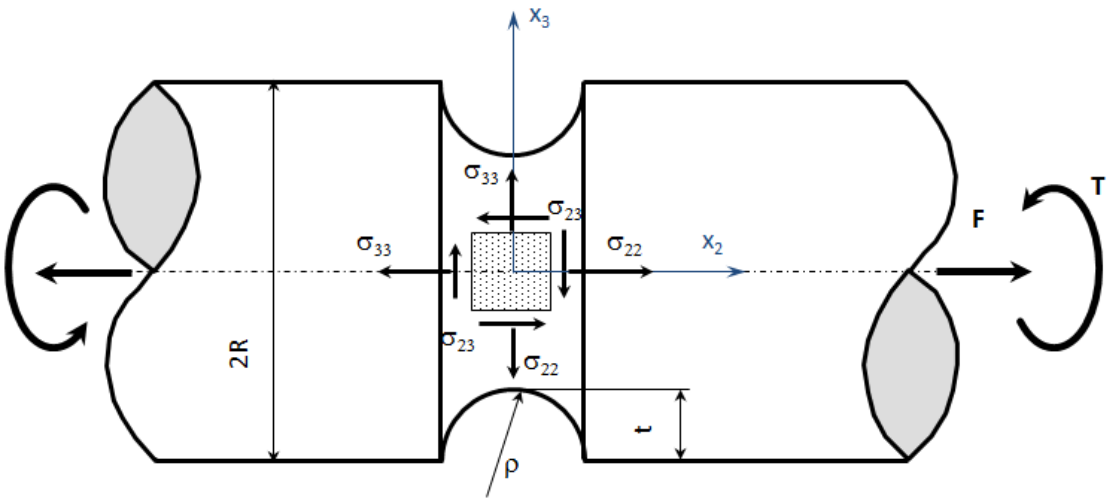

Figure 5-1: Geometry and stress state of SAE 1070 steel notched-shaft

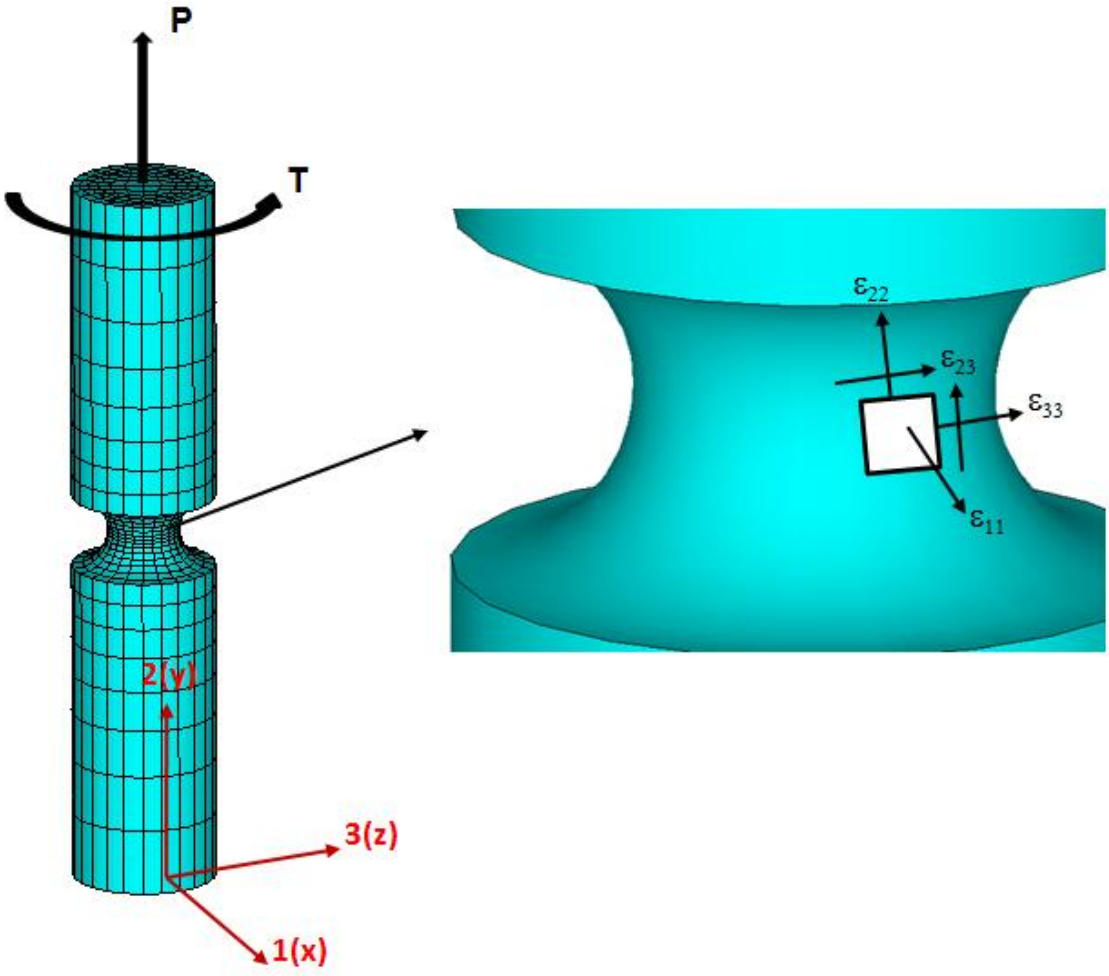

Figure 5-2: FEA model and strain state for SAE 1070 steel notched specimen

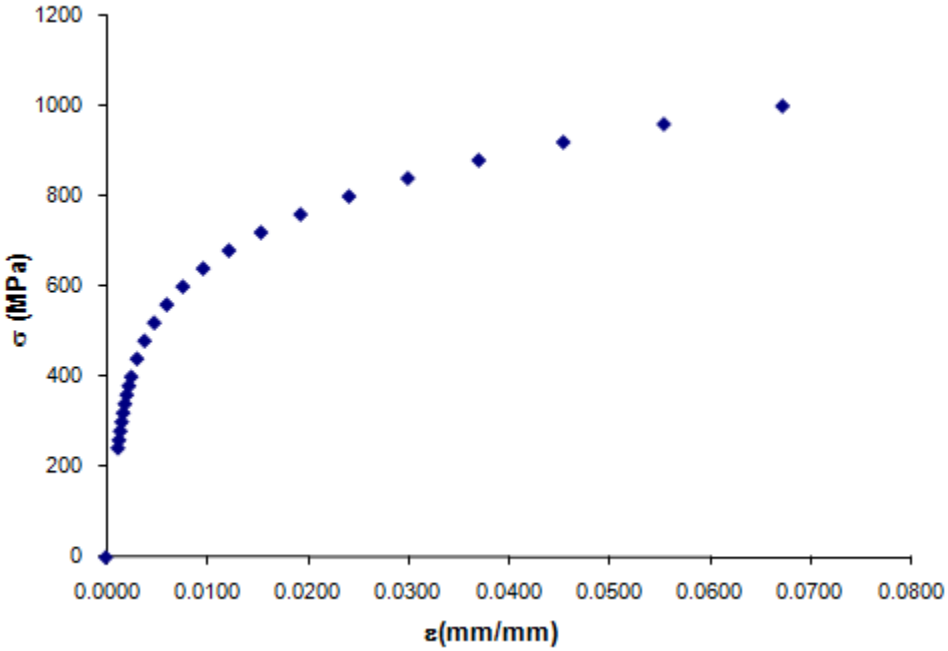

Figure 5-3: Discretization of SAE 1070 cyclic stress-strain curve

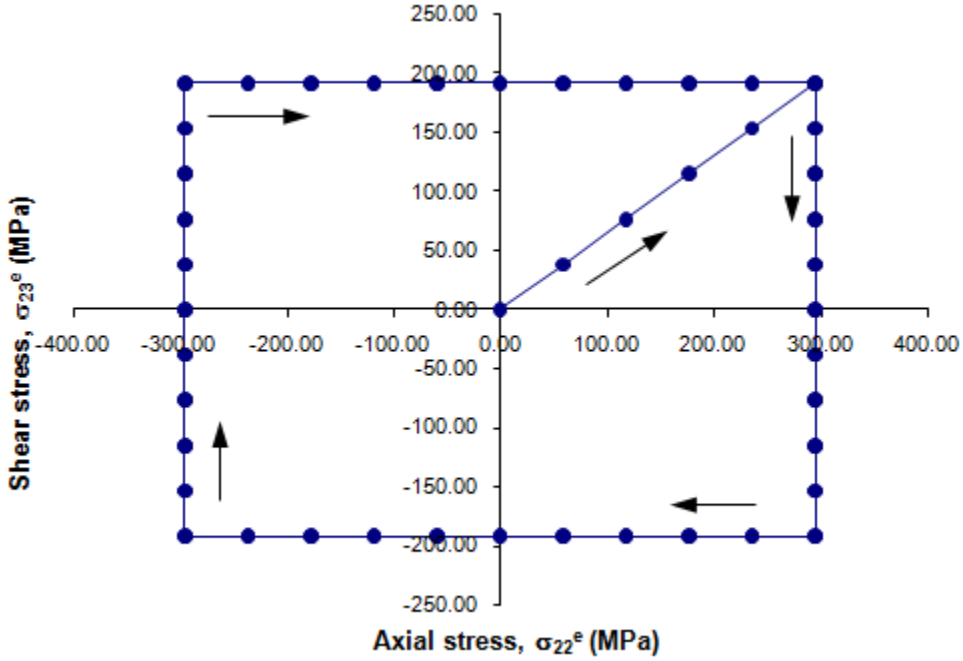

Figure 5-4: Box cyclic stress/load path - clockwise

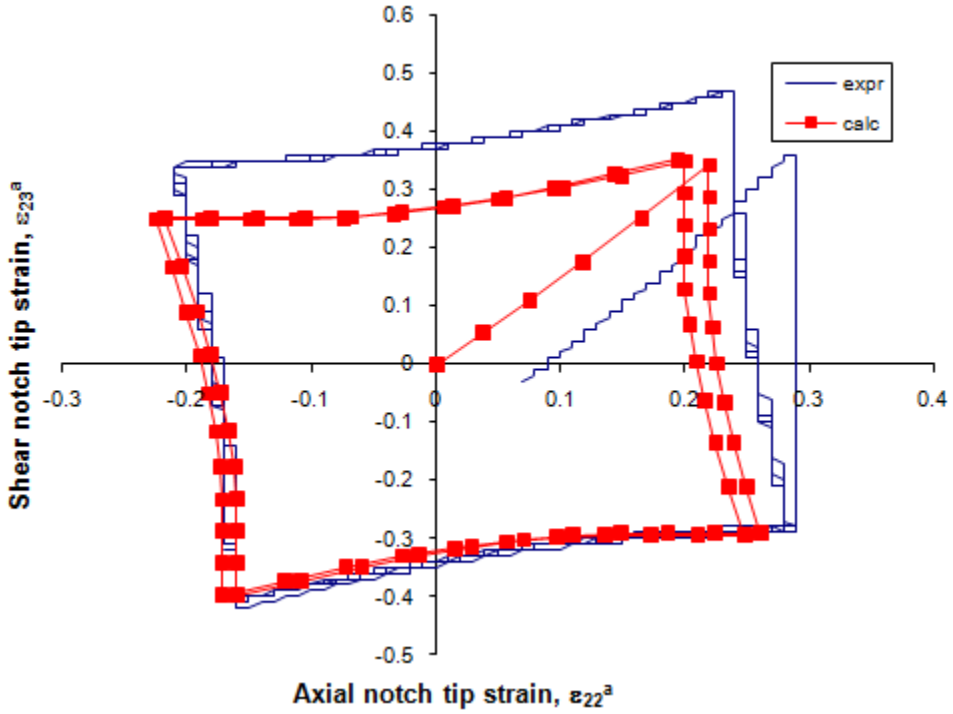

Figure 5-5: Experimental and calculated strain paths in the notch tip induced by the box input loading path - clockwise

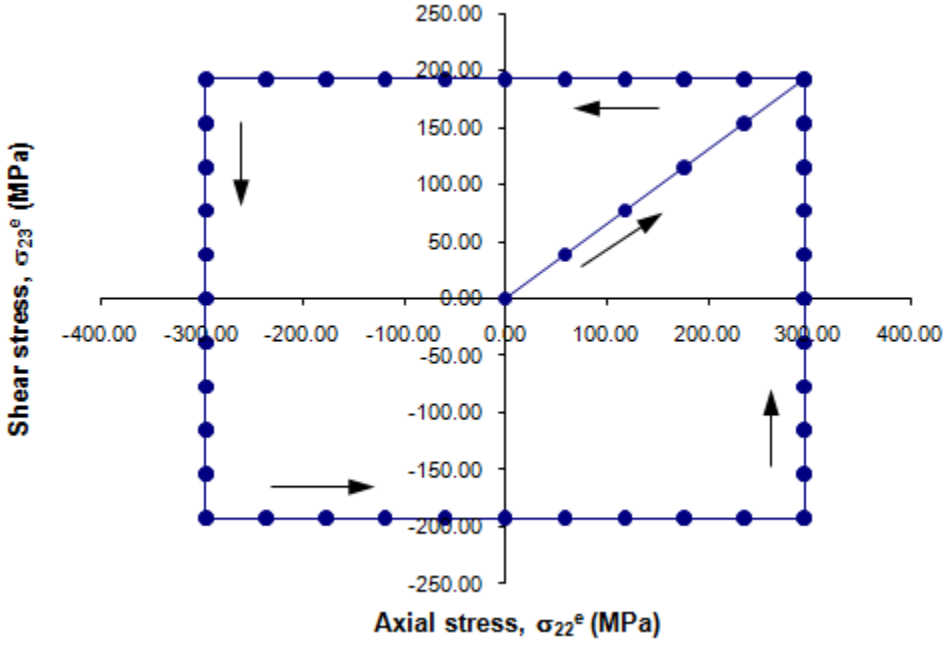

Figure 5-6: Box cyclic stress/load path – counter clockwise

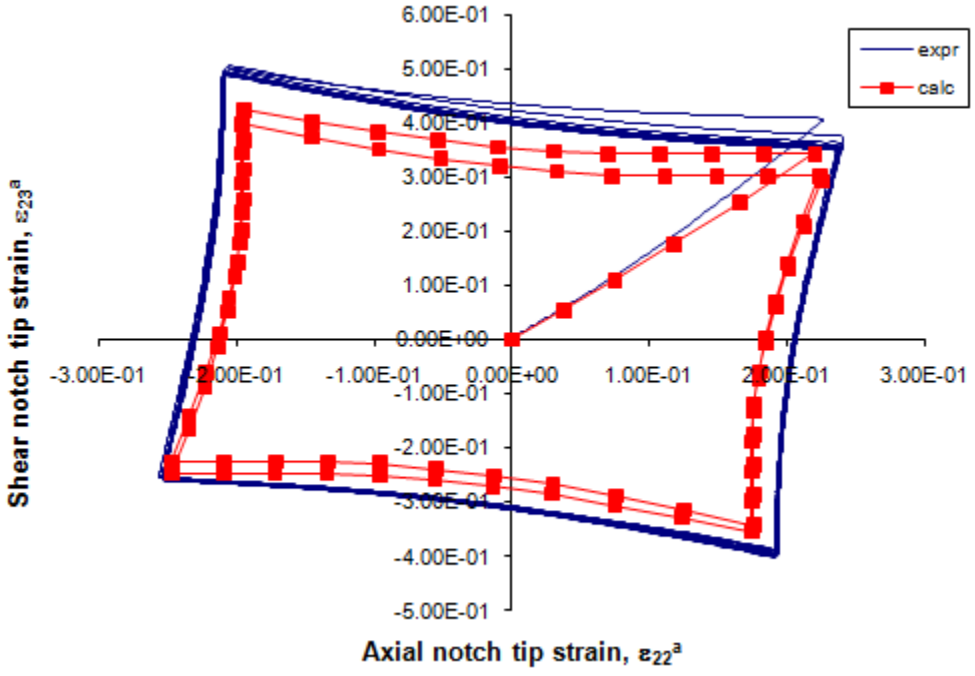

Figure 5-7: Experimental and calculated strain paths in the notch tip induced by the box input loading path – counter clockwise

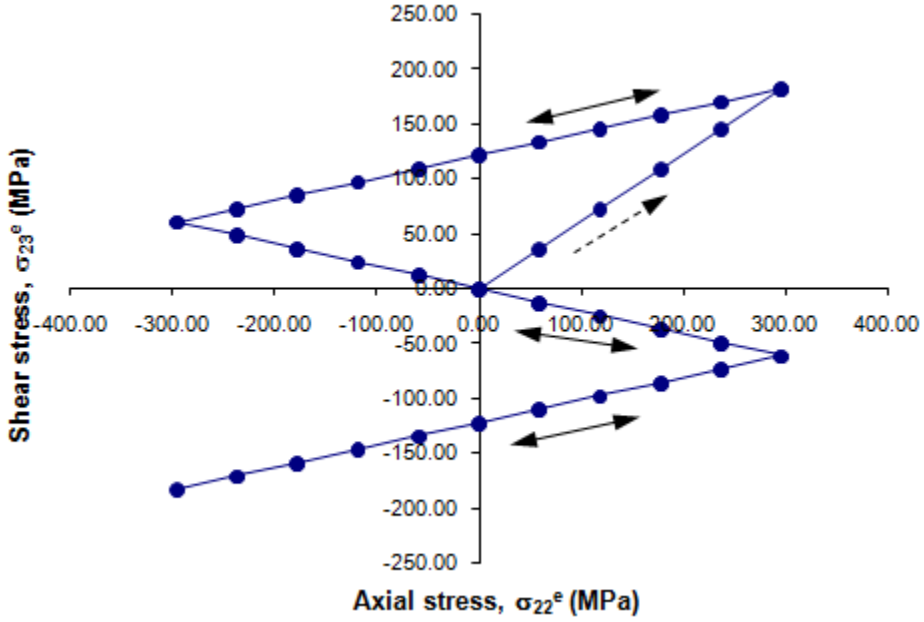

Figure 5-8: Unequal frequency (ratio 3:1) tension-torsion stress/loading path

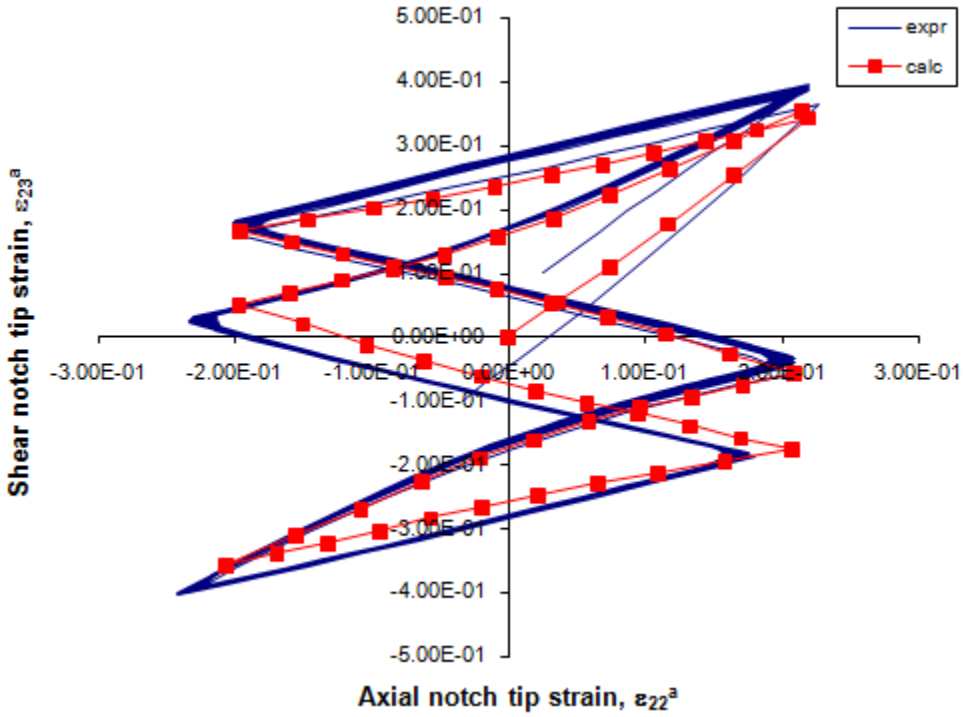

Figure 5-9: Experimental and calculated strain paths in the notch tip induced by the unequal frequency (ratio 3:1) tension-torsion input loading path

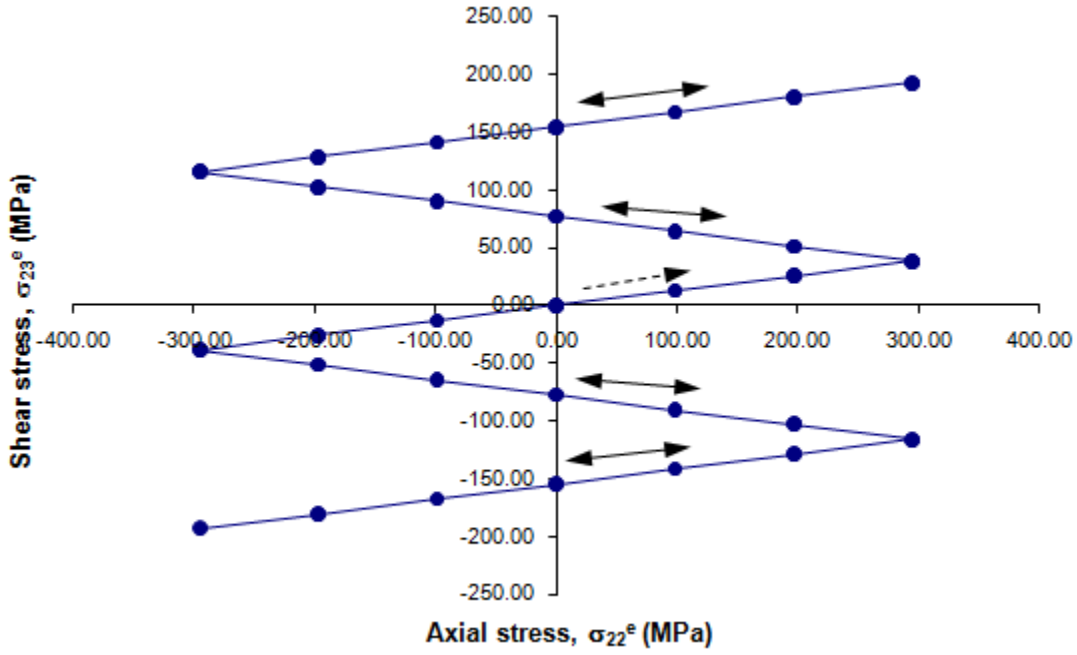

Figure 5-10: Unequal frequency (ratio 5:1) tension-torsion stress/loading path

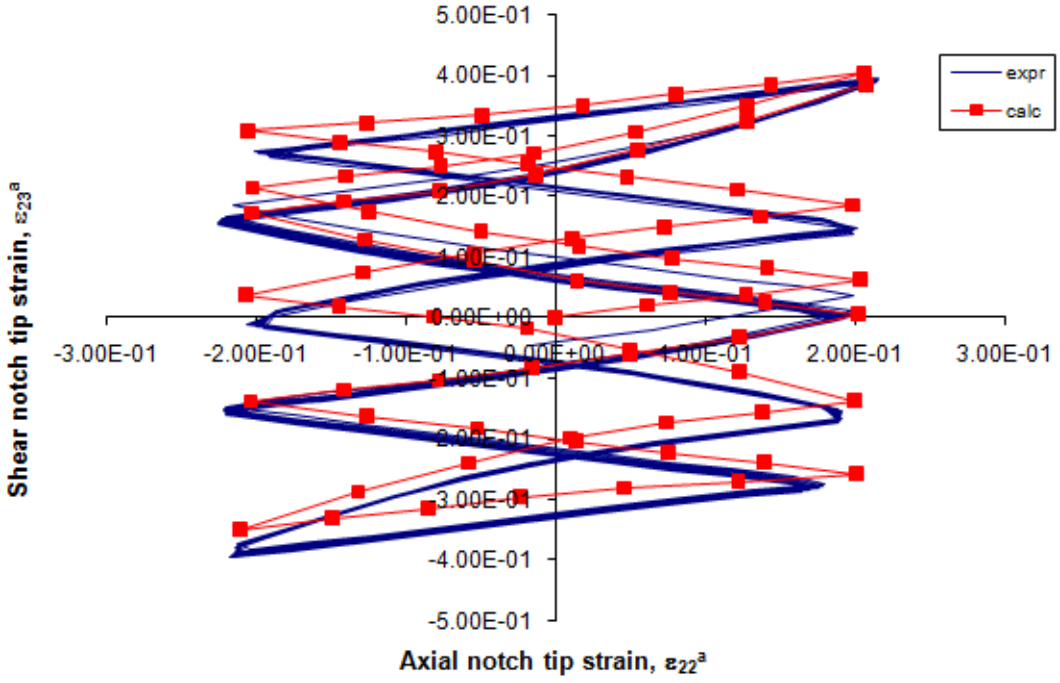

Figure 5-11: Experimental and calculated strain paths in the notch tip induced by the unequal frequency (ratio 5:1) tension-torsion input loading path

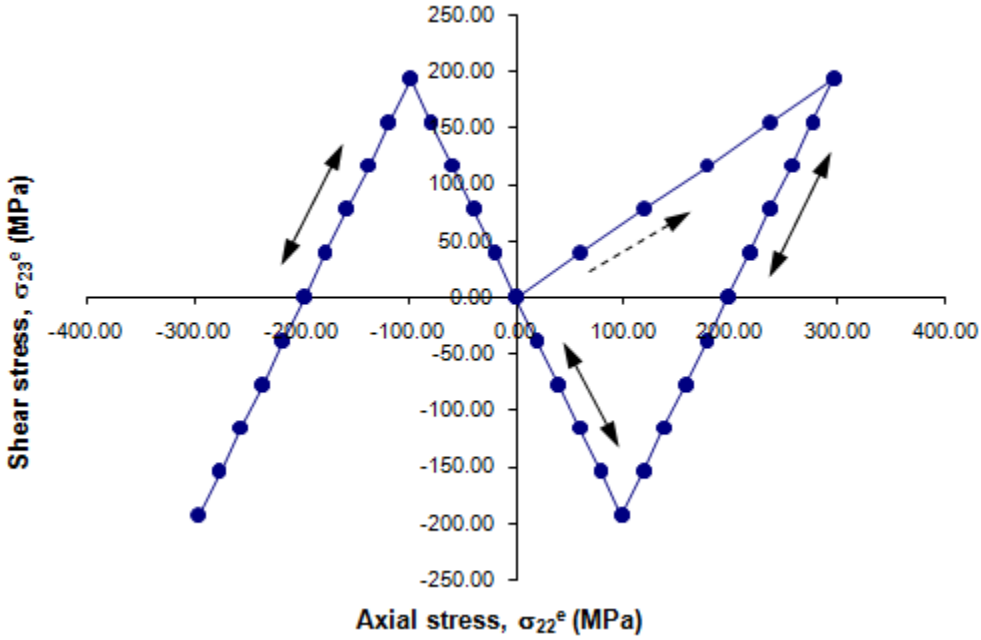

Figure 5-12: Unequal frequency (ratio 1:3) tension-torsion stress/loading path

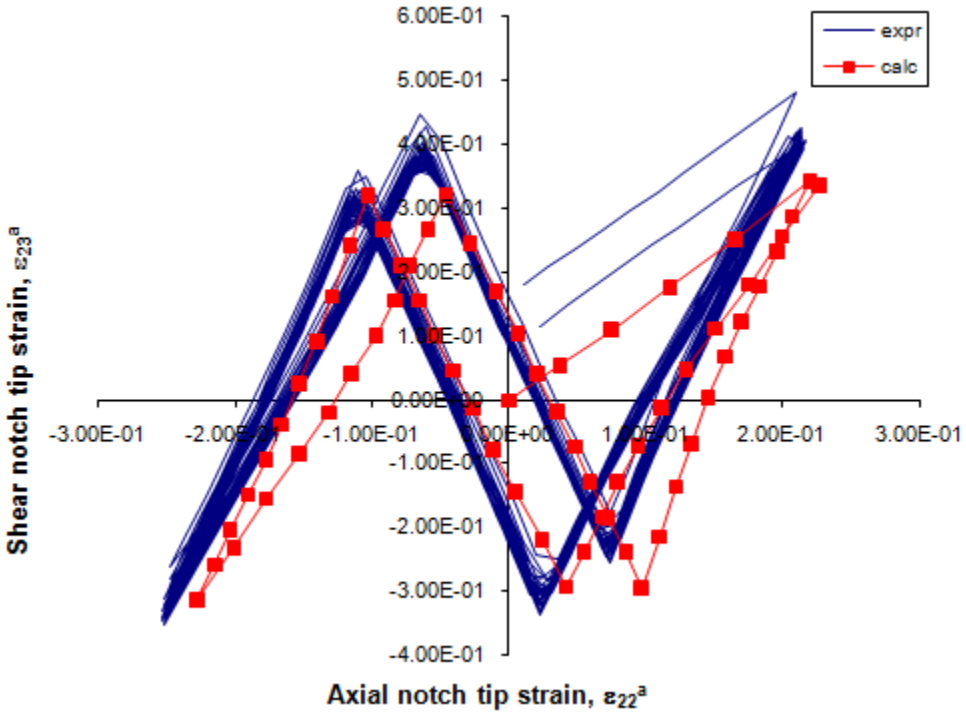

Figure 5-13: Experimental and calculated strain paths in the notch tip induced by the unequal frequency (ratio 1:3) tension-torsion input loading path

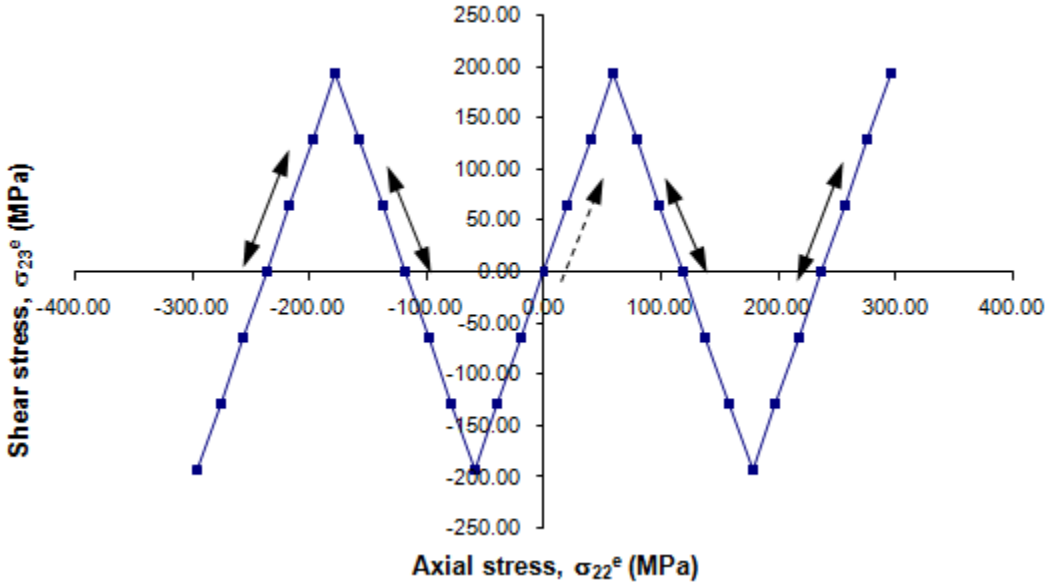

Figure 5-14: Unequal frequency (ratio 1:5) tension-torsion stress/loading path

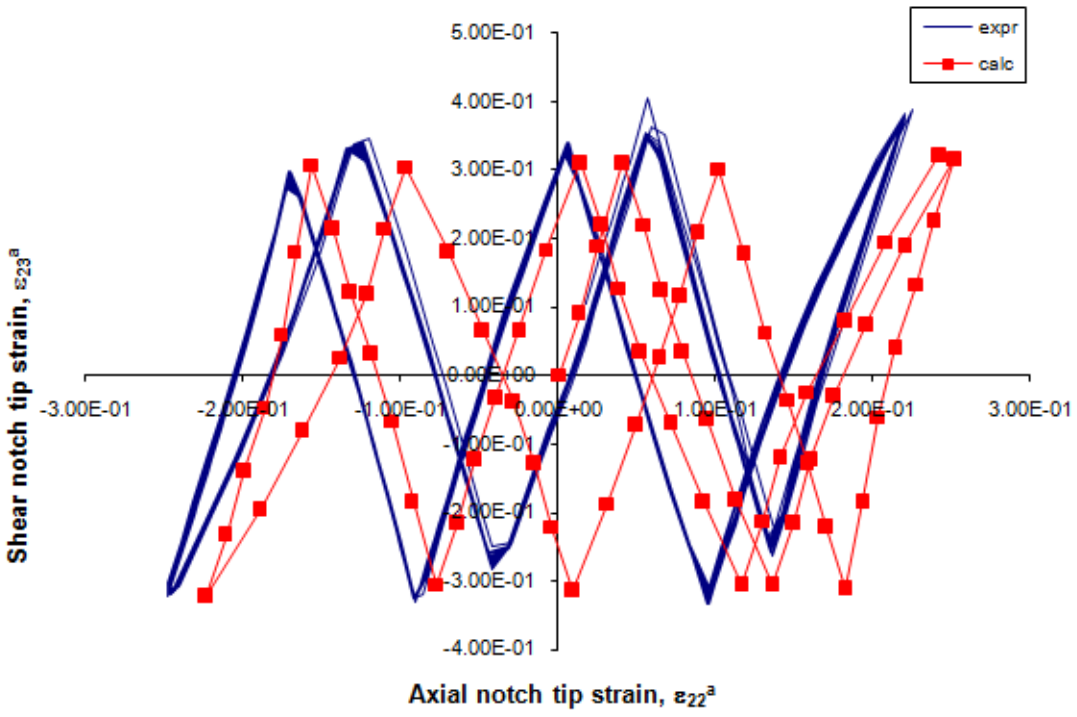

Figure 5-15: Experimental and calculated strain paths in the notch tip induced by the unequal frequency (ratio 1:5) tension-torsion input loading path

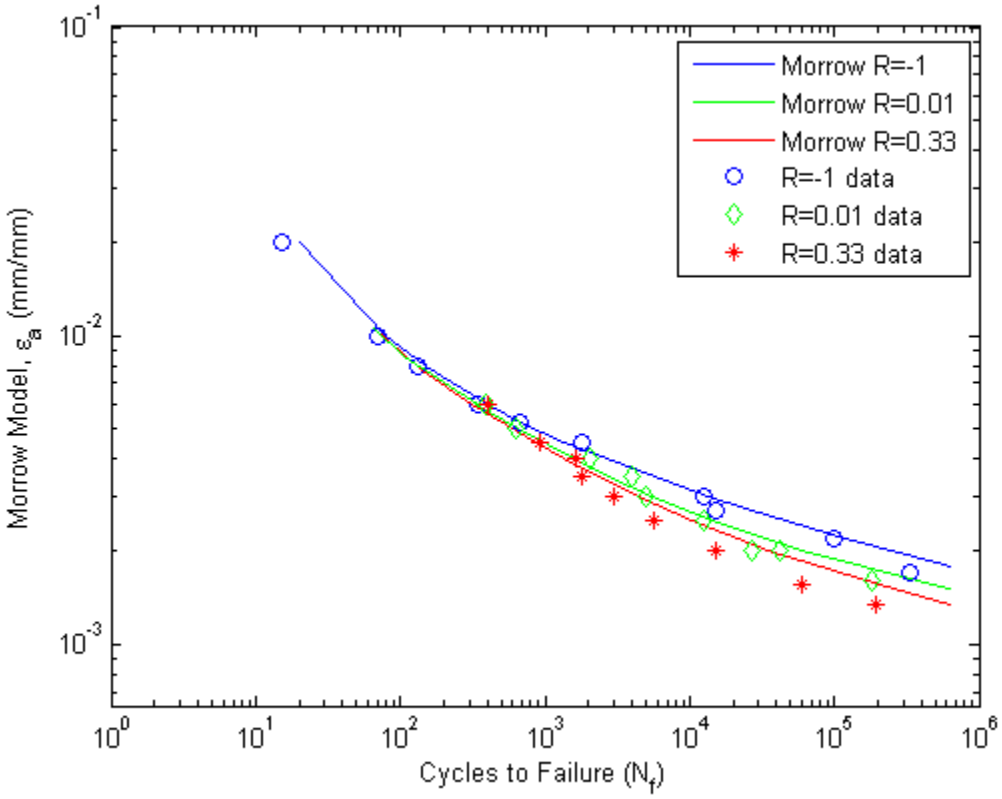
Morrow R=-1
Morrow R=0.01
Morrow R=0.33
R=-1 data
R=0.01 data
R=0.33 data
Morrow Model, ε_a (mm/mm)
Cycles to Failure (N_f)

(a)

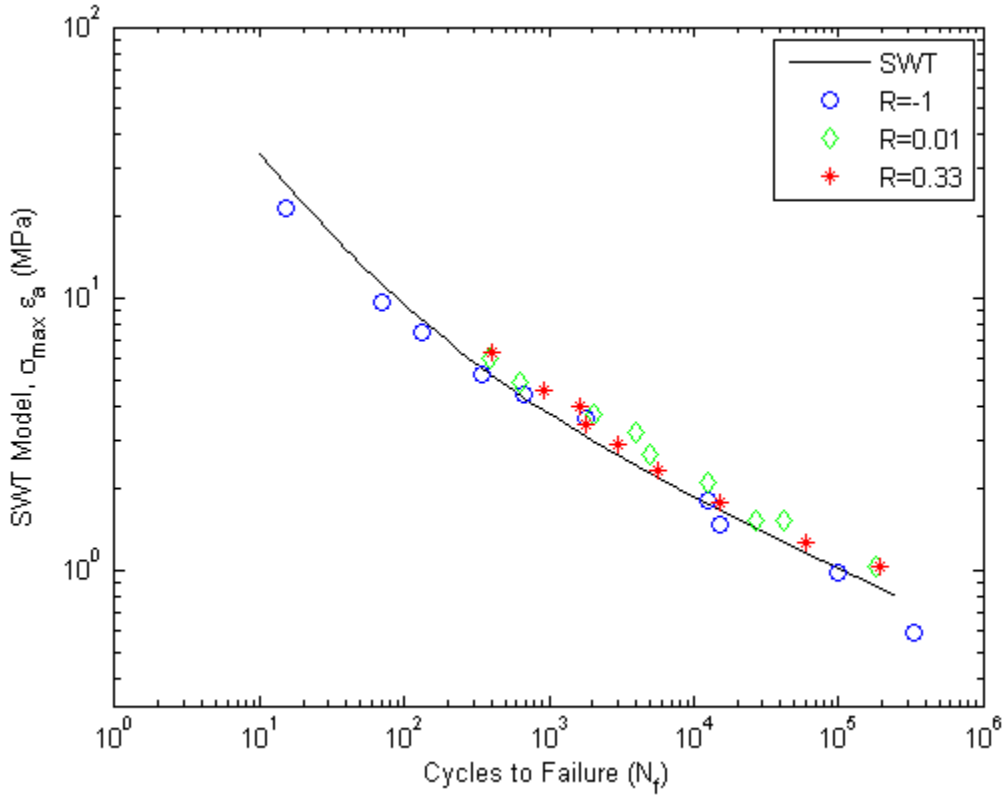
SWT
R=-1
R=0.01
R=0.33
SWT Model, σ_{max} ε_a (MPa)
Cycles to Failure (N_f)

(b)

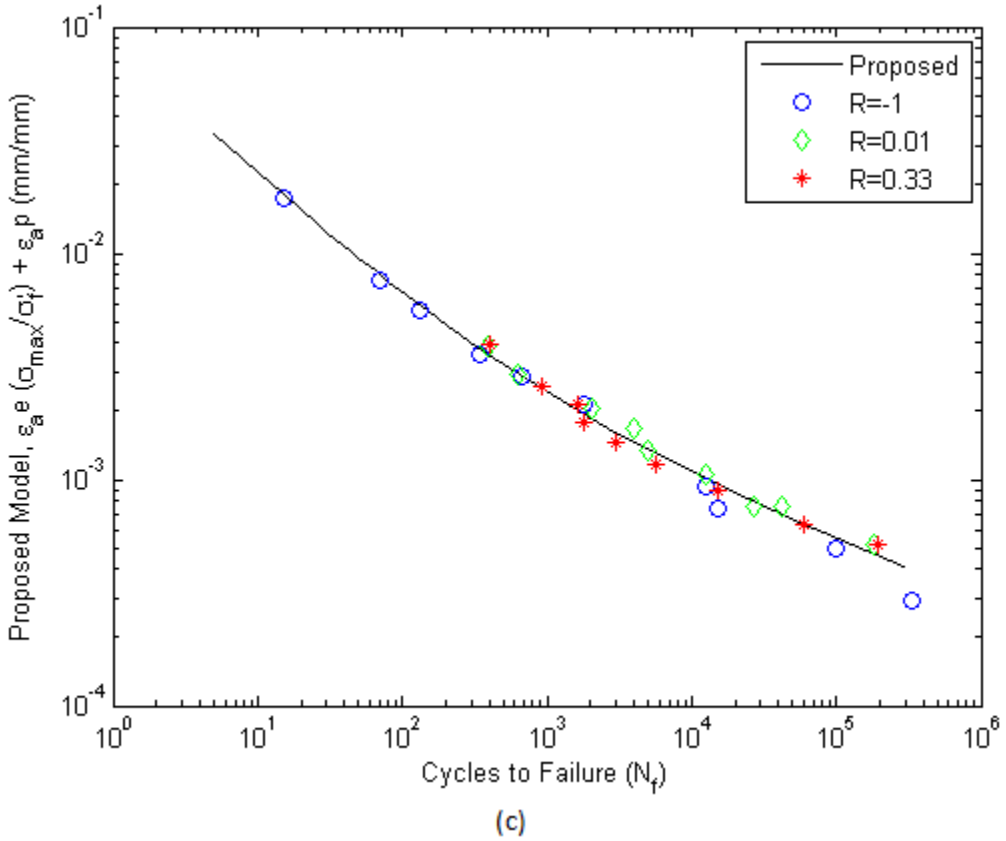

Figure 5-16: Comparison of Morrow parameter (a), SWT parameter (b) and Proposed fatigue damage parameter (c) for various strain ratios with experimental fatigue data of Incoloy 901

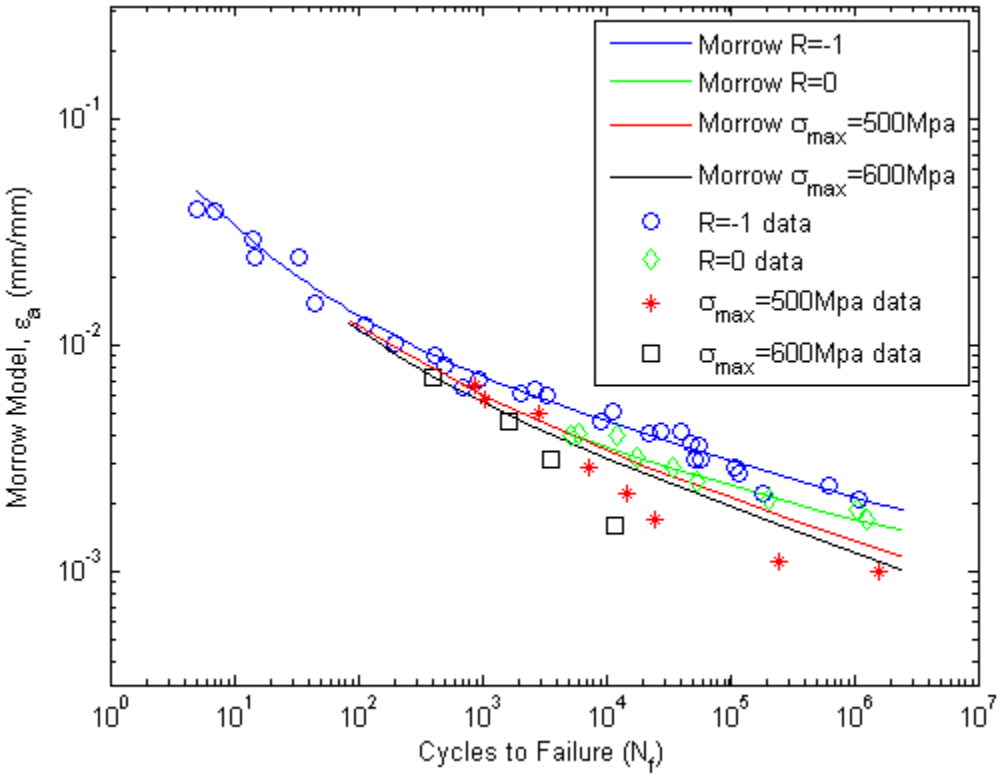
Morrow R=-1
Morrow R=0
Morrow σmax=500Mpa
Morrow σmax=600Mpa
R=-1 data
R=0 data
σmax=500Mpa data
σmax=600Mpa data
Morrow Model, εa (mm/mm)
Cycles to Failure (Nf)

(a)

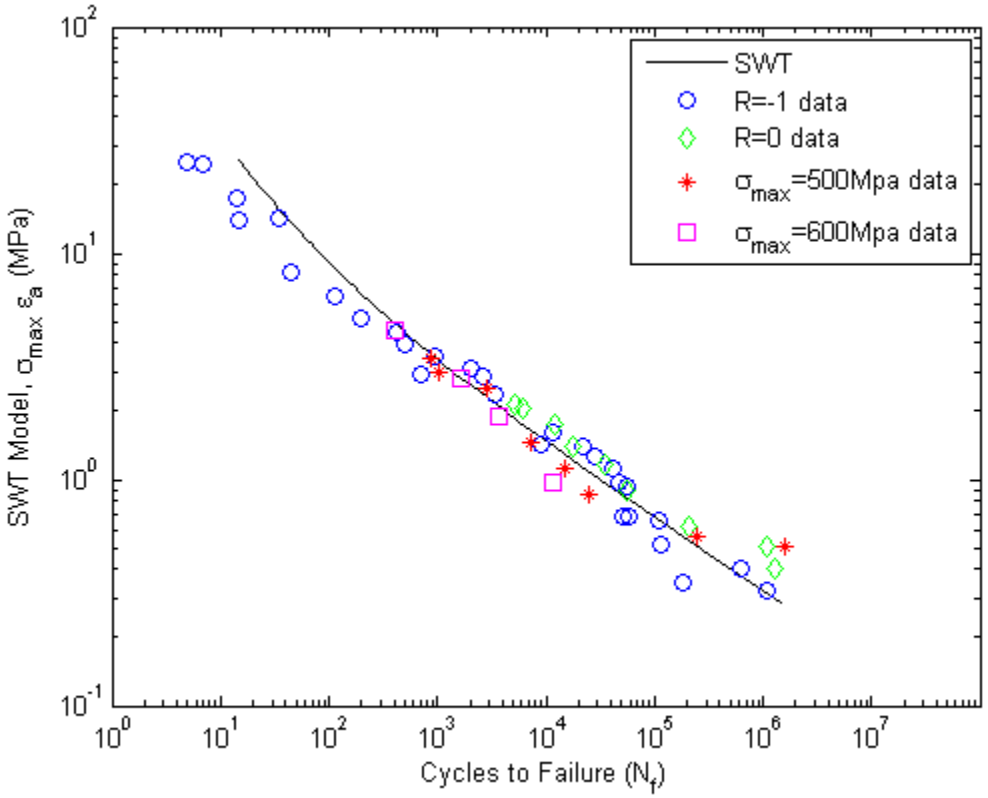
SWT
R=-1 data
R=0 data
σmax=500Mpa data
σmax=600Mpa data
SWT Model, σmax εa (MPa)
Cycles to Failure (Nf)

(b)

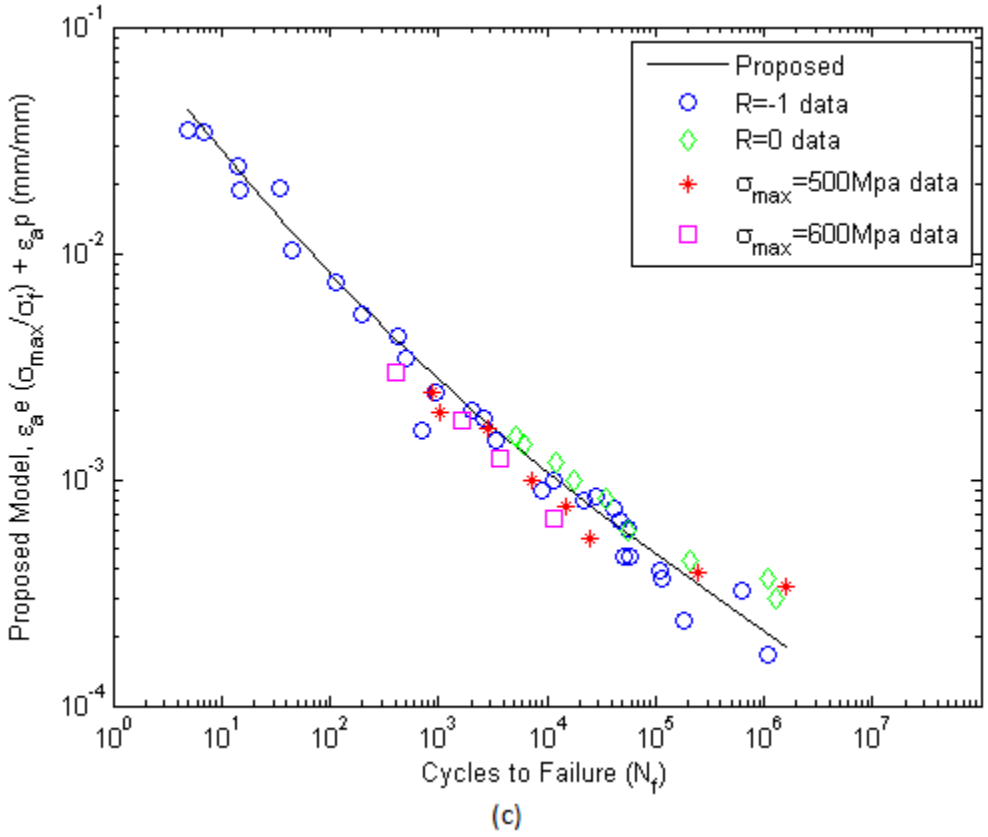

Figure 5-17: Comparison of Morrow parameter (a), SWT parameter (b) and Proposed fatigue damage parameter (c) for various strain ratios with experimental fatigue data of 7075-T651

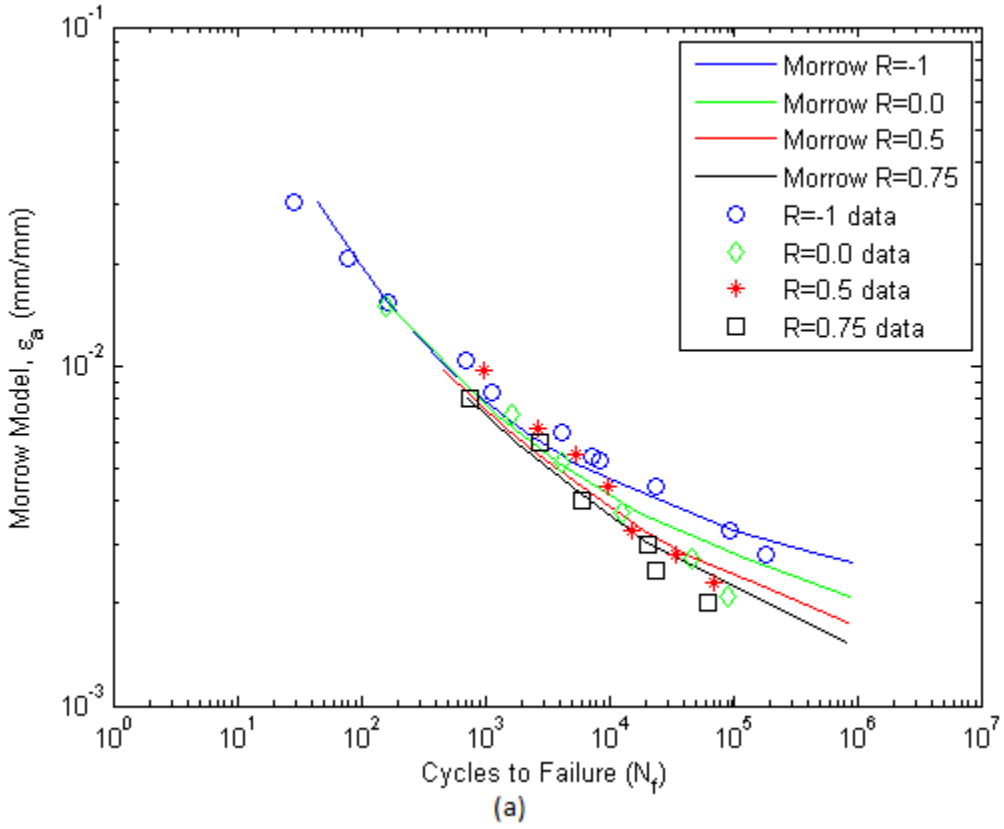
Morrow R=-1
Morrow R=0.0
Morrow R=0.5
Morrow R=0.75
R=-1 data
R=0.0 data
R=0.5 data
R=0.75 data
Morrow Model, ε_a (mm/mm)
Cycles to Failure (N_f)

(a)

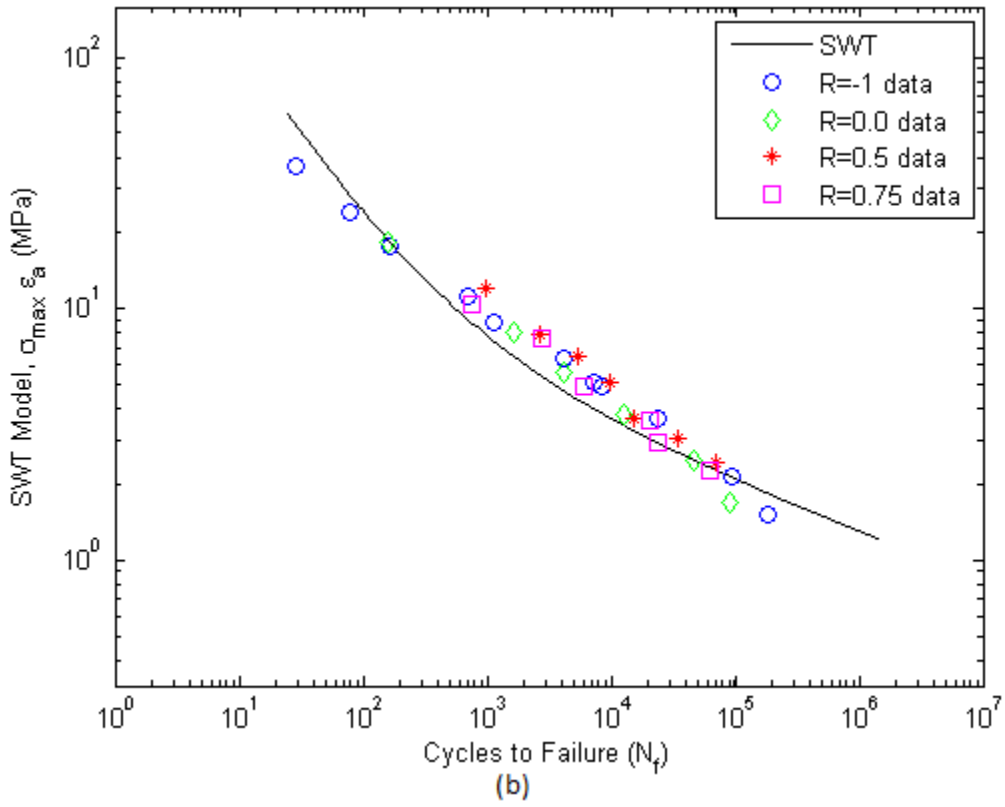
SWT
R=-1 data
R=0.0 data
R=0.5 data
R=0.75 data
SWT Model, σ_{max} ε_a (MPa)
Cycles to Failure (N_f)

(b)

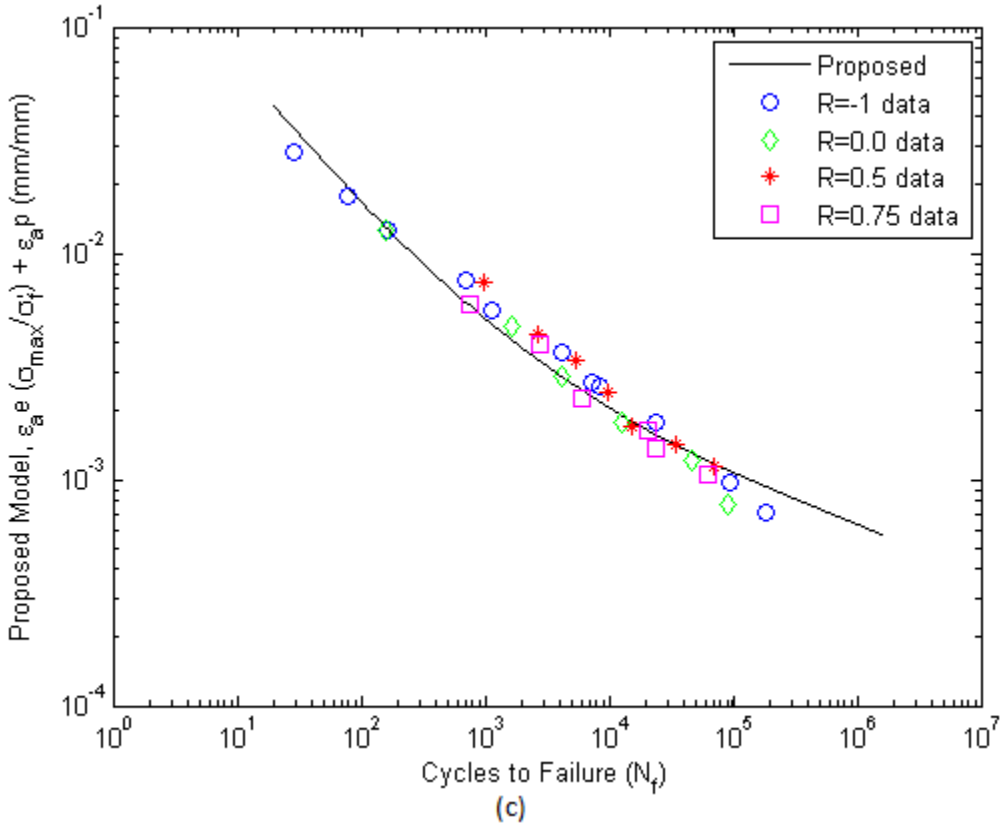

Figure 5-18: Comparison of Morrow parameter (a), SWT parameter (b) and Proposed fatigue damage parameter (c) for various strain ratios with experimental fatigue data of ASTM A723

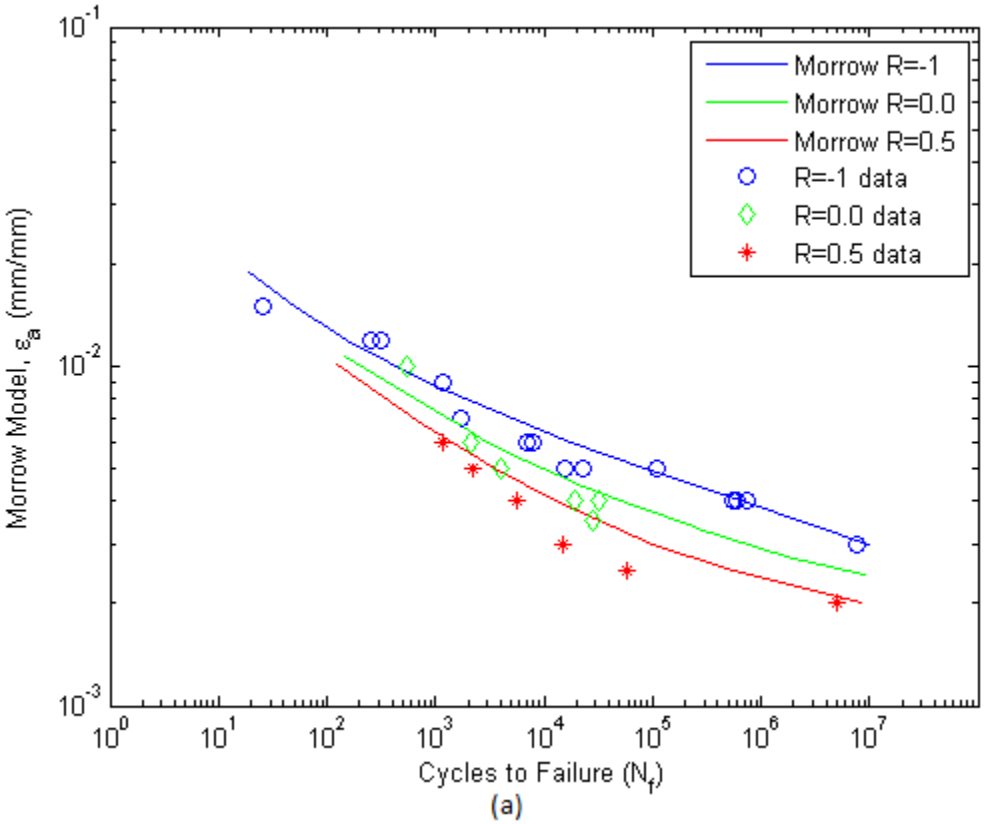
Morrow R=-1
Morrow R=0.0
Morrow R=0.5
R=-1 data
R=0.0 data
R=0.5 data
Morrow Model, ε_a (mm/mm)
Cycles to Failure (N_f)

(a)

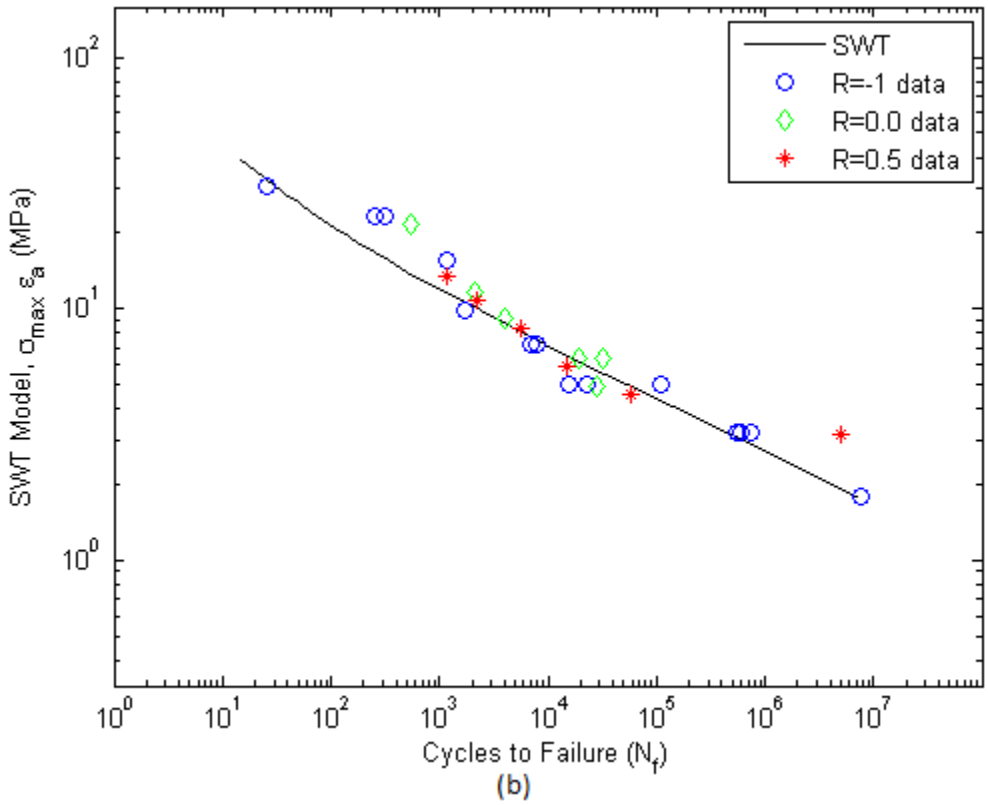
SWT
R=-1 data
R=0.0 data
R=0.5 data
SWT Model, σ_{max} ε_a (MPa)
Cycles to Failure (N_f)

(b)

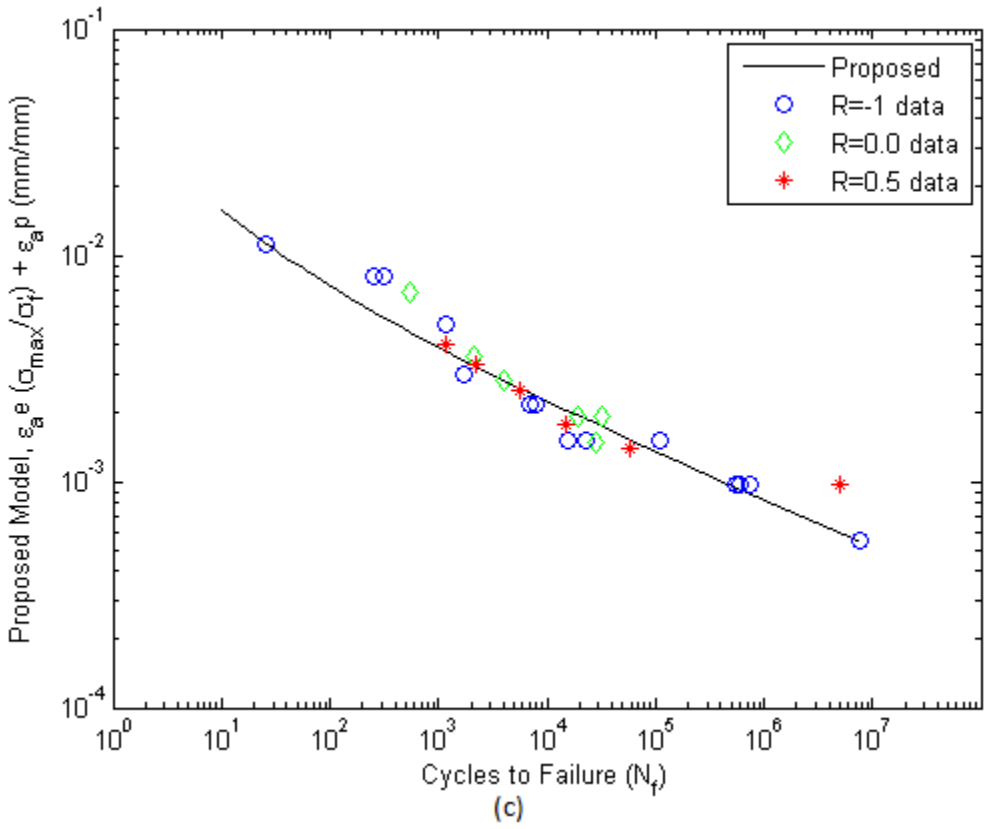

Figure 5-19: Comparison of Morrow parameter (a), SWT parameter (b) and Proposed fatigue damage parameter (c) for various strain ratios with experimental fatigue data of 1045 HRC55

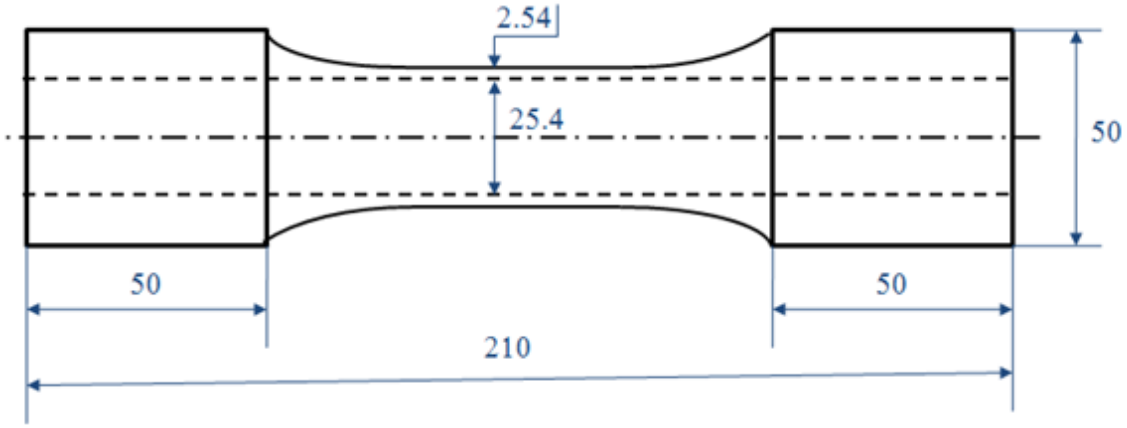

Figure 5-20: Geometry and dimensions of 1045 HR tubular specimens [86]. All dimensions in mm

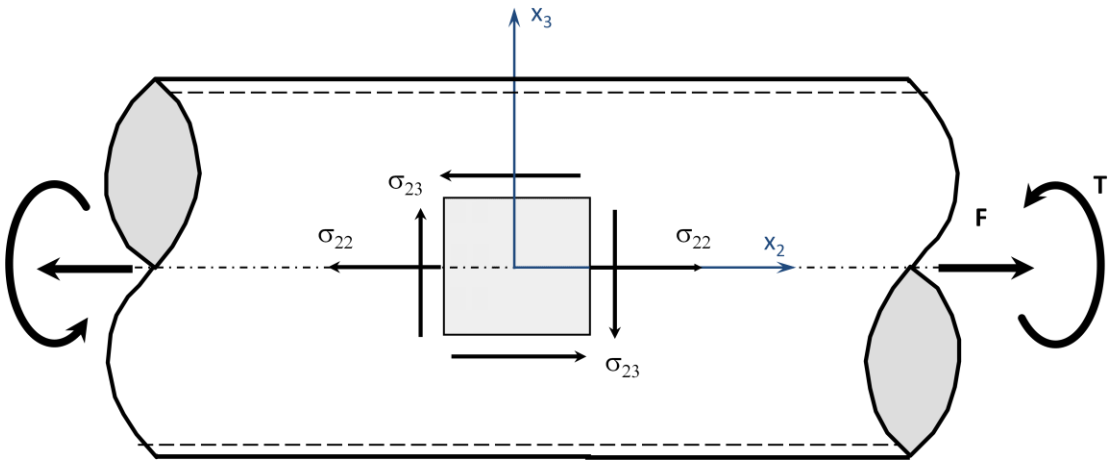

Figure 5-21: System of coordinate for the tubular specimen and the applied stress components σ_{ij}

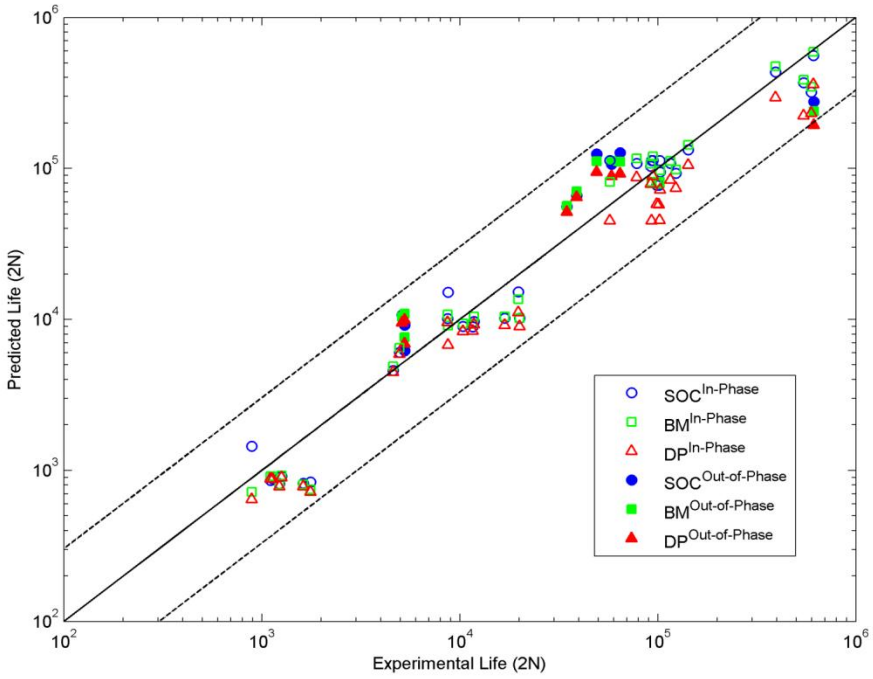

Figure 5-22: Comparison of Proposed Damage Parameter (DP), Fatemi-Socie (FS) and Brown-Miller (BM) parameter with experimental fatigue data of 1045 steel

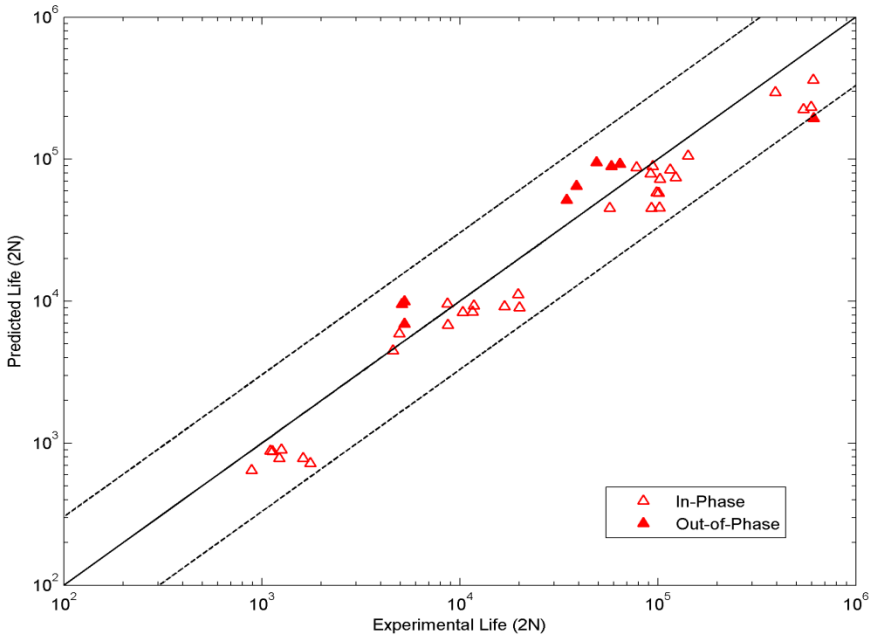

Figure 5-23: Comparison of Proposed Damage Parameter with in-phase and out-of-phase experimental fatigue data of 1045 steel

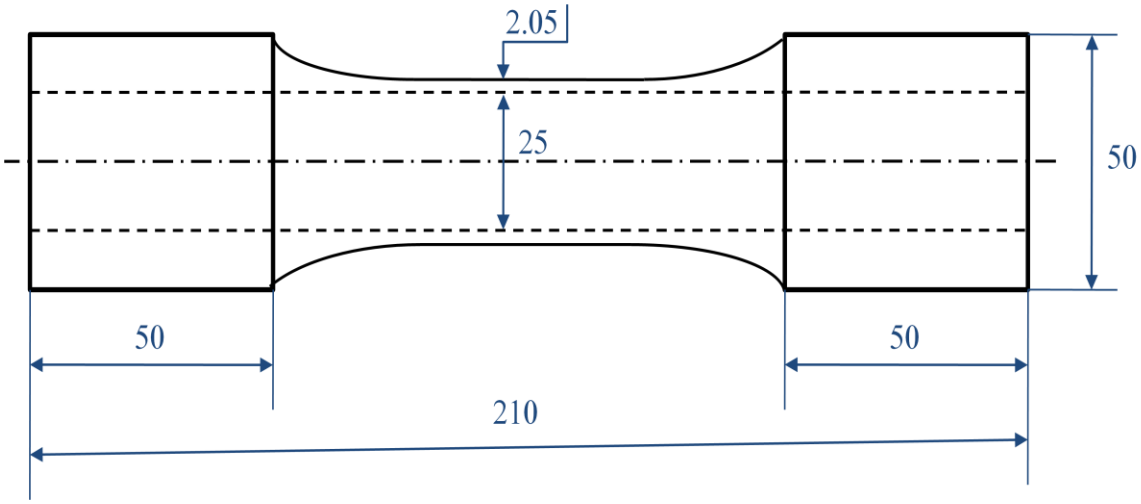

Figure 5-24: Geometry and dimensions of Inconel 718 tubular specimens [87]. All dimensions in mm

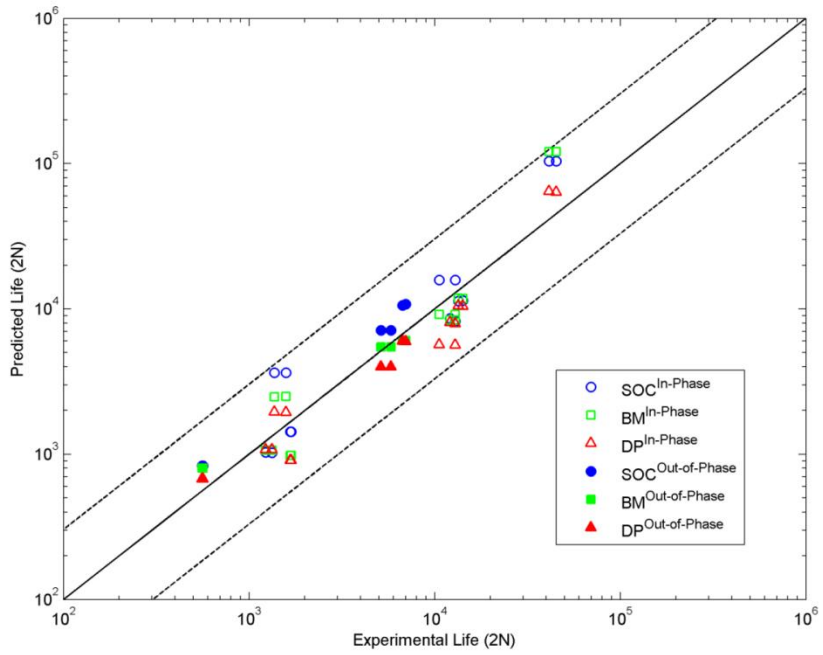

Figure 5-25: Comparison of Proposed Damage Parameter (DP), Fatemi-Socie (FS) and Brown-Miller (BM) parameter with experimental fatigue data of Inconel 718

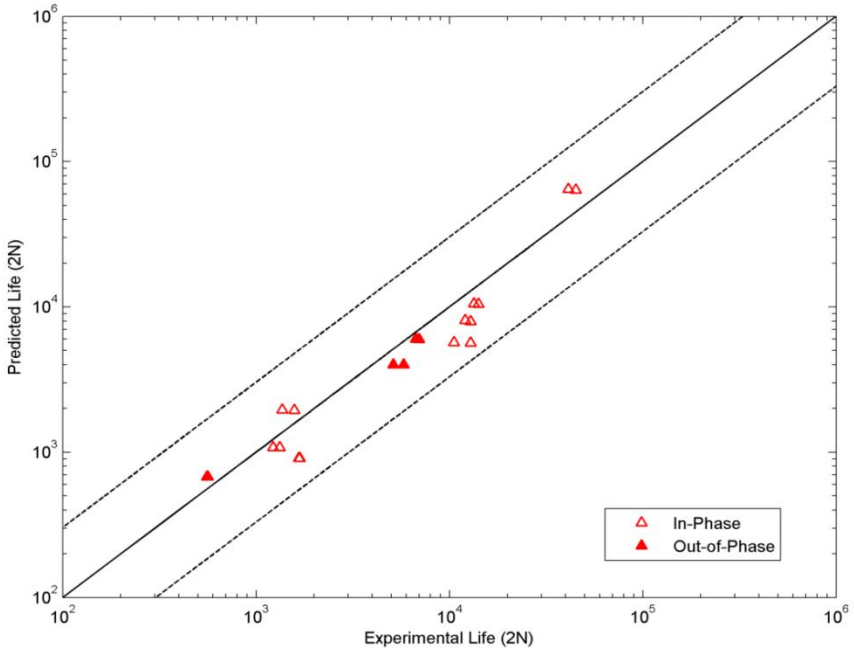

Figure 5-26: Comparison of Proposed Damage Parameter with in-phase and out-of-phase experimental fatigue data of Inconel 718

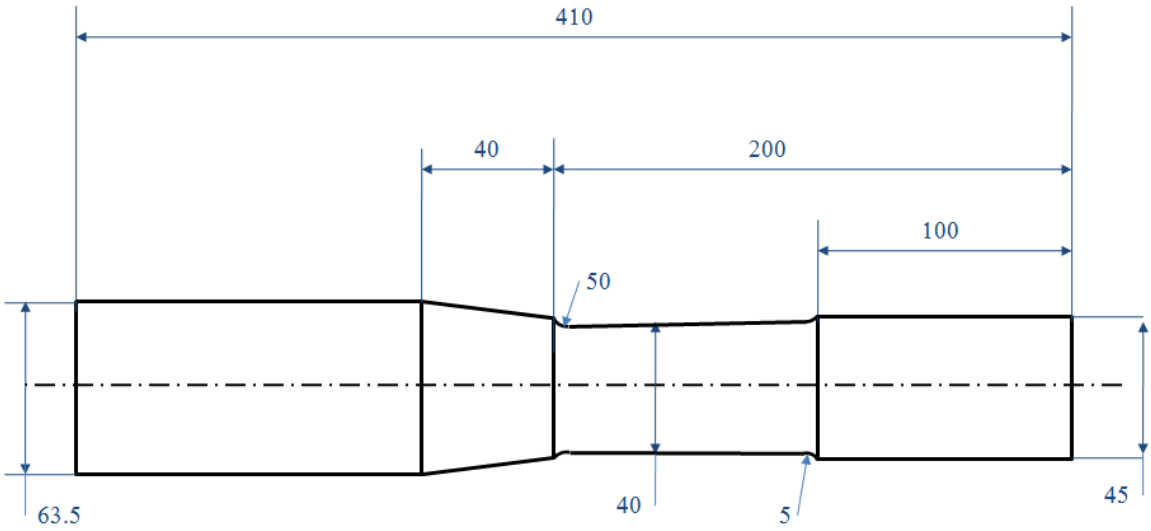

Figure 5-27: Geometry and dimensions of the SAE shaft [88], all dimensions in mm

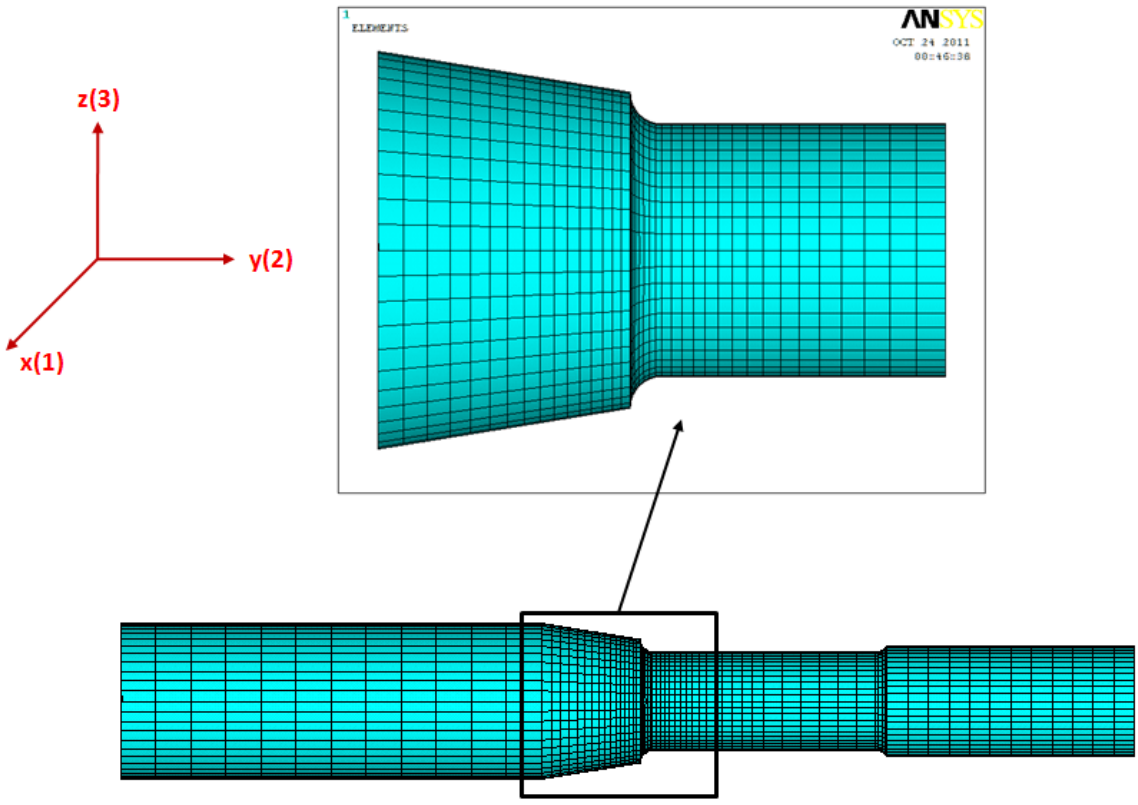

Figure 5-28: FEA model of the SAE shaft and refined mesh at notch region

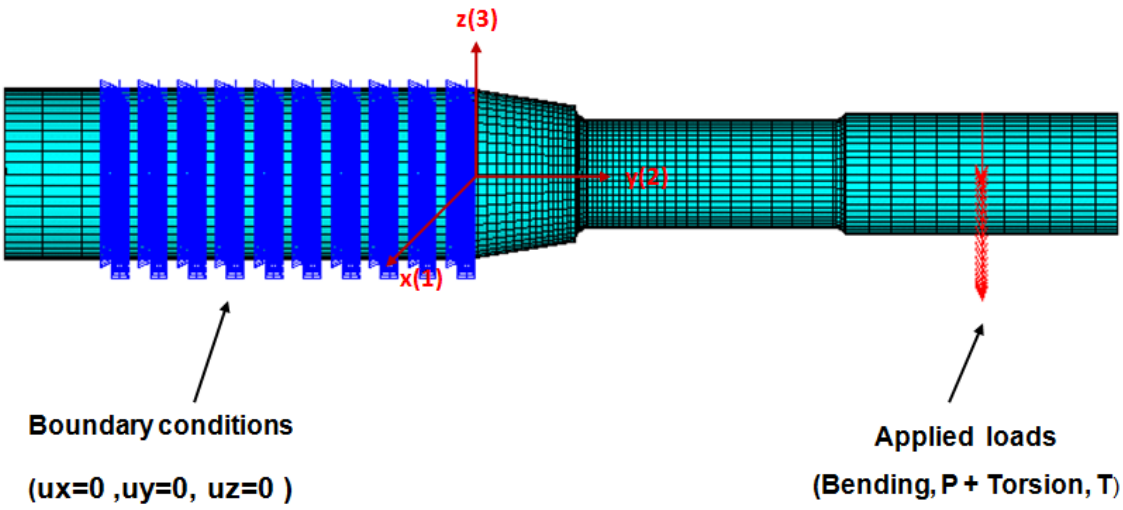

Figure 5-29: Boundary conditions and applied combined loads (bending and torsion) on the SAE shaft FEA model

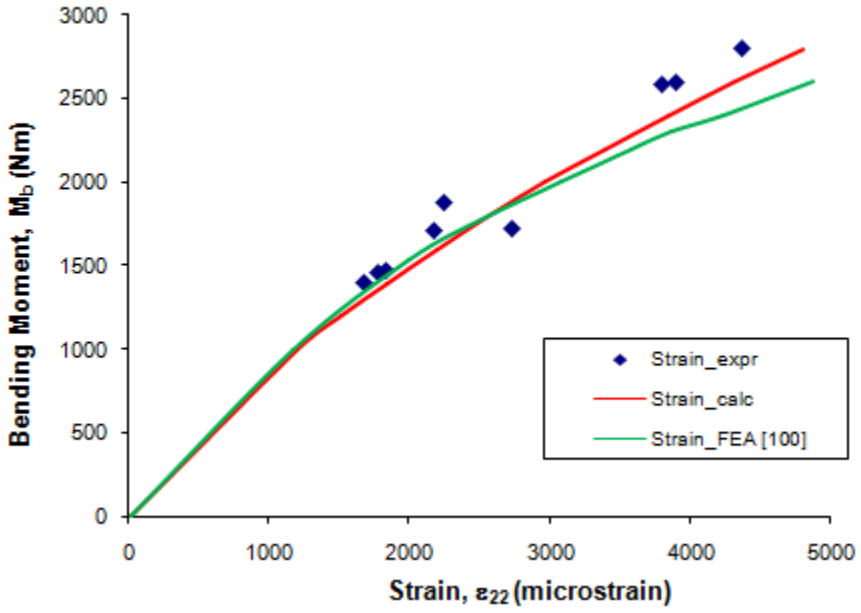

Figure 5-30: Comparison of computed and measured notch root strains on the SAE shaft for bending loading

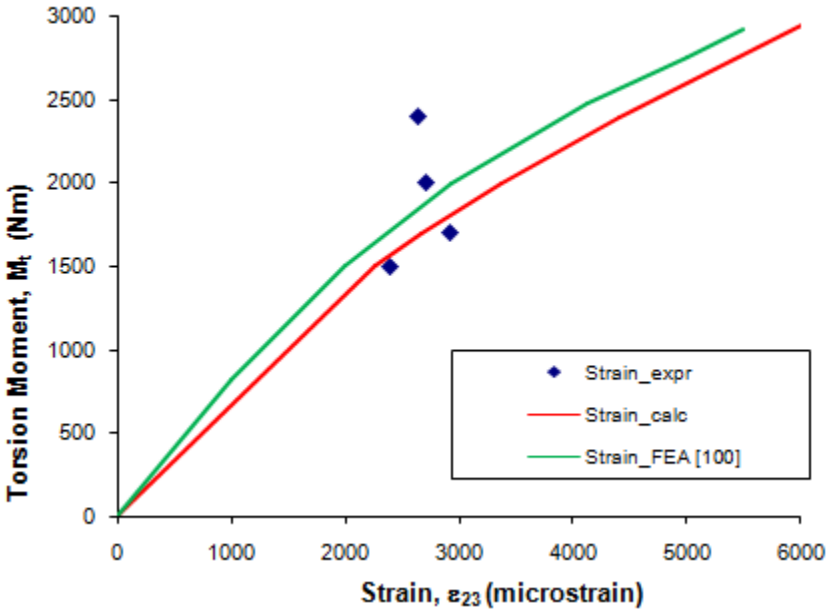

Figure 5-31: Comparison of computed and measured notch root strains on the SAE shaft for torsion loading

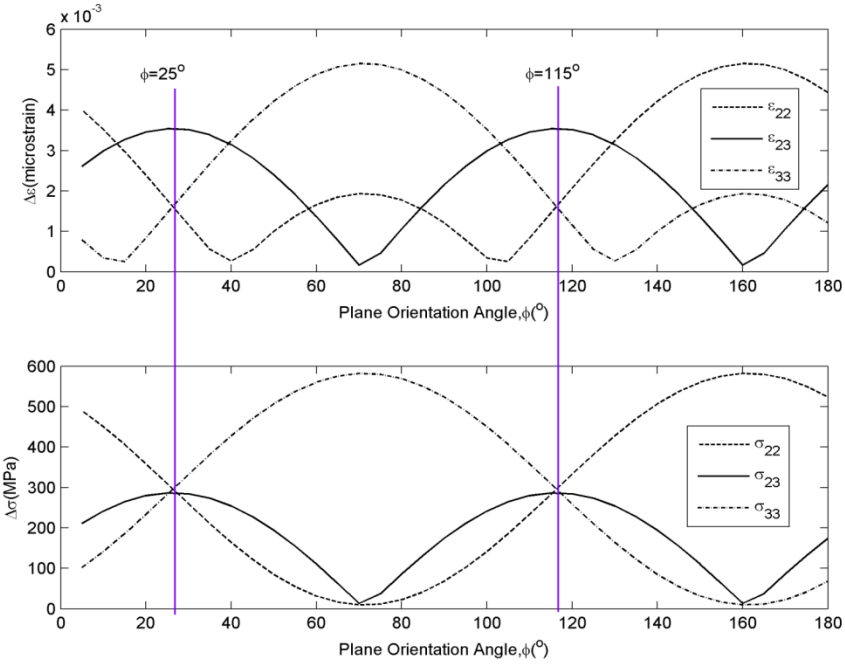

Figure 5-32: Stress and strain ranges with plane angle for the SAE shaft under in-phase loading (M_b=1300 Nm and M_t=1400 Nm)

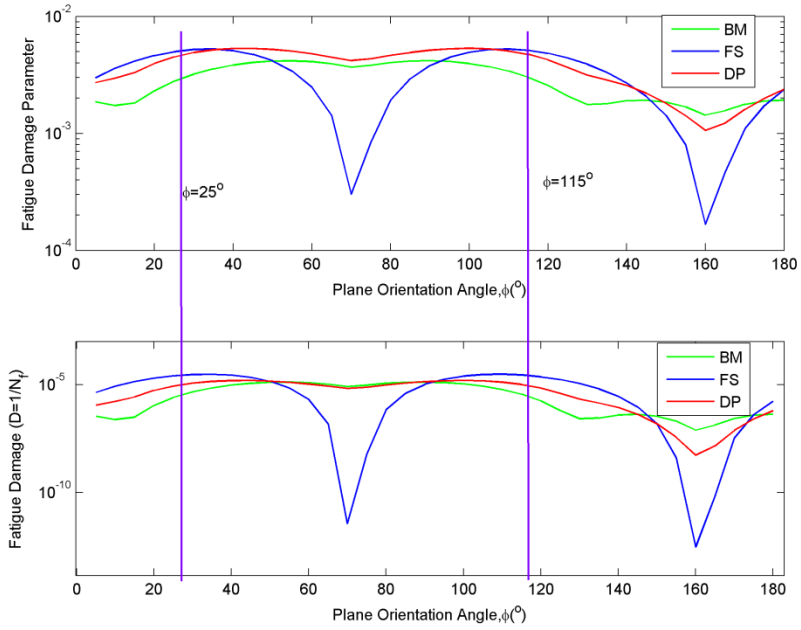

Figure 5-33: Variations of fatigue damage parameters with plane angle for the SAE shaft under in-phase loading (M_b=1300 Nm and M_t=1400 Nm)

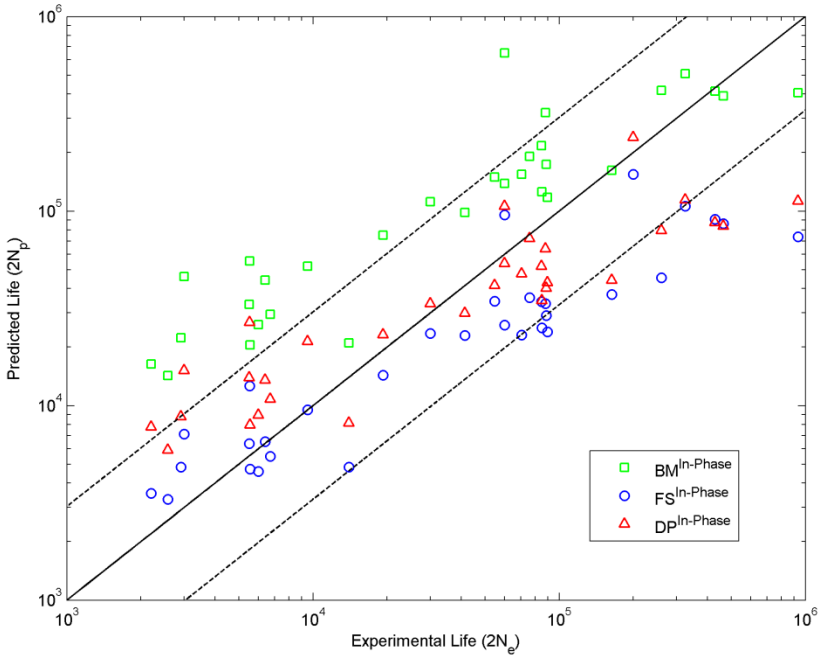

Figure 5-34: Comparison of Proposed Damage Parameter (DP), Fatemi-Socie (FS) and Brown-Miller (BM) parameter with in-phase experimental fatigue data of the SAE shaft

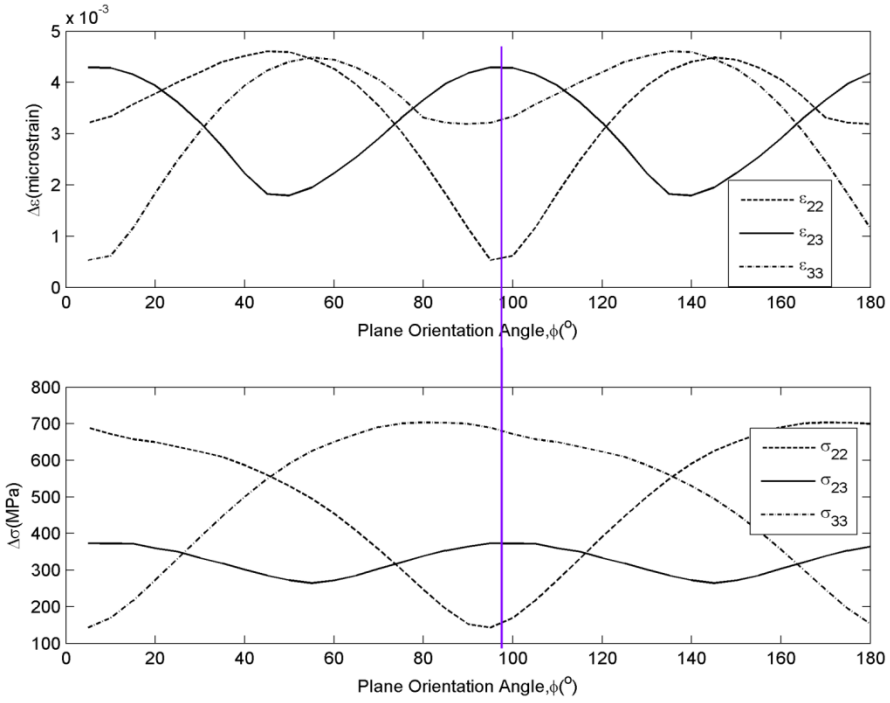

Figure 5-35: Variations of stress and strain ranges with plane angle for the SAE shaft under out-of-phase loading (M_b=1295 Nm, M_t=1710 Nm)

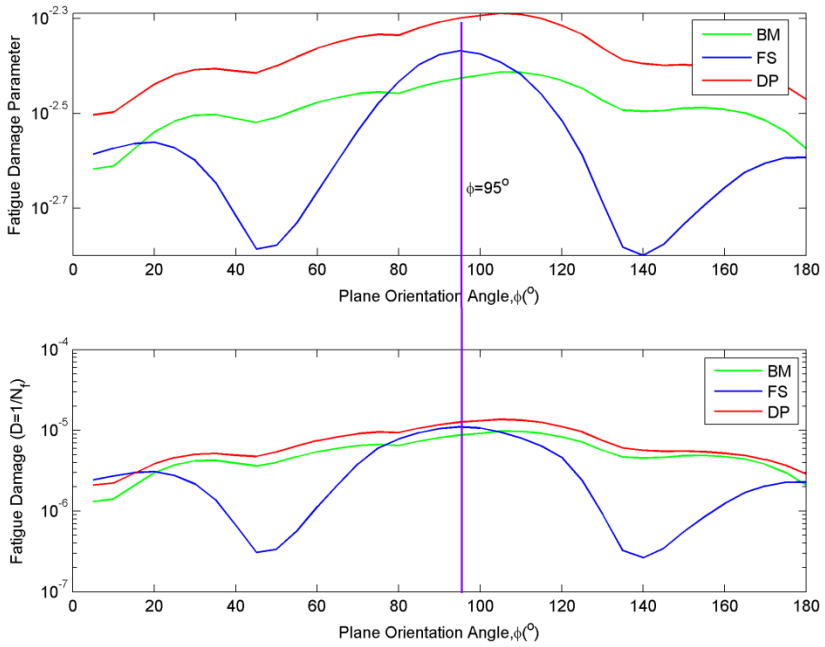

Figure 5-36: Variations of fatigue damage parameters with plane angle for the SAE shaft under out-of-phase loading (M_b=1295 Nm and M_t=1710 Nm)

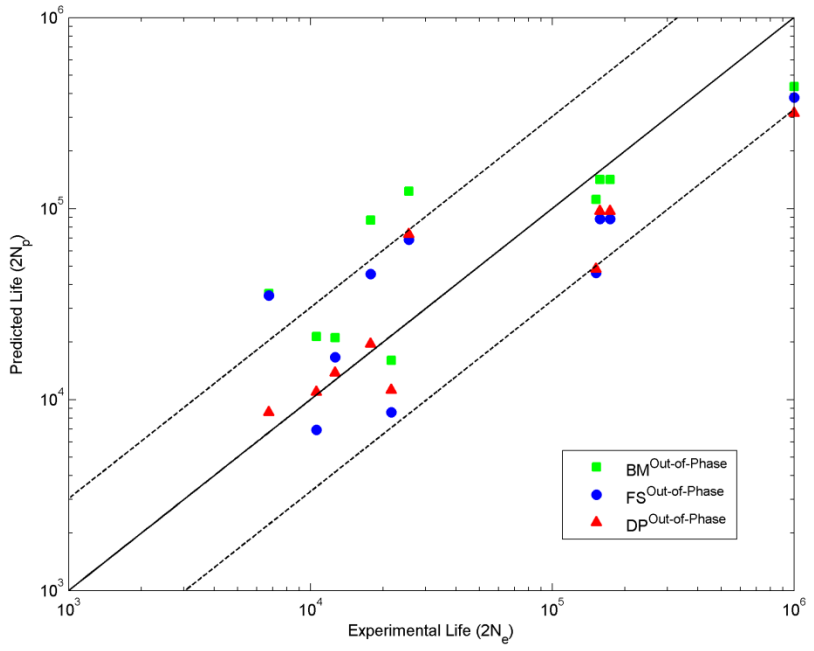

Figure 5-37: Comparison of Proposed Damage Parameter (DP), Fatemi-Socie (FS) and Brown-Miller (BM) parameter with out-of-phase experimental fatigue data of the SAE shaft

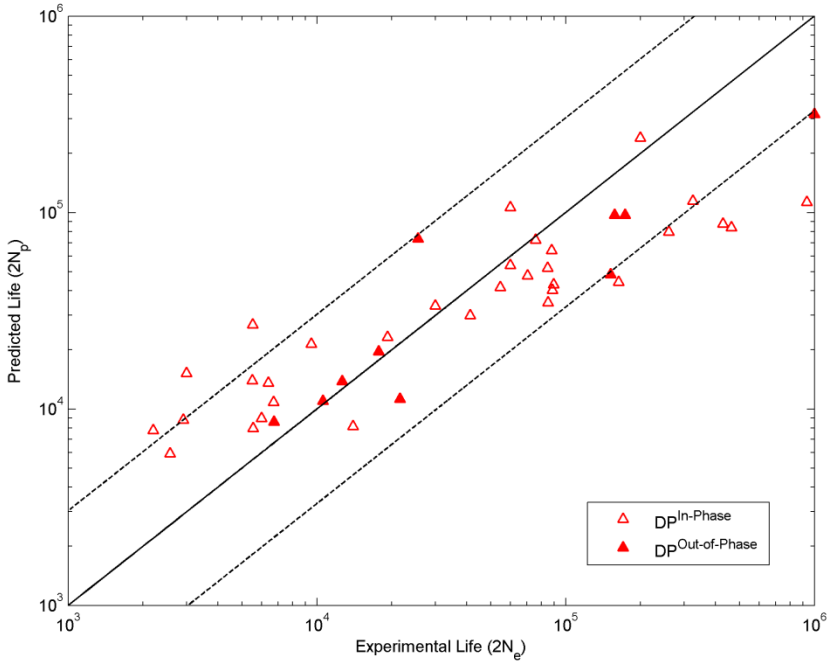

Figure 5-38: Comparison of Proposed Damage Parameter with experimental fatigue data of the SAE shaft under in-phase and out-of-phase loading

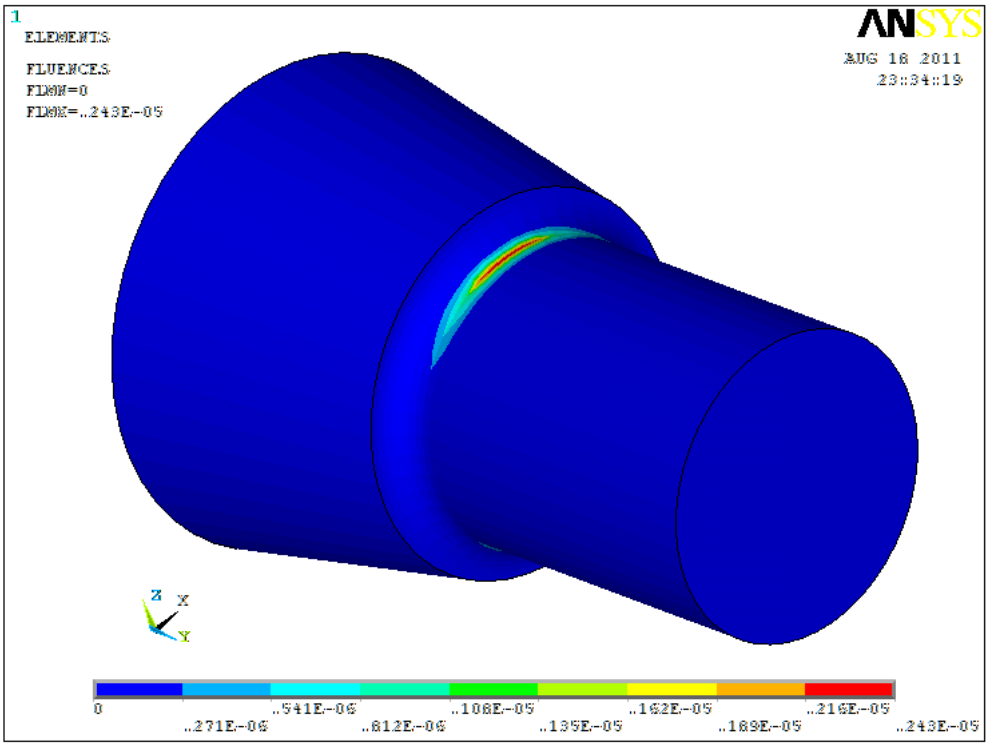

Figure 5-39: Damage contour around notch for SAE shaft under M_b=1400 Nm and M_t=0 Nm in-phase loading

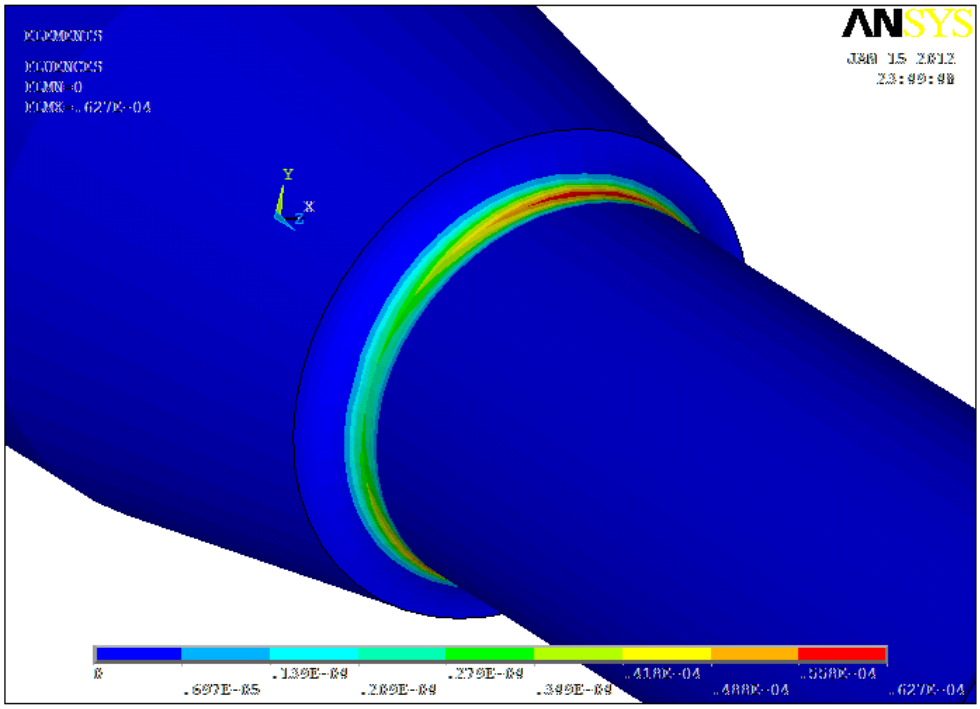

Figure 5-40: Damage contour around notch for SAE shaft under M_b=1150 Nm and M_t=2700 Nm in-phase loading

Chapter 6
Conclusions and Future Recommendations

Understanding of multiaxial fatigue problem is essential for the reliability assessment and the design against fatigue failure for mechanical components under realistic service conditions. Durability evaluation of vehicle suspension and driveline components based on experimental assessments is expensive and time-consuming. Therefore, analytical and numerical methods become an essential approach to conduct fatigue and durability analyses. The main objective of this research is to develop and validate a multiaxial fatigue analysis methodology for mechanical notched components subject to complex multiaxial loadings.

The proposed multiaxial fatigue analysis methodology for performing multiaxial fatigue life prediction for notched components has been developed and implemented in computer program(s). The multiaxial fatigue analysis methodology incorporates the elastic-plastic stress/strain model and the proposed multiaxial fatigue damage parameter. The elastic-plastic stress/strain model, which was originally proposed by Buczynski and Glinka [74], is used to compute elastic-plastic stress-strain responses from linear-elastic FE results for notch areas. The elastic-plastic stress/strain model is based on the Garud cyclic plasticity model integrated with the multiaxial Neuber correction rule. Chapter 3 presented the procedure for integrating the Neuber multiaxial notch correction rule and the Garud cyclic plasticity for numerical implementation of the notch stress and strain analysis from the pseudo elastic stress-strain histories (linear elastic FE results). The development and implementation of the proposed multiaxial fatigue damage parameter based on the maximum damage plane to predict the fatigue life for mechanical

components under the multiaxial loadings were discussed in Chapter 4. The proposed multiaxial fatigue damage parameter, which establishes the relation between the fatigue damage parameter and the fatigue life, includes all stress and strain components on the maximum damage plane in the formulation of the fatigue damage parameter. The multiaxial fatigue damage parameter was defined as the generalized strain amplitude on the maximum damage plane. The numerical implementation of the proposed multiaxial fatigue analysis methodology was also presented in Chapter 4.

The fatigue damage can be used as a design criterion and concept designs can be analytically assessed such that the predicted fatigue life of the component(s) can satisfy and/or exceed the expected service life. This capability allows design of components to be evaluated and optimized for the service life in the early design phase. The proposed multiaxial fatigue analysis methodology including the elastic-plastic stress/strain model, the multiaxial fatigue damage parameter, algorithms and procedures discussed in this study is efficient, robust and reasonably accurate to be used as a design tool for notched components in ground vehicles.

6.1 **Conclusions**

Application and validation of the multiaxial fatigue analysis methodology were presented by comparing computed results of the multiaxial fatigue analysis methodology to the experimental data in Chapter 5. The accuracy of local stress and strain histories is essential for the accurate fatigue life prediction. Therefore, the elastic-plastic stress/strain model was validated against the experimental results of SAE 1070 steel notched shaft obtained by Barkey. Based on the comparison between the experimental and computed strain histories for the several non-proportional load paths, the elastic-plastic stress/strain

model predicted notch strains with reasonable accuracy using linear-elastic FE stress histories.

The proposed multiaxial fatigue damage parameter has been applied to the uniaxial loading to account for mean stress effects on fatigue life. Four sets of experimental fatigue data for Incoloy 901 super alloy, ASTM A723 steel, 7075-T561 aluminum alloy and 1045 HRC 55 steel were used to investigate the prediction capabilities of the proposed fatigue damage parameter for mean stress correction. The proposed mean stress correction parameter was found to be superior over both the SWT and the Morrow parameter for Incoloy 901 super alloy and ASTM A723 steel. Both the proposed and SWT fatigue damage parameters provided equally good correlation with experimental data for 7075-T561 aluminum alloy and 1045 HRC 55 steel.

In case of multiaxial loadings, the prediction capability of the proposed multiaxial fatigue damage parameter was evaluated by comparing fatigue lives predicted by the proposed damage parameter with experimental data of the thin-walled tubular specimens machined from 1045 HR steel and Inconel 718 alloy subjected to the proportional (in-phase) and non-proportional (out-of-phase) loadings in Chapter 5. The proposed fatigue damage parameter was found to provide very good correlation with experimental fatigue data of 1045 steel and Inconel 718 thin-walled tube specimens under proportional and non-proportional loadings.

Since SAE notched shaft specimens represent complex stress-strain state of realistic engineering components, experimental data of the SAE 1045 notched shaft were used to verify the prediction capability of both the elastic-plastic stress/strain model and the proposed multiaxial fatigue damage parameter for notched components. The

experimental fatigue data of the SAE 1045 notched shaft under proportional and non-proportional loadings were compared to results of the analytical elastic-plastic stress/strain model for notch strains and the proposed fatigue damage parameter for fatigue lives. Computed strain histories at the notch root obtained from the elastic-plastic stress/strain model correlated well with experimental strain data of the SAE 1045 notched shaft. The proposed multiaxial fatigue damage parameter based on the generalized strain amplitude on the maximum damage plane satisfactorily correlated experimental fatigue data of the SAE shaft under proportional and non-proportional loadings specified in Chapter 5. In addition, the proposed fatigue damage parameter provided noticeable improvements to both the Brown-Miller and the Fatemi-Socie parameters in predicting fatigue lives for the SAE shaft under the proportional and non-proportional loadings.

6.2 **Summary of Contributions**

Main contributions of this thesis are summarized below:

- Development and numerical implementation of the multiaxial fatigue analysis methodology for notched components.
- Development of a macro using APDL and a computer program written in Fortran 90 to calculate linear elastic stress histories at critical notch areas for notched components under multiaxial load histories.
- Improvement of the multiaxial elastic-plastic stress-strain model (previously developed by Buczynski and Glinka [91]) to such a level of sophistication that it can be used for the elastic-plastic stress-strain analysis for notched components using linear-elastic FE stress histories. The paper describing the

improved multiaxial elastic-plastic stress-strain model has been accepted at International Conference on Fatigue Damage of Structural Materials IX, Hyannis, USA, 2012 [92].

- Development and validation of an original multiaxial fatigue damage parameter based on a critical plane approach to estimate fatigue life of notched components under the multiaxial loading. The paper analyzing the proposed multiaxial fatigue damage parameter has been accepted at International Conference on Fatigue Damage of Structural Materials IX, Hyannis, USA, 2012[93].

- Successful application of the multiaxial fatigue damage parameter to the uniaxial loading as a mean stress correction parameter. The paper showing prediction capabilities of the proposed mean stress correction parameter was published by Ince and Glinka [81].

6.3 **Recommendations for Future Work**

The proposed multiaxial fatigue analysis methodology for elastic-plastic stress and strain calculations and multiaxial fatigue life predictions at notches appears to be a relatively accurate and promising method for general engineering applications, specifically in the ground vehicle industry. However, additional experimental data including discriminating loading paths should be used to further assess prediction capabilities of the proposed multiaxial fatigue analysis methodology and verify its robustness. It has been shown that the proposed fatigue damage parameter is also successfully applied to the uniaxial loading as mean stress correction parameter. Application of the proposed multiaxial fatigue damage parameter to account for mean

stress effects for notched components under multiaxial loadings should also be investigated in future.

The proposed fatigue analysis methodology presented in this study represented a general approach for the fatigue damage assessment of notched components under constant amplitude multiaxial loadings. However, most of engineering components are subjected to variable amplitude multiaxial loadings. In order to apply the proposed multiaxial fatigue damage parameter to variable amplitude load histories, a cycle counting method is required to identify loading cycles and associate individual cycle to the fatigue damage. Banantine and Socie [75], Wang and Brown [94] and Langlais [95] cycle counting methods are some of known proposals for the multiaxial cycle counting method for the critical plane application. However, these cycle counting methods are derived from the extension of uniaxial cycle counting method and no multiaxial cycle counting method has been yet proven to work well for all types of loading conditions. Therefore, attempts should be made as a future research study to develop a comprehensive cycle counting method thus extending the proposed fatigue assessment methodology to include an effective multiaxial cycle count method. The proposed multiaxial fatigue analysis methodology can then be applied to fatigue life prediction for more general variable amplitude load histories. Better understanding of all elements of variable amplitude multiaxial fatigue life predictions such as load amplitude and load path dependence of load sequence effects and their associations with cumulative damage rules(a linear or non-linear cumulative damage rules) is a important research topic for future research study in the multiaxial fatigue analysis.

References

[1] Tipton, S.M. and Nelson, D.V**.,** Advances in Multiaxial Fatigue Life Prediction for Components with Stress Concentrations**,** International Journal of Fatigue, Vol. 19, No. 6, pp. 503-515, 1997.

[2] Ramberg, W., and Osgood, W. R, Description of stress-strain curves by three parameters, *Technical Note No. 902*, National Advisory Committee For Aeronautics, 1943, Washington DC

[3] Massing G., Proceeding 2nd International Congress on Applied Mechanics, Zurich, Switzerland, 1926.

[4] Hencky, H., Zur Theorie plastischer Deformationen. Z. Angew.Math. Mech., Vol. 4, pp.323–334, 1924.

[5] Prandtl, W., Spannungsverteilung in Plastischen Kerpern, Proceedings of the First International Congress on Applied Mechancis, pp. 43, 1924.

[6] Reuss, E., Beruecksichtigung der elastischen Formaenderungen in der Zeit- schrift fur Angewandte Mathematik und Mechanik, Vol. 10, pp. 266-274.

[7] Drucker, D.C., A More Fundamental Approach to Plastic Stress-Strain Relation, Proceedings of the Frist U.S. Congress of Applied Mechanics, ASME, pp. 487-491, 1952.

[8] Hill, R., The Mathematical Theory of Plasticity, Oxford University of Press, 1950.

[9] Bauschinger, J., Miitt. Mech.-Tech., vol. 13, Lab Munchen, 1886.

[10] Prager, W., A New Method of Analyzing Stresses and Strains in Work-Hardening Plastic Solids, Journal of Applied mechanics, Vol.23, pp. 493-496, 1956.

[11] Mroz, Z., 1967, On the description of anisotropic workhardening, Journal of the Mechanics and Physics of Solids, Vol. 15, pp. 163-175.

[12] Garud, Y.S., A New Approach to the Evaluation of Fatigue under Multiaxial Loadings, Journal of Engineering Materials and Technology, Vol. 103, pp. 118-125,1981.

[13] Chu, C. C., A Three-Dimensional Model of Anisotropic Hardening in Metals and Its Application to the Sheet Metal Forming, Journal of Mechanics and Physics of Solids, Vol. 32, No. 3, pp. 197-212, 1984.

[14] Krieg, R. D., A Practical Two Surface Plasticity Theory, Journal of Applied Mechanics, pp. 641-646, 1975.

[15] Dafalias, Y. F., and Popov, E.P., A Model of Nonlinearly Hardening Materials for Complex Loading, Acta Mechanica, Vol.21, No. 2-3, pp. 173-192, 1975.

[16] Philips, A., Tang, J. L., Riccuitti and M., Some New Observation on Yield Surfaces, Acta Mechanica, vol. 20, pp. 23-39, 1974.

[17] Tseng, N.T., and Lee, G.C., "Simple Plasticity Model of the Two-Surface Type", Journal of Engineering Mechanics, Vol.109, No.3, pp. 795-810, 1983.

[18] Amstrong, P. J., Frederick, C. O., A Mathematical Representation of the Multiaxial Bauschinger Effect, Tech. Rep. RD/B/N 731, Central Electricity Generating Board, 1966.

[19] Chaboche, J. L., Time-Independent Constitutive Theories for Cyclic Plasticity, International Journal of Plasticity, Vol. 2, No.2, pp. 149-188, 1986.

[20] Chaboche, J.L., and Nouailhas, D., Constitutive Modelling of Ratcheting Effects, Part I: Experimental Facts and Properties of the Classical Models , Journal of Engineering Materials and Technology, Vol. 111, pp. 384-392, 1989.

[21] Bower, A.F., Cyclic Hardening Properties of Hard-Drawn Copper and Rail Steel, Journal of Mechanics and Physics of Solids, Vol.37, No.4, pp.455-470, 1989.

[22] Ohno, N., and Wang, J.D., Two Equivalent Forms of Nonlinear Kinematic Hardening: Application to Non- Isothermal Plasticity" International Journal of Plasticity, Vol. 7, pp. 637-650, 1991.

[23] Voyiadjis, G. Z., and Kattan, P. I., A Generalized Eulirian Two-Surface Plasticity Model for Finite Strain, Acta Mechanica, Vol. 81, pp. 143-162, 1990.

[24] Jiang, Y., and Kurath, P., "A Theoretical Evaluation of Plasticity Hardening Algorithms for Nonproportional Loading", Acta Mechanica, Vol.118, pp. 213-234, 1996.

[25] Chen, X., Gao, Q., and Sun, X. F., Low Cycle Fatigue under Non-proportional Loading, Fatigue and Facture of Engineering Materials and Structures, Vol. 19, no. 7, pp. 839-854, 1996.

[26] Peterson, R.E., Stress Concentration Factors, John Wiley & Sons, New York, 1977.

[27] Stowell, E.Z., Stress and Strain Concentration at a Circular Hole in an Infinite Plate, NACA Technical Report 2073, 1950.

[28] Hardrath, H.F., Ohman, H., A Study of Elastic Plastic Stress Concentration factors due to Notches and Fillets in Flat Plate, NACA Technical Report 2566, 1951.

[29] Neuber, H., Theory of Stress Concentration for Shear Strained Prismatic Bodies with Arbitrary Stress–Strain Law, Journal of Appl. Mechanics, Vol. 28, pp. 544-550, 1961.

[30] Topper, T.H., Wetzel, R.M., and Morrow, J.D., Neuber's Rule Applied to Fatigue of Notched Specimens, Journal of Materials, Vol. 1, pp. 200-209, 1969.

[31] Molski, K., Glinka, G., A Method of Elastic-Plastic Stress and Strain Calculation at a Notch Root, Materials Science and Engineering, Vol. 50, pp. 93-100, 1981.

[32] Glinka, G., Energy Density Approach to Calculation of Inelastic strain–stress near notches and cracks, Engineering Fracture Mechanics, Vol. 22, pp.485–508, 1985.

[33] Hoffmann, M., Seeger, T., A Generalized Method for Estimating Multiaxial Elastic–Plastic Notch Stresses and Strains, Part I: Theory, Journal of Engineering Materials and Technology, Vol. 107, pp. 250-254, 1985.

[34] Hoffmann, M., Seeger, T., Stress–Strain Analysis and Life Predictions of a Notched Shaft under Multiaxial Loading, Multiaxial Fatigue: Analysis and Experiments AE-14, G.E. Leese, D.Socie Eds., Society of Automotive Engineers, Warrendale, PA, pp. 81–101, 1989.

[35] Moftakhar, A. A., Calculation of Time Independent and Time-Dependent Strains and Stresses in Notches, Ph. D. Dissertation, University of Waterloo, Department of Mechanical Engineering, Waterloo, Ontario, Canada, 1994.

[36] Moftakhar, A., Buczynski, A. and Glinka, G., Calculation of Elasto-Plastic Strains and Stresses in Notches under Multiaxial Loading, International Journal of Fracture, Vol.70, pp. 357-373, 1995.

[37] Hoffmann, M., Amstutz, H., and Seeger, T., Local Strain Approach in Non-Proportional Loadings, K. Kussmaul, D. McDiarmid, and D. Socie Eds., Fatigue under Biaxial and Multiaxial Loadings - ESIS 10, London, pp. 357-376, 1991.

[38] Barkey, M.E., Calculation of Notch Strains under Multiaxial Nominal Loading, Ph. D. Dissertation, University of Illinois at Urbana-Champaign, 1993.

[39] Barkey, M.E., Socie, D.F. and Hsia, K.J., A Yield Surface Approach to the Estimation of Notch Strains for Proportional and Non-proportional Cyclic Loading, ASME Journal of Engineering Materials and Technology, Vol. 116, pp. 173-180, 1994.

[40] Koettgen, V.B., Schoen, M., and Seeger, T., Application of Multiaxial Load-Notch Strain Approximation Procedure to Autofrettage of Pressurized Components, Advances in Multiaxial Fatigue, ASTM STP 1191, D.L. McDowell and R.Ellis, Eds., American Society for Testing and Materials, Philadelphia, pp. 375-396, 1993.

[41] Singh, M.N.K., Notch Tip Stress-Strain Analysis in Bodies Subjected to Non-Proportional Cyclic Loads, Ph.D. Dissertation, Dept. Mech. Eng., University of Waterloo, Ontario, Canada, 1998.

[42] Karolczuk, A. and Macha, E., A review of critical plane orientations in multiaxial fatigue failure criteria of metallic materials , International Journal of Fracture , Vol.134, pp. 267-304, 1995.

[43] Liu, Y. and S. Mahadevan, An unified multiaxial fatigue damage model for isotropic and anisotropic materials. International Journal of Fatigue, Vol. 29, pp.347-359, 2007.

[44] Li, B., L. Reis and M. de Freitas, Comparative study of multiaxial damage models for ductile structural steels and brittle materials, International Journal of Fatigue, Vol. 31, pp.1895-1906, 2009.

[45] Sines, G., Behavior of Metals under Complex Static and Alternating Stresses in Metal Fatigue, G. Sines and J.L. Waisman, eds., McGraw-Hill, New York, pp. 145-169, 1959.

[46] Sines, G., Failure of Materials under Combined Repeated Stresses with Superimposed Static Stresses, Tech. Note 3495, National Advisory Committee for Aeronautics, Washington, DC, 69 pp, 1955.

[47] Findley, W.N., A, Theory for Effect of Mean Stress on Fatigue of Metals under Combined Torsion and Axial Load or Bending, J. Eng. Ind., 301–306, 1959.

[48] McDiarmid, D.L., A Shear Stress Based Critical-Plane Criterion of Multiaxial Fatigue Failure for Design and Life Prediction, Fatigue and Fracture of Engineering Materials and Structures, Vol. 17, No. 12, pp. 1495-1485, 1994.

[49] Dang Van, K., Macro-Micro Approach in High-Cycle Multiaxial Fatigue, In Advances in Multiaxial Fatigue, (Edited By Mcdowell, D.L. And Ellis, R.), American Society for Testing and Materials STP 1191, Philadelphia, pp. 120-130, 1993.

[50] Yokobori, Y., Yamanouchi, H., Yamamoto, S., Low Cycle Fatigue of Thin-Walled Hollow Cylinder Specimens of Mild Steel in Uniaxial and Torsional Tests at Constant Amplitude, International of Fracture Mechanics, Vol.1, pp. 3-13, 1956.

[51] Brown, M.W., Miller, K.J. A Theory For Fatigue Failure under Multiaxial Stress–Strain Conditions, Proceedings of the Institute of Mechanical Engineers Vol. 187, 1973, pp. 745-755, 1973.

[52] Kandil, F.A., and Brown M.W., and Miller, K.J., Biaxial Low Cycle Fatigue Fracture of 316 Stainless Steel at Elevated Temperatures, Book 280, The Metals Society, London, pp. 203-210, 1982.

[53] Wang, C.H., Brown, M.W., A Path-Independent Parameter for Fatigue under Proportional and Nonproportional Loading, Fatigue and Fracture of Engineering Materials and Structures, Vol. 16, No. 12, pp. 1285-1298, 1993.

[54] Socie, D.F., Waill, L.A. and Dittmer, D.F., Biaxial Fatigue Of Inconel 718 Including Mean Stress Effects, I Multiaxial Fatigue (edited by Miller, K.J. and Brown, M.W.), ASTM STP 853, Philadelphia, 463–481, 1985.

[55] Fatemi, A., Socie, D.F., A Critical Plane Approach to Multiaxial Fatigue Damage Including Out-of-Phase Loading, Fatigue and Fracture of Engineering Materials and Structures, Vol. 11, No. 3, pp. 149-166, 1988.

[56] Smith, K.N., Watson, P. and Topper, T.H., A stress-strain function for the fatigue of materials, Journal of Materials, pp. 767-778, 1970.

[57] Liu, K.C., A Method Based On Virtual Strain-Energy Parameters for Multiaxial Fatigue Life Reduction, Advances in Multiaxial Fatigue (edited by McDowell, D.L. and Ellis, R.), ASTM STP 1191, PA, pp. 67-84, 1993.

[58] Chu, C.C., Conle, F.A., Bonnen, J.F., Multiaxial Stress-Strain Modelling and Fatigue Life Prediction of SAE Axle Shafts, Advances in Multiaxial Fatigue (edited by McDowell, D.L. and Ellis, R.), ASTM STP 1191, PA, pp. 37-54, 1993.

[59] Glinka, G., Shen, G. and Plumtree. A., A Multiaxial Fatigue Strain Energy Density Parameter Related to The Critical Fracture Plane, Fatigue of Engineering Materials and Structures, Vol.18, pp.37–46, 1995.

[60] Glinka, G., Shen, G. and Plumtree. A., Mean Stress Effects in Multiaxial Fatigue, Fatigue of Engineering Materials and Structures, Vol.18, pp.755–764, 1995.

[61] Pan, W., Hung, C., Chen, L., Fatigue Life Estimation under Multiaxial Loadings, International Journal of Fatigue, Vol. 21, pp. 3-10, 1997.

[62] Chen, X., Xu, S., Huang, D., A Critical Plane-Strain Energy Density Criterion for Multiaxial Low-Cycle Fatigue Life Under Non-Proportional Loading, Fatigue of Engineering Materials And Structures, Vol. 22, pp. 679-686.

[63] Varvani-Farahani, A., A New Energy-Critical Plane Parameter for Fatigue Life Assessment of Various Metallic Materials Subjected to In-Phase And Out-of-Phase Multiaxial Fatigue Loading Conditions, International Journal of Fatigue, Vol. 22, pp. 295–305, 2000.

[64] Jahed H., and Varhani-Farahani, A., Upper and Lower Fatigue Limits Model Using Energy-based Fatigue Properties, Vol. 28, pp. 467-473, 2005.

[65] Palmgren, A., Durability of ball bearings, ZVDI, Vol. 68, No. 14, Germany, pp.339-341,1924.

[66] Miner, M. A., Cumulative damage in fatigue, Journal of Applied Mechanics,Vol. 12, ASME Trans., Vol. 67, pp. A159-A164, 1945.

[67] Marco, S. M. and Starkey, W. L., A concept of fatigue damage, ASME Transaction, Vol. 76, No. 4, pp. 627-632, 1954.

[68] Robillard, M. and Cailletaud, G., Directionally Defined Damage in Multiaxial Low Cycle Fatigue: Experimental Evidence and Tentative Modelling, European Structural Integrity Society, ESIS Publication 10, Mechanical Engineering Publications, London, pp. 103-130, 1991.

[69] Harada, S. and Endo, T., On the Validity of Miner's Rule Under Sequential Loading of Rotating Bending and Cyclic Torsion, European Structural Integrity Society, ESIS Publication 10, Mechanical Engineering Publications, London, pp. 161-178, 1991.

[70] Shamsaie, N., Fatemi, A. and Socie, D.F., Multiaxial fatigue evaluation using discriminating strain paths, International Journal of Fatigue, Vol. 33, pp. 597-609, 2011.

[71] Kallmeyer, A.R., Krgo, A., Kurath, P., Evaluation of Multiaxial Fatigue Life Prediction Methodologies for Ti-6Al-4V, Journal of Engineering Materials and Technology, Vol. 124, pp. 229-237, 2002

[72] Jahed H., Lectures Notes of Linear and Non-Linear Stress Analysis, University of Waterloo, 2009.

[73] Socie, D.F., Marquis, G.B., Multiaxial Fatigue, Society of Automotive Engineers, Warrendale PA, 2000.

[74] Buczynski, A., and Glinka, G., Elastic-plastic Stress-Strain Analysis of Notches under Non-Proportional Loading Paths, in Proceedings of the International Conference on Progress in Mechanical Behaviour of Materials (ICM8), Victoria, May 16-21, 1999, eds. F. Ellyin and J.W. Provan, vol. III, pp. 1124-1130, 1999.

[75] Bannantine, J. A. and Socie, D. F., A variable amplitude multiaxial fatigue life prediction model, Fatigue under Biaxial and Multiaxial Loading, European Structural Integrity Society, ESIS Publication 10, Mechanical Engineering Publications, London, pp. 35-51, 1995.

[76] Shamsaie, N. and Fatemi, A., Multiaxial fatigue: An overview and some approximation models for life estimation, International Journal of Fatigue, Vol. 33, pp. 548-558, 2011.

[77] Chu C.C, Fatigue Damage Calculation Using the Critical Plane Approach, Journal of Engineering Materials and Technology, Vol. 117, pp.41-49, 1995.

[78] Basquin O.H., The exponential law of endurance tests, Am. Soc. Testing Mater Proc. 10,pp. 625–30, 1910.

[79] Socie, D. F. and Morrow J.D., Review of Contemporary Approaches to Fatigue Damage Analysis, Risk and Failure Analysis for Improved Performance and Reliability J. J. Burke and V. Weiss, eds., Plenum Pub. Corp. New York, NY, pp. 141-194, 1980.

[80] Smith, K.N., Watson, P. and Topper, T.H., A stress-strain function for the fatigue of materials, Journal of Materials 5, pp.767-778, 1970.

[81] Ince, A. and Glinka, G., A modification of Morrow and Smith-Watson-Topper mean stress correction models, Fatigue of Engineering Materials and Structures Vol.34, pp.854–867, 2011.

[82] Koh, S.K. and Stephens, R.I., Mean stress effects on low cycle fatigue for a high strength steel, Fatigue of Engineering Materials and Structures 14, pp.413-428, 1991.

[83] Fang, D. and Berkovits, A., Mean stress models for low cycle fatigue of a nickel-based superalloy, International Journal of Fatigue 16, pp.429-437, 1994.

[84] Zhao, T. and Jiang, Y., Fatigue of 7075-T651 aluminum alloy. International Journal of Fatigue 30, pp.834-849, 2008.

[85] Wehner, T. and Fatemi, A., Effects of mean stress fatigue behavior of a hardened carbon steel, International Journal of Fatigue 13(3), pp.241-248, 1991.

[86] Fatemi, A., Fatigue and Deformation under Proportional and Nonproportional Biaxial Loading, Ph. D. Dissertation, University of Iowa, Iowa, 1985.

[87] Koch, J.L., Proportional and Nonproportional Biaxial Fatigue of Inconel 718, Report No. 121, University of Illinois, Urbana-Champaign, 1985.

[88] Kurath, P. S., Downing, D. and Galliart, D., Summary of non-hardened notched shaft rounded robin program. In: Multiaxial Fatigue, Analysis and Experiments (Edited by G. E. Leese and D. Socie), SAE, AE-14, pp. 13-32, 1989.

[89] Fash, J.W., An evaluation of damage development during multiaxial fatigue of smooth and notched specimens, Report No. 123, University of Illinois, Urbana-Champaign, 1985.

[90] Das, J., and Sivakumar, S.M., An evaluation of multiaxial fatigue life assessment methods for engineering components, International Journal of Pressure Vessels and Piping, Vol. 76, pp.741–746, 1999.

[91] Buczynski, A., and Glinka, G., Elastic-plastic Stress-Strain Analysis of Notches under Non-Proportional Loading Paths, in Proceedings of the International Conference on Progress in Mechanical Behaviour of Materials (ICM8), Victoria, May 16-21, 1999, eds. F. Ellyin and J.W. Provan, vol. III, pp. 1124-1130, 1999.

[92] Ince, A., and Glinka, G., Computational Modelling of Multiaxial Elasto-plastic Stress-strain Analysis for Notched Components under Non-proportional Loading,

International Conference on Fatigue Damage of Structural Materials IX, Hyannis, MA, USA, 2012.

[93] Ince, A., and Glinka, G., A Critical Plane Damage Parameter for Multiaxial Fatigue Life under Proportional and Non-proportional Loadings, International Conference on Fatigue Damage of Structural Materials IX, Hyannis, MA, USA, 2012.

[94] Wang, C. H. and Brown, M. W., Life prediction techniques for variable amplitude multiaxial fatigue-part 1: theories, Journal of Engineering Materials and Technology, Vol. 118, pp. 367-370, 1996.

[95] Langlais, T. E., Vogel, J. H., and Chase, T. R., Multiaxial cycle counting for critical plane methods, International Journal of Fatigue, Vol.25, pp. 641-647, 2003.